Towards Switchable Biological Surfaces for On-Demand Biosensing in Cell Therapy Bioprocessing

By

Daniel Carroll

A thesis submitted to the University of Birmingham for the degree of
DOCTOR OF PHILOSOPHY

School of Chemical Engineering
College of Engineering and Physical Sciences
University of Birmingham

July 26, 2024

“The meeting of two personalities is like the contact of two chemical substances:

if there is any reaction, both are transformed.”

- Carl Jung

Abstract

Over the past two decades advancements in our understanding of biological processes has opened the door to new and effective therapeutic products. In particular, cell and gene therapies have established themselves as pillars of modern medicine, which are often used to respond to diseases not effectively treated by other methods. However, therapies derived from biological sources have a higher degree of natural variability compared to small drug molecules obtained through traditional chemical synthesis. Manufacturing of such therapeutics requires constant monitoring to ensure product yield and efficacy. However, current bioprocesses used for the manufacturing of cell therapy products rely on off-line or end-point diagnostics. This results in long feedback loops limiting the capacity to react to needs of the cell culture in real time. Therefore, the need for integrated biosensing platforms has never been higher. To this end, this research explores combining nanobodies (Nbs), electropolymerised films, and stimuli response surfaces for the robust, sensitive, and on-demand detection of key cellular biomarkers. The capacity of oligopeptides to modulate surface Nb-antigen interactions was successfully confirmed using electrochemical surface plasmon resonance. Furthermore, surface characterisation techniques including X-ray photoelectron spectroscopy, ellipsometry, and electrochemical impedance spectroscopy highlighted the need for better insulation of the gold surface to prevent non-specific interactions. This led to the fabrication and optimisation of different electropolymerised films which also facilitated the covalent attachment of the biomolecules

at the interface. Gold arrays were successfully fabricated in-house through clean-room manufacturing processes including thermal evaporation, spin coating, photolithography, and wet-etching. This platform was integrated with pre-existing potentiostats and the capacity of the working electrodes to be individually electrically addressed was demonstrated. This would allow the detection of multiple analytes from the same sample in an on-demand fashion. Different surface activation and receptor coupling strategies were then adopted from the literature, along with a tailored strategy being developed for the site-specific coupling of Nbs in a controlled orientation. This led to the development of a robust label-free biosensing platform by utilising changes in surface capacitance.

Overall, this works provides a solid foundation and outlines a road map to develop a sensitive biosensing platform with the capacity to modulate receptor-antigen interactions.

To my parents, Colin and Susan Carroll, and my partner, Niamh. Thank you for your support and encouragement. This work would not have been possible without you.

Acknowledgements

Firstly, I would like to thank my supervisor Prof. Paula Mendes for her continuous support and guidance. Your work ethic and persistent drive for knowledge and understanding has been an inspiration.

I would like also give thanks to the wider Mendes research group both past and present. In particular, I would like to thank Hannah who I shared my PhD journey with and was there for all the ups and downs. Thank you Marcos, your experience and knowledge makes you truly irreplaceable. Thank you Rob and Darius for making the office full of laughs and interesting conversations. Thank you to the wider staff at UoB who helped me along the way with advice and training when I needed it.

Thank you Niamh for all your love and support, and my family back home in Ireland, I would not have finished this work without you.

Contents

List of Figures

List of Tables

Acronyms

4-ABA 4-aminobenzoic acid

AC Alternating current

Ala Alanine

4-AMBA 4-aminomethoxybenzoic acid

BE Binding energy

CA Contact angle

CAR-T Chimeric antigen receptor cell therapy

4-CBDT 4-carboxybenzenediazonium tetrafluoroborate

Cdl Double layer capacitance

CE Counter electrode

CPS Counts per second

CV Cyclic voltammetry

C8K Cysteine-(εLysine)$_7$-εLysine

D.I Deionised water

DMF Dimethylformamide

DSC Disuccimidyl carbonate

DVS Divinyl sulfone

EDC 1-Ethyl-3-[3-dimethylaminopropyl]carbodiimide hydrochloride

eGFP Antigen - green fluorescent protein

ELISA Enzyme linked immunosorbent assay

EtOH Ethanol

FWHM Full width at half maximum

GA Glutaraldehyde

GFP Green fluorescent protein

Gly Glycine

His Histidine

LOD	Limit of detection
Lys	Lysine
Nb	Nanobody
4-NBDT	4-nitrobenzenediazonium tetrafluoroborate
NbGFP	Nanobody specific for green fluorescent protein
NHS	Nanobody N-hydroxysuccinimide
OCP	Open circuit potential
PAT	Process analytical technologies
PBS	Phosphate buffered saline
PCB	Printed circuit board
POC	Point of care
Ptyr	Polytyramine
$\mathbf{R}_{ct}$	Charge transfer resistance
RE	Reference electrode
RI	Refractive index
RU	Response units
SA	Succinic anhydride
SAM	Self-assembled monolayer
SMCC	succinimidyl 4-(N-maleimidomethyl)-cyclohexane-1-carboxylate
SPR	Surface plasmon resonance
TMAH	Tetramethylammonium hydroxide
UV	Ultra-violet
WE	Working electrode X-ray photoelectron spectroscopy

Chapter 1. Introduction

1.1 Outlook

Cell therapy, a pillar of modern medicine, involves the transfer of biological material into critically ill patients to produce a therapeutic response to diseases not efficiently treated by other methods [1]. Among these are some of the leading causes of mortality worldwide including cancer, diabetes, heart failure, and stroke [2–5].

Typically the manufacture of cell therapy products involves *in vitro* modification and cellular expansion of isolated immune cells to obtain enough product to achieve a beneficial impact on the patient (typically hundreds of millions of cells per treatment) [6, 7]. However, scaling and optimisation challenges have significantly hampered the translation of this technology into a manufacturing process [8]. Cell cultures are subject to variability and require continuous monitoring to ensure product quality and reproducibility [9]. Most in-line sensors measure simple physiological parameters such as temperature, pH, dissolved oxygen, CO_2, flow rate, and stirrer speed [10]. While complex analysis of key cellular attributes relies on offline or endpoint diagnostics via assays or spectrochemical techniques [11]. This leads to long feedback loops and low product yields as the bioprocess cannot respond to the requirements of the cell culture in real time.

Electrochemical biosensors offer a promising solution to this real-time analytical challenge. These sensors convert biomolecular interactions (antibody-antigen binding) into electrical signals [12]. However, since the first electrochemical, glucose oxidase (GOx) biosensor was introduced in the early 1960s by Leland Clark Jr. [13], widespread commercialisation and adaptation has not been

achieved due to a number of challenges. In particular, monitoring cell therapy bioporocessing has proven difficult as complex biofluids tend to easily foul and destroy the electrochemical biosensor's sensitivity and specificity [14]. This is largely due to lack of control over specific and non-specific surface interactions along with the limited robustness of the surface components used to fabricate the biosensing platform [15].

Recent developments could help overcome these limitations. Surfaces functionalised with nanobodies (Nbs) as receptor elements offer increased physiochemical stability while maintaining affinity and specificity [16]. These qualities could allow the biosensing interface to remain inactive for long periods without losing sensitivity or specificity [17]. In conjunction with Nbs, organic films can be electrochemically grafted to transducer elements (electrodes) to fabricate extremely robust support structures with superior physical, chemical, and electrochemical stability compared to traditional self-assembled monolayers (SAMs) [18–26].

The interactions between receptors and antigens, which are typically probed in these electrochemical biosensors, have been shown to be controllable using stimuli responsive surfaces [27]. In particular, charged oligopeptides can change their conformations in response to applied potentials. This would allow the active site of the receptor to be concealed or exposed to the surrounding environment, thus switching from the 'OFF' to the 'ON' state.

The following section outlines cell therapy bioprocessing in more detail and discusses major challenges facing the industry. A bottom-up approach to biosensor fabrication is then presented, starting with surface modification strate-

gies. This is followed by nanobodies and nanobody based biosensors. Electrically responsive surfaces are then introduced and finally, the motivation and aims of this research are outlined.

1.2 Cell Therapy Bioprocessing

Cell therapy is an established and rapidly advancing field, aimed at repairing or replacing damaged or diseased human cells, tissues, or organs to restore their normal function [28]. The treatment spans multiple therapeutic areas, such as immunotherapy, cancer therapy, and regenerative medicine. With the industry expected to reach an annual turnover of around £16bn worldwide by 2025 [29, 30]. Treatments use both stem cells and non-stem cells which can be either from the patient (autologous) or from a donor (allogeneic). The cells may be genetically modified or manipulated before being applied to the patient through various methods such as topical application, injection, infusion, or through the use of bioscaffolds or scaffold-free systems, as outlined in figure 1.2.1 [31–35].

Stem cell therapy, uses stem cells which are unspecialised cells found naturally in the body. These can develop into any type of cell and in some instances renew themselves an unlimited amount of times. This treatment is typically given to patients to replace cells that have been destroyed or have died, such as cancer patients in order to help them regain the ability to produce stem cells after treatment [36]. Another example is adoptive T-cell therapy. In this process, T cells, which are a type of immune cell, are taken from the patient's body. These cells are then altered or conditioned in a way that enables them to identify and combat

cancer cells specifically when they are returned into the patient's body [37].

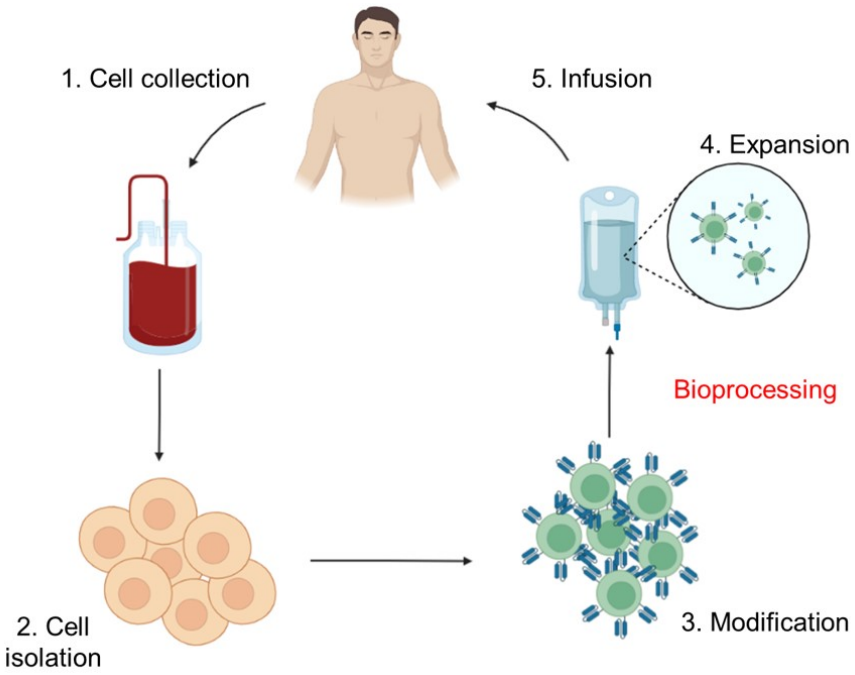

Figure 1.2.1: *Example of a typical cell therapy life cycle (T-cell therapy). 1) A sample, typically blood is collected from the patient/donor. 2) The relevant cells to be modified are isolated. 3) The isolated cell are modified to better recognise cancer in the body. 4) The cells are expanded to achieve a minimum therapeutic cell does. 5) The cell are infused back into the patient. Created with BioRender.*

Allogeneic and autologous cell therapies have their own set of benefits and drawbacks. Factors such as cell availability, manufacturing costs, and patient risks must be taken into account when selecting the most suitable cell therapy option for a particular patient [38]. Both types of therapies require *ex-vivo* expansion to achieve a clinically relevant dose of cells. However, a constant challenge facing the biopharmaceutical industry is producing high-quality, and consistent therapeutic products [39]. Unlike traditional chemical synthesis, these biologics have a much higher degree of natural variability, making them difficult to characterise and control. The genetic backgrounds of donor cells have been shown to contribute to stem cell heterogeneity and variability in clinical outcomes. Kilpinen et al. (2017) demonstrated that 5-46% of the variation in different induced pluripotent

stem cells (iPSCs) originated from genetic differences between individuals [40].

In addition to this, cells are highly responsive to extrinsic factors, such as the microenvironments within the bioreactor [41]. This includes the three-dimensional structures and molecules like growth factors, hormones, metabolites, and vitamins that surround the cells [42]. Small changes in these parameters can significantly impact the yield and quality of the cell therapy product. To address these challenges and mitigate risks, cell therapy manufacturing should be carried out under the principle of quality by design (QbD) [43, 44]. A key component of QbD is the implementation of Process Analytical Technologies (PAT), a framework set out by the American Food and Drug Association (FDA) in 2004 for innovative pharmaceutical development, manufacturing, and quality assurance [45].

To achieve this, it is important that cell differentiation state, developmental status, and viability are measured as close to real-time as possible. This allows for a more accurate assessment of the health of the cell culture and enables more effective process control. However, the real-time PATs currently in use typically measure parameters such as pH, dissolved oxygen, temperature, and glucose [43]. Meanwhile, the majority of complex analyses of key cellular attributes (KCAs), such as proteins and metabolites, still rely on offline or endpoint diagnostics via assays or spectrochemical techniques, (Flow cytometry, ELISA, PCR, and mass spectrometry). [46].

Electrochemical biosensors, with their unique capabilities, are poised to bridge this significant gap in the field. They offer numerous inherent advantages that have been well-documented in the literature. These include ease of minia-

turisation, which facilitates simple integration with bioreactor platforms. They also provide excellent detection limits, enabling precise and accurate measurements. Furthermore, these biosensors are cost-effective, offering a reduced cost alternative to more expensive traditional methods. They boast quick response times, require low sample volumes, and are easy to use. To achieve these properties functionalisation of conducting or semi-conducting surfaces is an important fabrication step in producing sensors with suitable physical/electrochemical properties. This is often the starting point for a bottom up approach to biosensor fabrication.

1.3 Surface Modification Strategies

1.3.1 Self-Assembled Monolayers (SAMs)

Molecular self-assembly is a prevalent phenomenon in biological systems, which underscores the inherent tendency of molecules to occupy the lowest possible energy state. This could involve bonding (covalently or non-covalently) with adjacent molecules or spatial reorientation/organisation [47, 48]. An argument could be made that life on earth would not exist without molecular self assembly, as it is the driving force behind protein folding, and the formation of lipid bilayers. Scientists have exploited this important phenomenon as an effective surface modification strategy. In particular, SAMs, which form as a result of the spontaneous adsorption of molecules onto a substrate, have been used extensively in biosensor fabrication [49].

SAM forming molecules contain three main units, as seen in figure 1.3.1: 1) the head group which has a strong affinity to the substrate, 2) the spacer element, which controls surface thickness and molecular organisation, 3) the end

group (–OH, –NH2, –COOH, or –SH), which facilitates bioconjugations and controls the wetting and interfacial properties [50, 51].

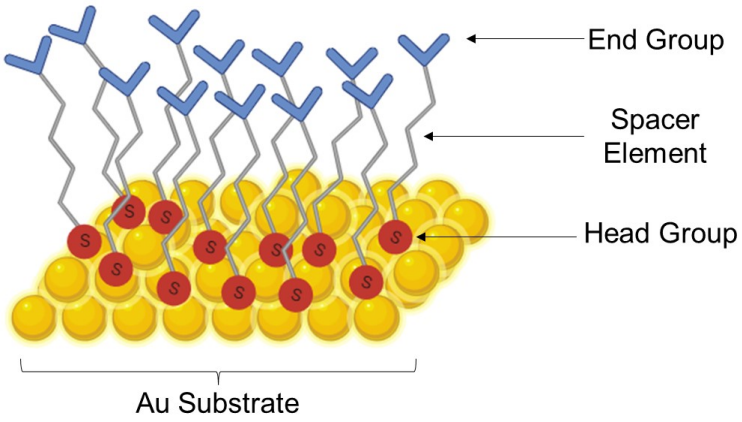

Figure 1.3.1: *Schematic representation of a thiol-SAM on a gold surface. Created with BioRender.*

SAMs can form on various substrates, including Au (gold), Cu (copper), and Ag (silver). Among these, Au surfaces are most commonly used for SAMs due to their resistance to tarnishing and excellent biocompatibility [52, 53]. Au is also an ideal material for several analytical techniques, such as ellipsometry and surface plasmon resonance (SPR), as it can be made to be highly reflective and it allows a surface plasmon wave to be generated when light is directed onto its surface. It also serves as an excellent electrode material for electroanalytical measurements. These characteristics make it straightforward to monitor surface changes or reactions on Au [54, 55].

Alkanethiols can be directly bonded to Au surfaces from high-purity solvents, such as absolute ethanol [48]. The formation of stable thiol-gold bonds drives this attachment. The bonding characteristics of alkane-thiol SAMs remain a topic of considerable debate in scientific literature, particularly concerning the fate of the hydrogen atom attached to the sulfur in these compounds. Histori-

cally, it was assumed that this hydrogen atom was lost during the formation of the gold-sulfur (Au-S) bond. However, conventional surface characterisation techniques, such as X-ray photoelectron spectroscopy (XPS), electrochemistry, and X-ray diffraction (XRD), have been unable to conclusively determine the protonation state of the sulfur atom in a SAM. Our understanding of the Au-S interface has evolved in recent years to recognize its complexity. For instance, Xue et al. (2014) demonstrated through atomic force microscopy (AFM) that coordinate bonds predominate at the Au-S interface at lower pH levels [56]. Conversely, surface bonds exhibit more covalent characteristics at higher pH levels. Inkpen et al. (2019) demonstrated using scanning tunneling microscopy (STM) and conductance measurements that SAMs prepared from solutions of dithiols do not exhibit chemisorbed characteristics [57]. This suggests that under these conditions, the hydrogen is actually retained. The substrate's structure also affects the properties of SAMs. Significant differences were observed in the rates of adsorption, desorption, and migration of thiols when SAMs were formed and compared on flat Au surfaces with Au clusters [58]. Therefore, the characteristics of a particular SAM result from numerous factors including: 1) the structure of the substrate; 2) the affinity of the head group to the substrate; 3) the structure of the alkane-thiol (chain length and number of thiols); 4) the intermolecular forces between alkane-thiol molecules on the surface; 5) the surrounding environment; and 6) the chemical functionality of the end groups. Furthermore, SAMs take time to form and organise themselves into compact monolayers. It is typically accepted that initially, thiols interact with the surface through physical interactions in a disorgan-

ised ‘laying down phase’. Over a period of hours, intermolecular forces cause alkane-thiols to organise themselves into a more rigid ‘standing phase’ (figure 1.3.2) [59].

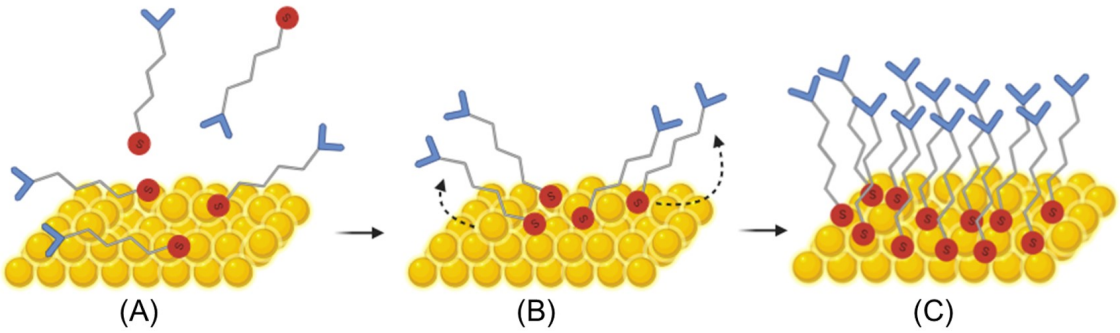

Figure 1.3.2: *Schematic representation of a thiol-SAM organising itself into a compact monolayer. (A) Initial ’lying down’ phase with weak physical interactions between the thiols and the Au surface. (B) Slow chemisorption during which the SAM molecules begin to self-organise, ’standing phase’. (C) Densely packed and organised monolayer. Created with BioRender.*

SAMs have played a pivotal role in the development of various electrochemical biosensors, with many exhibiting excellent limits of detection (LOD) and high specificity (table 1.3.1). Furthermore, SAMs not only provide support structures for subsequent bioconjugations but also insulate the electrode surface from non-specific interactions thus, preventing false signals [60, 61]. This is achieved through two main mechanisms: 1) the SAM molecules act as a physical barrier, shielding the underlying surface from the surrounding environment and 2) SAMs which have hydrating properties (-OH and -COOH groups) form a water barrier at the surface which increases the resistance to non-specific interactions. These properties can increase the biosensors overall sensitivity and specificity compared to unmodified electrodes.

Table 1.3.1: *Examples of electrochemical biosensor interfaces that are partly constructed through self-assembled monolayers (SAM) with their targets of interest and LODs.*

SAM	Target	LOD	Ref.
1,6-hexanedithiol	SARS-CoV-2 proteins	10^{-18} M	[62]
11-mercaptound-ecanoic acid (11-MUA)	3-phenoxybenzoic acid	1.7 x 10^{-5} M	[63]
11-MUA and 6-mercapto-1-hexanol	SARS-CoV-2 spike protein	3.4 x 10^{-10} M	[64]
3-Mercaptopropionic acid	troponin T	1.4 x 10^{-14} M	[65]
cysteamine	anatoxin-a	5 x 10^{-9} M	[66]

As seen in the table above, multi-component SAMs are sometimes used, which provide various benefits. These include tuning the electrochemical properties of the interface (making the film more or less conductive), and optimising the space between functional groups. This decreases the steric hindrance at the surface when receptor components are present. Yang et al. (2016) fabricated an impedimetric biosensor for the detection of Escherichia coli (*E.coli*) based on a mixed SAM (figure 1.3.3) [67]. 11-MUA and dithiothreitol (DTT) were co-assembled on gold electrodes. Next, N-hydroxysuccinimide and 1-Ethyl-3-[3-dimethylaminopropyl]-carbodiimide (NHS/EDC) were used to couple a well known lectin, Concanavalin A (Con A), which binds to carbohydrates on the E.coli's outer surface. The DTT help space out the lectins on the surface thus, reducing steric hindrance around the binding sites. Using $[Fe(CN)_6]^{4-/3-}$ as a redox probe to measure changes in the charge transfer resistance at the interface, the platform achieved a LOD of 75 cells/mL.

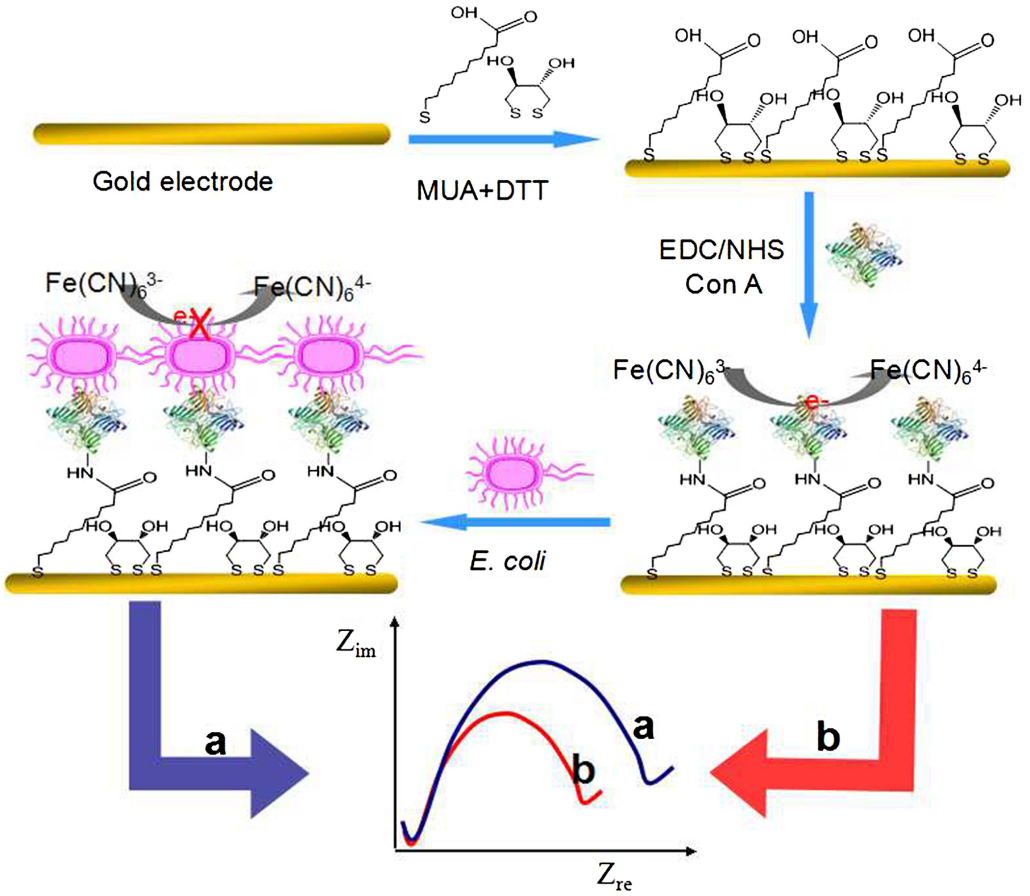

Figure 1.3.3: *Schematic of impedimetric lectin-based biosensor for determination of E. coli. Adapted with permission from reference [67].*

Despite the success of platforms based on SAMs, such systems do have limitations. The formation of these organised layers is time-consuming, typically 24-48 hours. Furthermore, the Au-S bonds are susceptible to oxidation, forming the corresponding sulfinates and sulfonates in air or solution, which severely limits their stability and shelf life [53, 68]. These factors have impeded the widespread commercialisation of SAM-based biosensors.

An increasingly popular alternative to SAMs, which may overcome these limitations, are electropolymerised films. These allow the covalent attachment of molecules to electrode surfaces, through free radical polymerisation at mildly reductive/oxidative potentials.

1.3.2 Electropolymerised Films

Due to their tunable physical, chemical, and electrical properties, electropolymerised films have become an important class of functional materials that have been applied to fabricate electrochemical biosensors [69]. These films are created through a process of electropolymerisation, which involves the polymerisation of monomer units in an electrolyte solution under the influence of an applied electric potential [70, 71]. Film formation and growth typically proceeds through the generation and reaction of free radical monomer units as depicted in figure 1.3.4 [72].

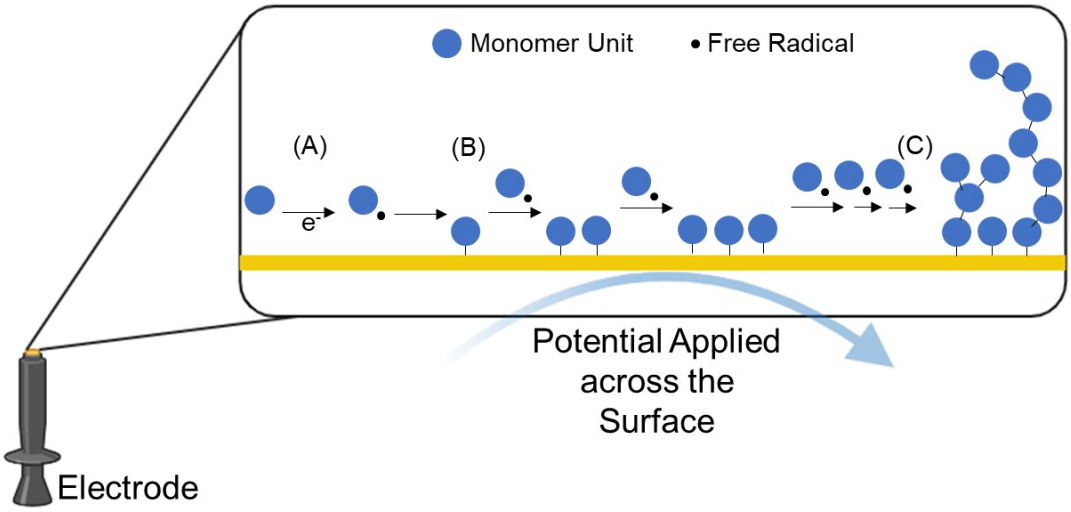

Figure 1.3.4: *Schematic of free radical polymerisation on an electrode surface. (A) A potential is applied across the surface (positive or negative) which generates a free radical monomer unit, typically through oxidation or reduction reactions. (B) This free radical monomer unit can then bind to the surface of the electrode. (C) The radicals produced can also bind to molecules already on the surface, this leads to film growth and branched polymer structures on the surface. Created with BioRender.*

Although the fabrication of these functionalisation layers requires more sophisticated equipment, there are numerous advantages: the electropolymerised films can be formed on a wide range of conducting materials, offering more flexibil-

ity in biosensor design [25]. They also tend to be more stable than SAMs, which can improve the longevity and reliability of the biosensor [24, 73, 74]. The film thickness can be controlled by adjusting the polymerisation time and the magnitude of the applied potential. Monolayers have also been produced by employing radical scavengers which prevents excess radicals from reacting with the molecules already attached to the surface [75]. Furthermore, the films can be formed over a period of seconds to minutes compared to multiple hours in the case of SAMs [76]. However, electropolymerised films tend to be more disorganised and have an increased surface roughness compared to well ordered SAMs. This is due to the free radical polymerisation process leading to branched polymer structures on the surface rather than well ordered mono/multi-layers (figure 1.3.5) [77]. This higher surface roughness can increase biosensor variability and hinder reproducibility [78, 79]. However, it is important to note surface roughness can also provide benefits such as an increased surface area for electrochemical reactions and enhancing the anti-biofouling properties of the sensing interface [14, 80]. Therefore, the impact of increased surface roughness would likely depend on the specific application and the materials used to fabricate the biosensor.

There are many different monomer units available for the electropolymerisation of films for electrochemical biosensors, each with unique functional groups and electrochemical properties. Diazonium salts and tyramine are most relevant to this research and are discussed in detail below.

Diazonium Salts

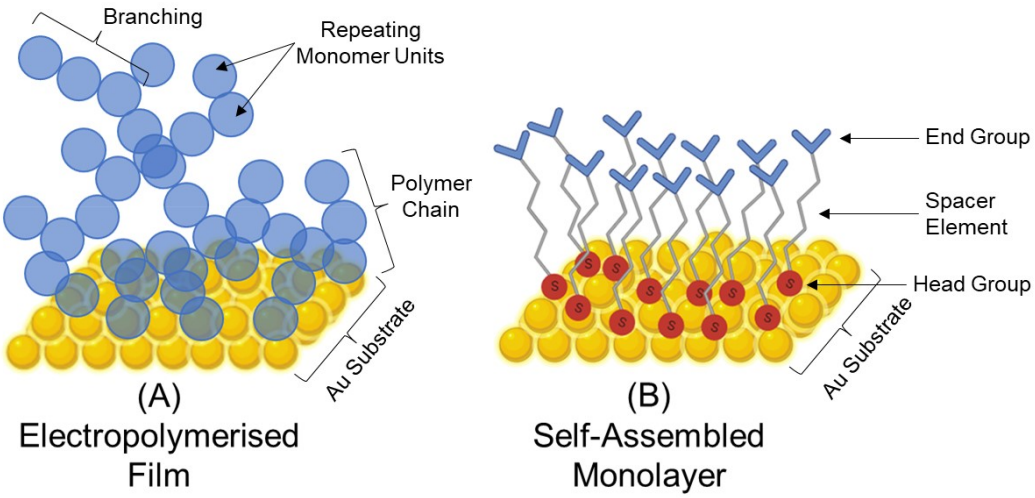

Figure 1.3.5: *Comparison of the surface organisation for (A) an electropolymerised film and (B) a self-assembled monolayer. Created with BioRender.*

Diazonium salts allow for the covalent attachment of aryl molecules through a concerted electron transfer homolytic cleavage of diazonium cations at mildly reductive potentials [76, 77]. The reaction is usually carried out in acetonitrile or acid aqueous conditions and can introduce aryl groups onto a number of surfaces (metals, carbon, silicon) bearing various terminal functionalities (alcohol, nitro, alkyl, carboxylic, esters) for further surface modifications [25]. Typically, aromatic diazonium compounds are used over aliphatic compounds due to the stabilising effect of the ring structure. This allows for the dispersal of the positive charge on the nitrogen around the ring [81]. The aromatic ring also stabilises the intermediate radial species thus, improving the grafting efficiency [82]. Film growth occurs when the radical species reacts at the 3 and/or 5 position on the ring of other already grafted molecules (figure 1.3.6 (B), route 2). Eventually this process self-terminates when the thickness of the film becomes too great for the electrons to tunnel across the barrier and generate new radicals [83]. However, other polymerisation routes can take place depending on the light and tempera-

ture conditions of the system [84]. These may include: Spontaneously generated aryl carbocations in solution reacting with already grafted molecules (figure 1.3.6 (B), route 1), Or the formation of azo bridges via the condensation of nonreduced diazonium molecules (figure 1.3.6 (B), route 3).

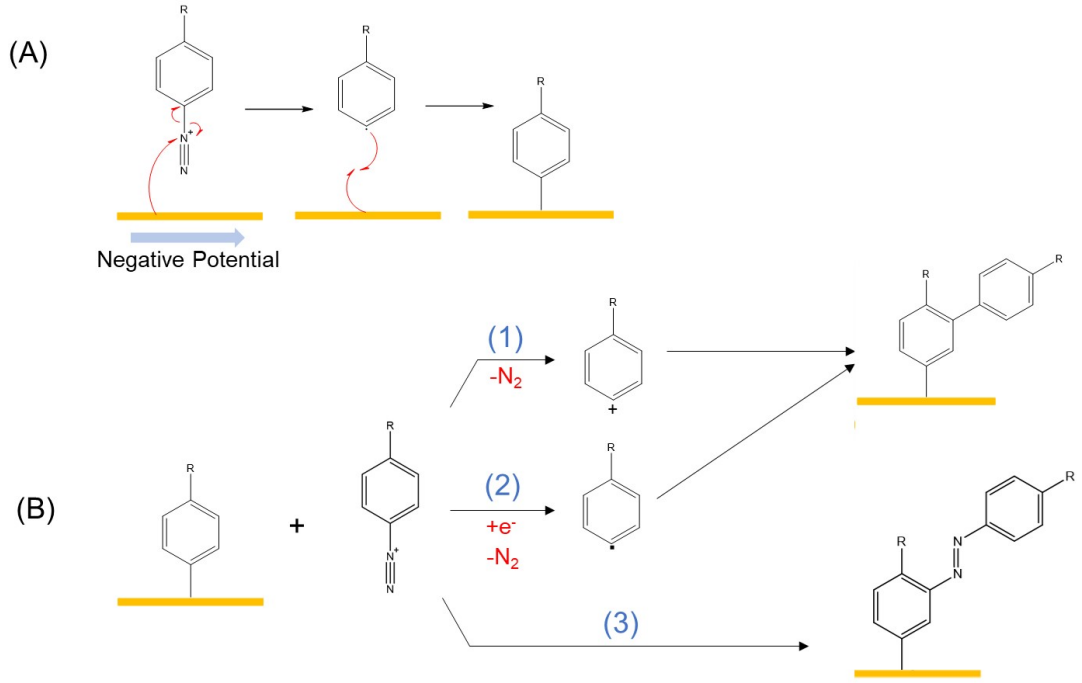

Figure 1.3.6: *(A) Electrochemical reduction of diazonium salts onto a surface by applying a negative potential. (b) Film growth proceeding through pathway: (1) Spontaneously dediazoniated aryl carbocations in solution reacting with already grafted molecules. (2) Free radical attack at the 3 and/or 5 position on the ring of other already grafted molecules. (3) The formation of azo bridges via the condensation of nonreduced diazonium cations on already grafted molecules. Created with ChemDraw.*

However, only a limited number of diazonium salts can be purchased commercially due to their relatively low stability and potential explosive capacity. Some diazonium salts violently decompose in the solid state forming nitrogen gas and aromatic molecules. The stability of these compounds largely depend on the specific counter ion present [85]. For example, phenyldiazonium chloride is extremely explosive, but benzenediazonium tetrafluoroborate is easily handled on

the bench. Therefore, the generation of diazonium compounds is often carried out in-situ using amine precursors. This process is known as diazoniation and can be achieved using $NaNO_2$ in acidic aqueous solutions (figure 1.3.7), or with t-butylnitrite or $NOBF_4$ in ACN [86].

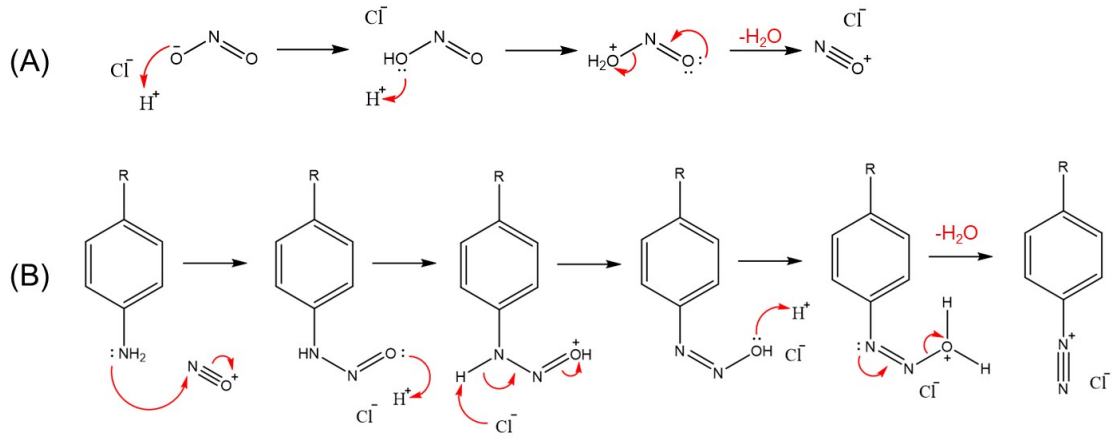

Figure 1.3.7: *(A) Reaction mechanism for the formation of a nitrosonium ion from sodium nitrite in acidic conditions. (B) Subsequent reaction of the nitrosonium ion with the amine precursor to form a aryl-diazonium salt. Created with ChemDraw.*

Diazonium salts have been used extensively in the literature for various types of electrochemical biosensors. Hayat et al. (2012) utilised in-situ diazoniation of 4-aminobenzoic acid (4-ABA) to form 4-carboxyphenyl diazonium salt, which was subsequently attached to screen printed carbon electrodes [87]. Antibodies specific for the naturally occurring food borne mycotoxin, ochratoxin A (OTA), were then coupled to the surface using NHS/EDC chemistry as seen in figure 1.3.8. Faradaic impedance spectroscopy allowed this electrochemical set-up to detect OTA down to a concentration of 10 µg/L.

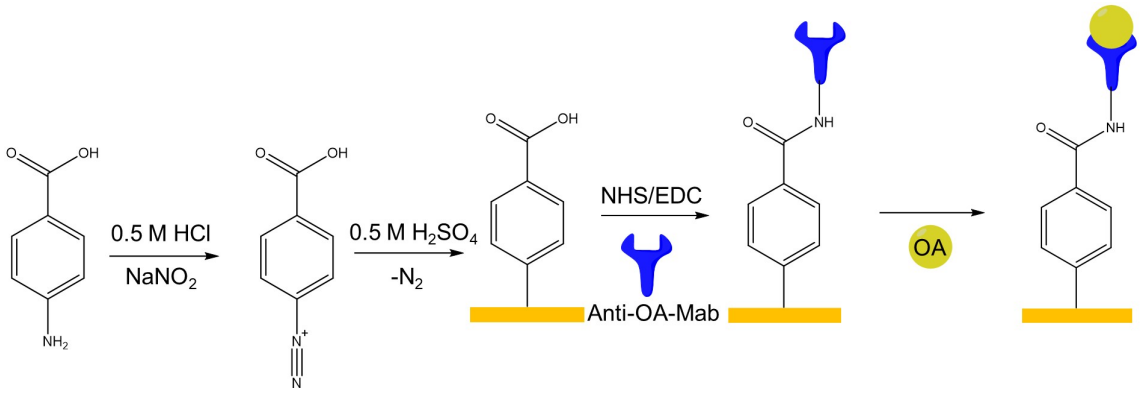

Figure 1.3.8: *A schematic presentation of the surface chemistry used for immobilization anti-okadaic acid (OA) monoclonal antibody on a screen printed electrodes (SPE). Adapted with permission from reference [87]*

This work demonstrates the usefulness of aryldiazonium species to act as a linkage between the electrochemical transducer and biosensor recognition elements. However, the fabrication process typically proceeds uncontrollably to form branched polymer structures on the surface. This has been shown to increase inter-sensor variability and reduced biosensor sensitivity. In recent years, efforts have been made to exert some control over film growth [88], including: 1) Controlling the charge passed during the electropolymerisation process. 2) Introducing unreactive functional groups at the 3 and/or 5 positions on the aryl ring to prevent free radical attack. 3) The use of radical scavengers to prevent newly generated radicals from reacting with already grafted molecules. 4) The use of ionic liquids to control the diffusion of diazonium species to the electrode surface. Gillan et al. (2021), reported on harnessing steric hindrance for controlled film growth as this method in relatively simple to investigate. By introducing a methyl group at the 3-position of the diazonium precursor (4-AMBA) the group was able to increase the sensitivity of the biosensing system compared to when the film was formed without the methyl substitution (4-ABA), as depicted in figure 1.3.9 below. Again

NHS/EDC chemistry was used to couple anti-C-reactive protein (CRP) antibodies to the surface. This system allowed for the sensitive detection of CRP down to a concentration of 0.1 ng/mL [88].

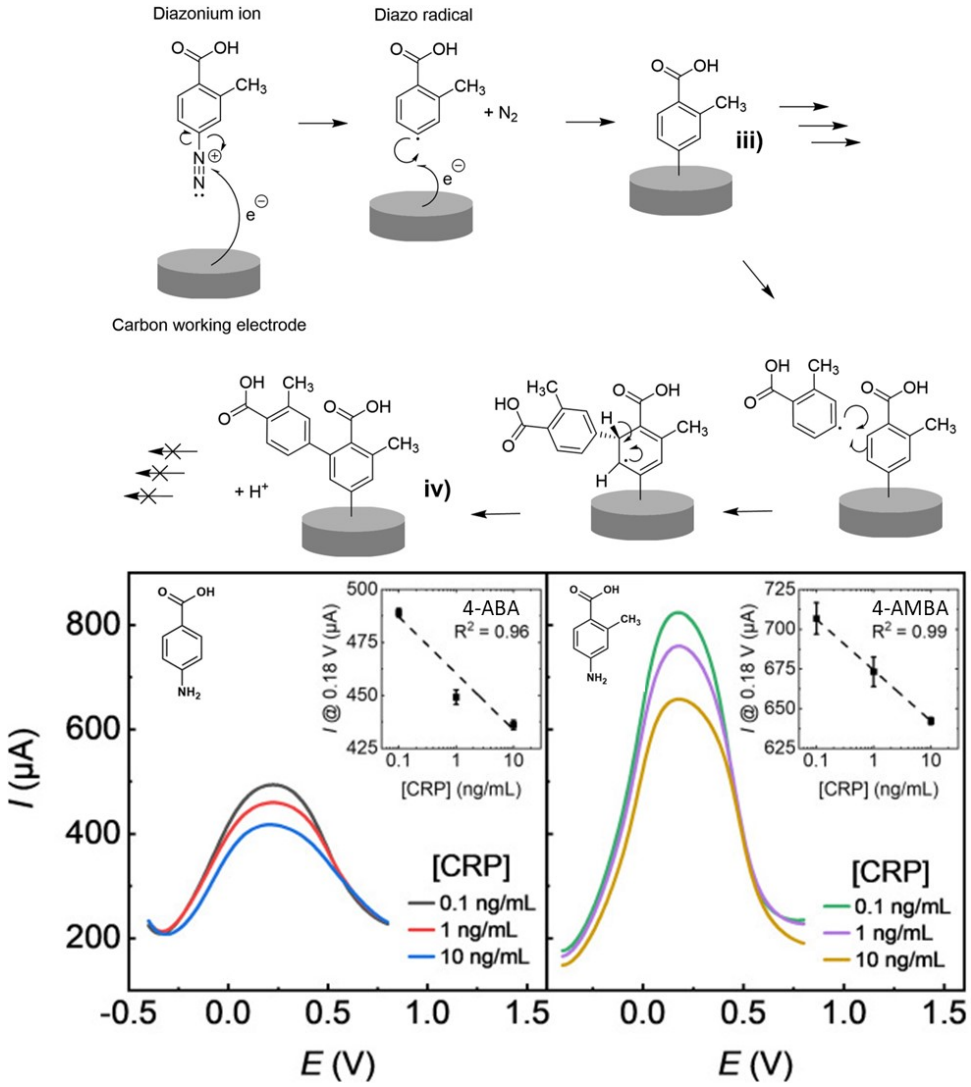

***Figure 1.3.9: Top**: Mechanism of electrografting AMBA diazonium precursor to carbon electrode surface to form iii), followed by single radical attack leading to structure iv), after which the methyl substituents hinder repeated radical attack. **Bottom:** Square wave voltammetry analysis using 5 mM $[Fe(CN)6]^{4-/3-}$ redox probe for sensor response to varying CRP concentrations using 4-ABA, left and 4-AMBA, right. Adapted with permission from reference [88].*

While high sensitivity is extremely important for electrochemical biosensor fabrication, this has already been achieved with biosensors based on SAMs. The major benefit in utilising diazonium grafting is the increased surface stability

of the aryl-electrode bond compared to the thiol-gold bond. Diazonium derived films have been shown to be much less susceptible to oxidation compared to SAMs, as well as having significantly higher resistance to temperature, electrical, and pH changes [24, 73, 89]. D'Amours et al. (2003), compared the stability of substituted aryl-diazonium precursors (4-carboxyphenyl, 4-nitrophenyl, 4-diethylaniline (DEA), and 4-bromophenyl) grafted to glassy carbon electrodes, towards applied potentials (figure 1.3.10). Stability measurements showed that films of 4-carboxyphenyl, 4-nitrophenyl, DEA, and 4-bromophenyl can be used in a potential window of 3.6, 4.6, 2.6, and 5.6 V, respectively. This is significantly greater than the 1.2 V observed for SAMs, depending on chain length, terminal group, and quality of the gold surface. This is beneficial for the fabrication of electrically responsive surfaces, which are discussed in more detail in section 1.6.

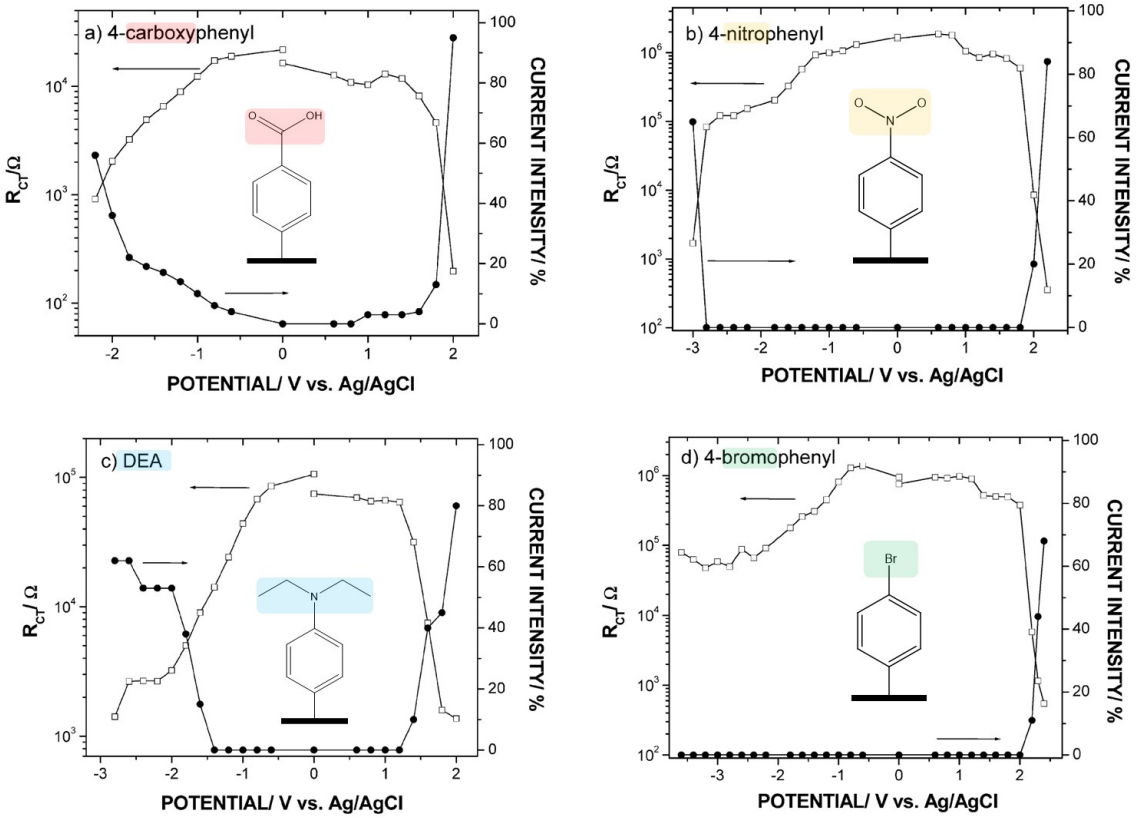

Figure 1.3.10: *Variation of charge-transfer resistance (□) and the current intensity (·) as a function of the applied potential for: (a) 4-carboxyphenyl; (b) 4-nitrophenyl; (c) DEA, and (d) 4-bromophenyl modified glassy carbon electrode. Adapted with permission from reference [24].*

Furthermore, the thermal stability of diazonium derived films were compared to equivalent SAMs by Civit et al. (2010). Gold surfaces were modified with mono- and dithiol molecules and compared with diazonium salts with one and two diazonium groups (figure 1.3.11). The modified surfaces were immersed in approximately 15 mL of phosphate buffer solution containing 500 mM NaCl that was maintained at a constant temperature ranging from 25 to 95°C. The surfaces were monitored using cyclic voltammetry and electrochemical impedance spectroscopy. The monothiol was the least stable and started to desorb around 65°C and was completely removed at temperatures above 95°C. The dithiols showed increased thermal resistance, with 26% of the SAM remaining after exposure to

95°C. On the other hand, both the diazonium salt derived layers responded equally well to the thermal treatment, with minor losses that can be attributed to the removal of non-specifically attached molecules over the entire temperature range.

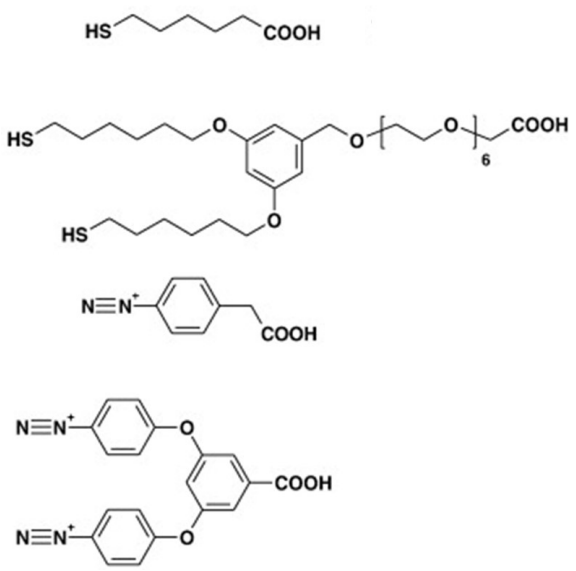

Figure 1.3.11: *Structures of thiols and diazonium salts used. Adapted with permission from reference [73].*

The increased stability of the diazonium derived films may help biosensing platforms reach widespread commercialisation by reducing the interfacial degradation during shipping or while the device is sitting idle. In addition to diazonium salts, tyramine presents another promising monomer unit for the electropolymerisation of films for electrochemical biosensors. Tyramine, a naturally occurring amine, can be oxidatively polymerised to form polytyramine, an insulating and biocompatible polymer.

Tyramine

Tyramine or 4-(2-aminoethyl) phenol, is an amine derivative of tyrosine which occurs naturally, particularly in fermented food. It has been identified as a versatile monomer for the fabrication of non-conducting polymer surfaces for electrochemical biosensors [90]. The structure of tyramine and the most accepted electropolymerisation mechanism, which occurs in the ortho-position to the hydroxyl group can bee seen in figure 1.3.12 below. Typically, the reaction is carried out in a methanol solution by applying an oxidative potential, with sodium hydroxide (NaOH) acting as a supporting electrolyte [91]. The free amine on the resulting polymer backbone enables further covalent surface modifications.

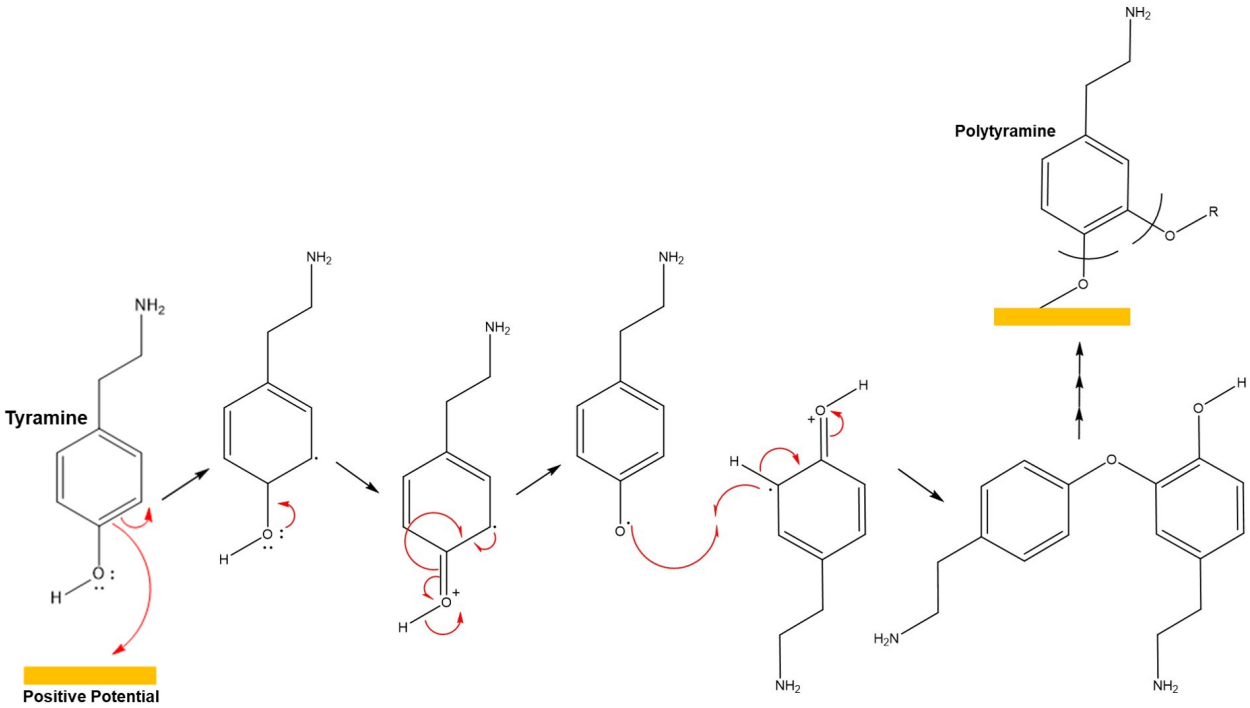

Figure 1.3.12: *Tyramine electropolymerisation mechanism.*

Polytyramine compared to diazonium derived films is much less conductive and often described as an insulating polymer [92]. This is due to the absence

of conjugated pi bonds which facilitate the propagation of electromagnetic waves through material. Instead the terminal amine is separated from the aryl-ring by a two carbon chain. Therefore, polytyramine is often used in capacitance based sensors as the non-insulating layer acts as a capacitor, facilitating a build up of charge at the sensing interface. Mahadhy et al. (2021), compared polytyramine films and 6-mercaptohexanol (MCH) SAMs for capacitive DNA biosensors (figure 1.3.13) [93]. Atomic force microscopy and cyclic voltammetry results suggested that the polytyramine film had greater insulating properties and offered greater surface area for the immobilisation of the capture probe compared to the MCH SAM. The polytyramine platform demonstrated greater sensitivity and larger signal amplitude. The linear responses for the complementary single-stranded DNA was 10^{-12} to 10^{-8} M for the polytyramine system, and 10^{-10} to 10^{-8} M for the MCH system. The LODs were 4.0×10^{-13} M and 7.0×10^{-11} M respectively.

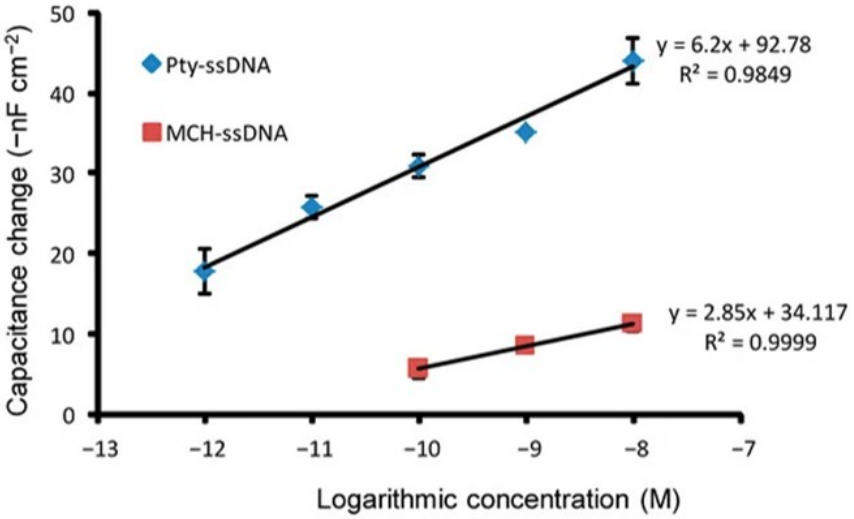

Figure 1.3.13: *Calibration curves showing linearity range for target single stranded DNA (ssDNA) hybridised with capture probe on the different sensor chips modified with Polytyramine (Pty)-ssDNA and MCH-ssDNA. Adapted with permission from reference [93].*

Furthermore, electropolymerised films have been shown to smoothen the

interfacial surface and reduce roughness by filling in surface pores and nanostructures [94, 95]. This is useful as screen printed electrodes (carbon or gold) are widely used in the biosensing field due to low cost production. However, these electrode types have suffered from inconsistent performances due to the uneven electrode surface generated from the manufacturing process. Similar to diazonium derived films, polytyramine has also demonstrated significantly higher stability (chemical, physical, and electrical) compared to SAMs [74, 91]. This could help overcome the significant storage stability issues biosensors have come up against. Situmorang et al. (1998), demonstrated that a glucose oxidase (GOx) based biosensors formed on electrodeposited polytyramine showed no loss in electrode response after four months of dry storage and exhibited only minor loss in response after 20 days of repeated use. The resultant biosensor had a linear range of 0.1–28 mM glucose and a detection limit of 0.01 mM. Furthermore, the authors highlight that the degradation after 20 days likely corresponds to a deactivation of the enzyme by the hydrogen peroxide produced during the oxidation of glucose. This suggest polytyramine surfaces coupled with high stability receptor components could be stable in storage for months at a time.

These properties have allowed polytyramine to be utilised in the development of a wide range of electrochemical biosensors for various target molecules over the past two decades. Ahmed et al. (2012), utilised electropolymerised polytyramine films in the development of an impedimetric immunosensor for the detection Streptococcus pyogenes (*S. pyogenes*) in human saliva, (figure 1.3.14) [94]. The polytyramine (Ptyr) surface was incubated in a biotin-NHS solution allowing

NeutrAvidin to be subsequently attached to the interface. Biotinylated antibodies specific for *S. pyogenes* where then bound to the NeutrAvidin on the surface. The biosensor showed linear response (10^5 cells/mL to 10^7 cells/mL) against *S. pyogenes.*

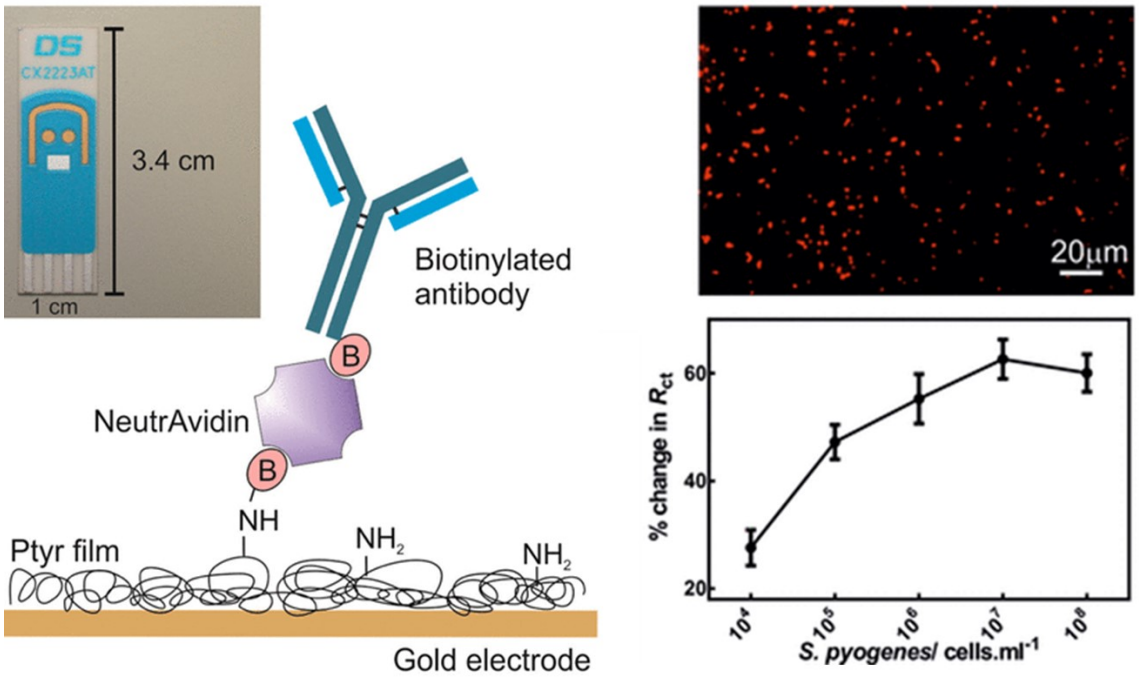

Figure 1.3.14: left: *Schematic of Biosensor for S. pyogenes. Biotinyl anti-S. pyogenes antibodies are conjugated to the free amine of the polytyramien film via biotin-NeutrAvidin interactions. The inset picture is a DropSens screen-printed gold electrode.* ***right:*** *Top, Fluorescence imaging of bound tagged S. pyogenes on the sensor surface (red dots). Bottom, Calibration curve of S. pyogenes immunosensor with cumulative addition of analyte; normalized data (n = 4). Adapted with permission from reference [94].*

More recently, Shamsuddin et al. (2021) developed a reagentless affimer and antibody based impedimetric biosensors for the colorectal cancer biomarker carcinoembryonic antigen (CEA), using polyoctopamine (polytyramine derivative) modified electrodes (figure 1.3.15). Both systems had similar LODs of around 11 fM, which was significantly below the clinical baseline levels of 25 pM. However, the affimer system had a more limited dynamic range (1-100 fM) compared to

the antibody system (1 fM - 100 nM). This work not only highlights the utility of polytyramine but also the importance of choosing the right receptor component for the particular application of the biosensing system.

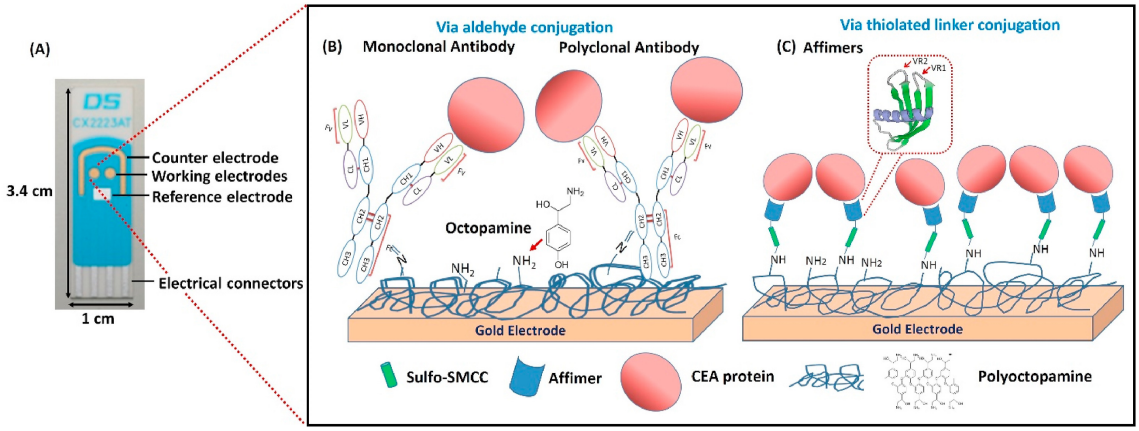

Figure 1.3.15: *(A) DropSens screen printed gold electrodes with two round gold working electrodes, a gold counter electrode and a silver reference electrode; (B) oriented immobilisation of the oxidised antibodies onto polyoctopamine (POct) film via covalent binding on DropSens screen printed gold electrode; (C) site-directed immobilisation of anti-CEA affimer conjugated to POct via sSMCC linker. Inset in (C) is the ribbon representation of the affimer. Adapted with permission from reference [95].*

Both diazonium grafting and the electropolymeristaion of tyramine have proven their usefulness in the development of electrochemical biosensors. However, these methods require specialised electrochemical set ups, which can be expensive to purchase, run, and maintain. Often a good starting point for the development of biosensing systems is directly modifying the transducer surface with the receptors and other macromolecules which will be used in the final biosensing platform. This is particularly true for gold surfaces which are known to be biologically ”sticky”. This allows an initial understanding of the concentrations needed for fabrication and the interactions occurring at the interface.

1.3.3 Direct Immobilisation of Macromolecules on Gold Surfaces

While the direct immobilisation of macromolecules on gold surfaces may seem straightforward in theory, it has proven to be quite challenging in practice [96, 97]. Macromolecules, such as proteins and peptides, can interact with gold surfaces through several different mechanisms:

1. Physical adsorption: This is non-covalent attachment which is easily reversible. Physical interactions depend on the electrostatic, hydrophobic, and van der Waals interactions between the macromolecules and the gold surface [98, 99].

2.Thiol bonding: This is a covalent process and is much less reversible compared to physical adsorption. Similar to the formation of SAMs (section 1.3.2), thiol bonding can occur between any thiol/dithiol functional groups exposed on the surface of macromolecules. Again, the driving force for this is the formation of the relatively stable thiol-gold bonds [100, 101].

3. Amine bonding: Another common functional group found in macromolecules are amines, they can donate their lone pair of electrons and bind to the gold surface. This is generally considered weaker than thiol-gold bonds and typically described as a weak covalent interaction. However, the strength of this amine-gold bonding can change significantly depending on factors such as the basicity of the amine and the condition of the gold surface [102].

Due to the multiple mechanisms through which macromolecules such as proteins can interact with the surface, there can be significant variability between the orientation of the individual proteins on the surface. For example, if there are functional groups in or around the binding site of an antibody which have the

capacity to bind to gold, it may lead to the receptor becoming inactive once on the surface, as the binding site is not facing out into the surrounding environment to bind to its target [96]. This can lead to variability in the biosensor's signal response.

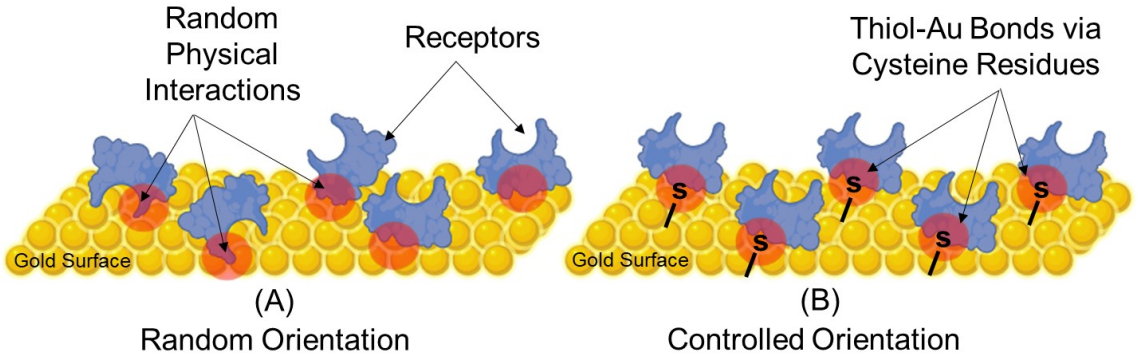

Figure 1.3.16: *Macromolecules attached directly to the gold surface: (A) Randomly through weak physical interactions. (B) Controlled through the formation of thiol-Au bonds. Created with BioRender.*

Efforts to address this issue have included engineering the macromolecules to include cysteine residues at specific sites on the molecule's surface (figure 1.3.16) [103–105]. Cysteines are naturally occurring amino acids which contain thiols, this can direct the molecules to interact with the surface in a more controlled manner. For example, if the binding site of a protein receptor is known to be located at the N-terminal, then having a cysteine functional group located at the C-terminal (depending on the tertiary structure of the protein) can increase the probability that the receptor's binding site will be facing away from the surface into the surrounding environment.

Electrochemical biosensing platforms use the electrode material to act as a transducer, which is responsible for converting chemical/physical changes at the interface into an electrical signal [106]. The general performance of the electro-

chemical system is largely determined by the surface architecture which connects the biological receptor component to the transducer [107]. This includes any functionalisation layers present (SAMs, polymer films) along with the linkage to the biological receptor. Besides optimising the electrochemical properties of these layers the receptor needs to be in close spatial contact with the transducer to ensure binding events take place within the effective range of the applied electric field [108]. This is often why directly coupling macromolecules to the surface can be beneficial. However, if binding events take place too far from the transducer the electric field can be screened and subsequently the system looses sensitivity. Likewise, if the receptors are easily removed from the surface when the system is idle or undergoing sample injections/buffer washes, then the platform will quickly become inactive. Therefore, careful consideration needs to be given to how the receptors and other surface components are attached to the interface.

1.4 Bioconjugation Strategies

The use of electropolymerised films and SAMs typically terminate the electrode surface with functional groups such as amines, carboxylic acids or alcohols [109, 110]. These groups allow a wide variety of different chemistries to be employed in order to attach receptors and other surface components to the biosensing interface.

1.4.1 Carbodiimide Coupling Chemistry

By far the most used surface bioconjugation strategy in the literature is NHS/EDC coupling. Mentioned briefly in discussing the fabrication of some of the biosensing platforms above, NHS/EDC is typically used for coupling carboxylic acid terminated surfaces to free lysine residues on biomolecules [111]. The process of immobilisation begins by activating the surface with a reactive compound known as 1-ethyl-3-(3-dimethylaminopropyl)carbo-diimide (EDC), which is facilitated by N-hydroxysuccinimide (NHS). Initially, EDC interacts with a carboxylic acid to create an active ester intermediate. This intermediate is subsequently substituted by an NHS ester, as depicted in Figure 1.4.1. The NHS ester, being more reactive, readily forms a stable amide bond with the primary amines. This technique can also be used for amine terminated surfaces if the biomolecule of interest has free carboxylic acid residues on its surface. The biomolecule would first need to be solubilised in a mixture of NHS/EDC to activate the carboxylic acids and then incubated on the amine surface [112]. However, this method can lead to receptors crosslinking in solution resulting in poor coupling yields and inactivated binding sites. In order to optimise the immobilisation, parameters such as solution pH, ionic strength, concentrations, and reaction times often need to be tightly controlled [113].

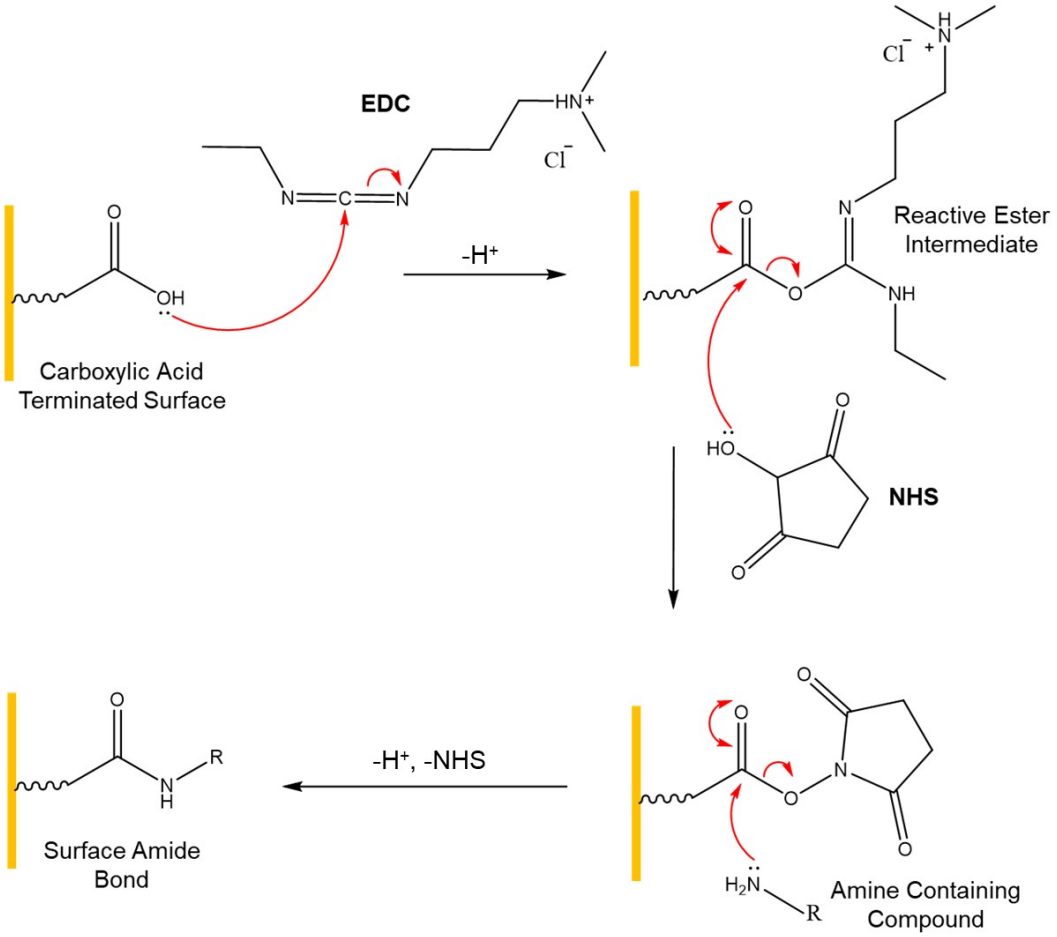

Figure 1.4.1: *Schematic illustration of the activation of a carboxylic acid terminated surface via NHS/EDC chemistry, followed by coupling of an amine containing compound. Created with ChemDraw.*

1.4.2 Glutaraldehyde Crosslinking

Glutaraldehyde (GA) has been extensively used as a crosslinking agent for numerous applications such as enzyme and cell immobilisation and hydrogel synthesis [114]. This homobifunctional molecule consists of two aldehyde groups separated by a three carbon alkyl chain. GA is very simple to use for coupling biomolecules due to the high reactivity of the terminal aldehyde residues with amines, thiols, alcohols, and imidazoles. [114, 115]. Therefore, amine terminated surfaces can be activated with GA forming Schiff base (imine) linkages, as de-

picted in figure 1.4.2. Excess and physically adsorbed GA is typically removed from the surface with deionised (DI) water before any biomolecules are incubated on the surface [116]. It is important to note that the exact reaction mechanism of GA with protein amino groups is still debated in the literature. Therefore, the scheme outlined in figure 1.4.2 below is not definitive [117, 118]

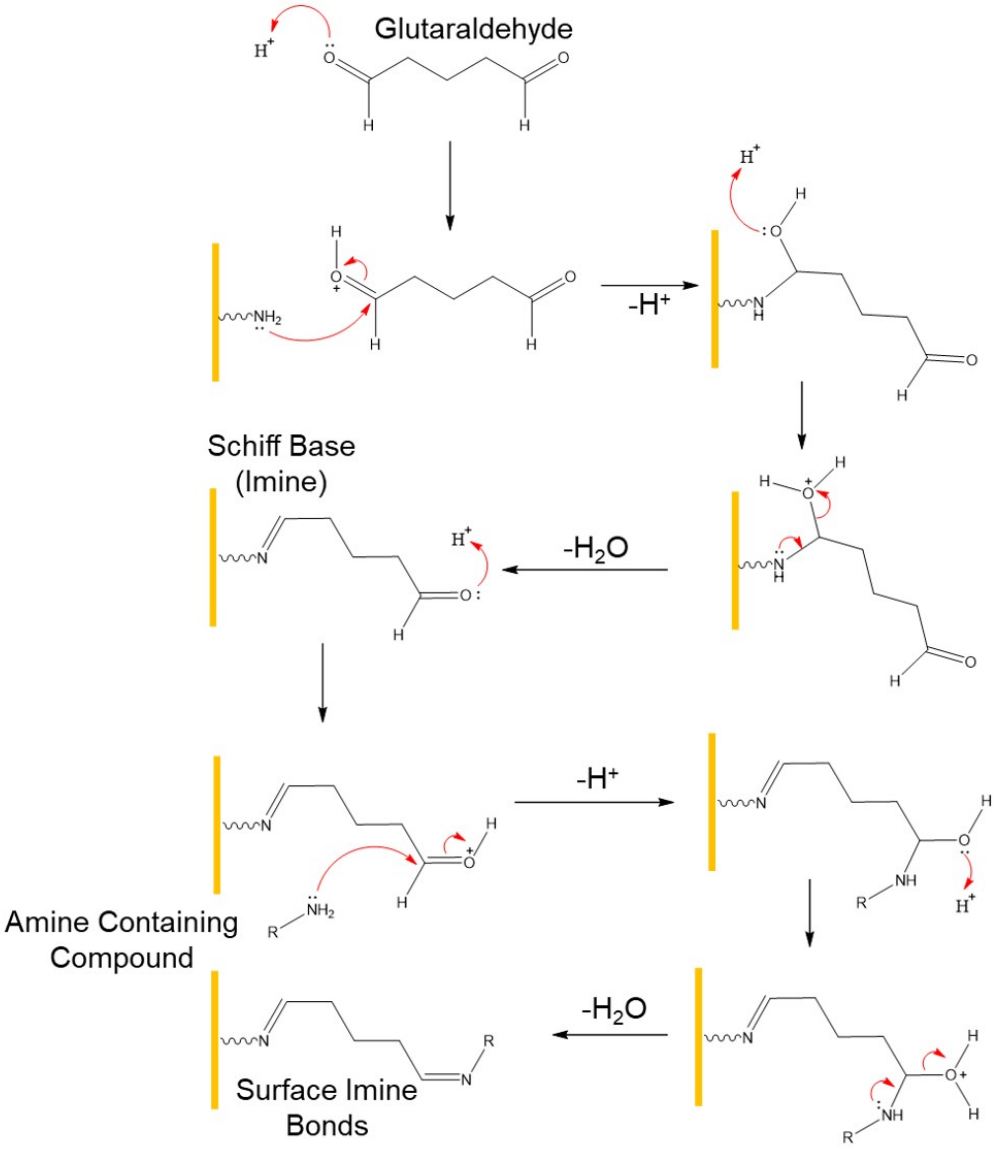

Figure 1.4.2: *Suggested mechanism for the activation of an amine terminated surface using glutaraldehyde followed by coupling of an amine containing compound. Created with ChemDraw. Adapted from reference [117].*

While glutaraldehyde remains a popular choice for surface bioconjuga-

tions, there are some disadvantages which should be considered. The formation of imine bonds are relatively unstable, particularly at acidic pHs and are broken up, regenerating both the aldehyde and amine groups [119]. Furthermore, GA can undergo self polymerisation in solution and exists in equilibrium between cyclic, linear, monomeric, and polymeric structures, depicted in figure 1.4.3. These different structures can interact in different ways with proteins which can lead to variability in biosensing platforms [118, 120]. Due to GA's high and non-specific reactivity it is also extremely difficulty to control the orientation of receptor components on the surface, which can lead to loss of activity, as discussed in section 1.3.3.

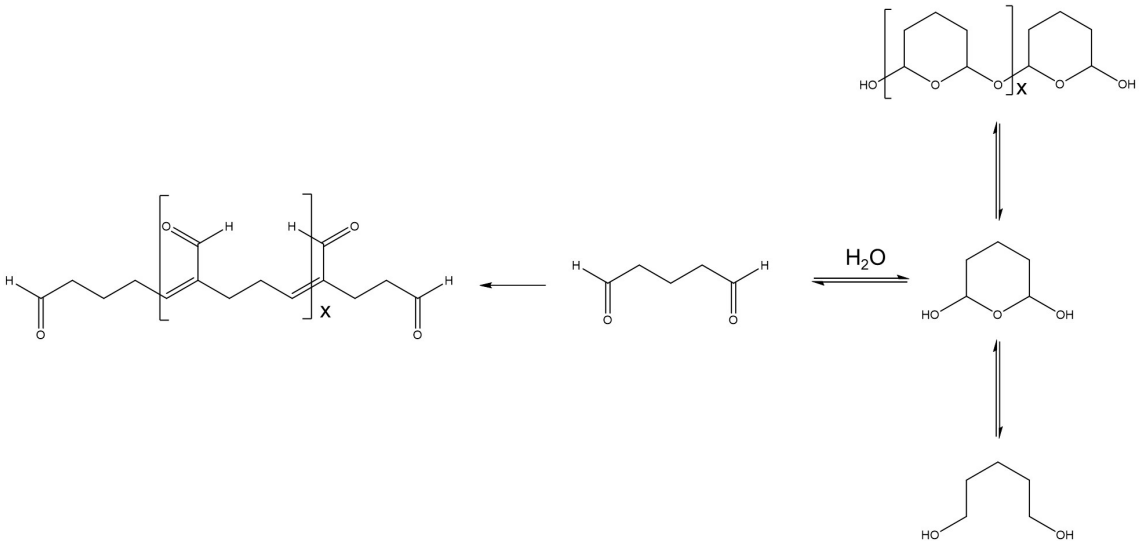

Figure 1.4.3: *possible structures of glutaraldehyde in aqueous solution. Adapted with permission from reference [119].*

While NHS/EDC and GA have been used extensively in the literature for various different coupling reactions, it is important that the particular bioconjugation strategy employed provides highly efficient and controlled surface coupling. This will result in the highest activity in the final biosensing platform. To this end, it

is important to understand which functional groups are to be coupled together. In the case of this research, the majority of surfaces are amine terminated and coupling was typically between other amines and thiols in the case of the oligopeptides. Therefore, the bioconjugation strategies have to be carefully chosen to be as selective as possible for these particular groups in order to avoid unwanted side reactions.

1.4.3 Succinimide Esters

Compounds containing succinimide ester groups are commonly used to activate surface amines and covalently couple biomolecules [121]. By targeting the native amino acids or functional groups on the biomolecules of interest, the succinimide ester compound can be tailored for site specific coupling.

DSC

DSC (N,N′-Disuccinimidyl Carbonate) is the smallest homo-bifunctional NHS ester crosslinking reagent available, which can activate both amine and alcohol terminated surfaces [121, 122]. Reaction of a primary amine with DSC creates a succinimidyl carbomate intermediate that is highly reactive toward nucleophiles. Therefore, DSC-activated surfaces can be used to couple biomolecules containing free lysine residues via a stable carbamide linkage (figure 1.4.4). This coupling method results in a small linkage between the surface and the biomolecule (approximately 0.5 nm, calculated with ChemDraw 3D). This allows biointeractions to occur as physically close to the electrode as possible, which is important for efficient signal transduction.

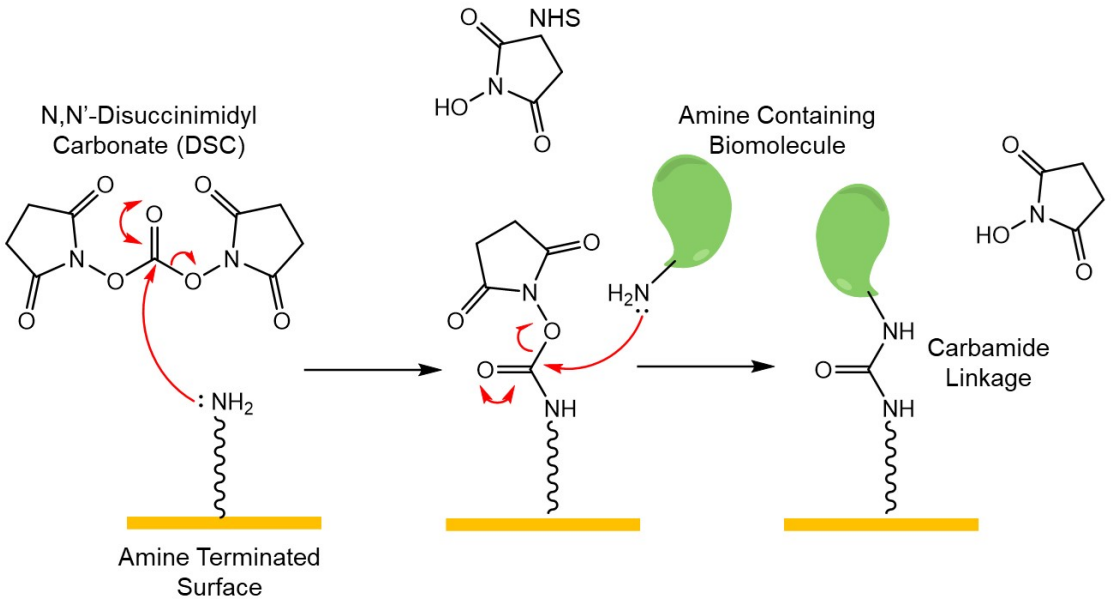

Figure 1.4.4: *Schematic of DSC reacting with an amine terminated surface to form a intermediate which is highly reactive toward nucleophiles. This activated surface can react with free lysine residues on biomolecules to form a stable carbamide linkage. Created with ChemDraw.*

DSC is rapidly hydrolysed in aqueous solutions and therefore anhydrous organic solvents are required to carry out surface activation. Subsequent conjugation with proteins and other biomolecules can be carried out in aqueous solutions. Typically, the reaction is optimised within a pH range of 7-9 using common buffer salts. This pH range limits the protonation of the amines ensuring nucleophlicity is maintained. Buffers containing amine components such as Tris should be avoided to prevent competing reactions [121]. This technique was used for the attachment of antibodies to a poly(2-hydroxyethyl methacrylate) brush interface, for the development of a surface plasmon resonance (SPR) biosensor aimed at detecting aflatoxin M1 (AFM1) [123]. The system allowed for highly sensitive detection of AFM1 in milk samples, with an LOD as low as 18 pg/mL. However, a drawback of this coupling technique is the need for organic solvents for surface

activation. Polymer surfaces exposed to organic solvents can undergo structural reorientation [124]. This can affect the stability of the surface and thus the usability of the biosensor. Therefore, it is often more desirable to be able to carry out surface activation under aqueous conditions.

sulfo-SMCC

Sulfo-SMCC (sulfosuccinimidyl-4-(N-maleimidomethyl)-cyclohexane-1-carboxylate) is another common coupling reagent which is water soluble. This is due to the presence of a negatively charged sulfonate group on its NHS ring. The charge provides enough polarity to the molecule to make it water soluble at room temperature [121]. Like DSC, one side of the sulfo-SMCC molecule contains a succinimidyl group however, the other side consists of a maleimide (figure 1.4.5). At neutral pHs this group is 1000 times more reactive towards thiols compared to amines [125]. This allows for more controlled bioconjugations if the number of thiols and their position on the biomolecule are known.

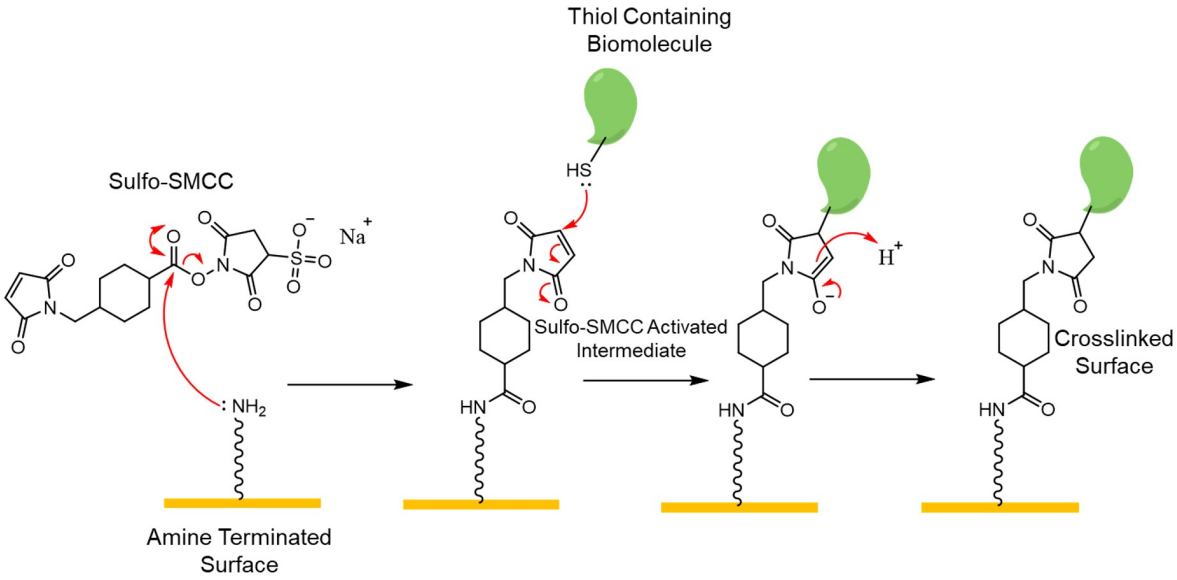

Figure 1.4.5: *Schematic of sulfo-SMCC reacting with an amine terminated surface to form a stable amide bond. The terminal maleimide can be then conjugated to a thiol containing compound to form a thioether linkage. Created with ChemDraw.*

Sulfo-SMCC may be the most popular crosslinker for protein conjugation purposes [121]. Billah et al. (2010) used sulfo-SMCC for the directed immobilisation of antibody fragments onto a thiol-gold SAM for myoglobin impedance based biosensing, (figure 1.4.6) [126]. The platform was able to detect myoglobin in both phosphate buffered saline and whole serum over the range of concentrations from 10^{-13} to 10^{-6} M. More recently, Li et al. (2022) employed sulfo-SMCC for the conjugation of aptamers to zwitterionic peptides on Au-nanoparticle modified glassy carbon electrodes. This system was used for the detection of *E.coli* O157:H7 and demonstrated a sensitive linear range from 15 to 1.5 x 10^5 colony forming units/mL (CFU/mL) and had a LOD of 4.0 CFU/mL [127].

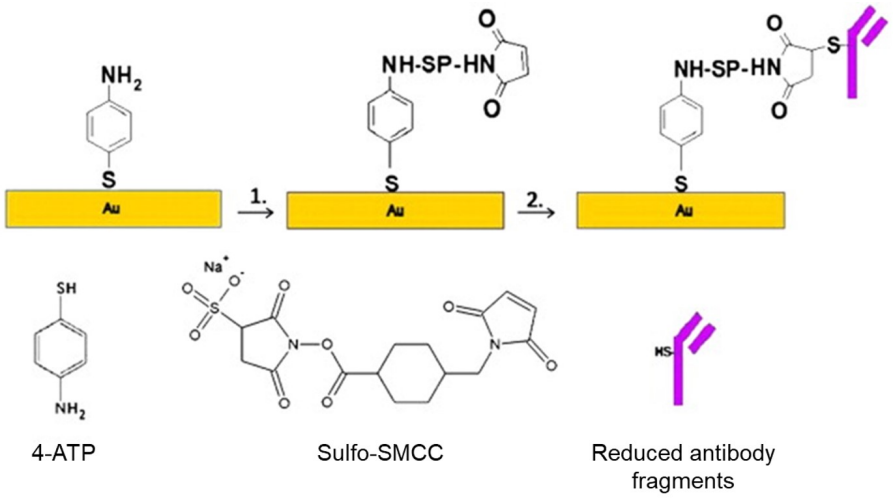

Figure 1.4.6: *Schematic showing 4-aminothiophenol (4-ATP) SAM based biosensor. Adapted with permission from reference [126].*

While DSC and sulfo-SMCC have been used extensively for coupling amine, alcohol, and thiol containing compounds many other succinimide ester crosslinking reagents exist. These offer a wide variety of different physical and chemical properties namely solubility and length, which can be tailored for specific applications. An excellent resource with many of these reagents discussed, is the book 'Bioconjugate Techniques' by Greg T. Hermanson [121]

1.4.4 His-Tagged Proteins

Currently in the fields of biosensing and biotechnology, there is a push towards improving the biological activity of immobilised proteins via the maximal exposure of its active site [128]. This calls for more controlled bioconjugation strategies in order to couple receptor components in a site specific manner. One powerful approach involves recombinant protein engineering, which allows the introduction of an affinity tag at the N- or C-terminus of a protein [129, 130]. In particular, the hexahistidine tag (His6-Tag) has been widely used due to its short motif and

minimal interference of protein expression and folding [131]. His6-Tags contain 6 repeating histidine residues which are amino acids with an imidazole side chain. Compared to other common amino acid residues on proteins which are used for immobilisation (lysine, arginine, cysteine), imidazol has a lower pK_a (6.04) which is deprotonated at neutral or slightly acidic conditions [132]. This allows the imidazole group to act as a nucleophilic agent under mild reaction conditions. Li et al. (2019) demonstrated the ability of the imidazol groups in a His6-Tag to undergo a Michael-type reaction with an alkene terminated surface. Gold surfaces were first functionalised with an hydroxy-EG_6-undecanethiol (EG6) SAM before being activated with divinyl sulfone (DVS) in the presence of triphenylphosphine (PPh_3) acting as a catalyst (figure 1.4.7).

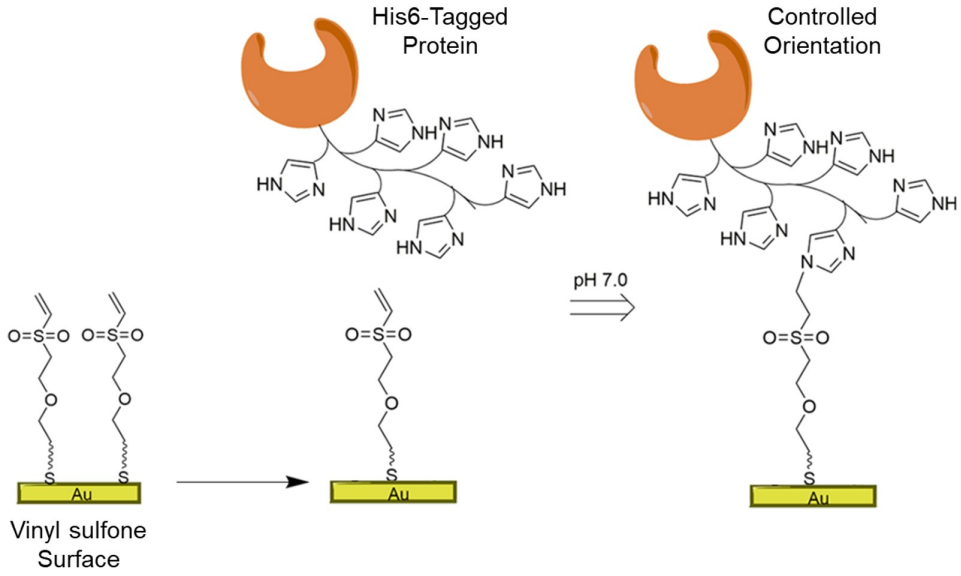

Figure 1.4.7: *Schematic showing site-specific immobilisation of His-tagged proteins onto VS-bearing surface. Adapted with permission from reference [132].*

This site-specific immobilisation strategy was compared with the same protein immobilised onto a carboxylic acid terminated SAM. This was achieved using NHS/EDC chemistry which results in random protein orientations on the

surface. The site-specific method resulted in a higher protein density on the surface (13.6 pmol/cm^2) compared to the randomly orientated system (9.6 pmol/cm^2). Furthermore, a solution-based competitive fluorescence assay was carried out to examine the binding between horseradish peroxidase (HRP) and the immobilised proteins. From the optical density measurements the response of the site-specific method was roughly twice that of the randomly orientated system. This report demonstrates that site-specific immobilisation of proteins via a His6-Tag can improve receptor density and biosensing sensitivity.

Proteins fused with His-Tags can be easily isolated after production in high purity and yield by Ni^{2+} affinity chromatography. This is facilitated through the reversible coordination interaction between immobilised Ni^{2+}-nitrilotriacetic acid (NTA) and the His residues [133]. This opens up another possible route for orientated and reversible attachment of proteins containing His-Tags on solid surfaces. Chavan et al. (2021) took advantage of this and developed a highly sensitive device for salivary cortisol [134]. A glassy carbon electrode was initially modified by electro-deposition of 4-aminobenzoic acid (4-ABA) and activated using NHS/EDC chemistry. (S)-N-(5-amino-1-carboxypentyl)-iminodiacetic acid (ANTA) was subesquently coupled to the surface, which acts as a chelating center for the Ni^{2+} ions through three carboxylate groups and a tertiary amine (figure 1.4.8). Recombinant apoferritin (R-AFTN) protein was immobilised on the Ni-NTA moiety via interaction of two imidazole side chains of the His-tag. Anti-cortisol antibodies were then attached to G protein-coupled receptors via their Fc domains. The system showed a LOD of 0.95 ng/mL and an excellent sensitivity of 7.91 μA/(ng/mL)

towards cortisol in PBS.

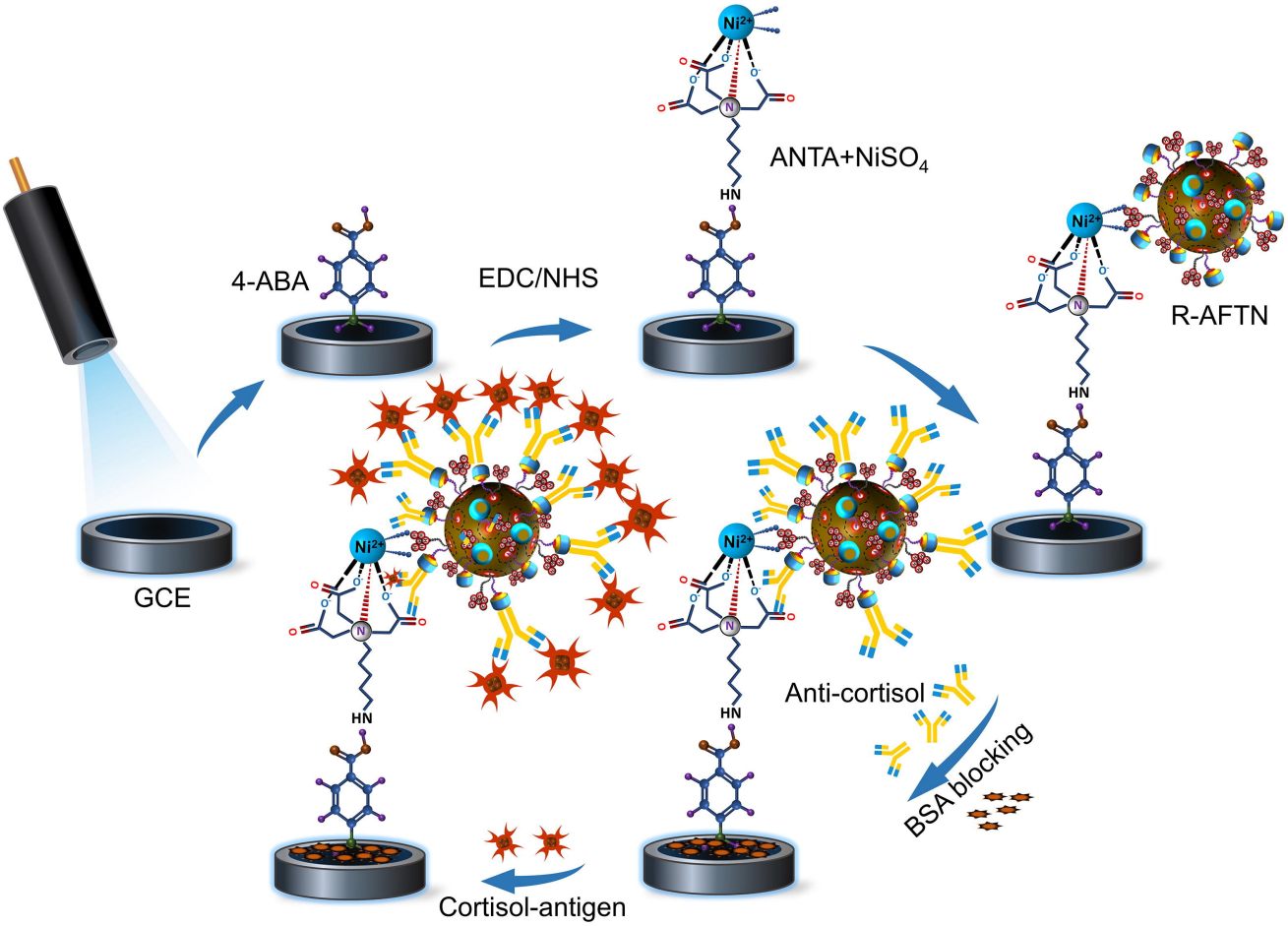

Figure 1.4.8: *Schematic illustration of the step-by-step modification of the glassy carbon electrode toward a cortisol Biosensor. Adapted with permission from reference [134].*

The bioconjugation strategies discussed above have demonstrated their capability for successfully coupling receptors and other surface components in the development of highly specific and sensitive biosensing platforms. However, due to the particular physical and chemical properties of different biosensing interfaces, and specific requirements for fabrication and application, it can be difficult to predict in advance which technique will provide optimal activity for the final device. Therefore, biosensor fabrication nearly always involves lengthy periods of optimisation and researchers should keep an open mind to multiple dif-

ferent bioconjugation strategies. Other techniques which were not used in this research but are highly relevant to the field include: Click chemistry which has been shown to produce high yields and selectivity by carbon-hetero bond formation [135, 136]. Also, exploiting streptavidin-biotin interactions which is one of the strongest non-covalent bonds found in nature, has facilitated the fabrication of numerous biosenisng platforms [137–139].

1.5 Nanobodies and Nanobody Based Biosensors

Arguably the most important component of any biosensing platform is the biorecognition element. This is the unit responsible for providing target specificity and it has a major impact on the sensitivity, selectivity, and stability of the overall biosensor [140]. For electrochemical biosensing platforms some of the most utilised biorecognition elements include enzymes, antibodies, aptamers, and nucleic acids [141–144]. While these have proven extremely useful for biosensor development, they do have limitations. Namely, biological receptor components rely on strict physiological conditions in order to retain their activity [145]. Enzymes and proteins are often comprised of several subunits, which are subject to denaturating [146]. This often means biosensing platforms have poor long term stability which limits their commercial capacity.

A promising alternative which has attracted much attention in recent years are single domain antibodies, commonly termed nanobodies (Nbs) [147]. These are the antigen binding sites of camelid heavy chain only antibodies (VHH), as depecited in figure 1.5.1. Nanobodies have reduced paratopes (part of the Nb which

recognises and binds to the antigen) along with extended and flexible complementarity determining region 3 (CDR3) loops (binding sites of the Nb). This makes them capable of binding concave and hidden epitopes, which their larger antibody counter parts may not be able to access [148, 149]. Hydrophobic residues which would be responsible for interacting with the light chains in traditional antibodies are replaced with more hydrophilic amino acids, which increases the Nbs solubility [148, 150, 151].

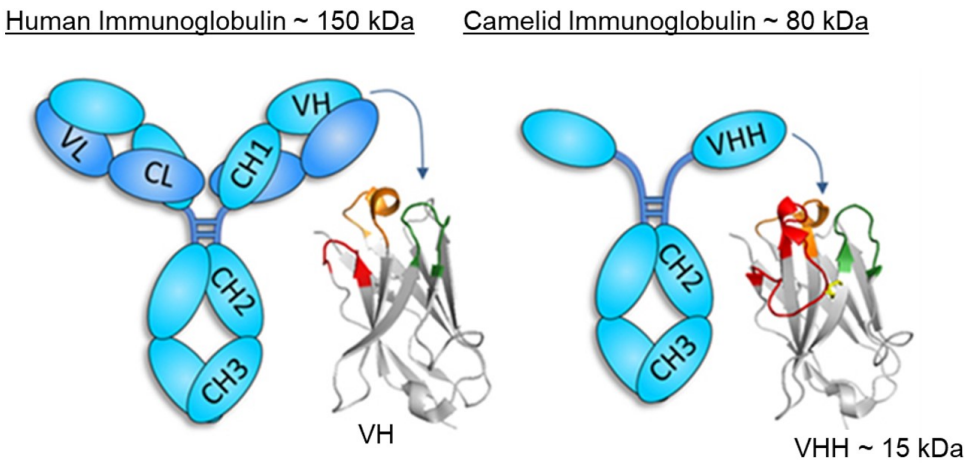

Figure 1.5.1: *Comparison of human and camelid antibodies and fragments. VH = variable heavy domain, VL = variable light domain, CH = constant heavy domain, CL = constant light domain, VHH = single variable domain on a heave chain (nanobody). Adapted with permission from reference [148].*

For the application of biosensing devices one of the major benefits of using Nbs is their excellent stability under stringent physical/chemical conditions. Ladenson et al. (2006) utilised anti-caffeine Nbs derived from llamas for the development of a caffeine enzyme-linked immunosorbent assay (ELISA). The platform was shown to recover its reactivity after exposure to temperatures up to 90°C and was able to sensitively detect caffeine in drinks as hot as 70°C [152]. Chen et al. (2016) further demonstrated this increased thermal stability of Nbs (N-18)

by comparing them with equivalent monoclonal antibodies for the development of a sandwich ELISA for the cancer biomarker alpha-fetoprotein (AFP) [153]. Both systems were exposed to a range of temperatures (37 - 95°C) for 10 minutes in a water bath and the retention in binding activity was compared (figure 1.5.2). Only after heating the Nb platform to around 70-75°C did the binding activity drop below 75%, with a maximum loss of around 40% after exposure to temperatures above 90°C. On the other hand, the antibody platform had already lost over 50% of its activity after treatment at 55-60°C and lost more than 90% after the temperature went above 85°C.

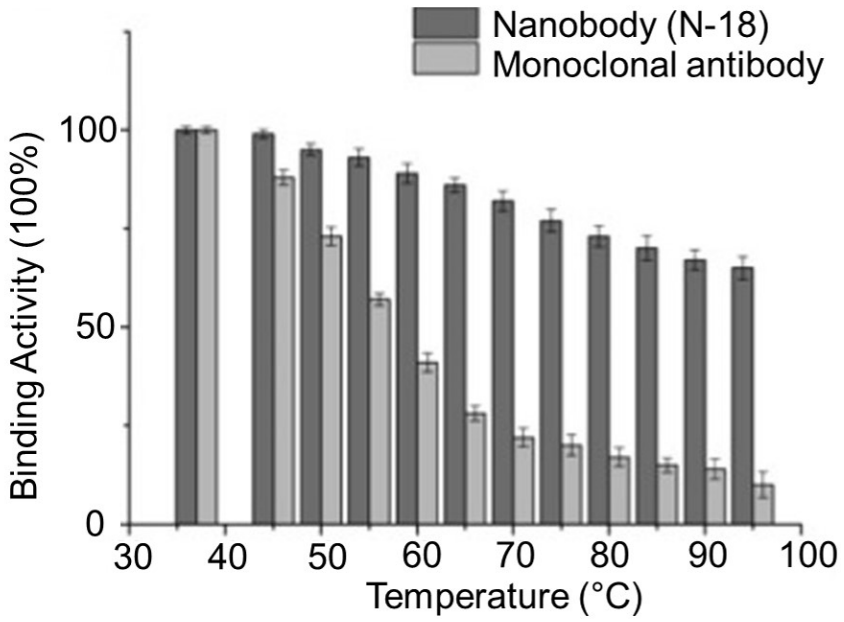

Figure 1.5.2: *Thermal stability analysis of nanobody N-18 with the equivalent monoclonal antibody against AFP at 37, 45, 50, 55, 60, 65, 70, 75, 80, 85, 90 and 95 °C for 10 minutes in a water bath. Adapted with permission from reference [153].*

This increased thermal stability has translated to prolonged shelf lives. When microelectrodes functionalised with antibodies for the detection of ricin were substituted by Nbs, the sensor's shelf life increased 7-fold [154]. This facilitates

the development of biosensors which will not rapidly degrade while the device is sitting idle. This could open the door to on-demand biosensing platforms with surfaces stable enough to be able to carry out detection only when is necessary.

Nbs have also been shown to tolerate the presence of organic solvents. He et al. (2014) developed a Nb based enzyme immunoassay for aflatoxin which remained active in the presence of 80% methanol, 80% acetone, or 20% acetonitrile [155]. This allowed the platform to detect 0.01 ng/mL of aflatoxin spiked into a 70% methanol solution. Other Nb based biosensors have shown to be unaffected by the presence of dimethylsulfoxide (DMSO) in the detection of 3-phenoxybenzoic acid (3-PBA), a metabolite of insecticides (figure 1.5.3) [156]. The platform showed a LOD of 0.01 ng/mL and was robust enough to recover 3-PBA from spiked urine samples within a range of 80 to 112%.

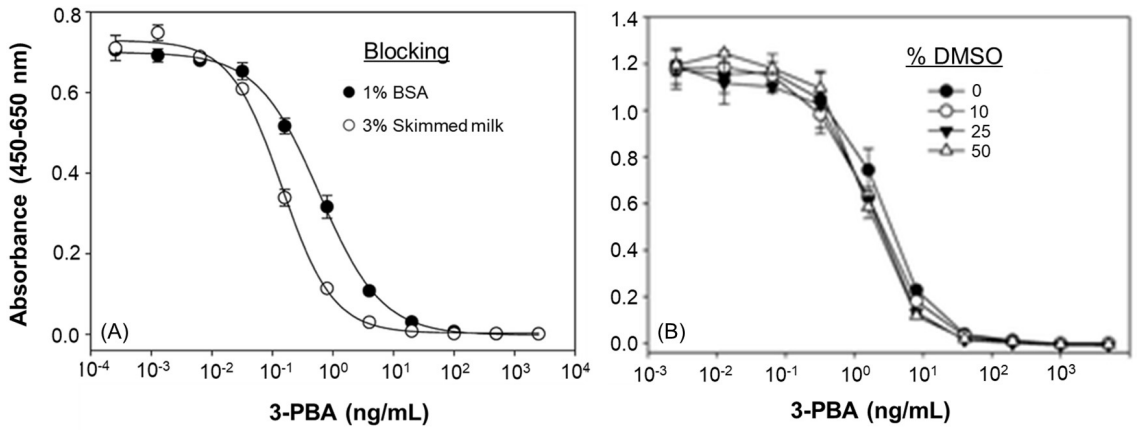

Figure 1.5.3: (A) *Competitive binding of the Nb with 3-PBA, surface blocked with 1% BSA and 3% skimmed milk.* ***(B)*** *Effects of DMSO on the performance of the assay. Adapted with permission from reference [156].*

The small size of Nbs (4 nm x 2.5 nm x 3 nm) also allows higher surface densities, which, together with controlled orientation has been shown to improve the performance of biosensing platforms [148].

The enhanced physical and chemical properties of Nbs discussed above have facilitated the development of extremely sensitive and robust biosensing platforms in recent years. In particular, SARS-CoV-2 and MERS spike proteins have been detected in saliva with attomolar sensitivities [62, 157]. Guo and co-workers functionalised Nbs to organic electrochemical transistors (OECT) with controlled orientation via nanobody–SpyCatcher fusion proteins on disposable gate electrodes (Figure 1.5.4) [62]. The platform demonstrated accuracy and sensitivity on par with reverse transcription-polymerase chain reaction (RT-PCR) tests, in the detection of endogenous spike proteins from unmodified nasopharyngeal samples.

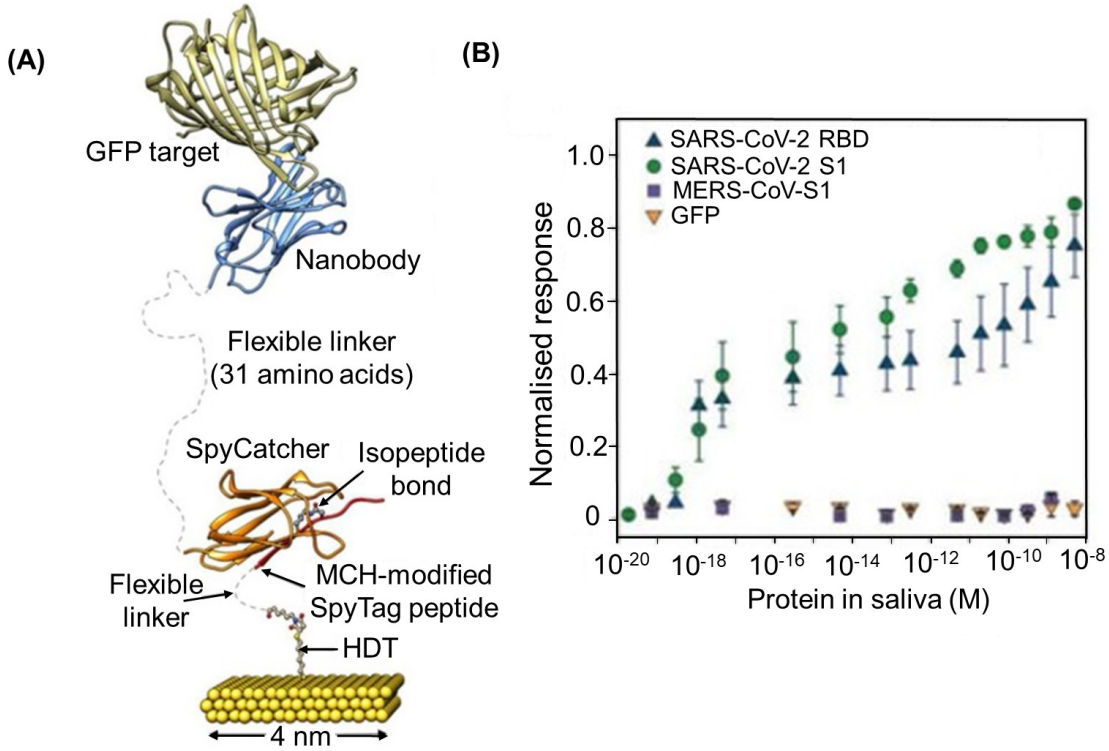

Figure 1.5.4: A) *Structural model of the complete biorecognition layer assembled from 1,6-hexanedithiol (HDT), SpyTag, and nanobody–SpyCatcher.* ***B)*** *Response to SARS-CoV-2 proteins, GFP and MERS-CoV S1 spiked into human saliva. Nature©, adapted from reference [62].*

In summary, literature reports have demonstrated Nbs capacity to act as robust and reliable biological recognition components for biosensing platforms. Coupled with other surface modification techniques previously discussed, such as electropolymerised films and site specific covalent coupling strategies, almost all the necessary components for the development of sensitive and stable analytical devices have been demonstrated. However, to date receptor-target interactions have predominantly been evaluated under static conditions [15]. One exciting area of research involving the use of stimuli to control surface interactions could open the door to on-demand control over receptor-target interactions. This would allow for analytical devices to be directly integrated within bioreactor platforms

and detection to be carried out only when necessary.

1.6 Electrically Responsive Surfaces

Control over the specific capture of biomolecules at the sensing interface would allow the detection of target molecules to be carried out only when required [158]. This would allow the biosensing platform to be in constant contact with the analyte solution and detection of specific antigen(s) to be carried out at predetermined time points. This would be particularly useful for cell therapy bioprocessing as the cells secrete different biomarkers depending on their stage of development and overall health. This would allow response to the needs of the cell culture in real time rather than relying on end stage analysis when the therapeutic product has already been produced. By this point it is already too late to make any alterations to the bioprocess and the quality of the therapeutic product cannot be improved. For this, the biosensor needs to remain inactive for long periods of time while not binding to any antigens in the surrounding environment. The system would then need to switch to its active 'ON' state when required. An exciting area of research which could facilitate this involves the use of external stimuli to modulate the chemical and physical properties of surfaces. Such systems are broadly described as smart stimuli responsive surfaces and literature reports have demonstrated control over surface properties such as bacterial adhesion, protein affinity, surface wettability, and antibody-antigen interactions [15, 159–161]. This has been achieved by perturbing the surfaces with changes in pH, temperature, light, and electrical potentials [27, 162, 163]. Different stimuli have their own ad-

vantages and disadvantages in relation to on-demand biosensing, such as ease of actuation and the level of spatial control. [164, 165]. Most relevant to this body of work are electrically responsive surfaces which are discussed in detail below.

For biomedical applications, electrical stimuli are particularly attractive as they provide fast response times, allow the development of individual switchable regions on the same surface, and are typically biologically compatible [166]. Furthermore, in the case of electrochemical biosensing platforms, the conductive surface serves to both activate the surface and measure the response [164]. Other stimuli such as light, temperature, or pH would require additional read-out equipment adding to the cost and complexity of the system. Literature reports have demonstrated that charged alkyl molecules functionalised to electrode surfaces can undergo conformational changes in response to applied potentials. Lahann et al. (2003) created a surface which could change its wettability in an on-demand fashion [167]. This was achieved using 16-mercaptohexadecanoic acid (2-chlorophenyl)diphenylmethyl ester (MHAE) as a precursor to form a hydrophilic SAM (MHA) on gold. The end group consisted of a negatively charged carboxylate which was electrostatically attracted to the surface when a positive potential was applied (figure 1.6.1). This in turn exposed the hydrophobic alkyl chain resulting in the surface switching from hydrophilic to hydrophobic.

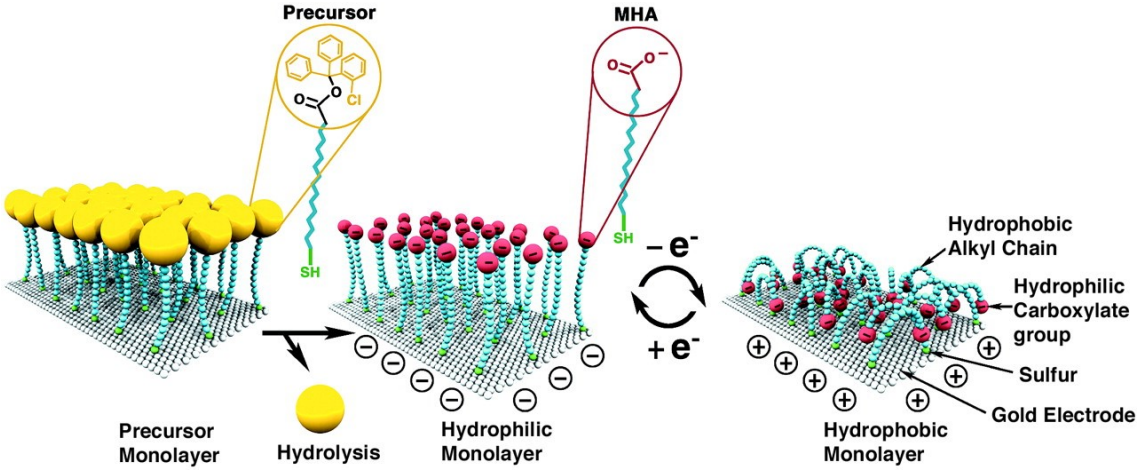

Figure 1.6.1: *Schematic representation of the transition between straight (hydrophilic) and bent (hydrophobic) molecular conformations of MHA in response to a positive potential. Adpated with permission from reference [167]*

Mu et al. (2007) further exploited this mechanism by using MHA SAMs for controlled protein separation, (figure 1.6.2) [168]. This system allowed solutions of avidin and streptavidin to be seperated with an efficiency of 80-90%.

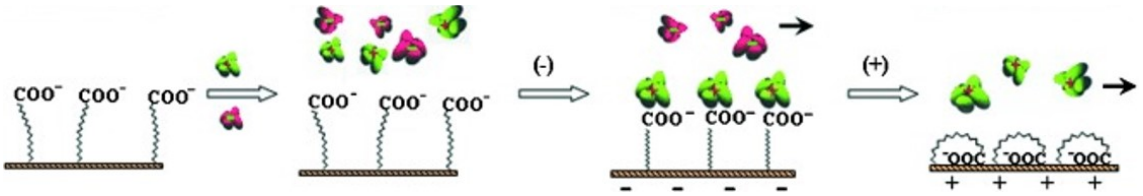

Figure 1.6.2: *Schematic representation of the electrically controlled separation of avidin (green) and streptavidin (pink). Adpated with permission from reference [168]*

Prazetti et al. (2013) highlighted the importance of surface packing density in order to efficiently change the conformation of the alkyl chains [169]. Alkane thiol SAMs have been shown to interact with each other laterally once adsorbed on a surface, this can compromise the efficiency of switching due to steric hindrance [170]. In order to prevent phase-segregation, the SAMs were formed using a bulky end-group (dendron) which can be successively removed by hydrolysis allowing the insertion of mercaptoethanol (MET) as a backfiller (figure 1.6.3).

This two component SAM system facilitated control over bacterial adhesion at the interface. Under a negative potential, the exposed negative carboxylate anions interact with the positively charged regions of the bacteria allowing bacterial adhesion. Then under positive potential the surface changes from positively charged to neutral and hydrophobic, preventing the bacteria from attaching.

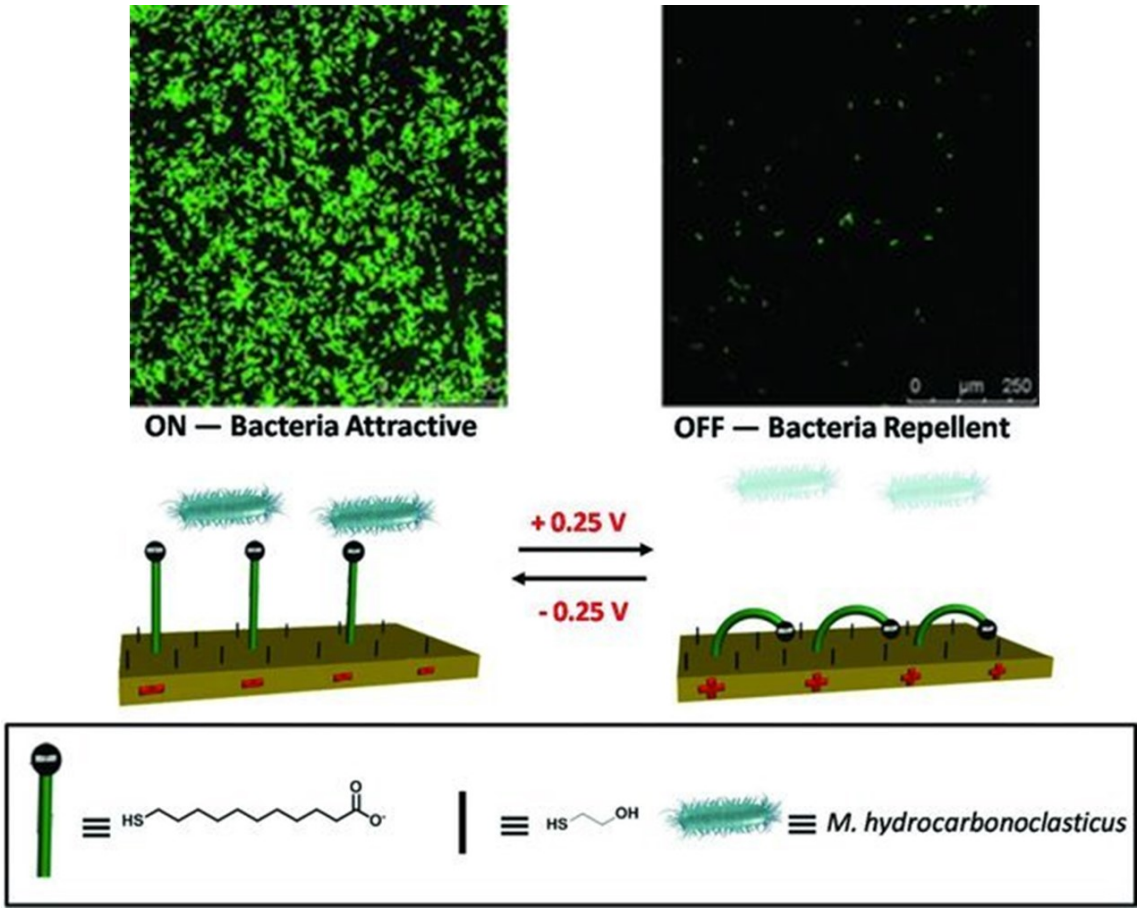

Figure 1.6.3: Top: *Fluorescent microscopy images of 'ON' (bacteria attractive) state and 'OFF' (baterial repellent) state.* ***Bottom:*** *Schematic representation of an electrically switchable two-component SAM that is able to reversibly and rapidly switch its molecular conformation in response to an applied potential. Adpated with permission from reference [169]*

More recently, electrically switchable surfaces have also been developed to control specific antibody-antigen interactions [15]. This was achieved by forming a mixed SAM consisting of a positively charged oligopeptide with a terminal

progesterone unit (progesterone-C7-4KC) and oligo(ethylene glycol) thiol (C11EG6) acting as a spacer, (figure 1.6.4). By applying a negative potential the positively charged progesterone-C7-4KC units were electrostatically attracted downwards which caused the progesterone unit to be concealed by the surrounding C11EG6 molecules. This provided enough steric hindrance around the progesterone that the associated antibody could not effectively bind. When a positive potential was applied the progesterone-C7-4KC units experience electrostatic repulsion and the progesterone was extended out into the surrounding environment, allowing it to then interact with the antibody.

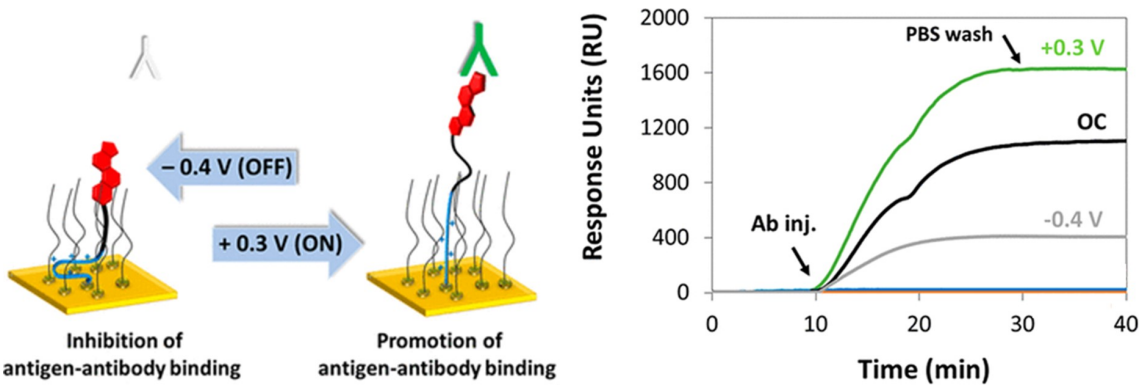

Figure 1.6.4: Left: *Schematic representation of the dynamic progesterone-C7-4KC and C11EGS mixed SAM, switching from an 'OFF' (-0.4 V) to an 'ON' (+0.3 V) state. Red = progesterone, green = anti-progesterone antibody.* ***Right:*** *Antibody binding monitored with surface plasmon resonance (SPR). Adpated with permission from reference [15]*

The switching efficiency was monitored using surface plasmon resonance (SPR) and found to be 73% between the 'OFF' and 'ON' states of the system. This approach has the capacity to be adapted for other antigen-antibody systems and meets the needs for *in situ* long-term assessment of biological processes.

1.7 Motivation and Aim of Research

As of 2022 there were 178 on-going cell and gene therapy clinical trials in the UK alone [171]. As the demand increases (commercialisation phase) cell expansion becomes labour intensive and costly [172]. Suspension cultures in bioreactors have proven to be the most cost effective approach for cellular expansion to date [173]. However, as our understanding of biology improves the importance of cytokines and other cell signalling molecules has become more understood for cell differentiation, expansion, and activation [174]. Currently there exists few (if any) analytical devices for the real-time measurement of such molecules, resulting in poor confidence in production trajectory [11]. This has resulted in end-point diagnostics leading to long feedback loops, high production costs, low yields, and suboptimal bioprocessing. Ideally what is needed is an integrated analytical device which is capable of carrying out sensitive detection of multiple different target molecules (cytokines) over different time points. This would allow the development of the therapeutic product to be continuously monitored. The platform must be able to carry out detection on-demand, preventing premature binding events at the receptors binding site. This would allow the biosensor to be integrated within the bioreactor in a closed system reducing the risk of contamination during sample extraction. To this end, inspired by the advancements in surface modification strategies discussed above, this research aims to open a path towards smart, switchable, and stable nanobody surfaces for on-demand biosensing. To achieve this, gold arrays will be fabricated, allowing electrodes to be individually or collectively electrically addressed. This will facilitate electrochemical detection of

multiple different targets over a prolonged period of time. The electrode surfaces will be modified with electropolymerised films in order to insulate the electrode surface and also provide a stable interfacial support structure for coupling the receptor components. Due to their benefits discussed in section 1.5 above, nanobodies will be employed as the receptor components. Finally, charged oligopeptides coupled to the surface (in conjugation with the nanobodies) will be used to control nanobody-antigen interactions. This will allow the system to switch from an 'OFF state' (extended peptides) where the binding sites of the nanobodies are concealed, to an 'ON state' (collapsed peptides) where the binding sites are exposed to the surrounding environment. This will be achieved through electrostatic attraction/repulsion when potentials are applied across the surface. A schematic of the purposed biosensing platform can be seen in figure 1.7.1 below.

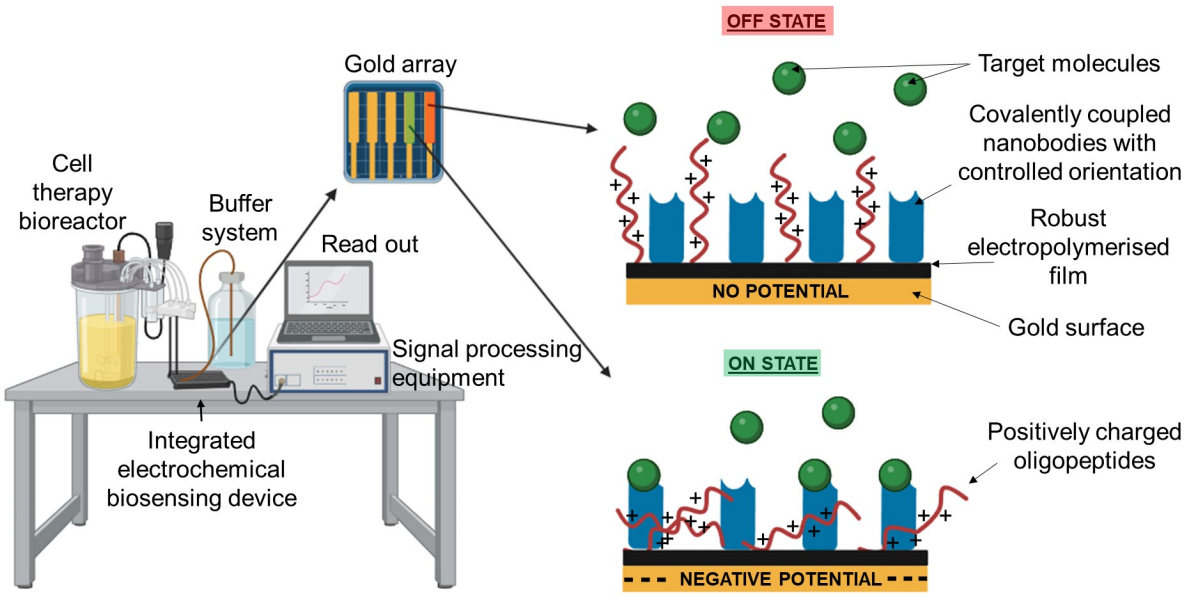

Figure 1.7.1: *Proposed electrochemical biosensor integrated with a bench top bioreactor, showing surface architecture and conformational differences of the charged oligopeptides between the 'ON' and 'OFF' states. Created with BioRender.*

In order to demonstrate proof of concept, anti-eGFP (enhanced green flu-

orescent protein) nanobodies were used as a model system. It is hoped that once the final system has be optimised, multiple different nanobodies can be used for the detection of a wide range of target molecules. In order to successfully fabricate the purposed biosensing platform shown in figure 1.7.1, the following objectives were outlined:

Objective 1. Demonstrate the capacity of charged, surface bound oligopeptides to under go confirmational changes in response to applied potentials.

Objective 2. Fabricate a robust and controllable electropolymerised film and a working gold array.

Objective 3. Optimise nanobody coupling and antigen detection

Chapter 2. Principles Behind the Experimental Techniques

Abstract: *In this chapter, the working principles behind the most common surface characterisation techniques used in this work are discussed. These techniques were primarily used for monitoring the sequential fabrication of the biosensing interface, allowing changes in the physical, chemical, and electrochemical properties to be detected. The techniques outlined include surface plasmon resonance, electrochemical impedance spectroscopy, cyclic voltammetry, ellipsometry, and X-ray photoelectron spectroscopy. Other techniques were also used however, instead of discussing them here they are given a brief introduction when they arise in the research chapters.*

2.1 Surface Plasmon Resonance (SPR)

Surface plasmon resonance (SPR) offers the most advanced optical based biosensor technology which allows for real-time, label-free detection of surface interactions [175]. The working principle of SPR measurements is based on the excitation of electrons in a thin metal sheet such as gold or silver. Consider the set up in figure 2.1.1 below, p-polarised light (in the plane of incidence) is shone through a prism with a gold slide positioned on top. As the angle (ϕ) of the incident light changes, the intensity of the reflected light will pass through a minimum known as the resonance angle or SPR-dip. This indicates that there is an energy transfer occurring between the incident light and the electrons at the surface. This is due to the photons of the p-polarised light inducing oscillations of the free electrons at the dielectric interface [176]. The oscillating electrons generate an evanescent electric field that penetrates through the gold surface and decays exponentially into the surrounding environment (approx. 300 nm from the interface) [175]. If there is a change in the refractive index (RI) in the immediate vicinity of the gold

surface it will cause the surface plasmon wave to go out of resonance and result in a change to the angle of reflected light (from A to B in figure 2.1.1 below). This phenomenon can be exploited as a sensitive detection method for any changes in mass at the interface, such as proteins binding to receptors attached to the gold surface.

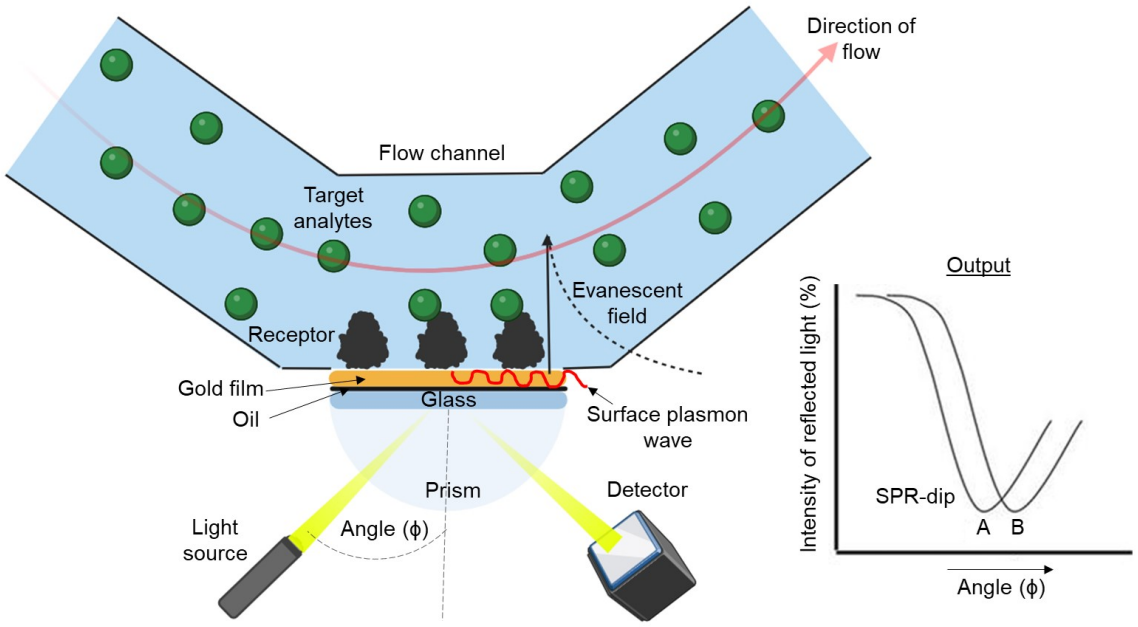

Figure 2.1.1: *Experimental set-up of surface plasmon resonance excitation. Created with BioRender.*

Measuring this change in RI from A to B as a function of time produces what's known as a sensorgram (figure 2.1.2). If this change is due to biomolecular interactions such as antibody-antigen binding, the kinetics of this interaction can be studied in real time [176]. The vast majority of SPR binding responses can be fitted to the Langmuir model, which describes a 1:1 interaction between one receptor and one target molecule [177, 178]. The complex that forms follows pseudo-first-order kinetics and there is the assumptions that the binding is equivalent for all binding sites and is not limited by mass transport. This interaction

can be described by reaction 1 below, where A represents the target analyte, B represents the receptor, k_a is the association constant, and k_d is the dissociation constant.

$$A + B \underset{k_d}{\overset{k_a}{\rightleftharpoons}} AB \quad (1)$$

In a SPR experiment first a running buffer is allowed to flow through the system until a stable baseline is established at angle A (figure 2.1.2). After the sample is injected the RI changes to angle B as a function of time, following a single exponential binding curve which is indicative of antibody-antigen interactions. This is often termed the association phase. Eventually a steady state will be reached (saturation point) where there is no more available receptor binding sites and the rate of k_a is equal to that of k_d. For strong surface interactions such as antibody-antigen interactions, only non-specifically bound antigens will be removed during the washing phase. This will result in the establishment of a new baseline which can be used to measure the binding response when compared to the original baseline.

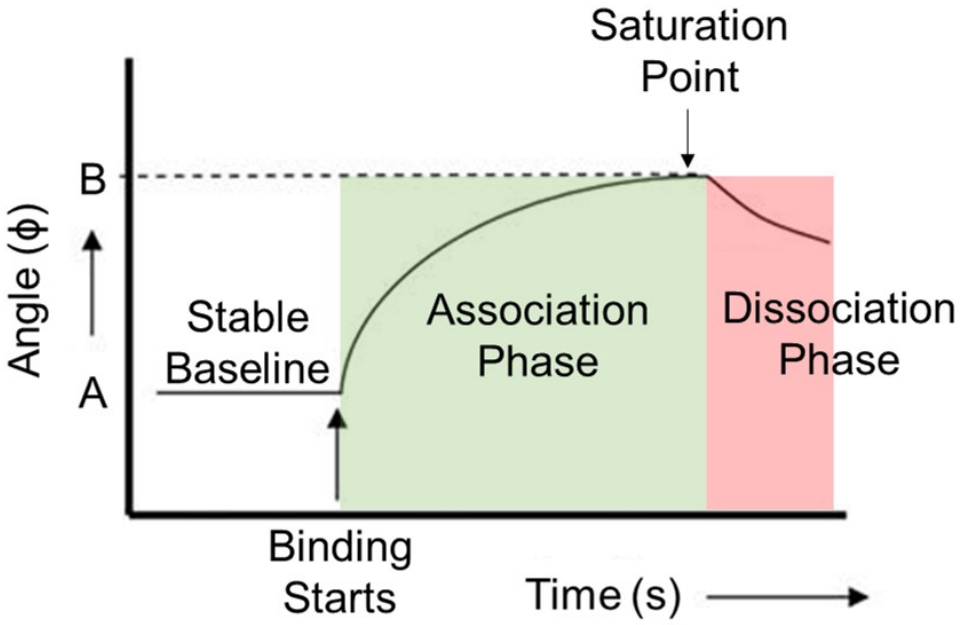

Figure 2.1.2: *Typical SPR sensorgram.*

In this body of work, SPR was used to measure nanobody-antigen interactions therefore, the binding kinetics can be assumed to follow the Langmuir model discussed above. The binding response was reported as the difference between the new baseline formed after the washing phase and the original baseline established during the stabilisation phase. For proteins, 1000 RU approximately represents binding of 1 ng/mm^2 of material onto the surface however, this can vary depending on the particular SPR equipment used [179].

2.1.1 Electrochemical Surface Plasmon Resonance (E-SPR)

For the development of electrically responsive surfaces, the SPR equipment (Reichert SPR 7500) had to be modified with an electrochemical flow cell. This consisted of a three-electrode set up which could be connected to a potentiostat for the controlled application of electrical potentials across the surface, (figure 2.1.3).

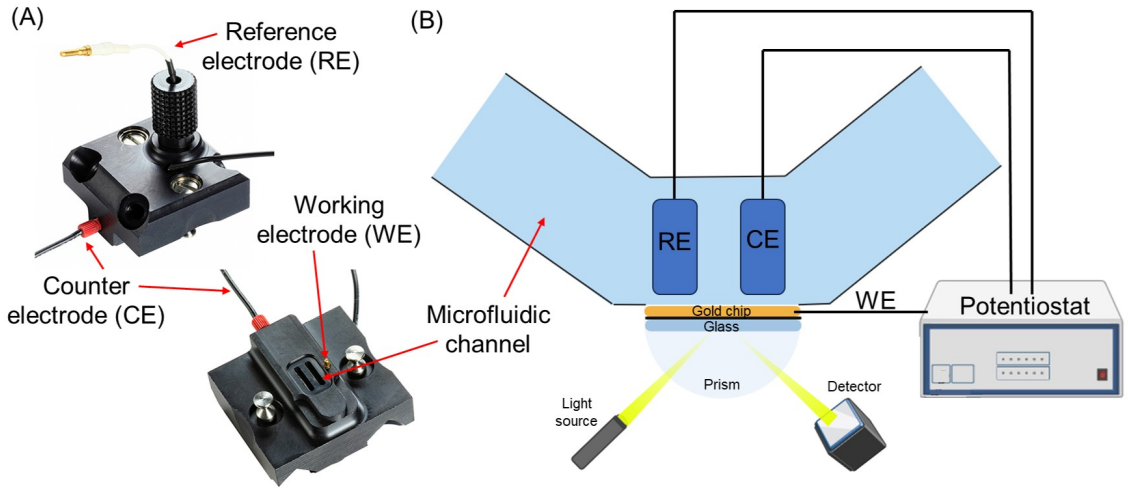

Figure 2.1.3: (A) *Electrochemical flow cell for Reichert 7500 SPR, showing connections for the reference, counter and working electrodes.* ***(B)*** *Schematic of the E-SPR set up. Created with BioRender.*

The gold SPR chip acts as the working electrode (WE), this is where the reactions of interest take place. The counter electrode (CE) consists of a platinum wire, the potentiostat controls the voltage difference between these two electrodes, causing a current to flow. The potentiostat sets the desired potential difference between the WE and the reference electrode (RE). To maintain this potential difference, the potentiostat allows current to flow through the CE. The amount of current is then adjusted based on the desired potential and the actual potential measured at the WE. The potential difference can be kept constant via a feedback mechanism with respect to the RE (Ag/AgCl) and also with an voltage reference in the potentiostat's internal circuitry [180, 181]. When the Ag/AgCl RE is submerged in a saturated solution of KCl and AgCl the reversible redox reaction as see in reaction 2 occurs, providing a stable potential of +0.222 V at 25°C vs the standard hydrogen electrode (SHE). [182].

$$AgCl_{(s)} + e^{-} \rightleftharpoons Ag_{(s)} + Cl^{-}_{(aq)} \quad (2)$$

In this body of work, E-SPR allowed for the real-time measurement of specific antigen interactions with modified gold surfaces under applied potentials.

2.2 Electroanalytical Techniques

2.2.1 The Electrochemical Cell

Typically for electrochemical measurements a potential is applied across the system of interest and the resulting current response in measured. For this, two main electrode configurations are used, the simplest requiring only two electrodes and a voltage source (figure 2.2.1 a). The chemistry of interest occurs at the WE while the the other electrode acts as both a CE and RE. Ideally, the CE/RE allows current to flow completing the circuit and maintains a constant interfacial potential [183]. Two electrodes measure the whole cell and are often used in batteries and fuel cells or when the CE/RE potential can be expected to not significantly drift during the experiment [184]. This occurs when low currents or short timescales are used. In order to complete the circuit, the electrodes are submerged in a conductive electrolyte solution (figure 2.2.1). This allows an electrolytic current to flow between the electrodes [185]. However, the intrinsic resistance of this solution causes a voltage drop across the system which can result in a shift in peak potential, an increase in peak separation, a decrease in the magnitude of the current, and poor control over the potential of the WE [186].

In order to overcome these limitations, the CE/RE can be split into two separate electrodes and the voltage source replaced by a potentiostat (figure 2.2.1 b). This allows the current to flow between the WE and CE while not affecting the

interfacial potential of the RE. The potentiostat allows current to flow through the CE which is then adjusted based on the desired potential and the actual potential measured at the WE. The potential difference can be kept constant via a feedback mechanism with respect to the RE. [187].

The electrode materials vary depending on their function and the overall application of the system. For electrochemical biosensing the WE acts as a transducer while the CE creates a connection to the electrolyte completing the circuit. Conducting materials such as gold, carbon, platinum, and silicon are commonly used for these [107]. The RE should have a stable and well known potential so any changes in the measured potential can be attributed to reactions occuring at the WE. For this body of work, an Ag/AgCl RE was used which acts as a reversible redox electrode with the equilibrium between the solid AgCl and the solid Ag metal. The overall reaction can be described as:

$$\begin{aligned} AgCl_{(s)} + e^- &\rightleftharpoons Ag_{(s)} + Cl^-_{(aq)} \\ Ag^+_{(aq)} + e^- &\rightleftharpoons Ag_{(s)} \end{aligned} \tag{3}$$

According to IUPAC, the Ag/AgCl electrode has a standard potential of +0.22249 $\pm$ 0.013 V vs standard hydrogen electrode (SHE) at 25 $^\circ$C [182]. The RE passes negligible current and therefore, the voltage drop between the WE and RE is very small. The RE is typically placed in close proximity to the WE to further reduce the voltage drop.

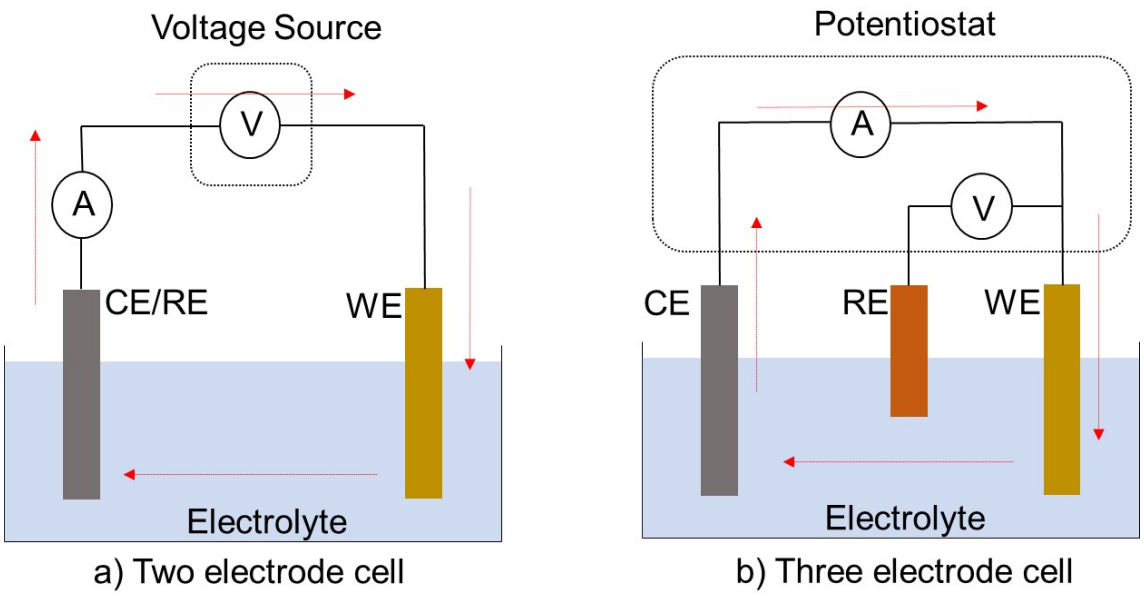

Figure 2.2.1: *Red arrows indicated the flow of current in* ***a)*** *a two electrode cell and* ***b)*** *a three electrode cell. A = ammeter, V = voltmeter.*

2.2.2 Cyclic Voltammetry (CV)

Cyclic voltammetry (CV) is a popular electroanalytical technique used to investigate oxidation and reduction processes along with electron transfer initiated reactions [188]. It is carried out by cycling the potential of the WE and measuring the resulting current response (figure 2.2.2). For applications such as biosensing and monitoring surface modifications, redox probes are commonly used. These are typically metal complexes with well defined and understood oxidation and reduction processes [189]. Ferri/ferrocyanide ($Fe(CN)_6^{-4/-3}$) is a commonly used probe which consists of an iron center with six cyanide ligands arranged in an octahedral coordination structure [190]. $Fe(CN)_6^{-4/-3}$ can be oxidised and reduced between it's -4 and -3 oxidation states via a single electron transfer process:

$$Fe(CN)_{(6)}^{-4} \longrightarrow Fe(CN)_{(6)}^{-3} + e^{-}$$
$$Fe(CN)_{(6)}^{-3} + e^{-} \longrightarrow Fe(CN)_{(6)}^{-4} \quad (4)$$

This process can be monitored using CV, yielding fundamental information regarding the redox reaction itself which indirectly provides information about the electrode surface. Figure 2.2.2 shows a typical CV response for $Fe(CN)_6^{-4/-3}$. The potential first scans in the negative direction starting at a specific potential (a) and ends at a lower potential (d). The potential is then scanned back to the starting potential at point (g), completing one cycle. Numerous scans can be carried out and the scan rate is typically set somewhere between 10 - 200 mV/s.

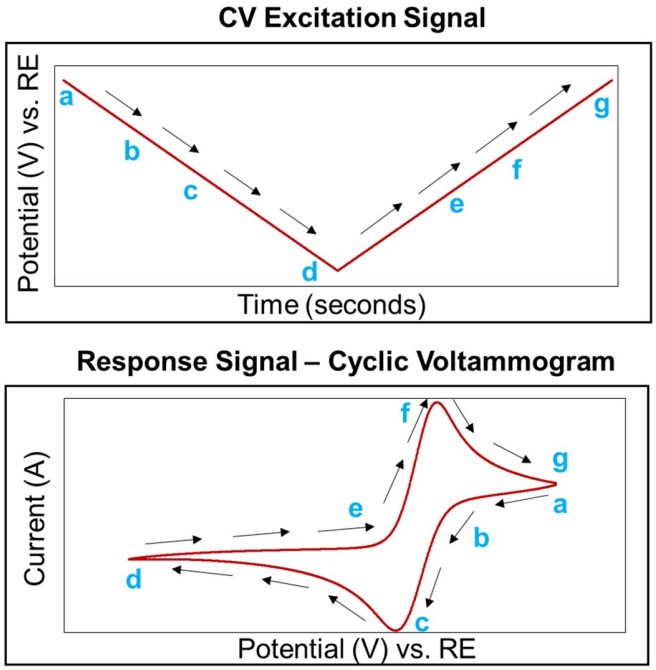

Figure 2.2.2: top: *Excitation potential starting at potential (a) reaching a minimum at point (d) and returning to the starting potential at point (g).* ***bottom:*** *Response signal (cyclic voltammogram) of* $Fe(CN)_6^{-4/-3}$ *showing reduction and oxidation peaks at points (c) and (f) respectively.*

As the potential is scanned in the negative direction it begins to reduce the

$Fe(CN)_6^{-3}$ and the current exponentially decreases (b). For a reversible process (electrons are transferred quickly without significant thermodynamic barriers), the reduction is controlled by the diffusion of the $Fe(CN)_6^{-3}$ to the electrode surface and the proportion of $Fe(CN)_6^{-3}$ which has been consumed [191]. The amount of $Fe(CN)_6^{-3}$ being consumed continues to increase giving rise to a reduction peak in the voltammogram. After this point the current is limited by the mass transport of $Fe(CN)_6^{-3}$ from the bulk solution to the electrode interface, which is relatively slow over electrochemical timescales. This is understood through Fick's laws which describe the spontaneous movement of any material from an area of high concentration to an area of lower concentration. The current then decreases until a steady state is reached, in which decreasing the potential further has no effect on the current response (d). The potential is then scanned back in the positive direction where the oxidation of $Fe(CN)_6^{-4}$ mirrors the reduction process. This gives rise to the characteristic 'duck' shape in the cyclic voltammogram (figure 2.2.2) [188].

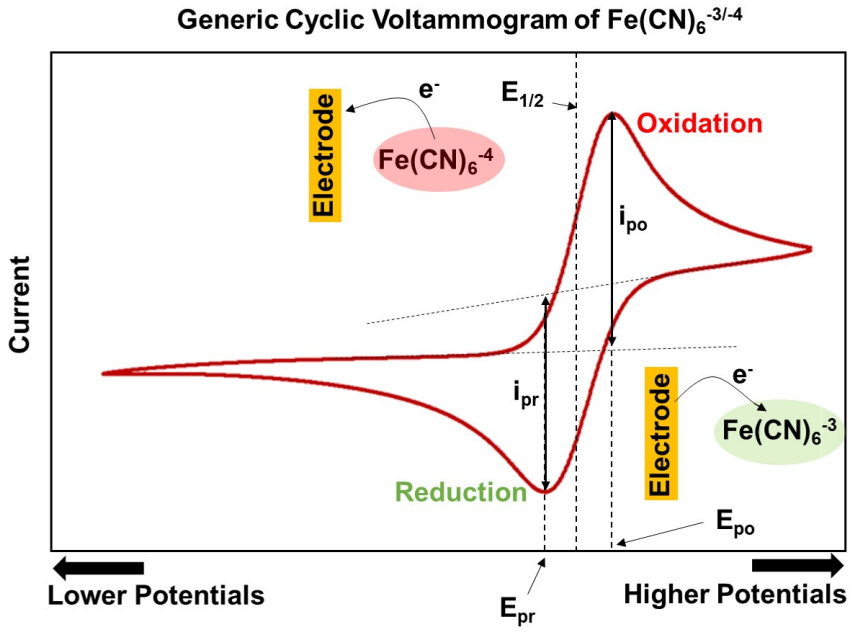

Figure 2.2.3: *Cyclic voltammogram of $Fe(CN)_6^{-4/-3}$. i_{pr} = peak reduction current, i_{po} = peak oxidation current, E_{pr} = reduction peak potential, E_{po} = oxidation peak potential.*

CV is described by a number of fundamental equations which describe the electrochemistry occurring during the experiment. These allow redox behavior, kinetics, diffusion coefficients, concentration analysis, and electrode surface properties to be studied.

Nernst Equation: Relates the potential to the concentration of the redox species [192].

$$E = E^{\circ} - \frac{RT}{nF} \ln \frac{[red]}{[ox]} \tag{5}$$

Where E = the cell potential, E° = the standard cell potential, R = the universal gas constant, T = temperature in kelvin, n = the number of electrons transferred in the redox reaction, F = Faraday's constant, [red] = concentration of the reduced species, and [ox] = concentration of the oxidised species.

Butler-Volmer Equation: Relates the potential to the current density [193].

$$i = i_0 \left(\exp\left(\frac{-\alpha_a n F \eta}{RT} \right) - \exp\left(\frac{\alpha_c n F \eta}{RT} \right) \right) \quad (6)$$

Where i = the current density, i_0 = the exchange current density, α_a and α_c = the anodic and cathodic charge transfer coefficients, n = the number of electrons transferred in the redox reaction, F = Faraday's constant, η = the overpotential, R = the universal gas constant, and T = temperature in kelvin.

Randles-Sevcik Equation: Relates the peak current to the concentration and diffusion coefficient of the redox species [194].

$$i_p = 0.4463 n F A C \sqrt{\frac{n F v D}{RT}} \quad (7)$$

Where i_p = the peak current, n = the number of electrons transferred in the redox reaction, F = Faraday's constant, A = the electrode area, D = the diffusion coefficient of the redox species, ν = the scan rate, C = the concentration of the redox species, R = the universal gas constant, and T = temperature in kelvin. These equations are useful for extracting valuable information from cyclic voltammograms which allow for an understanding of the physical/chemical processes occurring in the system under investigation.

In this body of work, CV is used to monitor modifications to the WE's surface (biosensing interface). Films deposited on the WE's surface can act as a physical and/or electrostatic barrier, thus reducing electron transfer between the redox probe and the electrode surface. This reduction in redox activity can be used to monitor the surface after each fabrication step (figure 2.2.4).

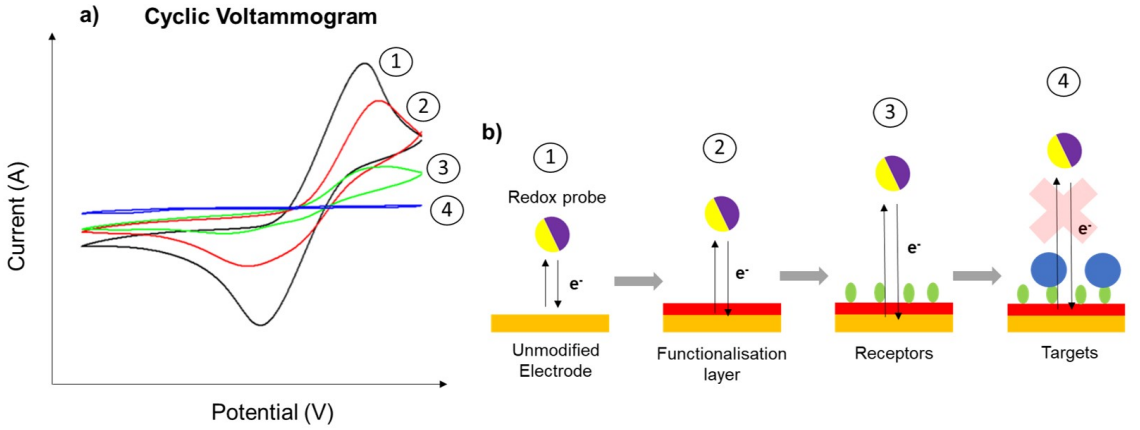

Figure 2.2.4: a) *Cyclic voltammogram showing the activity of the redox probe decreasing for each surface fabrication step 1 - 4.* ***b)*** *Corresponding surfaces measured using cyclic voltammetry, once the target analyte is bound the redox activity is completely suppressed.*

2.2.3 Electrochemical Impedance Spectroscopy (EIS)

Electrochemical impedance spectroscopy (EIS) is an electroanalytical technique widely used in sensing, corrosion studies, semiconductor science, energy storage and conversion technologies [195]. This electroanalytical technique is attractive due to some of its inherent advantages such as it being non-destructive, low cost, highly sensitive, easily miniaturised and relatively simple to design. EIS involves the perturbation of an electrochemical system by applying a sinusoidal voltage or current and measuring the subsequent response over a wide frequency range (figure 2.2.5). EIS is an extremely powerful technique, assessing the system's surface and bulk electrical properties. However, an electrochemical cell's voltage-current relationship is non-linear i.e. doubling the voltage does not necessarily double the current. Therefore, a small alternating potential (10 mV) is typically used, as over that small potential window the voltage-current relationship will be pseudo-linear. The electrochemical system under investigation must also be in

a steady state (not changing over time) and the measured signal must only be related to the applied excitation signal (not due to any external sources) [196]. This ensures the signal is only shifted in phase (ϕ) and amplitude (equations (8) and (9)), allowing accurate impedance analysis to be carried out. The excitation potential can be presented as a function of time:

$$E_t = E_0 \cdot \sin(\omega t) \tag{8}$$

where E_t = the potential at time t, E_0 = amplitude, and ω = the radial frequency where $\omega = 2\pi f$ (f = the applied frequency). The current response is subsequently describe by the equation:

$$I_t = I_0 \cdot \sin(\omega t + \phi) \tag{9}$$

Where I_t = the current at time t, I_0 = the new amplitude, and ϕ = the shift in phase (figure 2.1.8)

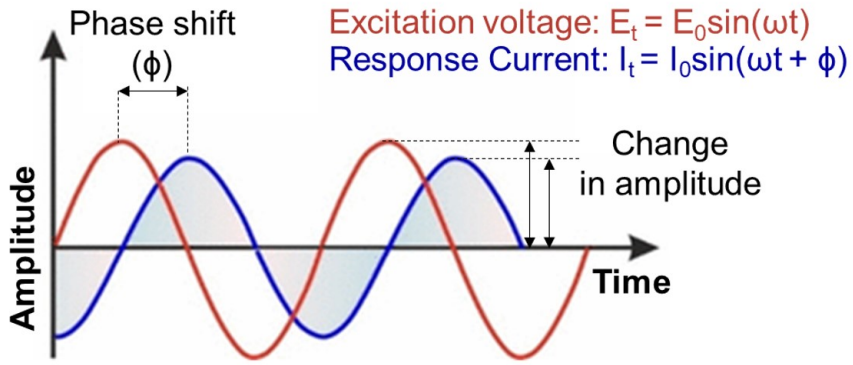

Figure 2.2.5: *EIS excitation potential (red) and corresponding current response (blue).*

The impedance (Z), which is a measure of the system's opposition to alternating current due to the combined effects of resistance and reactance, can be obtained from the following equation which is derived from Ohm's law [197].

$$Z = \frac{E_t}{I_t} = Z_0(cos\phi + jsin\phi) \quad (10)$$

where j = the imaginary number used to represent the square root of –1, and Z_0 = the magnitude. Physical components in the electrochemical system under investigation, can be described using equivalent circuit elements such as resistors and capacitors. For example, films on the electrode surface can act as a barrier to charge transfer across the interface and can be described electrically as a resistor. Likewise, the build up of ionic charge at the electrical double layer (EDL) acts like a capacitor and can be described as such (figure 2.2.6). Common circuit elements used to model biosensing interfaces are listed in table 2.2.1 and include: An ohmic resistor (R), a capacitor (C), a constant phase element (CPE) which acts as an imperfect capacitor, and a Warburg impedance element (W) which is used to model diffusion processes. The phase angle of the elements are also listed which are a measure of the time difference between the voltage and current waveforms, with a phase angle of -90° for a capacitor indicating that the current leads the voltage by a quarter of a cycle.

Table 2.2.1: *Common impedance elements used for modelling electrochemical systems.* α *= transfer coefficient (0* $\leq \alpha \leq$ *1), and Q = a model parameter analogous to capacitance.*

Impedance element	**Impedance Value**	**Phase angle**	**Frequency dependence**
R	$Z = R$	$0°$	No
C	$Z = \frac{1}{j\omega C}$	$-90°$	Yes
CPE	$Z = \frac{1}{Q(j\omega)^\alpha}$	$0 - 90°$	Yes
Warburg	$Z = \frac{\sigma}{\sqrt{\omega}}(1-j)$ σ = The Warburg Coefficient	$-45°$	Yes

These circuit components can be combined in series and/or parallel pro-

ducing equivalent circuit models which are used to approximate experimental EIS data. Faradaic EIS (redox probe present) is typically used when sensitivity to resistance changes is important, while non-Faradaic EIS (no probe) is used when sensitivity to capacitive changes is important [198]. Figure 2.2.6 (a), shows an expansion of the Randles circuit model which is commonly used in faradaic EIS to investigate biosensing interfaces [194]. EIS data is complex and can be visualised in a number of different ways. Most common are are Bode and Nyquist plot as seen in figure 2.2.6 (b) and (c) respectively. Each have their advantages and highlight different information, Bode plots provide a clear view of the impedance and phase shift across different frequencies, while Nyquist plots offer a sensitive and direct way to visualise changes in the impedance spectrum [199]. Fitting the models to the experimental data allows estimation of parameters such as solution resistance, double layer capacitance, and charge transfer resistance. Monitoring changes to these parameters following receptor-target interactions can be used as the detection method in electrocheimcal biosensing.

2.3 Ellipsometry

Ellipsometry is an optical technique used for sensitive and non-destructive measurements of thin films on reflective materials (gold, titanium, SiO_2 etc.) [200]. Parameters such as composition, thickness, conductivity, and porosity, have an effect on the optical properties of organic films and ellipsometry can provide information on all of these. It has the capacity to analyse a wide range of films and is very sensitive to thin films below 10 nm [201]. In order to understand how this

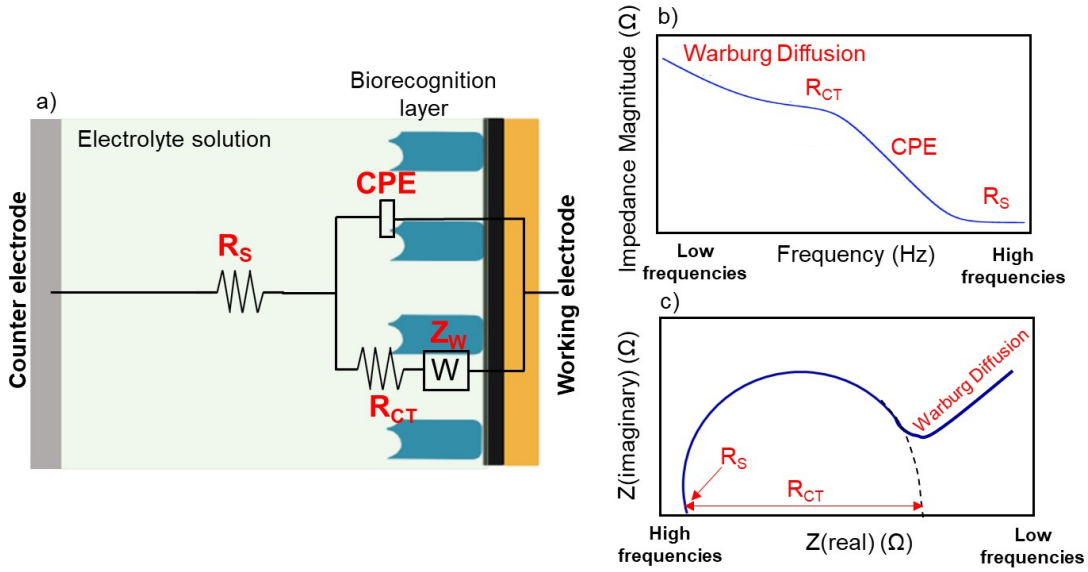

Figure 2.2.6: a) *Expansion of the Randles circuit used to model a typical biosensing interface. R_s = solution resistance, CPE = constant phase element, R_{ct} = charge transfer resistance, and Z_w = Warburg diffusion. Typical faradaic EIS response of system a) represented in a Bode plot* ***b)*** *and Nyquist plot* ***a)*** *.*

technique actually works it is useful to understand the nature of light as described by James Clerk Maxwell (1831-1897) and how this light interacts with materials. Maxwell describes light as a wave consisting of electric (E) and magnetic (B) fields which are both mutually perpendicular and perpendicular to the direction the light is propagating (Z), as seen in figure 2.3.1 below [202].

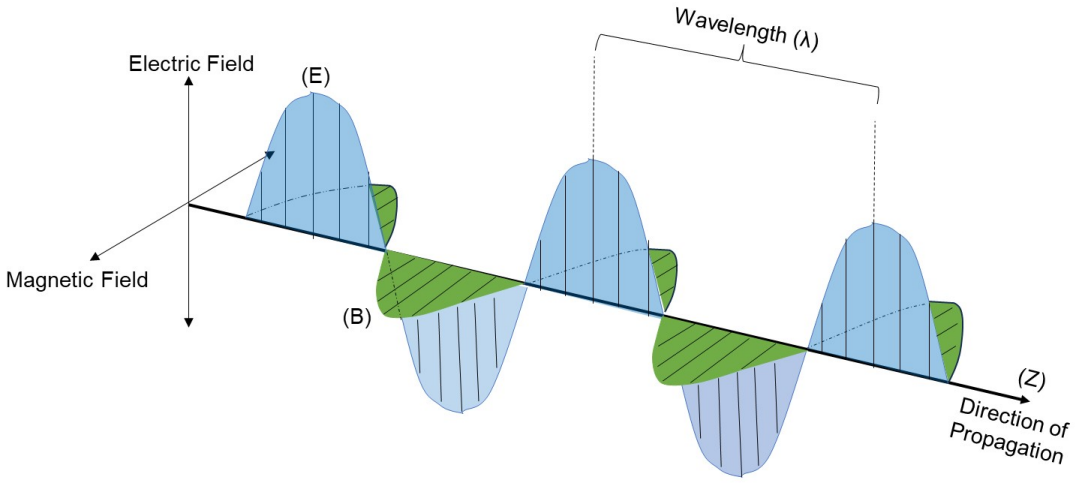

Figure 2.3.1: *The electric (E) and magnetic (B) fields of a light wave propagating in the (Z) direction.*

The variation with time of E in relation to the direction of propagation is known as the polarisation. The B field is typically disregarded when defining the polarisation state of light, as its effects on most materials are negligible [202]. The E field can be decomposed in two vectors - the 's' (parallel to plane of incidence) and the 'p' (perpendicular to the plane of incidence) components. When light is unpolarised, the E field oscillates randomly, this is the case for light originating from most natural sources (e.g. the sun). However, light can exist in three polarisation states (figure 2.3.2) including linearly, circularly, and elliptical polarised. For linearly polarised light, the 's' and 'p' components of E are equal in phase, but not necessarily in amplitude. For circularly polarised light, the 's' and 'p' components are 90° out of phase but equal in amplitude, and finally, for elliptically polarised light, the 's' and 'p' components have an arbitrary relationship to each other.

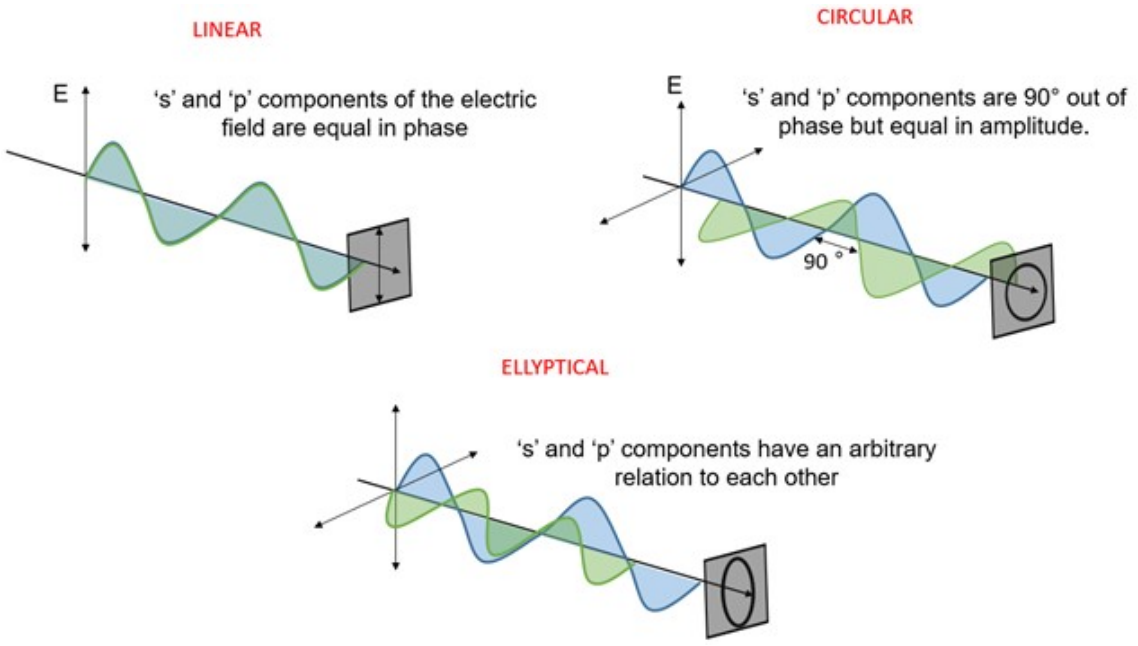

Figure 2.3.2: *Linearly polarised light wave (top left) with 's' and 'p' components equal in phase and amplitude. Circularly polarised light wave (top right) with 's' and 'p' components 90° out of phase but equal in amplitude. Elliptically polarised light wave (bottom) with 's' and 'p' components having an arbitrary relationship to each other.*

The optical properties that determine how light interacts with a material

are usually represented as a complex number. The complex refractive index ($\dot{n}$) contains the index (n) and the extinction coefficient (k). The index describes the velocity of light as it travels through a particular material compared to the speed of light in a vacuum (c). The extinction coefficient describes the loss of wave energy to the material

$$\dot{n} = n + ik \tag{11}$$

The principle of ellipsometry is simple, a beam of linear 45° polarised light ('s' and 'p' components of E are equal in phase and amplitude) is directed onto a sample. Maxwell's equations must be satisfied when the light interacts with the sample, producing boundary conditions. The light will reflect and refract at the interface (see figure 2.3.3 below). The 's' and 'p' components of E are treated separately and can be calculated using the Fresnel equations [203].

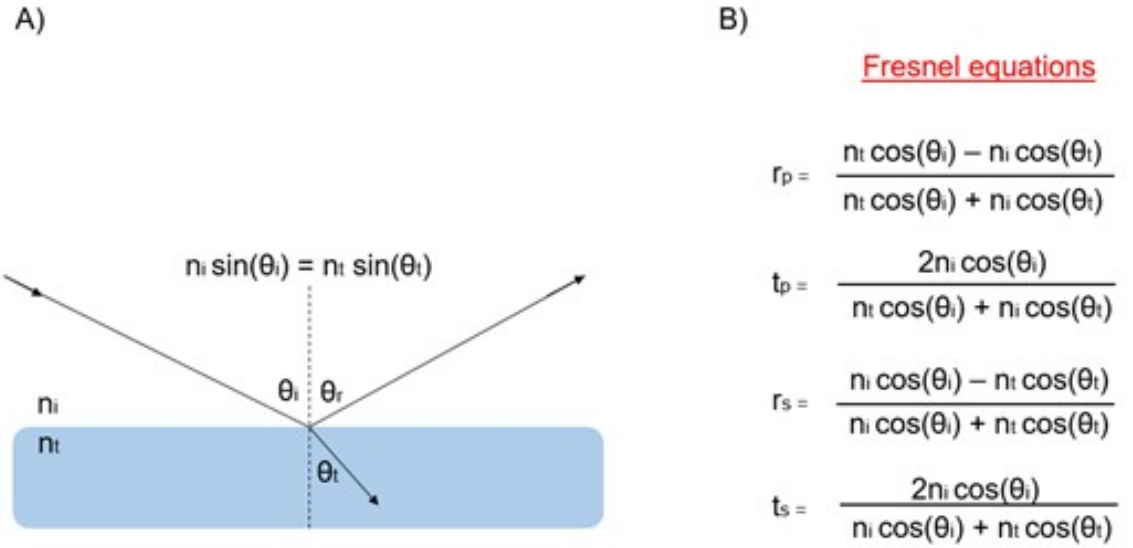

Figure 2.3.3: A) *Light reflects and refracts which is described by Snell's law, incident angle (θi), reflected angle (θr), refracted angle (θt).* ***B)*** *Fresnel equations which describe the amount of light transmitted and reflected at the interface between materials.*

This model can be extended to thin films and multilayer structures which contain multiple interfaces. The light will be reflected and transmitted at each

interface it encounters producing multiple beams of light. It is important to track the relative phase of each light component to determine the overall reflectance or transmittance correctly. A schematic of a typical ellipsometer is presented in figure 2.3.4 below.

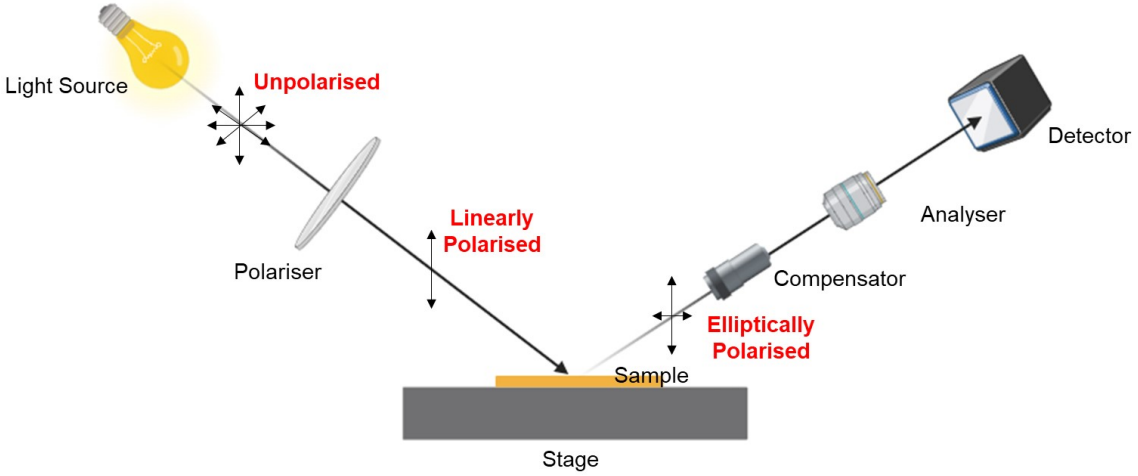

Figure 2.3.4: *Schematic of a typical ellipsometer set up.*

As seen in figure 2.3.4, unpolarised light is directed towards the sample of interest on a stage. The light is linearly polarised via a built in polariser then reflected off the sample. The resulting light is now elliptically polarised and passes through a compensator, an analyser and into a detector. The change in amplitude of the 's' and 'p' components of E are normalised to their initial values and denoted by 'Rs' and 'Rp' respectively. These values can be used to calculate the reflectance ratio (ρ) using equation (12) below [204]. The measured parameters allow calculation of the sample's properties, including film thickness and refractive index.

$$\rho = \frac{Rp}{Rs} = tan(\Psi)e^{i\Delta} \tag{12}$$

ρ can also be related to Ψ and Δ (11) however, as ellipsometry is an indirect method of determining the optical constants of a material, these values must be approximated with appropriate mathematical and physical models [205]. For example, this research involves the characterisation of thin organic films (1-10 nm) on gold surfaces which can be processed using a layered model (substrate/SAM/Air). SAMs are considered transparent, allowing the extinction coefficient (k) to be set

to zero and the refractive index set to 1.49 [206]. Light passes through these films and reflects off the underlying gold layer. The gold's optical properties can be directly measured before any films are deposited which increases the accuracy of the measurement compared to using literature standard optical constants. The unknown optical constants are varied until the best agreement between the measured and calculated Ψ and Δ values are obtained. The thickness can then be recorded with an associated mean squared error (MSE) value, with a MSE closer to zero indicating a more accurate model.

2.4 X-ray photoelectron spectroscopy (xps)

X-ray photoelectron spectroscopy (XPS) is one of the most widely used surface sensitive, analytical techniques available [207]. The measurement involves bombarding the surface with monochromatic X-rays, under ultra high vacuum (UHV) and measuring the kinetic energy (KE) and intensity of the emitted electrons [208]. The energy of the emitted electrons can be described by the following equation:

$$BE = h\upsilon - KE - \phi_{spec} \tag{13}$$

Where BE = the electron's binidng energy, hυ = the energy of the X-ray, KE = the measured kinetic energy of the emitted electron, and ϕ_{spec} = the spectrometer's work function (specific correction factor for the particular instrument) [209]. The BE provides information regarding the element and atomic orbital from which the electron was ejected along with the chemical environment of the atom. The typical set up of an XPS experiment can be seen in figure 2.4.1 below.

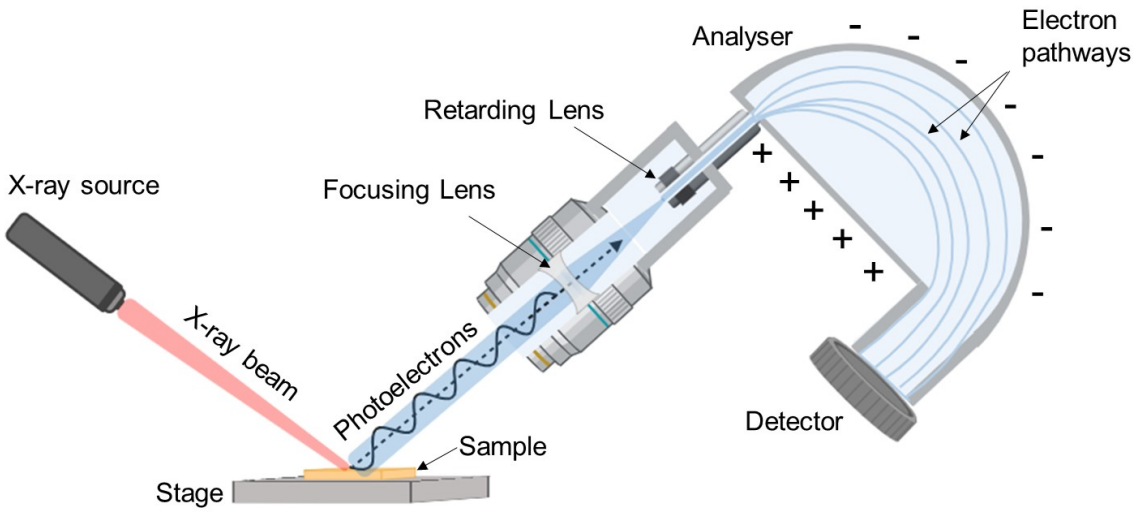

Figure 2.4.1: *Schematic of XPS instrumentation setup.*

The measurements are carried out under UHV conditions to minimise collisions between the ejected electrons and gas molecules in the environment. Common X-ray sources are Al $K\alpha$ (1486.6 eV) and Mg $K\alpha$ (1253.6 eV) [210]. The electrons pass through a lens system and into an analyser consisting of two hemispherical electrodes (figure 2.4.1). These deflect the passing electrons according to their KE before hitting a detector, equation (13) can then be used to work out the associated binding energy.

XPS is only sensitive to the top layer of the material under investigation (up to 10 nm). This is due to the ejected electrons loosing energy via inelastic collisions (short mean free path) and being unable to escape the sample [209, 211]. Electrons which do escape but have lost energy, add to the background noise of the XPS spectrum. While photoelectrons which escape without inelastic collisions create sharp peaks. When an electron is ejected another higher energy electron can drop down and fill the 'hole' left by the ejected electron causing a release in energy. This excess energy can cause one of two process to occur: 1) Enough

energy will be produced to release another electron (auger electron). 2) The energy will be released in the form of X-ray radiation (figure 2.4.2). Auger electrons can also be detected and typically result in broader peaks in the spectrum.

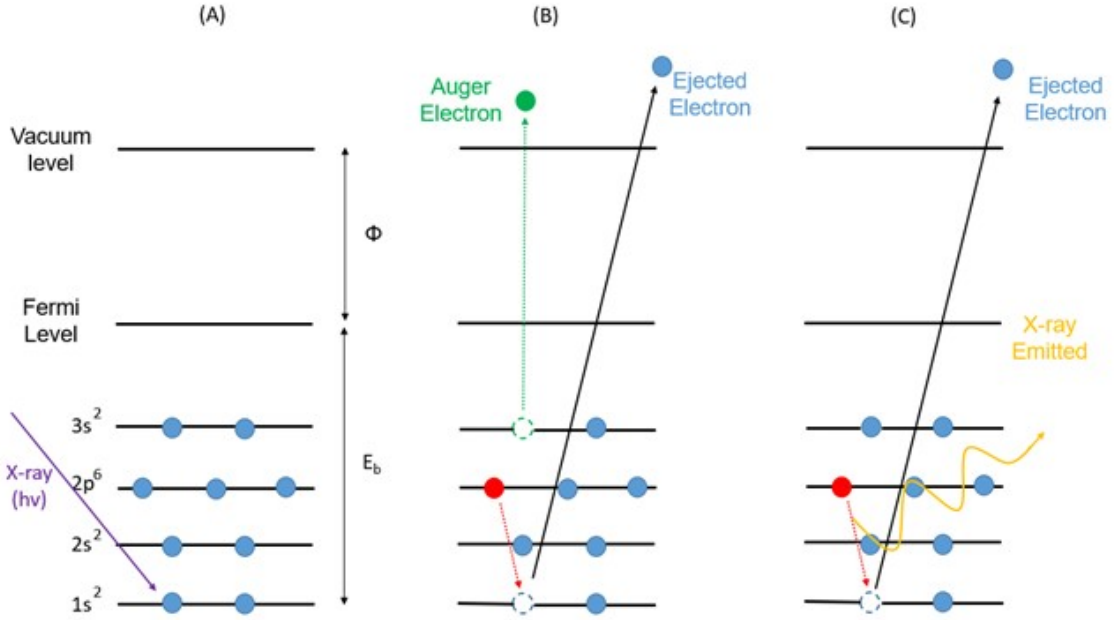

Figure 2.4.2: ***A)*** *X-ray hits inner orbital electron causing it to be ejected.* ***B)*** *Auger electron pathway.* ***C)*** *X-ray fluorescence pathway.*

XPS measurements typically involve a survey spectrum scan to identify all the elements present in a sample. The binding energies are then plotted vs their associated intensities (counts per second). Specific peaks can then be focused on in high resolution scans, which allows for more exact intensities, peak shapes and spectral shifts to be detected. Appropriate analysis of the individual peak areas can provide quantitative data of the ratios of each element present, their oxidayion states, and chemical environment. For this research, XPS was used to confirm the presence of particular elements on Au electrodes, thus monitoring the success of each fabrication step.

Chapter 3. Nanobody-Peptide System on Bare Gold Surfaces

Abstract: *This chapter details the development of NbGFP and C8K oligopeptide surfaces for the detection and modulation of eGFP binding. Herein, gold substrates are first functionalsied with NbGFP which are then characterised using ellipsometry, XPS, SPR, and EIS. Different NbGFP-C8K ratios are then introduced to the surface. eGFP binding and the system's 'switching' efficiency is investigated using SPR and eSPR. Finally, the architecture and behaviour of the NbGFP-C8K surfaces are investigate using ellipsometry, XPS, SPR, eSPR, and EIS.*

3.1 Introduction

The inherent properties of nanobodies (Nbs) including their small size, stability, high selectivity, and high affinity has seen them incorporated into a wide range of different sensing technologies in recent years (section 1.5). However, while many systems have demonstrated great sensitivity and stability, control over specific receptor-antigen interactions has been lacking [14]. In order for analytical devices to be successfully integrated with bioreactor platforms, the sensing interface must have the capacity to rapidly switch from an inactive 'OFF' to an active 'ON' state. This process should involve the protection of the Nb's binding site until specific analysis of the bioprocess is required. This would prevent premature binding events, which undermines the system's sensitivity before the target analyte has been detected, produced, introduced, or needs to be detected. Coupled with the rapid response times of electrochemical biosensors, this would allow near real time, on-demand detection of key biomarkers in a highly controlled fashion.

A promising approach to facilitate the development of such dynamic interfaces, has been highlighted in recent years by the Mendes research group [158, 169, 212–216]. In particular, Gomes et al. (2018) reported on the use of electrical

potentials to induce conformation changes in surface bound, charged oligopeptides for on-demand control over antibody-antigen interactions [158]. The system consisted of a mixed SAM including an oligopeptide covalently linked to a progesterone unit (pro-C7-4KC) and a hexaethylene glycol-terminated thiol (C11EG6), see figure 3.1.1. The oligopeptide included 4 lysine residues which are positively charged under physiological conditions. Through electrostatic interactions the peptides were attracted towards the surface under a negative potential, where the progesterone unit was concealed by the surrounding C11EG6 molecules. Through steric hindrance this reduced the antibody's capacity to bind to the progesterone. Under a negative surface potential the oligopeptides were then repelled away from the surface where it could more freely interact with the antibody in the surrounding environment.

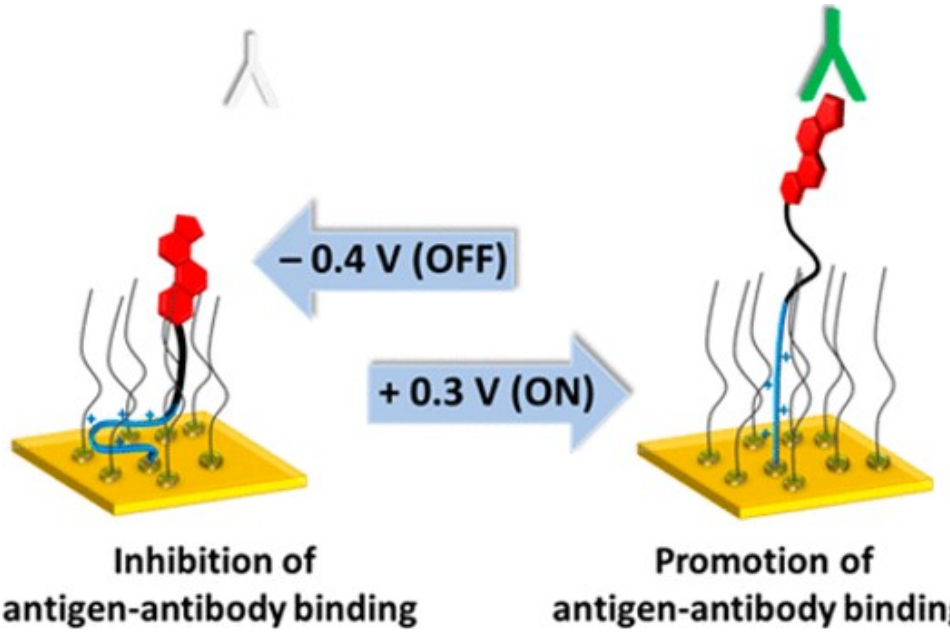

Figure 3.1.1: *Schematic showing the dynamic interface with the peptides conformation being controlled by applying electrical potentials. Adapted with permission from [158].*

This research chapter aims to take this technology further by developing a multicomponent surface consisting of nanobodies and naturally charged oligopep-

tides (figure 3.1.2). The nanobodies (Nbs) will act as the biorecognition elements while the oligopeptides will control the Nb-antigen interactions. In an ideal situation, when no potentials are being applied, the oligopeptides will naturally extend. This extension conceals the Nb binding sites, thereby preventing antigen interactions. Then when a potential is applied across the electrode, the oligopeptides are electrostatically attracted towards the surface. This reveals the Nb binding sites, allowing antigen to bind.

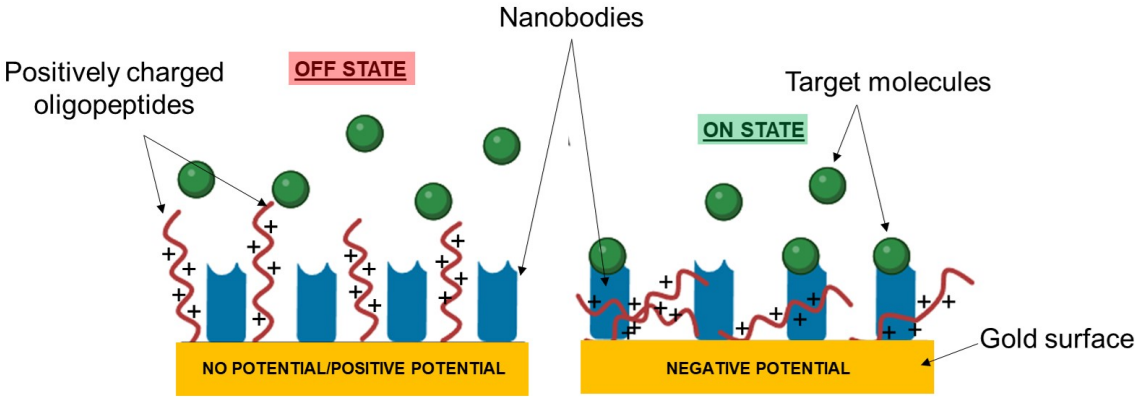

Figure 3.1.2: *Schematic of the proposed system with positively charged oligopeptides being controlled by applying potentials across the electrode's surface.*

3.2 Aims and Objectives

Aim: In order to demonstrate proof-of-concept, it should be possible to directly attached Nbs and oligopeptides to Au substrates. In the case of Nbs, these surface interaction would be highly non-specific, as discussed in section 1.3.4. However, statistically there should be some Nbs in the correct orientation to bind to its associated antigen in the surrounding environment. The oligopeptides can be specifically designed to include a terminal thiol residue which should allow the peptides to interact with the surface through thiol-Au bonds. By optimising the Nb-peptide

ratios it should be possible to conceal the Nb's binding site under open circuit potential (OCP) and then reveal the binding site when the oligopeptides change their confirmation in response to applied potentials (figure 3.1.2).

Objective 1: Functionalise bare Au substrates with nanobodies and oligopeptides.

Objectives 2: Characterise the NbGFP and oligopeptides surfaces

Objective 3: Demonstrate through antigen binding studies and control experiments that the oligopeptides have the capacity to change their surface confirmation.

3.3 Results and Discussion

3.3.1 Formation and Characterisation of Nanobody Surfaces

Notes: *In this body of work nanobodies specific for enhanced green fluorescent protein (eGFP) were used as a model system (purchased from Proteintech or NanoTag Biotechnologies) . In theory, this approach could be adapted for the detection of any analyte providing the associated nanobody can be produced.*

Gold substrates were cleaned for 10 minutes in a 7:3 (v/v) mixture of sulfuric acid (H_2SO_4) and hydrogen peroxide (H_2O_2) know as piranha solution. They were then rinsed with copious amounts of water and ethanol (EtOH) before being dried under a stream of argon (Ar) gas. A sodium acetate buffer (pH 5.6) containing 3.6 μM NbGFP was then immediately incubated on the clean gold surface for 22-24 hours. A pH of 5.6 was chosen as it was previously reported to reduce the amount of NbGFP coupled to 11-MUA SAMs which in turn yielded higher eGFP binding due to reduced steric hindrance around the Nb's binding site [164]. The NbGFP has an isoelectric point (Ip) of approximately 9 therefore, at this pH the Nb would have a net positive charge which may also help space out the Nb's on the gold surface resulting in higher levels of eGFP interactions.

3.3.1.1 Ellipsometry and XPS analysis of NbGFP surfaces

Ellipsometry measured the thickness of the Nb on the surface to be 3.7 $\pm$ 0.1 nm (n = 3), which was in good agreement with the approximate NbGFP dimensions of 4 x 2 x 2 nm (figure 3.3.1) [217]. As the orientation of the Nb's on the surface is unknown an ellipsometry thickness of between 2 nm (maximum Nb width and depth) and 4 nm (maximum Nb length) would be expected. The surface roughness

of the underlying polycrystalline gold substrate was taken into account during the ellipsometry measurement as it was used as a baseline to fabricate the overall model of the interface (see chapter 7).

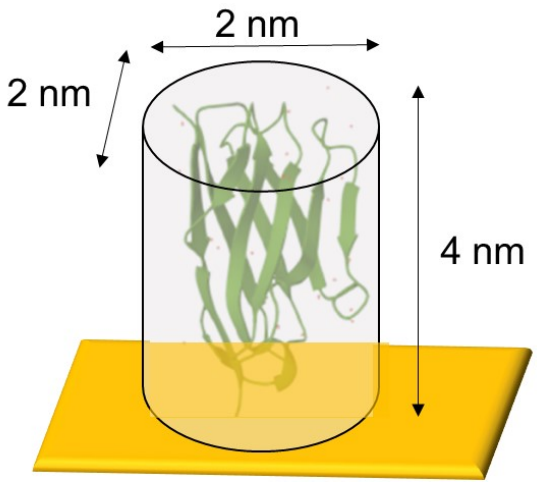

Figure 3.3.1: *Schematic showing the physical dimensions of the NbGFP used in this research. length = 4 nm, width = 2 nm, and depth = 2 nm. Not drawn to scale*

In order to further characterise the surface and confirm the presence of NbGFP, X-ray photoelectron spectroscopy (XPS) was carried out. Figure 3.3.2 shows the high resolution XPS spectra of the Au 4f, C 1s, O 1s, N 1s, and S 2p regions for the bare Au and NbGFP surfaces. No sulphur was detected on the NbGFP surface or bare Au samples, while this was expected for bare Au it is more surprising for the NbGFP surface. This suggests that either there are no thiol groups on the Nb's surface or the concentration is too low to be detected using XPS. The relative atomic percentages and the ratios of carbon, oxygen, nitrogen, and sulphur to gold were also analysed and compared between the two surfaces, which can be seen in figure 3.3.3.

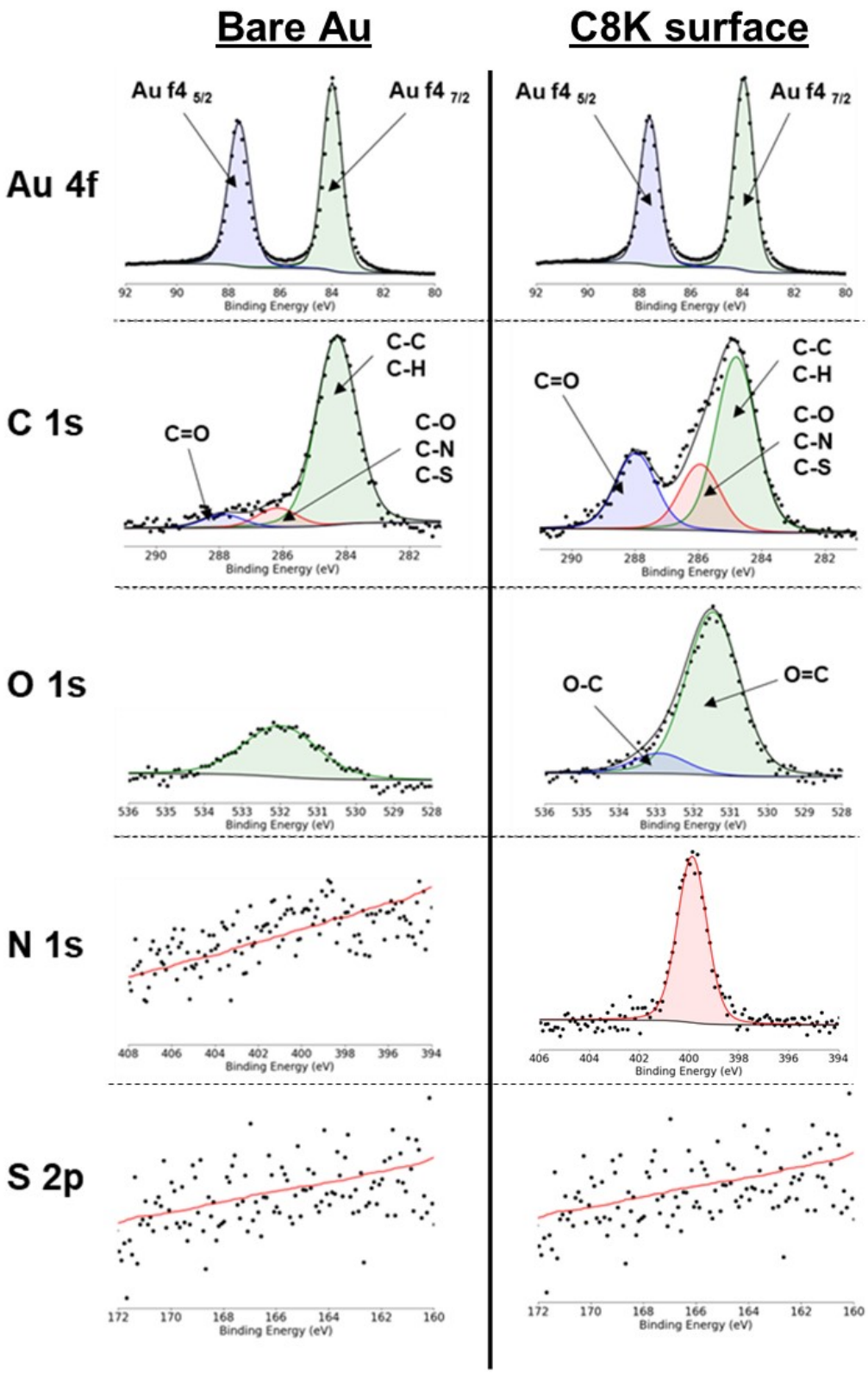

Figure 3.3.2: *High resolution XPS spectra of the Au 4f, C 1s, O 1s, and N 1s regions for the bare Au surface (left column) and the NbGFP surface (right column). Four measurements were carried out across two different samples.*

	Relative Atomic %		Components	Relative Components %	
	Bare Au	NbGFP surface		Bare Au	NbGFP surface
Au	52.5 ± 2.1	22.0 ± 1.4	4f 7/2	28.5 ± 2.3	11.7 ± 0.7
			4f 5/2	23.1 ± 0.2	9.0 ± 0.5
C	40.5 ± 3.5	53.3 ± 1.3	C-C/C-H	32.3 ± 6.1	29.8 ± 2.7
			C-O C-N C-S	4.0 ± 2.0	11.7 ± 1.8
			C=O	3.4 ± 0.5	11.6 ± 0.6
O	7.5 ± 2.1	13.3 ± 0.5	O=C	8.5 ± 2.0	12.7 ± 0.7
			O-C	--	1.7 ± 0.6
N	--	11.3 ± 1.3	N 1S	--	11.3 ± 0.6
S	--	--	S 2p	--	--

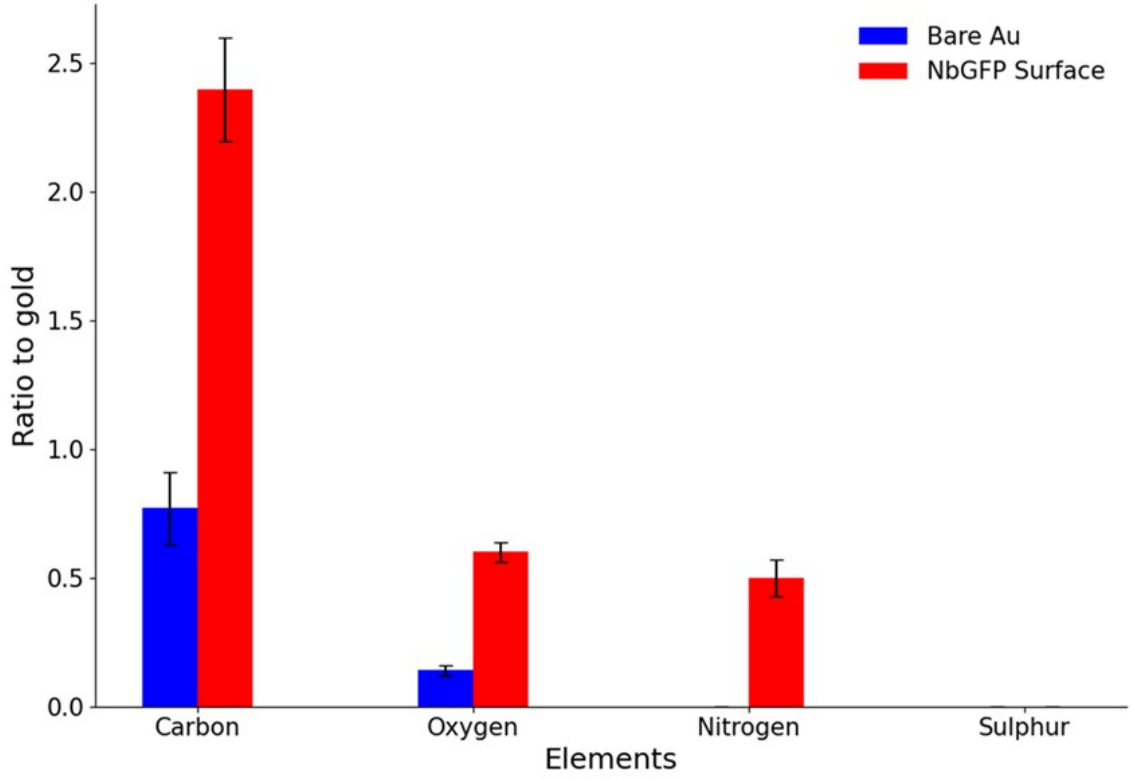

Figure 3.3.3: top: *Relative atomic and component percentages for the bare Au and NbGFP surfaces.* ***bottom:*** *Comparison of the ratios of carbon, oxygen, nitrogen, and sulphur to gold for the two samples. Four measurements were carried out across two different samples and all values are reported as the average ± the standard deviation of the sample (n = 4).*

Nitrogen and sulphur could not be detected on the bare Au surface, indicating the cleaning method used was successful. The appearance of the N 1s peak (atomic % = 11.3 $\pm$ 1.3) on the NbGFP surface can therefore be attributed to the presence of Nbs, as nitrogen is a common element in all amino acids and exists in many amino acid side chains. Following NbGFP incubation, there was a substantial increase in the C=O peak by 241%. Additionally, the C-O, C-S, and C-N subpeaks, which could not be individually separated at this resolution, saw an increase of 193%. Furthermore, the O 1s spectra showed a peak shoulder at 533 eV, this is characteristic of the O-C peak which was not detected on the bare Au sample. After NbGFP incubation the ratio of C, O, and N to Au all significantly increased after NbGFP incubation (figure 3.3.3, bottom). These results along with the ellipsometry thickness measurements confirm the successful modification of Au substrates with NbGFP. However, from this data it is not clear that the Nbs are in an appropriate orientation to capture the eGFP target. It could be the case the the binding sites have been inactivated because they are facing down towards the surface. Therefore, surface plasmon resonance (SPR) and electrochemical impedance spectroscopy (EIS) were used to monitor the interactions of eGFP with the NbGFP surface.

3.3.1.2 SPR and EIS detection of NbGFP-eGFP interactions

The NbGFP surface was placed inside the SPR's flow cell and a running buffer of phosphate buffered saline (PBS) was injected until a stable baseline was achieved. 14 μg/mL eGFP in PBS was injected and the change in refractive index (RI) was monitored as a function of time (figure 3.3.4). The change in RI is reported as response units (RU) which corresponds to a change in mass at the interface (eGFP binding). The system was then flushed out with PBS buffer to remove any non-specifically bound eGFP. The new baseline corresponds to the eGFP bound to NbGFP on the surface, as seen in figure 3.3.4.

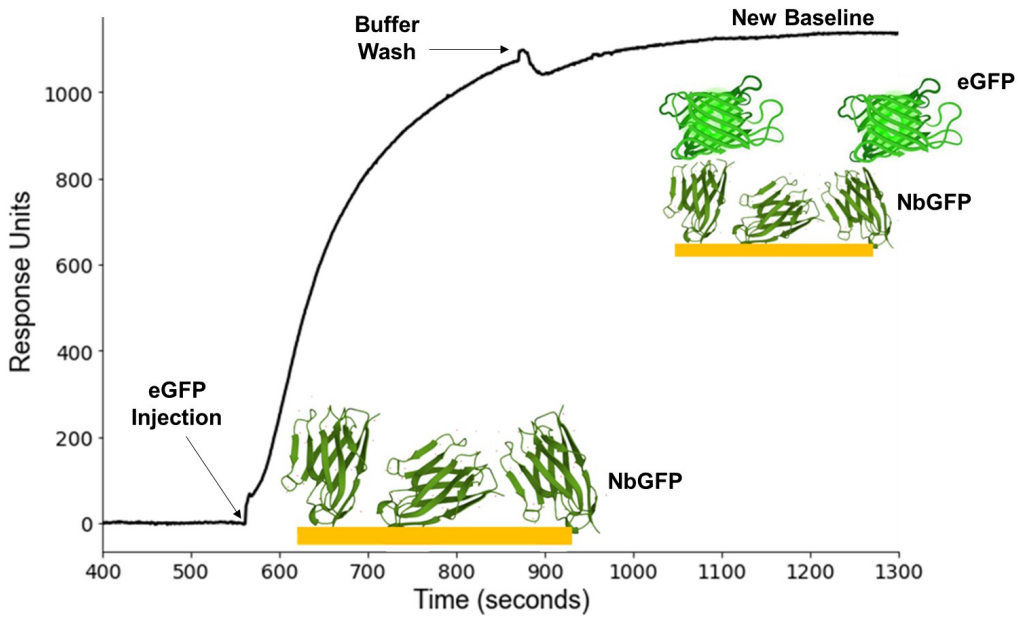

Figure 3.3.4: *SPR trace: 14 μg/mL eGFP injection on NbGFP surface.*

The binding response of the eGFP was 1080 $\pm$ 74 RU (n = 3), with the single exponential binding curve indicative of receptor-antigen interactions. This corresponds to a mass changes of approximately 1.08 ng/mm^2 or 1 eGFP molecule per 42 nm^2 (1000 RU = 1 ng/mm^2) [218]. Assuming a footprint of approximately

12.5 nm^2 for eGFP, an estimated 30% of the surface was covered with eGFP [219]. After the washing phase the the SPR trace does not drop back down, but instead quickly reaches a stable steady state (new baseline). This suggests that the eGFP strongly interacts with the surface and indirectly suggests that the Nb's are stable and will not be removed during PBS washes.

In order to investigate eGFP binding via EIS, gold rod electrodes, with a working electrode area of 0.03 cm², were purchased from IJ Camberia Scientific (Figure 3.3.5 (A)). Prior to each use, the electrodes were manually polished with a 0.05 µm alumina slurry to achieve a mirror-like finish. They were then sonicated in 100% ethanol for 10 minutes to remove excess alumina particles (Figure 3.3.5 (B)). The electrodes were electrochemically cleaned in 0.5 M H_2SO_4 by scanning the potential between 1.6 and -0.4 V until a reproducible cyclic voltammogram was obtained, typically around 12 cycles (figure 3.3.5 (C)). The electrochemical properties of the electrode were investigated using the ferri/ferro-cyanide ($Fe(CN)_6^{-3/-4}$) redox probe. The oxidation and reduction peak currents as a function of scan rate were investigated using cyclic voltammetry (Figure 3.3.5 (D)). The peak currents were plotted against the square root of the scan rate, which showed a linear relationship (Figure 3.3.5 (E)). This is the characteristic behaviour of a solution-based, pseudo first-order redox probe, which is expected for $Fe(CN)_6^{-3/-4}$. These results demonstrate that the electrode surface is clean and suitable for further electrochemical experiments.

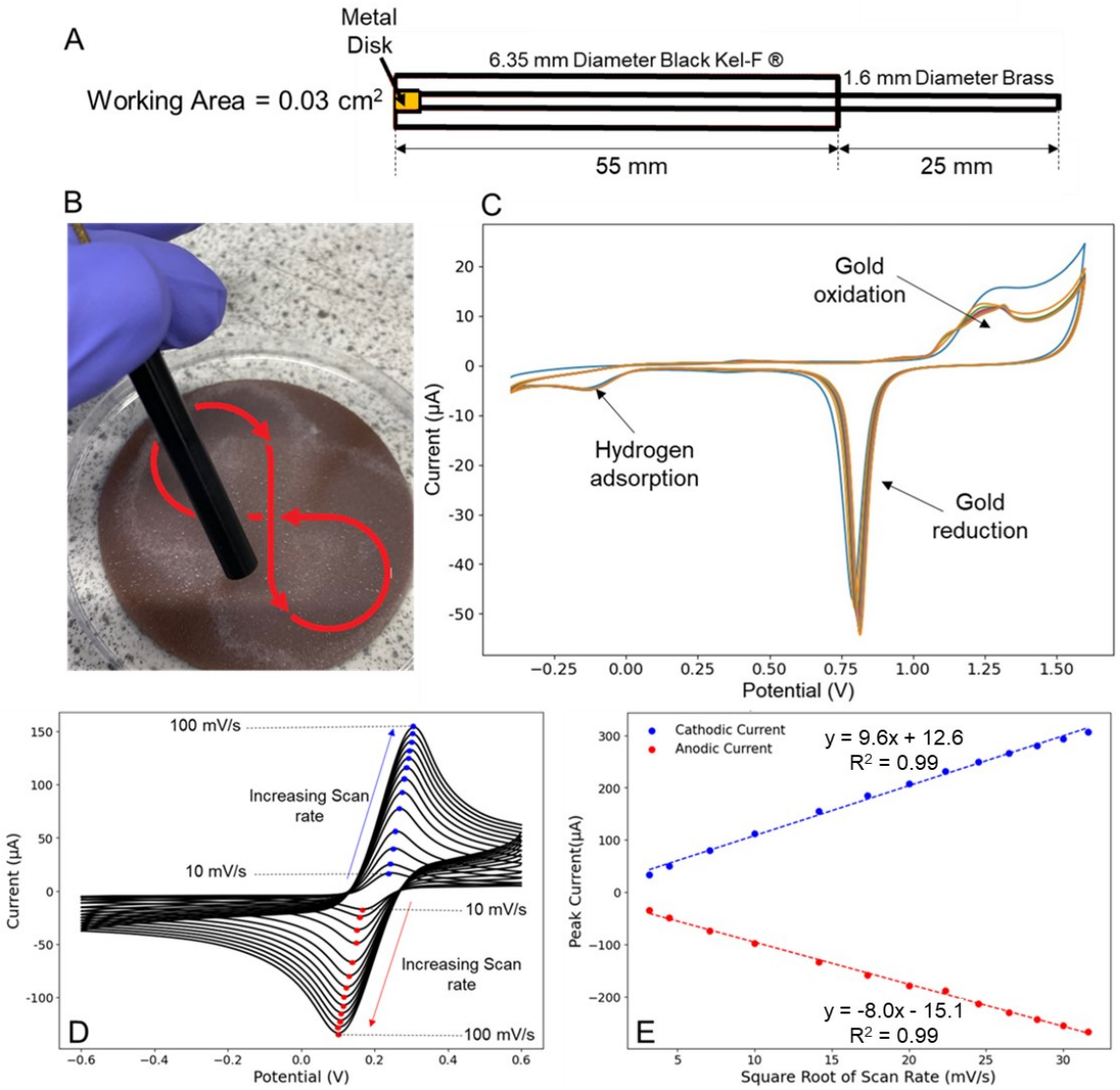

Figure 3.3.5: A) *Schematic of the gold rod electrodes purchased from IJ Camberia Scientific.* ***B)*** *Image showing the manual polishing of the electrode in aluminium slurry, following a 'figure of 8' motion.* ***C)*** *Cyclic voltammogram of the bare gold electrode in 0.5 M H_2SO_4, scanning the potential from 1.6 to -0.4 V.* ***D)*** *Cyclic voltammogram of 10 mM $Fe(CN)_6^{-3/-4}$ with scan rates ranging from 10 to 1000 mV/s.* ***E)*** *Oxidation and reduction peak current as a function of the square root of the scan rate.*

NbGFP was functionalised onto the electrodes, following the same procedure used for modification of the SPR substrates. Faradaic-EIS was carried out in 10 mM $Fe(CN)_6^{-3/-4}$ in 1 X PBS containing 1 M KCl and was used to compare the surfaces before and after NbGFP incubation (figure 3.3.6 (A)). The bare Au response was a straight line at a 45° angle indicating a diffusion dominated process.

This is a typical response for a clean electrode in a strong electrolyte solution. After NbGFP incubation the high frequency domain of the Nyquist plot showed an increase in charge transfer resistance (R_{ct}), which can be seen in figure 3.3.6 (A) where the cyan plot begins to take on a semi-circular shape. This corresponds to the NbGFP on the surface acting as a physical and/or electrostatic barrier to charge transfer from the redox probe to the electrode surface. The response was modelled to extract quantitative information using a Randles equivalent circuit model as discussed in section 2.2.3. These results demonstrate that NbGFP was successfully functionalised on the electrode's surface. The NbGFP surface was then incubated overnight at 4° C in PBS and subsequently measured every 30 minutes until a stable PBS baseline was established. 14 μg/mL eGFP in PBS was incubated on the surface of the electrode for 30 minutes with gentle aspiration every 5 minutes. The R_{ct} increased by 22.1 $\pm$ 2.9% after eGFP incubation, demonstrating that EIS is a sensitive technique which can be used to measure the presence of eGFP.

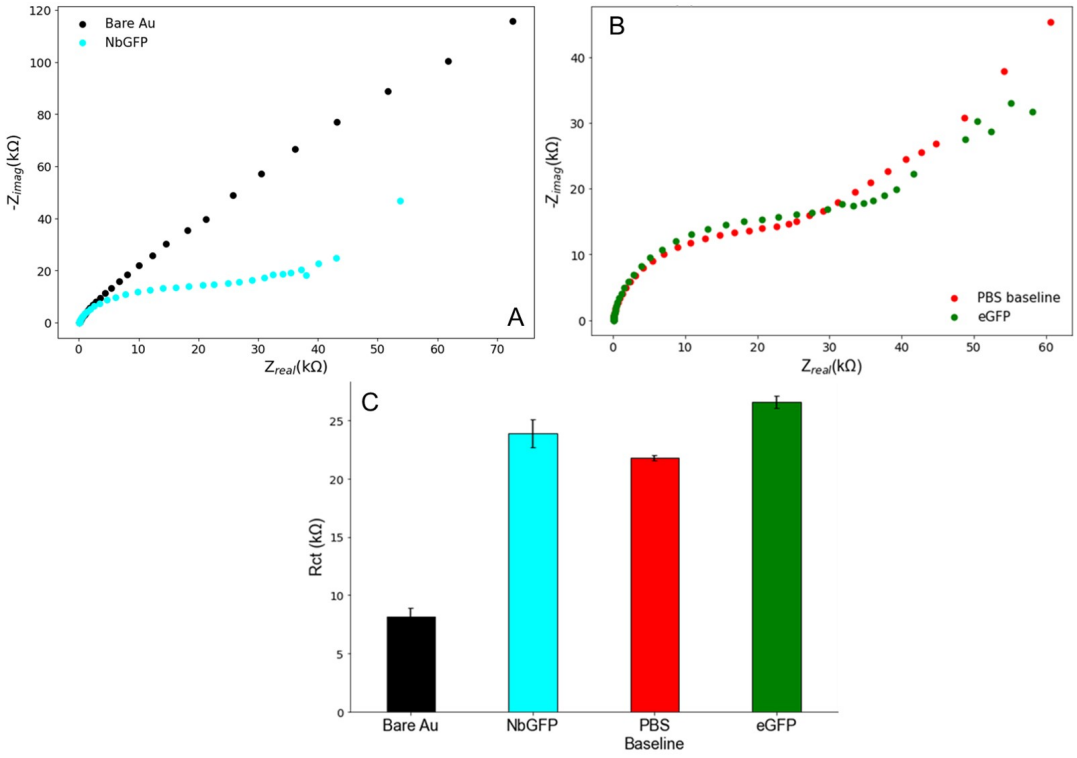

Figure 3.3.6: A) *Nyquist plots of the bare Au and NbGFP surfaces using 10 mM* $Fe(CN)_6^{-3/-4}$. ***B)*** *Nyquist plots of the stabilised NbGFP surface and after eGFP incubation using 10 mM* $Fe(CN)_6^{-3/-4}$. ***C)*** *Comparison of the* R_{ct} *values across the four surfaces, n = 3.*

3.3.2 Formation and Characterisation of Nanobody-Peptide Surfaces

3.3.2.1 Investigation of NbGFP-C8K ratios via SPR

The oligopeptide C8K (purchased from Peptide Protein Research Ltd (UK)) , composed of a C-terminal cysteine and eight subsequent lysine residues (figure 3.3.7), was selected for this study due to its theoretical length of approximately 6.8 nm (as calculated using ChemDraw). This length was anticipated to introduce steric hindrance around the Nb binding site. Given that the lysine residues in C8K have a pK_a of 10.54, they should be protonated and carry a net positive charge under physiological conditions (pH 7.35 to 7.45) [220].

This section explores the possibility of controlling eGFP binding by ap-

plying electrical potentials, which have the potential to alter the conformation of the oligopeptides through electrostatic interactions. It is hypothesised that under a positive potential, the C8K will be repelled from the surface, thereby reducing eGFP binding. Conversely, under negative potentials, the C8K should be drawn towards the surface, exposing the binding site to the surrounding environment and, as a result, increasing eGFP binding.

C8K was functionalised onto the gold surfaces through the same method used for the NbGFP. Different molar ratios where initially incubated with the Nb in a sodium acetate buffer (pH 5.6) for 24 hours.

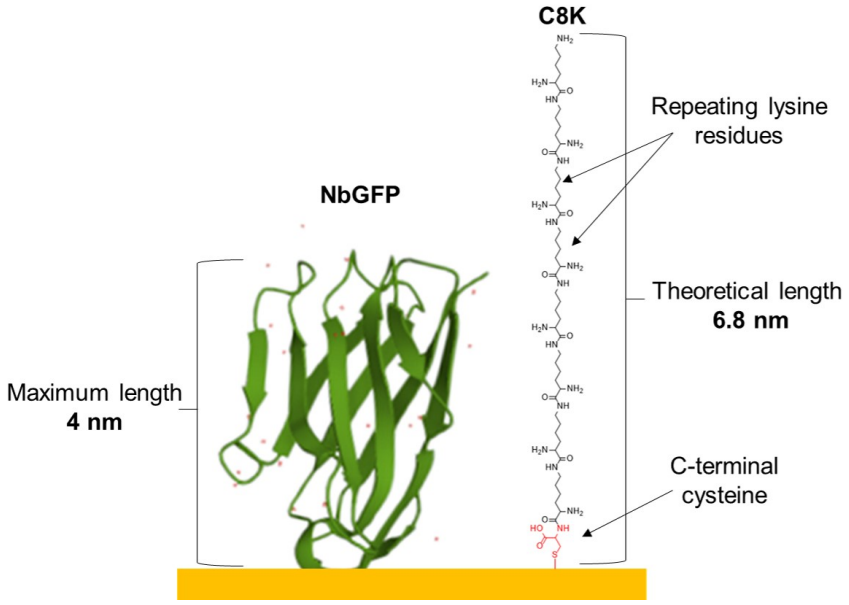

Figure 3.3.7: *Maximum thickness on NbGFP on the gold surface vs the theoretical length of C8K, as calculated with ChemDraw. Figures are not to scale.*

SPR was employed to examine the impact of three distinct molar ratios of NbGFP-C8K on eGFP binding. These ratios included 1:0, 1:5, and 1:100 which were investigated under open circuit potential (OCP) and +0.3 V. It was initially hoped, that under OCP the NbGFP-eGFP interactions would be significantly limited. This would mean there would be no energy require to hold the system in an

'OFF' state. A voltage of +0.3 was chosen as it has been previously demonstrated to not oxidise thiol-gold bonds [23]. The eGFP binding responses are summarised in figure 3.3.8.

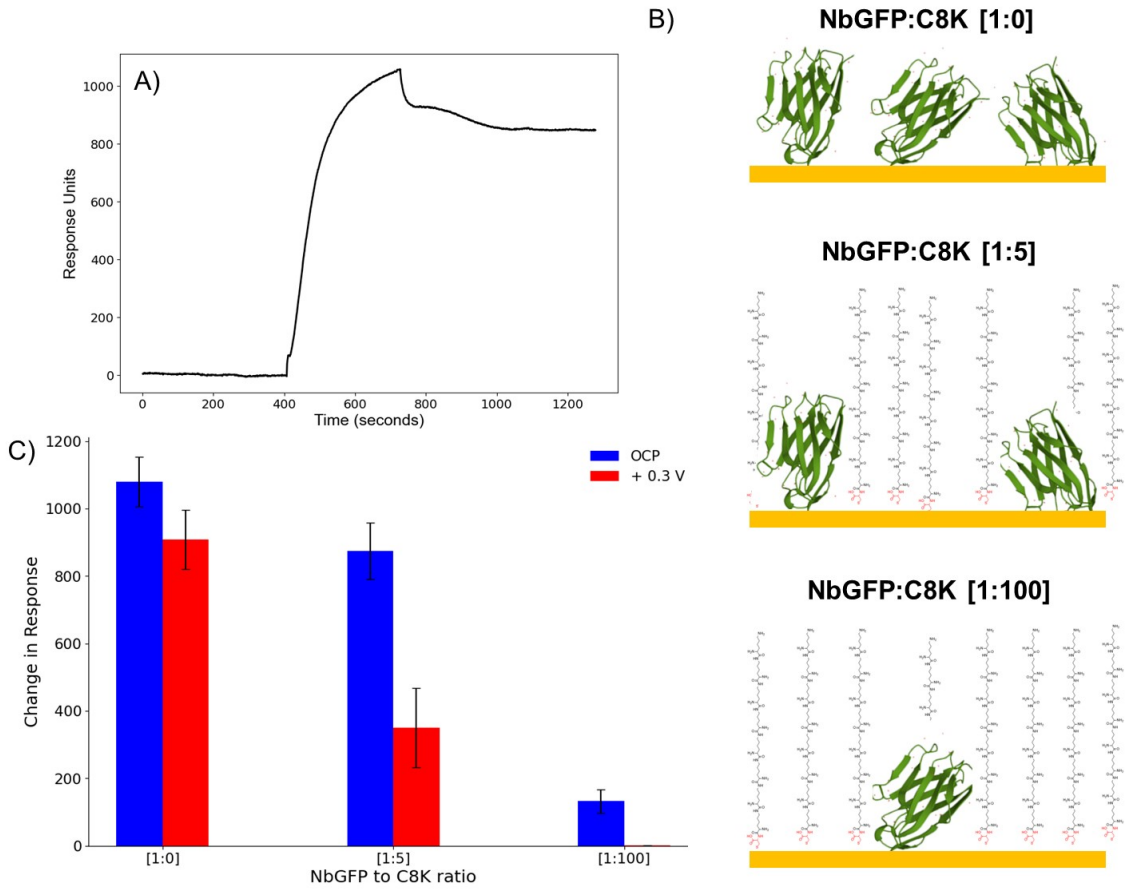

Figure 3.3.8: *A) Example of SPR trace for eGFP binding on a NbGFP-C8K ratio of 1:5. B) visual representations of NbGFP and C8K ratios on the gold surface. These figures are not to scale and are unlikely to represent the actual configuration of the functionalised surface. C) SPR binding response of eGFP on different molar ratios of NbGFP-C8K, at open circuit potential (blue) and +0.3 V (red), n= 3.*

Increasing the NbGFP-C8K ratio resulted in a decrease in the eGFP binding response under OCP. This can be explained by considering the lower concentrations of NbGFP on the surface as the concentration of C8K increases. When only NbGFP was incubated on the surface, applying a positive potential (+0.3 V) has a minimal effect on eGFP binding. This suggests that the NbGFP is stable and does not get removed when a potential of +0.3 V is applied for up to 30 min-

utes. When a ratio of 1:100 (NbGFP:C8K) was used the binding response was too small (<200 RU) to accurately investigate the switching response under a positive potential. Typically, for the SPR equipment used in this research, there can be a 200 RU variation between experiments. The 1:5 ratio still had significant eGFP binding under OCP (874 $\pm$ 84 RU), but showed good switching efficiency of $\approx$ 60 % to 350 $\pm$ 118 RU, when +0.3 V was applied. Therefore, this ratio was selected for further investigations and control experiments.

3.3.2.2 Ellipsometry and XPS of NbGFP-C8K [1:5] Ratios

In order to get a better understanding of the organisation of the NbGFP-C8K [1:5] surfaces, the thicknesses of the NbGFP, C8K, and NbGFP-C8K [1:5] surfaces were measured and compared using ellipsometry (figure 3.3.9).

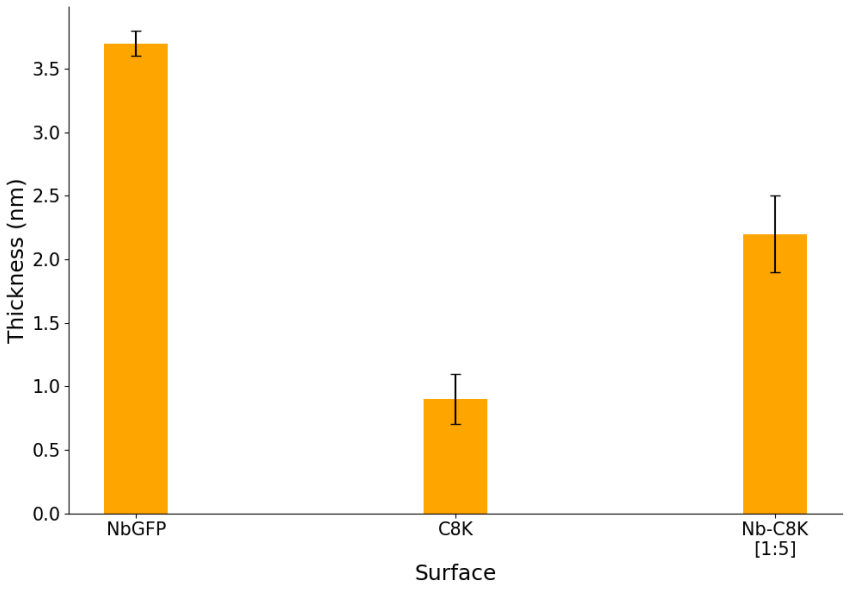

Figure 3.3.9: *Ellipsometry thickness of NbGFP, C8K, and NbGFP-C8K [1:5] surfaces formed in sodium acetate buffer (pH 5) over 22-24 hours. n = 3.*

As previously seen, the measured thickness of the NbGFP surface (3.7 ± 0.1 nm) is in good agreement with the expected thickness from the physical dimensions

of the Nbs. However, the measured thickness of just C8K on the surface (0.9 $\pm$ 0.2) is significantly lower than the theoretical thickness of 6.8 nm (depicted in figure 3.3.7). This suggests that the C8K oligopeptides have a high degree of flexibility and adopt a flat or 'lying down' conformation on the surface. The mixed NbGFP-C8K [1:5] system had a measured thickness of 2.2 $\pm$ 0.3 which was more than the C8K surface but less than the NbGFP surface. This suggests that there is significantly less NbGFP on the surface in the mixed system. This is likely due to the oligopeptides taking up a large surface area, preventing NbGFP from interacting with the gold surface.

Again, the surfaces were investigated with XPS in order to confirm the presence of C8K on the surface and gain a greater understanding of the surface architecture in the mixed system. Figure 3.3.10, shows the high resolution spectra for the Au 4f, C 1s, O 1s, and N 1s XPS regions on bare Au, NbGFP only, C8K only, and NbGFP-C8K [1:5] surfaces. Across all samples, sulphur could not be detected therefore, the spectra were omitted from figure 3.3.10 (included in appendix, Figure 1). This was unexpected as the C8K oligopeptides contain a terminal cysteine residue which should be the dominant group responsible for interacting with the Au surface. However, this could further suggest that the C8K oligopeptides are disorganised and spaced out on the surface, resulting in the concentrations of sulphur in the particular XPS surface analysis area being too low to be detected.

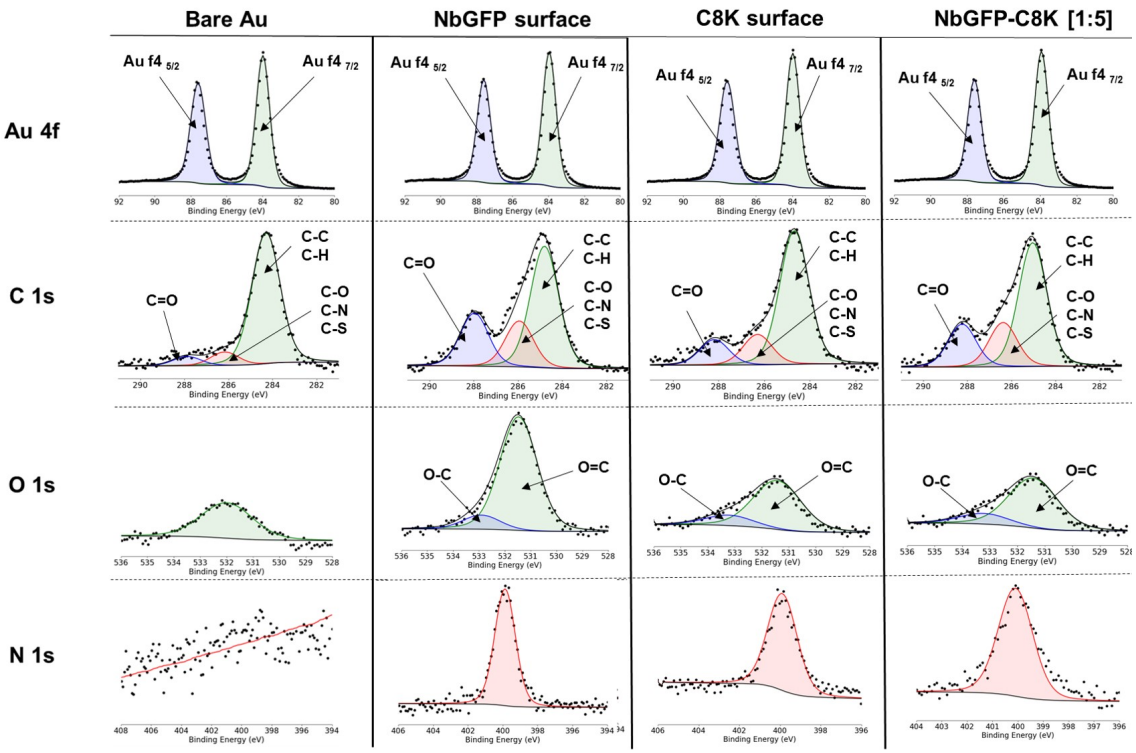

Figure 3.3.10: *High resolution XPS spectra of the Au 4f, C 1s, O 1s, and N 1s regions for the bare Au, NbGFP, C8K, and NbGFP-C8K [1:5] surfaces. Four measurements were carried out across two different samples.*

The C8K surface showed an increase in the C=O and C-O/C-S/C-N subpeaks of 157% and 1833% respectively compared to bare Au (figure 3.3.11, top). The N 1s peak along with the O=C subpeak were also detected on the C8K surface which could not be seen on bare Au. Coupled with the ellipsometry and SPR data these results confirm the presence of C8K on the surface. However, the XPS measurements had high inter- and intra-sample variability for the C8K surfaces. The ratio of C/Au ranged between 0.8 to 11.7 (figure 3.3.11, bottom), indicating a disorganised and highly variable C8K film. The ratios of O/Au and N/Au also exhibited higher variability than those on the other surfaces investigated. These results coupled with the low ellipsometry thickness (0.9 ± 0.2), support the hypothesis that on bare gold, the C8K oligopeptides are lying flat on the surface. This

orientation allows them to take up a variable surface area (or 'footprint'), which in turn prevents high packing densities.

	Relative Atomic %			NbGFP-C8K		Relative Components %			NbGFP-C8K
	Bare Au	NbGFP	C8K	[1:5]	Components	Bare Au	NbGFP	C8K	[1:5]
Au	51.8 ± 2.5	21.8 ± 1.2	25.8 ± 22.9	35.3 ± 1.5	4f 7/2	28.5 ± 2.5	11.7 ± 0.7	14.1 ± 12.7	19.4 ± 0.9
					4f 5/2	23.1 ± 0.3	8.9 ± 0.5	10.7 ± 9.6	14.8 ± 0.8
C	40.0 ± 3.4	53.2 ± 1.2	51.5 ± 17.4	44.8 ± 3.1	C-C/C-H	32.2 ± 6.1	29.8 ± 2.7	32.9 ± 7.2	28.2 ± 2.8
					C-O C-N C-S	0.6 ± 0.8	11.7 ± 1.8	11.6 ± 6.5	8.8 ± 0.6
					C=O	2.8 ± 0.2	11.6 ± 0.6	7.2 ± 3.4	8.3 ± 0.8
O	7.2 ± 1.2	13 ± 0.8	13.8 ± 3.3	11.3 ± 0.4	O=C	7.2 ± 1.2	12.7 ± 0.7	11.0 ± 1.7	9.1 ± 0.4
					O-C	--	1.7 ± 0.6	3.6 ± 2.7	2.5 ± 0.5
N	--	11.3 ± 1.1	8.0 ± 2.4	8.3 ± 1.8	N 1S	--	11.3 ± 1.1	7.6 ± 1.9	8.6 ± 0.8
S	--	--	--	--	S 2p	--	--	--	--

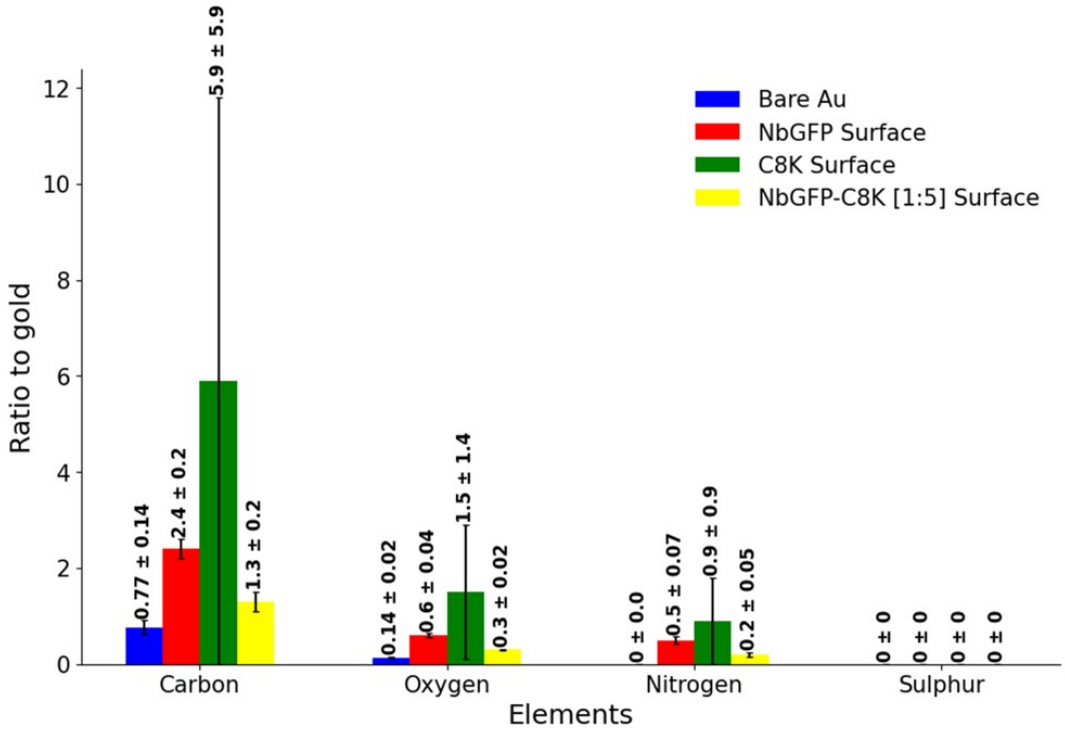

Figure 3.3.11: top: *Relative atomic and component percentages for the bare Au, NbGFP, C8K, and NbGFP-C8K [1:5] surfaces.* ***bottom:*** *Comparison of the ratios of carbon, oxygen, nitrogen, and sulphur to gold for the four samples. Four measurements were carried out across two different samples and all values are reported as the average ± the standard deviation of the sample.*

When NbGFP was incubated simultaneously with C8K in a 1:5 ratio, the variability between XPS measurements dropped dramatically, compared to when only C8K was incubated. The C/Au and O/Au ratios dropped from 5.9 ± 5.9 and 1.5 ±

1.4 to 1.3 $\pm$ 0.2 and 0.3 $\pm$ 0.02 respectively. These results suggest that the Nbs may help organise the surface and space out the peptides. These results have demonstrated successful immobilisation of NbGFP and C8K oligopeptides onto the surface. Therefore, the NbGFP-C8K [1:5] system was used for further eGFP binding experiments and control studies.

3.3.2.3 Investigating eGFP binding on NbGFP-C8K [1:5] surfaces using EIS

In order to gain greater understanding of how the mixed NbGFP-C8K [1:5] system forms on the Au surface, they were also functionalised on the electrode following the same procedure used for NbGFP. However, when C8K was present there was no increase in the R_{ct} (figure 3.3.12 (A)). Likewise, after the system was stabilised in PBS overnight, eGFP incubation had no effect on the EIS response. These results suggest that when the C8K is present much less NbGFP is available on the surface for binding. This supports the ellipsometry data in section 3.3.2.2, which suggested that the C8K oligopeptides adopt a flat conformation on the surface, taking up a large surface area. Furthermore, the absence of significant charge transfer resistance indicates that the positive charges on the C8K oligopeptides are electrostatically attracting the anionic $Fe(CN)_6{}^{-3/-4}$ redox probe. Conversely, this could also indicate the the oligopeptides are poorly packed resulting in a large proportion of the gold surface exposed.

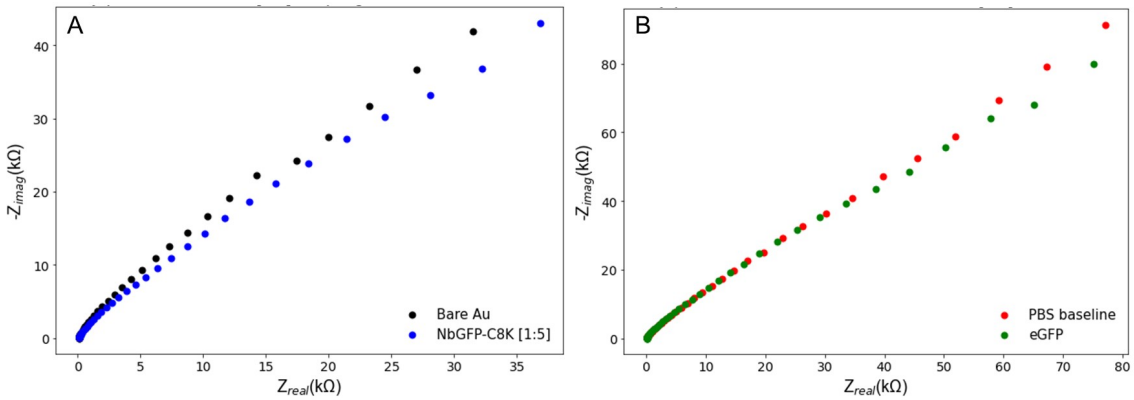

Figure 3.3.12: A) *Nyquist plot of the bare Au and NbGFP-C8K [1:5] surfaces.* ***B)*** *Nyquist plots of after eGFP was incubated on the stabilised NbGFP-C8K [1:5] surface, n = 3.*

3.3.2.4 Investigating eGFP binding on NbGFP-C8K [1:5] surfaces using SPR under negative potentials

When a potential of +0.3 V was applied during eGFP binding on the NbGFP-C8K [1:5] system the SPR response decreased by 60%. If this response is due to the conformation of the oligopeptides extending and preventing eGFP from interacting with NbGFP on the surface, then a negative potential should reveal more Nb binding sites to the surrounding environment and thus increase eGFP binding.

A potential of -0.4 V was chosen as this is within the potential window where thiol-gold bonds should not be reduced [23]. The NbGFP-C8K [1:5] samples were placed inside the SPR and a running buffer of 1 X PBS was injected until a sable baseline was established. When the -0.4 V potential was applied the SPR quickly drops and reestablishes a new baseline (figure 3.3.13 (B) and (C)). This corresponds to the applied potential reorganising the electric double layer (EDL) and potentially removing weakly bound species from the surface.

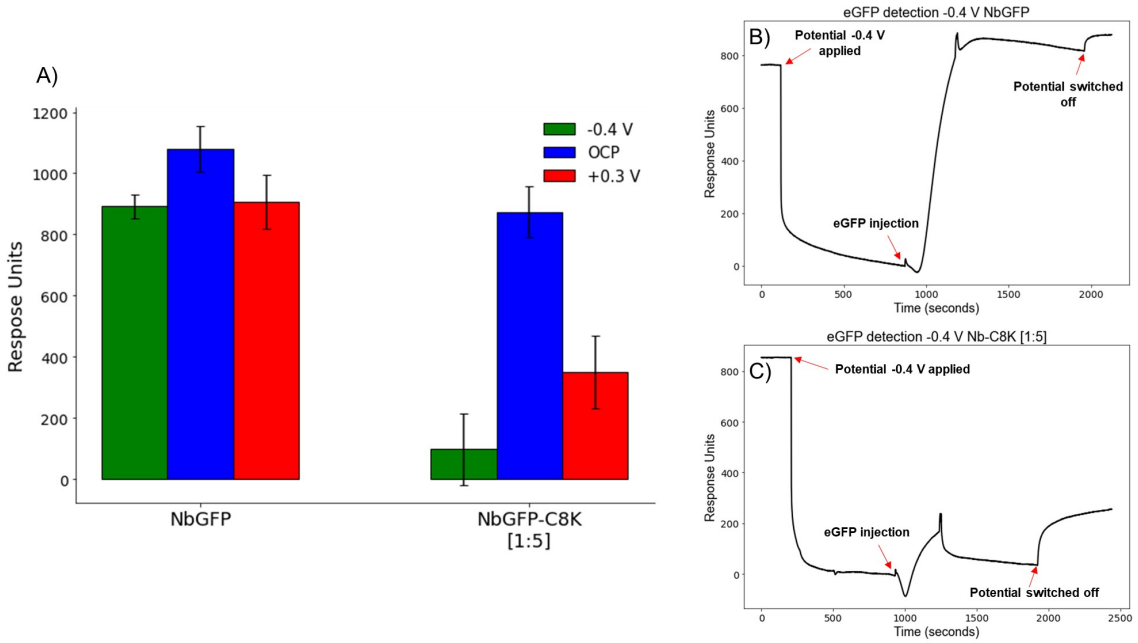

Figure 3.3.13: A) *eGFP binding response on NbGFP and NbGFP-C8K [1:5] surfaces under -0.4 V (green), OCP (blue), and +0.3 V (red), n = 3.* ***B)*** *SPR trace of eGFP binding on NbGFP surface under -0.4 V.* ***C)*** *SPR trace of eGFP binding on NbGFP-C8K [1:5] surface under -0.4 V.*

The potential of -0.4 V had a minimal effect on eGFP binding on the NbGFP system (figure 3.3.13 (A)). However, with the NbGFP-C8K [1:5] system, it was expected that the eGFP binding would remain the same as OCP or increase. This is because the C8K should be attracted to the surface, exposing more of the Nb's binding sites to the surrounding environment. However, the opposite effect was observed, with eGFP binding dropping from 874 $\pm$ 84 RU under OCP to 98 $\pm$ 118 under -0.4 V. A possible explanation for this could be that the oligopeptides are indeed still being attracted towards the surface, but they are collapsing on top of the Nbs. This would essentially 'cap' the Nb's binding sites, preventing eGFP interactions. Another possible explanation is that the -0.4 V is having a negative effect on the NbGFP-C8K surface which is disrupting the eGFP binding. However, as it did not significantly effect the eGFP binding on the NbGFP surface

it is difficult to say what is actually happening. Therefore, the potential window of the buffer (PBS) was probed on the different surfaces to investigate if any faradaic reactions are present at the applied potentials (figure 3.3.14). This was achieved by scanning the potential between +0.6 and -1 V and measuring the resulting current response.

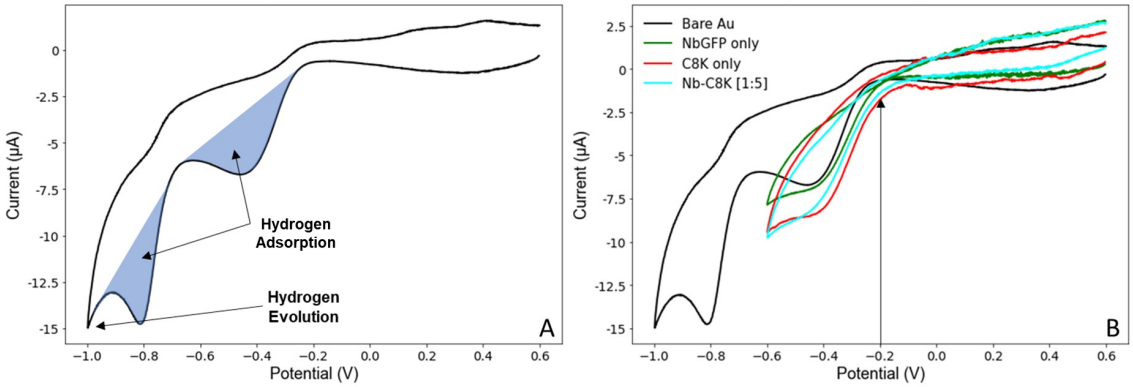

Figure 3.3.14: A) *Cyclic voltammogram of Bare Au substrate in PBS.* ***B)*** *Cyclic voltammogram of Bare Au (black), NbGFP (green), C8K (red), and NbGFP-C8K (cyan) surfaces in PBS. All potential and current measurements are in reference to the Ag/AgCl reference electrode.*

At +0.3 V only transient, non-faradaic processes could be observed in the cyclic voltammogram (figure 3.3.14 (A)). However, at more negative potentials a large reduction peak can be observed which corresponds to the hydrogen evolution reaction. This peak contains two sub-peaks corresponding to hydrogen adsorption on the Au surface [221]. The first hydrogen adsorption reaction reaches a maximum peak current at -0.4 V, which is the same potential used to change the conformation of the C8K oligopeptides. Therefore, each surface (NbGFP, C8K, and NbGFP-C8K [1:5]) were also investigated using cyclic voltammetry (figure 3.3.14 (B)). It can be seen that this peak (-0.42 V) is present across all the surfaces which could be having a disruptive effect on the C8K oligopeptides on the surface. Therefore, the eGFP binding and switching efficiency was again investi-

gated at -0.2 V as this is the highest magnitude negative potential which produces a low faradaic current (figure 3.3.14 (B)). These results are summarised in figure 3.3.15 below.

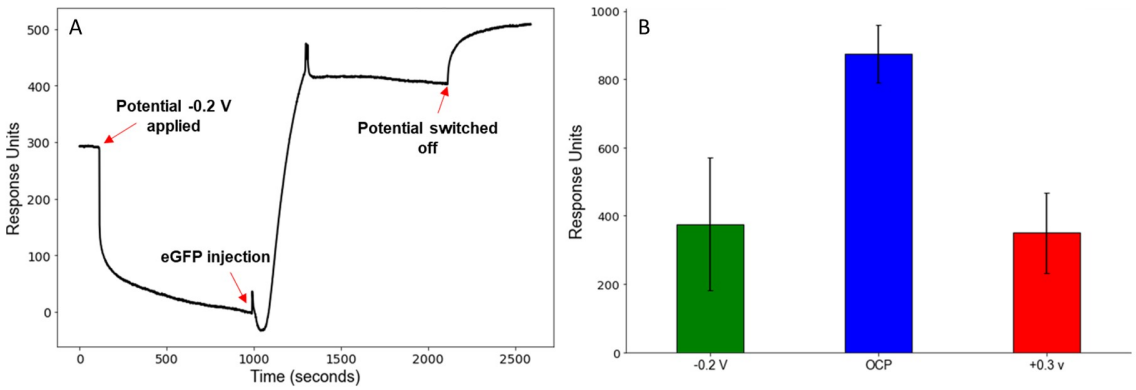

Figure 3.3.15: A) *SPR trace showing eGFP binding under -0.2 V.* ***B)*** *eGFP binding response under -0.2 V, OCP, and +0.3 V, n = 3.*

The eGFP binding still significantly decreases under a potential of -0.2 V to 376 $\pm$ 195 RU. This supports the hypothesis that the decrease in eGFP binding is due to the 'capping' of the Nb's binding site and not due to a negative effect cause by the applied potential. However, to get a better understanding of the interactions occurring at the surface a number of control experiments were designed. eGFP was injected onto each surface (Bare Au, NbGFP only, C8K only, and NbGFP-C8K [1:5]) and the binding responses were compared (figure 3.3.16).

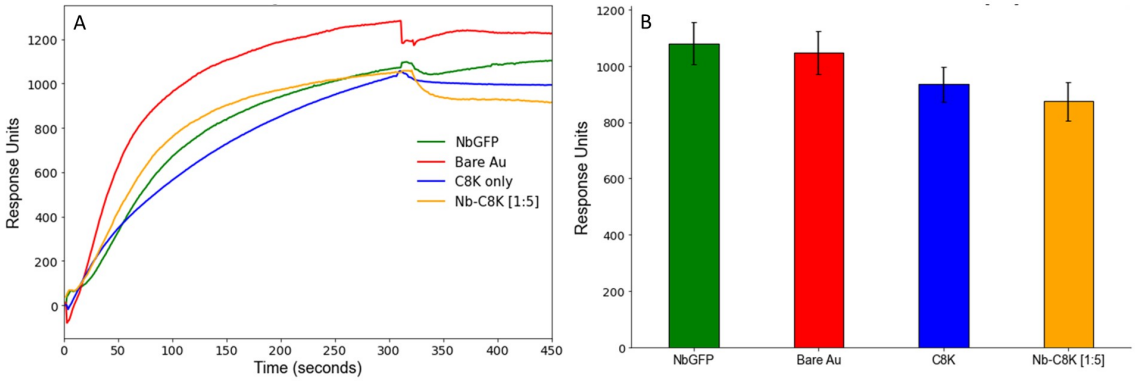

Figure 3.3.16: A) *SPR trace for eGFP binding on bare Au (red), NbGFP only (green), C8K only (blue), and NbGFP-C8K [1:5] (orange).* ***B)*** *Comparison of the eGFP binding responses across the four different surfaces, n = 3.*

Surprisingly, the same level of eGFP binding across all four surfaces was observed. This finding implies that the previously reported binding cannot be conclusively attributed to interactions between NbGFP and eGFP. These results suggest that eGFP exhibits a strong affinity for bare gold (Au). If the NbGFP and C8K oligopeptides fail to form densely packed films, leaving a significant portion of the Au surface exposed, it would be challenging to distinguish between non-specific interactions with the Au and genuine NbGFP-eGFP interactions. However, it was previously reported in figures 3.3.12 and 3.3.14 that when the oligopeptides are present the applied potentials significantly reduce the eGFP binding with the surface. Therefore, to get a better understanding of the effect the C8K has on the surface, eGFP binding was investigated under positive and negative potentials across all four surfaces (figure 3.3.17).

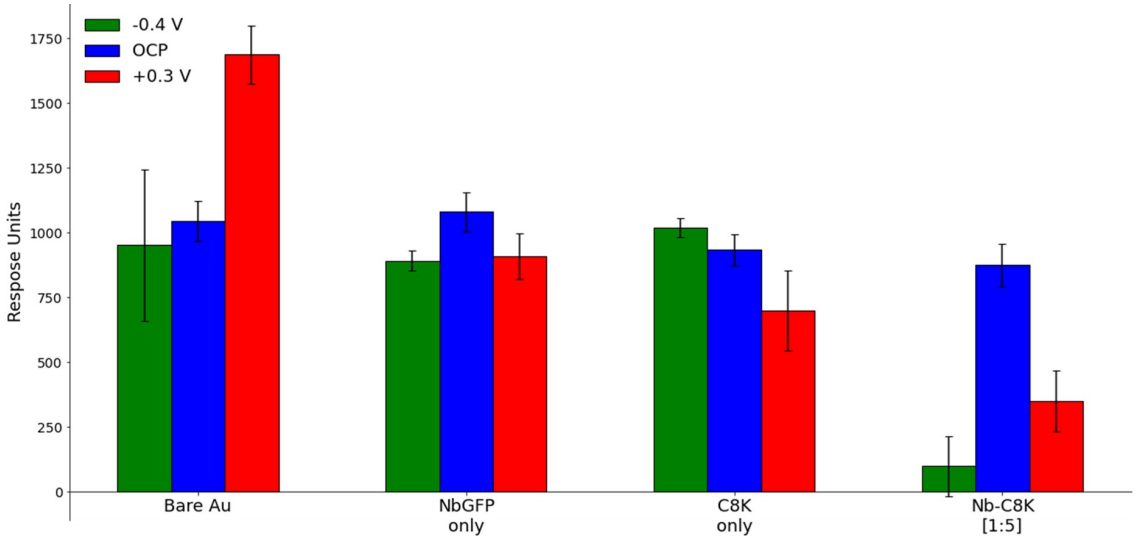

Figure 3.3.17: *eGFP binding under -0.4 V (green), OCP (blue), and +0.3 V (red) across the four different surface, n = 3.*

On the bare Au surface the negative potential did not seem to significantly effect eGFP binding. However, under a positive potential the binding response increased by 641 RU from 1046 $\pm$ 77 under OCP to 1687 $\pm$ 113 RU. This can be explained by considering the eGFP would be negatively charged under the experimental conditions and electrostatically attracted to the surface. Interestingly, this effect disappeared when the surface was functionalised with NbGFP. This indicates that the Nbs screened the electrostatic attraction resulting in lower binding.

The presence of only C8K on the surface resulted in a decrease in eGFP binding from 934 $\pm$ 64 to 699 $\pm$ 156 RU under a potential of +0.3 V. However, a negative potential did not have a significant impact on eGFP binding. When NbGFP and C8K were both on the surface the positive and negative potentials significantly reduced eGFP binding. These results support the hypothesis that the oligopeptides are changing their conformation on the surface which modulates eGFP binding. However, as suggested from the ellipsometry, XPS, and EIS

results the C8K surfaces are highly disorganise therefore, in the C8K system there seems to still be a large amount eGFP interacting with the exposed gold surface.

To investigate if the switching is recoverable two control experiments were designed. The first involved switching the potential off half way through the eGFP injection. If the oligopeptides revert back to their OCP confirmation then the eGFP binding should increase. The second experiment involved a full eGFP injection under a potential of -0.4 V then switching off the potential and allowing the system to reach an equilibrium before injecting eGFP again. This would allow more time for the oligopeptides to reorganise themselves on the surface and also ensure a stable SPR baseline before eGFP binding begins. The results of these two experiments are presented in figure 3.3.18.

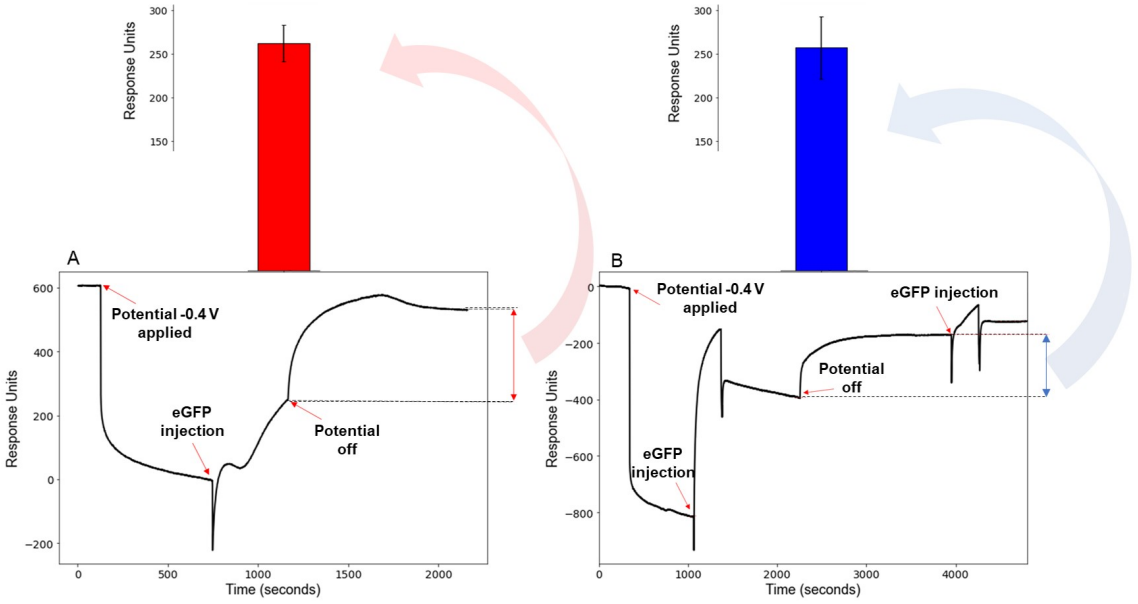

Figure 3.3.18: A) *SPR trace of eGFP injection on NbGFP-C8K [1:5] surface with the potential switched off half way through the injection.* ***B)*** *SPR trace of the potential switched off after eGFP injection, the system allowed to reach equilibrium before eGFP was injected again, n = 3.*

In Figure 3.3.18 (A), the initial baseline drop is observed when a potential of -0.4 V is applied. The system is then allowed to restabilise before the injection

of eGFP. Midway through the injection, the potential is turned off, leading to an increase in the eGFP binding response by approximately 250 RU. However, when the potential was turned off after the full injection of eGFP (as shown in Figure 3.3.18 (B)), the SPR response also increased by around 250 RU, even without any eGFP being injected. This suggests that the observed change is not due to an increase in eGFP binding to NbGFP, but rather a result of the surface reorganising itself in response to the change in electrical potential. When eGFP was reinjected, the baseline increased by only 51 ± 5 RU. These results indicate that under these experimental conditions, the switching is not reversible.

3.4 Conclusion

This research chapter was primarily concerned with the modification of gold substrates with NbGFP and C8K oligopeptides, for the detection and modulation of specific eGFP interactions. NbGFP could be directly attached to the gold surface via incubation in sodium acetate buffer (pH 5.6) for 20-22 hours. This was confirmed using ellipsometry, XPS, and SPR. C8K oligopeptides could also be attached to the surface using the same method, which again was confirmed using ellipsometry, XPS, and SPR. The molar ratios of NbGFP-C8K in the incubation solution was then optimised to give the best switching response. A ratio of 1:5 was chosen as under a potential of +0.3 V the system showed a switching efficiency of $\approx$ 60%. Unfortunately, under OCP there was no significant reduction in the level of eGFP binding which was monitored using SPR. This indicates that energy needs to be put into the system to hold the surface in the 'OFF' state, which

is undesirable due to cost and practicality. The system was also investigated under a potential of -0.4 V which produced a dramatic decrease in eGFP binding. This was unexpected as the positively charged oligopeptides should have been attracted down towards the surface thus, revealing the Nb's binding sites to the surrounding environment. This may be explained by considering the oligopeptides are 'capping' the Nbs as they are being pulled towards the surface. For the first time, these results demonstrate that the conformation of the C8K oligopeptides can be changed in response to applied potentials, which in turn can be used to modulate NbGFP-eGFP interactions on the surface.

However, from the control studies it seems that the C8K oligopeptides take up a large surface footprint and due to their high flexibility adopt a flat confirmation on the surface. This prevents high packing densities leading to highly disorganised films. This leads to a large amount of non-specific interactions between the eGFP and the surface. Therefore, it is extremely difficulty to determine how much specific NbGFP-eGFP interactions the oligopeptides are controlling. Therefore, it would be beneficial to be able to insulate the gold surface from non-specific eGFP interactions, and also have a more robust and controllable method for coupling NbGFP and C8K molecules to the interface. This also may allow the C8K units to conceal the Nb's binding sites under OCP.

To this end, the next research chapter is partly concerned with the development of electropolymerised films which can be controlled in terms of their physical and electrochemical properties. Such films would allow the covalent attachment of the NbGFP and C8K components. This should also allow the application of higher

magnitude potentials across the interface, which could result in higher control over NbGFP-eGFP interactions.

Chapter 4. Electropolymerised films and their Integration onto Gold Arrays

Abstract: *This chapter involves the optimisation of electropolymerised films along with the fabrication of a work gold electrode array. Herein, different monomer units are initially investigated and control over their physical and electrochemical properties are probed as a function of applied potential time. The films are characterised using contact angle, ellipsometry, cyclic voltammetry, and electrochemical impedance spectroscopy. Then through clean room fabrication processes gold electrode arrays are fabricated along with hardware to allow for connection to preexisting potentiostats. The platform is characterised using electroanalytical techniques, atomic force microscopy, and optical microscopy. Finally, the optimised electropolymerised film is transferred to the gold array and characterised using cyclic voltammetry and electrochemical impedance spectroscopy.*

4.1 Introduction

As discussed in section 1.3.2, electropolymerised films have emerged as a crucial class of functional materials employed in the fabrication of electrochemical biosensors. Literature reports demonstrate precise control over the physical and electrochemical properties of these films by tuning parameters such as monomer concentration, scan rate, number of scans, solvent choice, and the magnitude of applied potentials [71, 222–224]. These films serve as robust support structures for the covalent attachment of receptors and other surface components, significantly enhancing the stability of surface architectures. Additionally, they act as insulating layers, shielding the underlying electrode material from the surrounding environment. This insulation minimises non-specific surface interactions, thereby improving biosensor sensitivity [14].

However, it is evident from the literature that there is no universal approach to biosensor fabrication. The choice of electrode material, functionalisation layer,

bioconjugation strategy, and receptor components must be carefully considered within the context of the analytical biosensing technique and the ultimate application of the platform. Consequently, optimisation becomes essential at every step of the biosensor fabrication process to yield the most effective analytical device. This chapter investigates different monomer units for the controlled fabrication of electropolymerised films.

Furthermore, it would be a significant advancement in monitoring cell and gene therapy bioprocessing if multiple analytes could be simultaneously monitored across different time points during the process. Electrode arrays have the capacity to facilitate this, as the individual electrodes in the array can be functionalised with different receptor components. Moreover, the electrodes can be individually electrically addressed. In the proposed system of this thesis (section 1.7), this would allow Nbs on one electrode to be shielded from the surrounding environment while simultaneously allowing Nbs on an adjacent electrode to bind to their associated target. Therefore, part of this chapter also investigates the fabrication of gold arrays and the associated hardware in order to integrate the electrodes with preexisting potentiostats.

4.2 Aims and Objectives

Aim 1: Finding the appropriate monomer will allow electropolymerisation of films with controllable physical and electrochemical properties. This will allow the surface films to be optimised in terms of their thickness and density, ultimately improving the overall biosensing response.

Aim 2: Once optimised the electropolymerised film should be transferable to gold arrays.

Objective 1: Investigate commonly used monomers for the fabrication of electropolymerised films.

Objective 2: Demonstrate control over the physical and electrochemical properties of the film, particularly focusing on thickness and capacity to insulate the gold surface from the surrounding environment.

Objective 3: Through thermal evaporation, photolithography, and wet etching fabricate a work gold electrode array.

Objective 4: Fabricate the associated hardware needed to connect the gold array to the preexisting potentiostats.

Objective 5: Demonstrate that the arrays work and the electrodes can be individually and simultaneously electrically addressed.

Objective 6: Transfer the optimised electropolymerised film to the gold array.

4.3 Results and Discussion

Notes: *Initially, either the gold rod electrodes discussed in section 3.3.3 or Au/Si substrates were used in the optimisation of the electropolymerised films. This is specified in the individual figure captions along with the working electrode area.*

4.3.1 Monomer Investigation

This section involves the investigation of different monomer units for the formation of electropolymerised films. In order to optimise the biosensing response, control over the physical and electrochemical properties of the underlying support structure would be extremely advantageous.

4.3.1.1 Pyrrole-3-carboxylic acid (P3C)

Polypyrrole derivatives are among the most extensively studied conducting polymers in the scientific literature [225]. They are easily oxidised, water soluble, cheap, and readily available which has seen them used in biosensors, mechanical actuators, anti-static coatings, and drug delivery systems [226, 227]. In particular, pyrrole-3-carboxylic acid (P3C) has been shown to produce a high density of surface carboxylic acid groups which can be covalently conjugated with receptor components with common coupling strategies, as discussed in section 1.4. Figure 4.3.1 shows the most commonly referred to mechanism for the electropolymerisation of P3C (Diaz's Mechanism) [225].

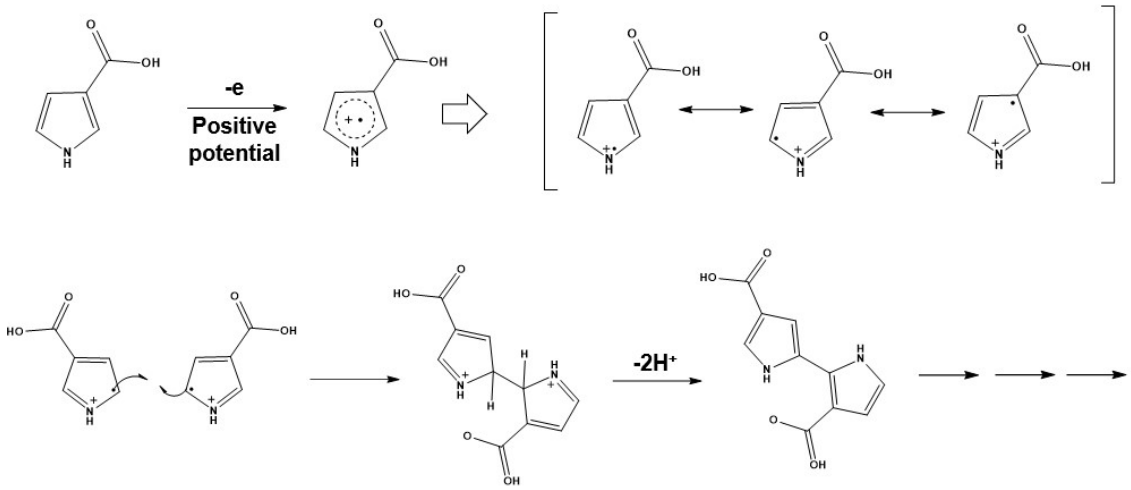

Figure 4.3.1: *Suggested mechanism for the electropolymerisation of pyrrole-3-carboxylic acid.*

100 mM P3C was dissolved in PBS (pH 7.3-7.4) and poured into the electrochemical cell. The potential was scanned from 0.0 to 1.2 V in order to find the oxidation potential of P3C (figure 4.3.2).

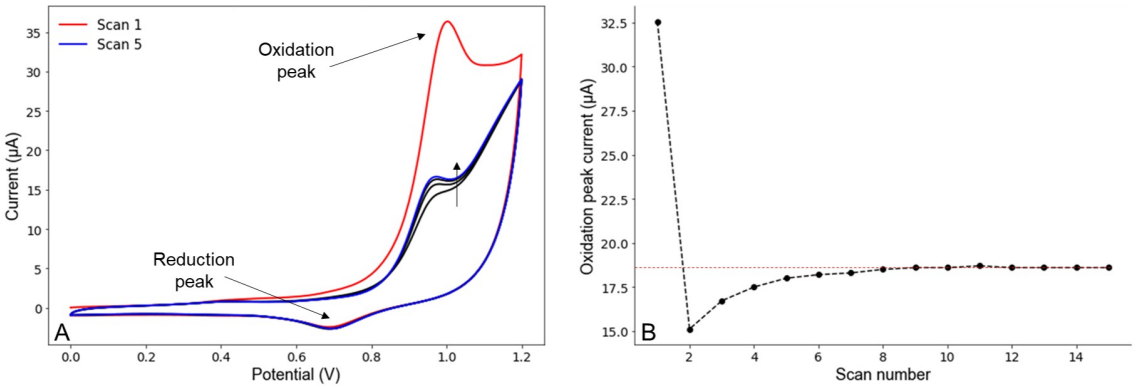

Figure 4.3.2: ***A)*** *Cyclic voltammetry of 100 mM P3C in 1 X PBS (pH 7.3-7.4), scan 1 = red, scan 5 = blue.* ***B)*** *Peak oxidation current vs number of scans. Electrode area = 0.03 cm^2 (geometric surface area.*

The first CV scan produced a large oxidation peak at 1 V (approx. 36 μA) which may correspond to the electropolymerisation of P3C. However, this peak is also in the same potential window as gold oxidation [228]. On subsequent scans this peak initially decreases in magnitude which is characteristic of a surface which has undergone partial passivation. However, the oxidation peak current then in-

creased in magnitude reaching a maximum after 8-10 scans (figure 4.3.2 (B)). This is likely due to the conductive nature of the P3C derived surface. Figure 4.3.2 (A) also shows a persistent, small magnitude reduction peak just below 0.7 V which is likely due to a small amount of gold-oxide being reduced. Therefore, it is difficult to conclude the extent to which P3C is being deposited onto the surface.

Faradaic EIS and CV were employed to further investigate the electrochemical properties of the surface (figure 4.3.3). The CV and EIS response were reported in the presence of 10 mM $Fe(CN)_6^{-3/-4}$, after a different number of potential cycles (2-20) and also after holding the potential at 1.1 V for 10 minutes.

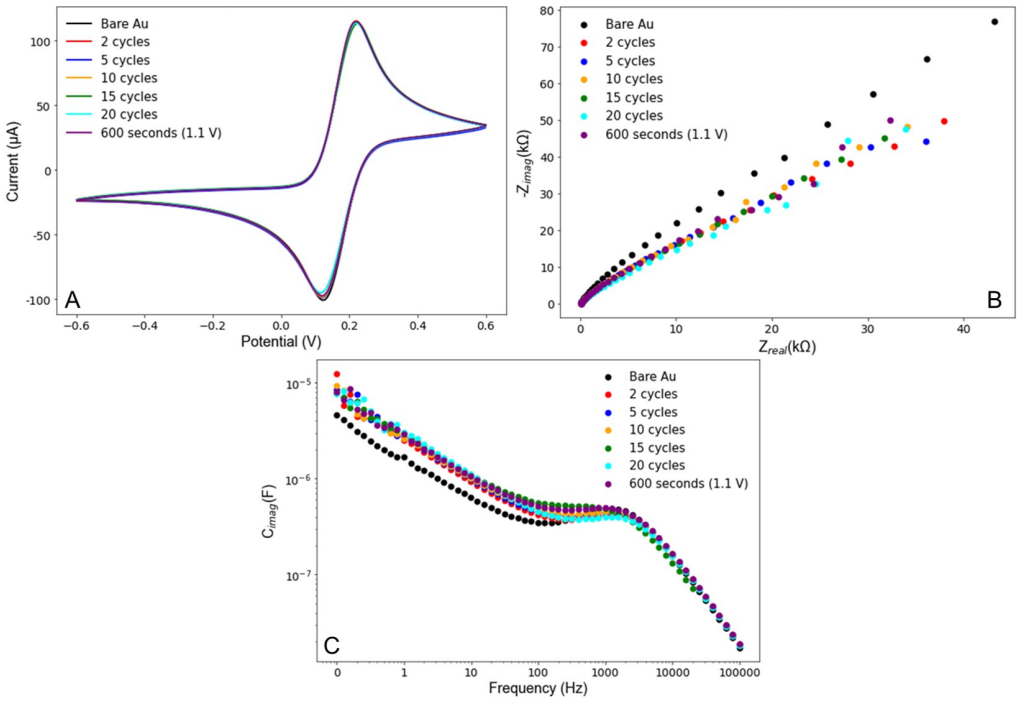

Figure 4.3.3: A) *Cyclic voltammetry of 10 mM $Fe(CN)_6^{-3/-4}$ on the electropolymerised P3C surface after different numbers of cycles between 0 and 1.2 V and after holding the potential at 1.1 V for 10 minutes. The same surfaces were investigated using faradaic EIS (10 mM $Fe(CN)_6^{-3/-4}$) and are represented in a Nyquist plot* ***B)*** *and a Bode plot* ***C)****. Electrode area = 0.03 cm^2.*

Regardless of the number of cycles or after holding the potential at 1.1 V for 10

minutes, there was no change in the redox activity of the $Fe(CN)_6^{-3/-4}$ probe at the surface (figure 4.3.3 (A)). Likewise, there was only an extremely small shift in the EIS response compared to the bare Au surface, which did not change as the number of cycles increased (figure 4.3.3 (B) and (C)). The EIS response was characteristic of a diffusion controlled system, as suggested by the straight, 45° response seen in the Nyquist plot (Warburg diffusion). Therefore, even if small amounts of P3C are being electrodeposited onto the surface, there is no control over the electrochemical properties of the system under these fabrication conditions.

Other literature reports suggest that P3C can be electropolymerised onto electrode surface using dilute sulfuric acid instead of PBS [222]. Therefore, these experiments were repeated in 0.5 M H_2SO_4 and the electrochemical properties of the surface investigated. However, this did not increase the control over the electropolymerisation of P3C or improve control over the electrochemical properties. The CV and EIS for these experiment can be found in the appendix (figure 2).

4.3.1.2 4-carboxybenzene diazonium (*in situ*)

Diazonium salts have been used extensively in the literature for surface modifications, as discussed in section 1.3.2. However, only a limited number of aryl diazonium salts are commercially available due to their relatively low stability. Therefore, they are often produced in situ from amine precursors and used for surface electropolymerisations straight away. To this end, 10 mM of 4-aminobenzoic acid (4-ABA) was mixed with 8 mM $NaNO_2$ in 0.5 M HCl at 0°C and allowed to react

for 5 minutes [229, 230]. The diazotization reaction seen in figure 4.3.4, produced the corresponding 4-carboxybenzene diazonium cations (4-CBD).

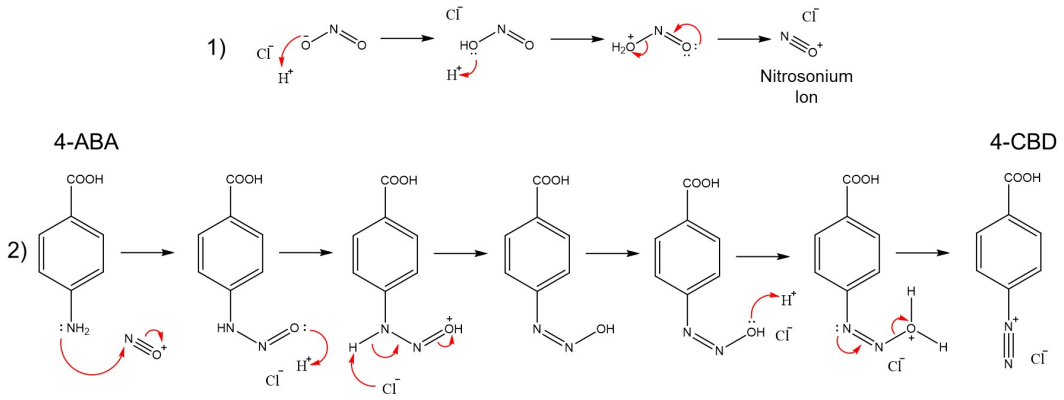

Figure 4.3.4: *Reaction scheme **1)** shows the formation of the nitrosonium ion which goes on to react with 4-ABA in scheme **2)** to produce the corresponding 4-CBD.*

This reaction was carried out inside the electrochemical cell and immediately electropolymerised to freshly cleaned Au/Si wafers by scanning the potential from 0.6 to -0.6 V (figure 4.3.5).

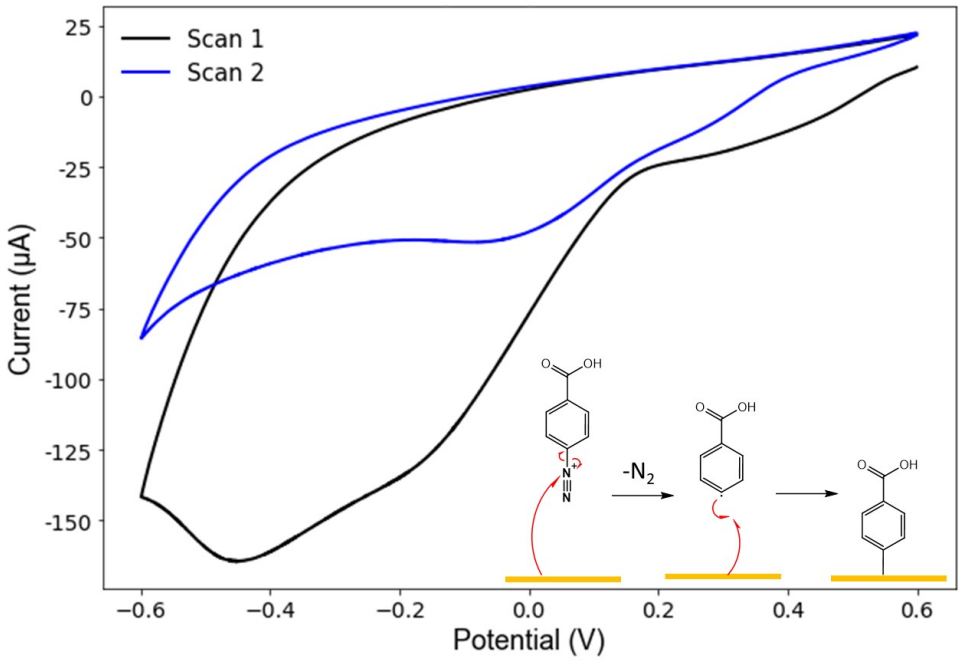

Figure 4.3.5: *Cyclic voltammogram of the reduction of 4-CBD and associated reaction scheme. Scan rate = 100 mV/s, Electrode area = 1.54 cm^2.*

This resulted in a broad reduction peak around -0.4 V. There was also a second peak located at -0.2 V which is likely a result of the polycrystalline nature of the

gold surface. Different crystallographic site on the surface would have different work functions (energy require for an electron to escape the surface) resulting in multiple peaks. However, this peak is in the same potential range as the hydrogen evolution reaction on gold [228]. Therefore, its was not clear from one scan if the reduction peak corresponded to diazonium reduction or hydrogen evolution. The disappearance of this peak on the second scan is consistent with a surface which has been functionalised and suggest that the reduction peak is related to the modification of the gold surface. Literature reports also suggest that the broadness of this peak can be explained by the polycrystalline nature of the gold surface containing multiple crystallographic orientations [231–233]. Different crystallographic sites will have different work functions and therefore, require slightly different potentials to reduce the diazonium cations.

From this, a potential of -0.6 V was chosen to carry out a thickness vs time study as this ensured complete reduction of the diazonium cations. As described in section 1.3.2 the radicals produced can also react with the ’3’ and/or ’5’ positions on the aryl ring of molecules that have already been functionalised to the surface. Therefore, it would be expected that the film increases in thickness and density when the potential is applied for longer time periods. The surface was investigated using CV, ellipsometry, and contact angle (CA) as a function of applied potential time (figure 4.3.6). CA measures the wettability of the surface by recording the angle of contact between a water droplet and the surface. The advancing angle is recorded as the droplet spreads out on the surface and the subsequent receding angle is measure as the droplet is pulled back into the dispenser. The difference

between the two is known as the hysteresis and can indicate the roughness of the surface [234, 235].

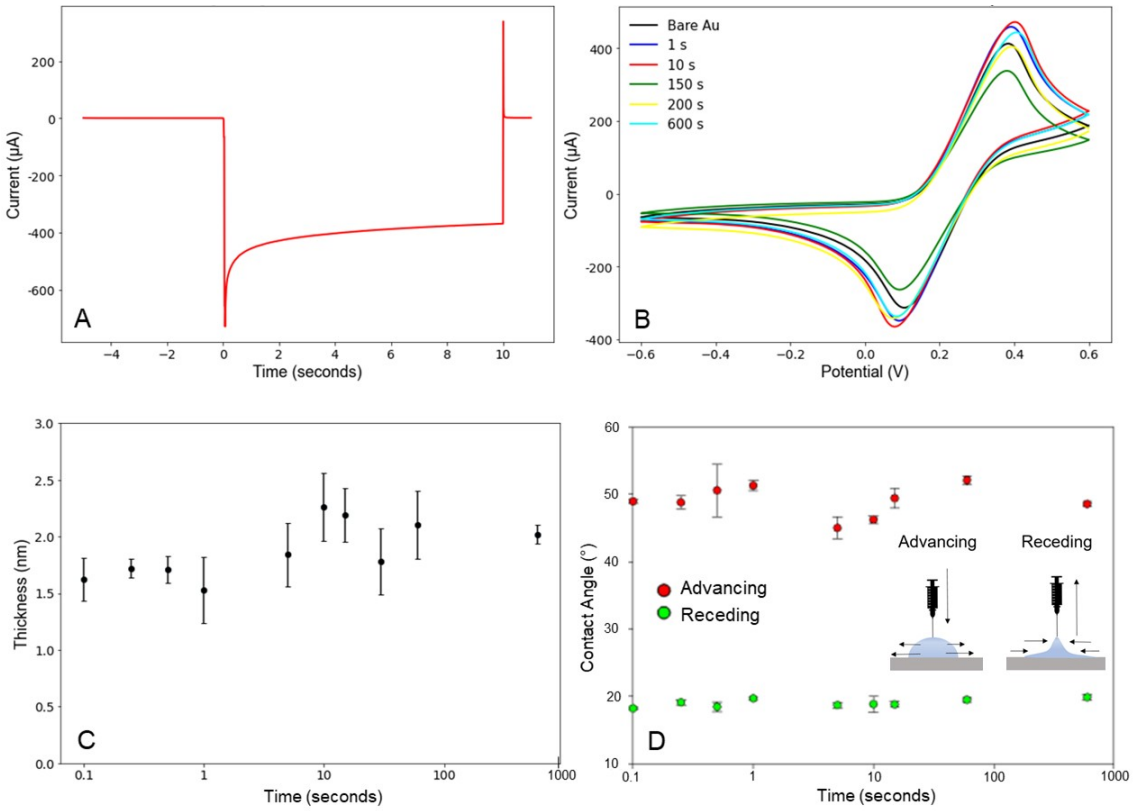

Figure 4.3.6: A) *Chronoamperometry scan showing the current passed during 4-CBD electropolymerisation when the potential was held at -0.6 V for 10 seconds.* ***B)*** *CV of 10 mM* $Fe(CN)_6^{-3/-4}$ *on the surfaces after the potential was held at -0.6 V for different time periods.* ***C)*** *Ellipsometry thicknesses of the films after electropolymerisation for different time periods.* ***D)*** *The measured advancing and receding water contact angles of the surfaces after electropolymerisation for different time periods. Electrode area = 1.54* cm^2*, n = 3.*

Figure 4.3.6 (A) presents the chronoamperometry scan of the *in-situ* produced 4-CBD, in response to an applied potential of -0.6 V held for 10 seconds. The negative current response should correspond to the reduction of 4-CBD, forming the associated aryl radicals. However, figure 4.3.6 (B) shows no clear reduction in the activity of $Fe(CN)_6^{-3/-4}$ as the potential was held for different time periods. There is a slight increase in the peak to peak separation as the potential was applied for longer time periods. This is indicative of slower electron trans-

port kinetics suggesting that the surface has been modified. The film's thickness, as depicted in Figure 4.3.6 (C), remained consistent between 1.5 and 2.5 nm, irrespective of the duration of applied potential. This thickness corresponds to approximately 2-3 4-CBD molecules and coupled with the CV results suggests the presence of a thin, disorganised film on the surface.

A similar trend is observed for the measured contact angles (figure 4.6.6 (D)), with the advancing angle remaining constant around 50° and the receding angle remaining just below 20°. The measured advancing contact angle (CA) of bare gold was 67 ± 3.3° (n = 3) therefore, the drop in CA likely corresponds to the presence of carboxylic acid residues on the surface, introduced by the 4-CBD. Carboxylic acid groups are hydrophilic, forming hydrogen bonds with water molecules however, 50° is still relatively high for a substrate which should contain carboxylic acid groups. For example, SAMs formed from 11-MUA commonly have advancing CAs around 20° with a hysteresis less than 15° [164]. These values are characteristic of a well ordered hydrophilic surface. In this case the hysteresis is around 30° suggesting a rough and disorganised surface.

The results presented together in figure 4.3.6, suggest that the generated 4-CBD radicals form loosely packed (pin holes present), heterogenous structures on the surface. These characteristics are undesirable as there is no observed control over the physical and electrochemical properties of the film and there is likely a large amount of surface gold exposed to the surrounding environment. Therefore, it was decided to investigate a diazonium salt which was stable enough to be bought commercially and did not need to be generated *in-situ*.

4.3.1.3 4-Nitrobenzenediazonium Tetrafluoroborate (4-NBDT)

The diazonium salt was selected based on the expected ease of coupling biomolecules to the modified surface. A carboxylic acid containing diazonium salt could not be found, so instead 4-nitrobenzenediazonium tetrafluoroborate (4-NBDT) was chosen. While nitro groups are not suitable for surface coupling reactions, they have been shown to reduce to the corresponding primary amine under negative potentials [236–238].

10 mM 4-NBDT was dissolved in 0.5 M H_2SO_4, and similar to 4-CBD the reduction potential of 4-NBDT was investigated using CV (figure 4.3.7). A large reduction peak, consisting of two subpeaks was observed between 0.3 and 0.4 V. This is convenient as no reduction peak was observed in this potential window when CV was carried out on the gold electrode in 0.5 M H_2SO_4 (figure 3.3.5 (C)). Therefore, this peak can be more confidently ascribed to the reduction of 4-NBDT compared to the reduction peak at -0.4 V, in the case of 4-CBD. The disappearance of this peak on the second scan is consistent with a surface which has been functionalised. The reaction scheme for this surface modification is the same as the one described for 4-CBD, and can be seen in figure 4.3.7.

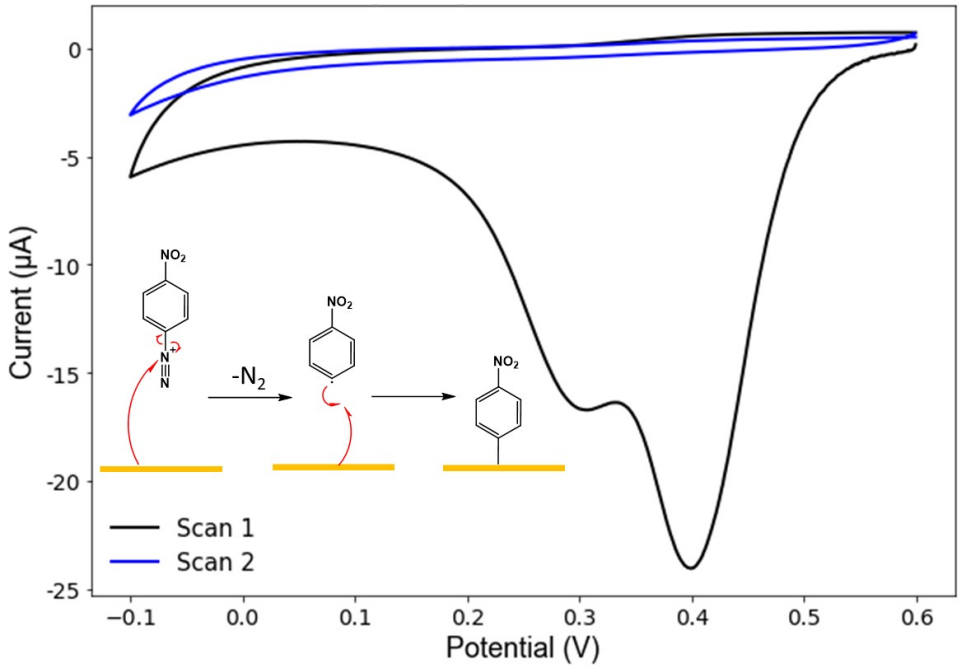

Figure 4.3.7: *Cyclic voltammogram of the reduction of 10 mM 4-NBDT in 0.5 M H_2SO_4 and the associated reaction scheme. Electrode area = 1.54 cm^2.*

From this, a reduction potential of -0.4 V was chosen to investigate the physical and electrochemical properties of the film as a function of applied potential time. This ensured a complete reduction of the diazonium salt. The thickness, CV, and EIS results are presented in figure 4.3.8 below. By comparing the ellipsometry thickness with the activity of the $Fe(CN)_6^{-3/-4}$ redox probe (figure 4.3.8 (A) and (B)), film growth seems to occur in two distinct phases. Phase I, which lasted around 25 seconds is characteristic of an increase in film density but not a significant increase in film thickness. This is evident by the gradual decrease in the activity of the redox probe while the ellipsometry thickness changed very little (less than 2 nm over this time period). This suggests that the radicals produced, more easily react with the gold surface rather than the aryl rings of the molecules that have already been functionalised to the surface. Then in phase II, when there is no more gold available for binding, the radicals are forced to react with

the ’3’ and/or ’5’ position of the aryl rings on the surface. This initiates free radical polymerisation, resulting in a dramatic increase in film thickness after 25 seconds (figure 4.3.8 (A)). The film grew from a minimum thickness of 2.2 $\pm$ 0.2 nm after 0.1 seconds, to a maximum of 8.9 $\pm$ 0.5 nm after 600 seconds. The activity of the $Fe(CN)_6^{-3/-4}$ redox probe sequentially decreased until it was completely suppressed after 25 seconds. This suggests after 25 seconds of applying a potential of -0.4 V the gold surface is well insulated from the surrounding environment.

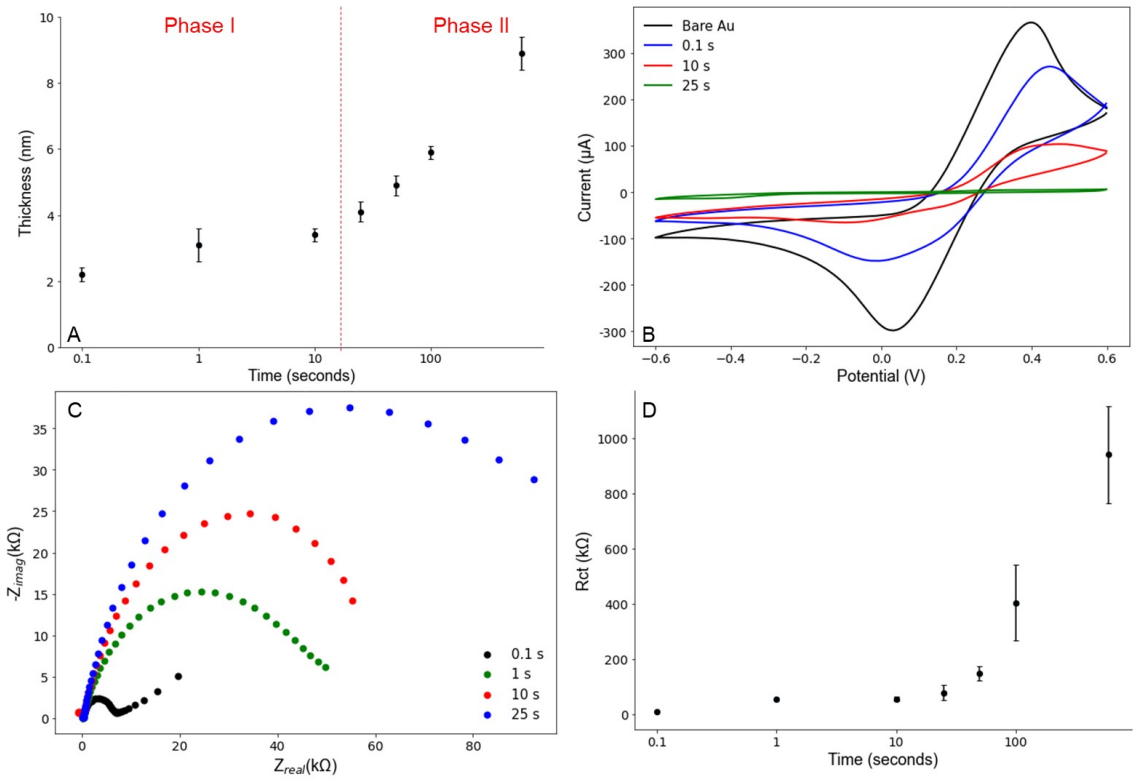

Figure 4.3.8: *10 mM 4-NBDT was electropolymerised onto Au/Si substrates by applying a potential of -0.4 V for varying time periods.* ***A)*** *The resulting film thickness,* ***B)*** *the activity of 10 mM $Fe(CN)_6^{-3/-4}$ in 1 x PBS (1 M KCl),* ***C)*** *the EIS response displayed in a Nyquist plot and* ***D)*** *the associated R_{ct} values. For (B) and (C) only the responses for the first 25 seconds were included in the plots for clarity. Electrode area = 1.54 cm^2, n = 3.*

As the film increased in thickness and density the R_{ct} increased accordingly (figure 4.3.8 (C) and (D)). This is expected, as if the film is growing in length and becoming more densely packed it becomes more difficult for charges to be exchanged

across the interface.

These results demonstrate that the film's thickness can be controlled to near nanometer precision in a reproducible manner by controlling the applied potential time. Furthermore, the majority of literature reports recommend acetonitrile as the solvent of choice for this surface electropolymerisation reaction [25, 239–241]. This method removes the need for organic solvents making the process cleaner, cheaper, and safer while retaining high control over film fabrication.

An electropolymerisation time of 25 seconds was chosen for further investigations, as this produced the thinnest film (4.1 $\pm$ 0.3 nm) while still fully suppressing the activity of the redox probe. This is important as the receptor needs to be in close spatial contact with the transducer (gold electrode) in order for biointeractions to be detectable. However, the gold surface should still be completely insulated to prevent non-specific interactions from the environment.

In order to carry out further bioconjugations the nitro group needed to be converted to the corresponding primary amine. This was achieved electrochemically, with 0.1 M KCl in 10% ethanol by scanning the potential between 0 and -1 V [236]. This resulted in a reduction peak around -0.85 V, which according to the literature corresponds to the 6 electron transfer process depicted in figure 4.3.9 [237, 238]. The reduction peak significantly decreased by the third cycle, suggesting that the majority of the NO_2 groups had been converted to NH_2 groups.

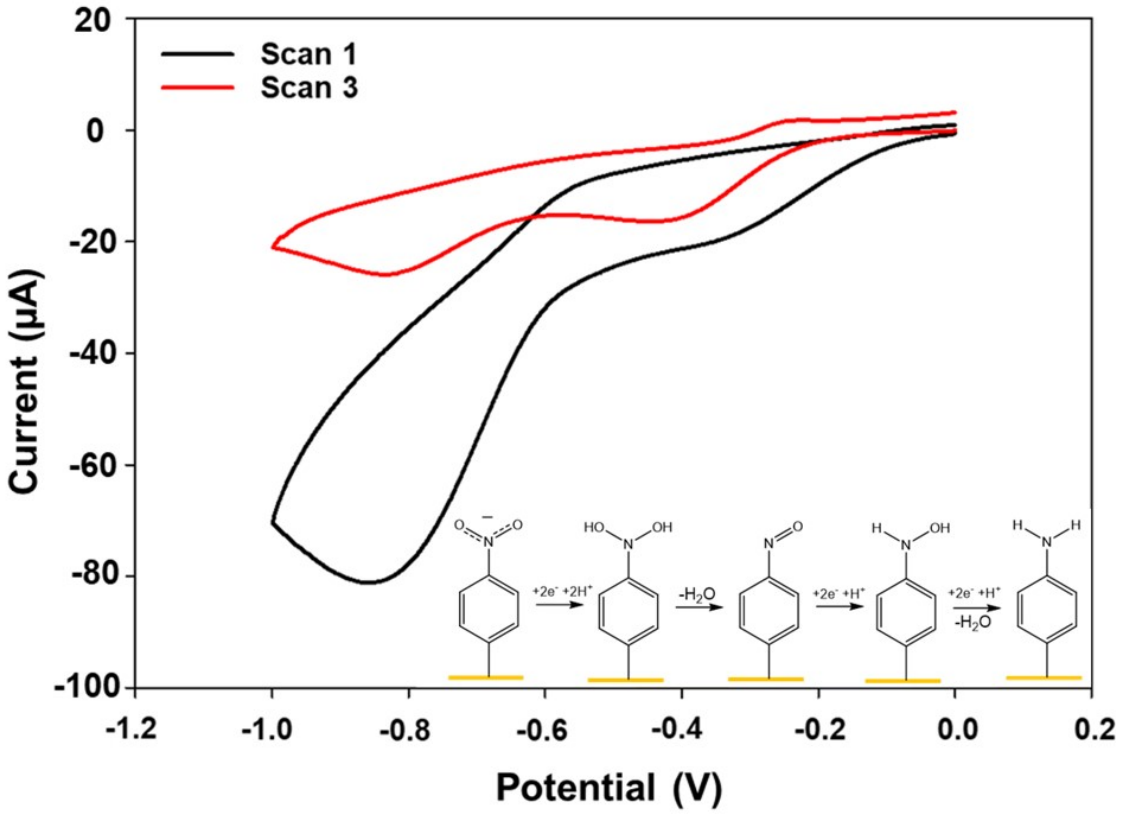

Figure 4.3.9: *Cyclic voltammogram of NO_2 surface in a 10% ethanol solution containing 1 M KCl and the proposed electrochemical pathway. Electrode area = 1.54 cm^2.*

To ensure no physical damage occurred during this reduction process, the film was characterised before and after NO_2 reduction (figure 4.3.10). The thickness of the film remained unchanged, suggesting that the NO_2 reduction process does not remove a significant amount of the electropolymerised film from the surface (figure 4.3.10 (A)). Both the NO_2 and NH_2 surfaces have the capacity to form hydrogen bonds with water molecules therefore, the advancing CAs seem slightly higher than expected (just below 80° in both cases). However, this may be explained by considering the polymeric nature of the films on the surface. Unlike SAMs, the electropolymerisation process results in branched 'tree-like' structures on the surface. This would expose hydrophobic C-C, C=C, and C-H regions which in turn would cause an increase in the measured CA. This is also reflected in the

large hysteresis value for both surfaces (around 50°), which is characteristic of a rough and disorganised film (figure 4.3.10 (B)).

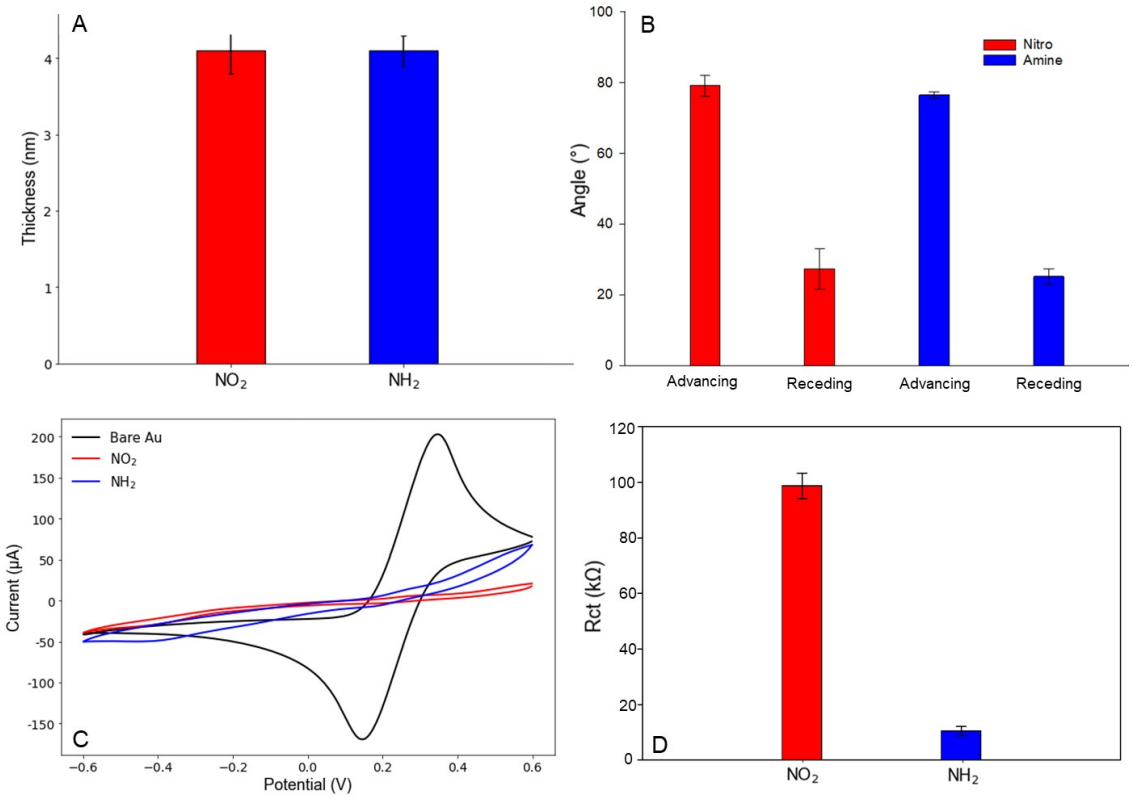

Figure 4.3.10: *Red = nitro terminated surface before reduction, blue = surface after reduction.* ***A)*** *Ellipsometry thickness,* ***B)*** *Contact angles,* ***C)*** *cyclic voltammetry in the presence of 10 mM* $Fe(CN)_6^{-3/-4}$ *in PBS (1 M KCl), and* ***D)*** R_{ct} *values. Electrode area = 1.54* cm^2*, n = 3*

As NO_2 was electrochemically reduced to NH_2 a change in the electrochemical properties of the films was expected. A significant increase was observed in the redox activity of $Fe(CN)_6^{-3/-4}$ at the NH_2 surface (figure 4.3.10 (C)). This can be explained by considering that the NO_2 groups have a net negative charge, which would repel the anionic redox probe via electrostatic repulsion. Meanwhile, the NH_2 surface would have a neutral or partially positive charge character, which would allow the redox probe to get physically closer to the surface. This would increase the chances of charge transfer occurring across the interface, which is reflected in the difference between the CVs (figure 4.3.10 (c)) and also

the R_{ct} (figure 4.3.10 (D)).

The fabricated film showed suitable reproducibility and control over the electrochemical properties of the interface. Therefore, at this point it was decided to focus on developing the gold arrays and associated hardware. The usability of this platform could then be investigated by transferring the optimised 4-NBDT film to the array.

4.3.2 Gold Array Design and Fabrication

One of the most essential characteristics of contemporary analytical devices is miniaturisation, smaller biosensors on a planar surface will allow for simple integration with existing bioreactor platforms [242]. Furthermore, decreasing the size of the working electrodes has been shown to offer other advantages such as lower detection limits and faster response times [243]. Having multiple working electrodes will also allow detection of multiple analytes from the same sample, across different time points.

In order to facilitate this, an array with 7 gold WEs surrounding a larger gold CE and silver RE was designed using CAD software (figure 4.3.11).

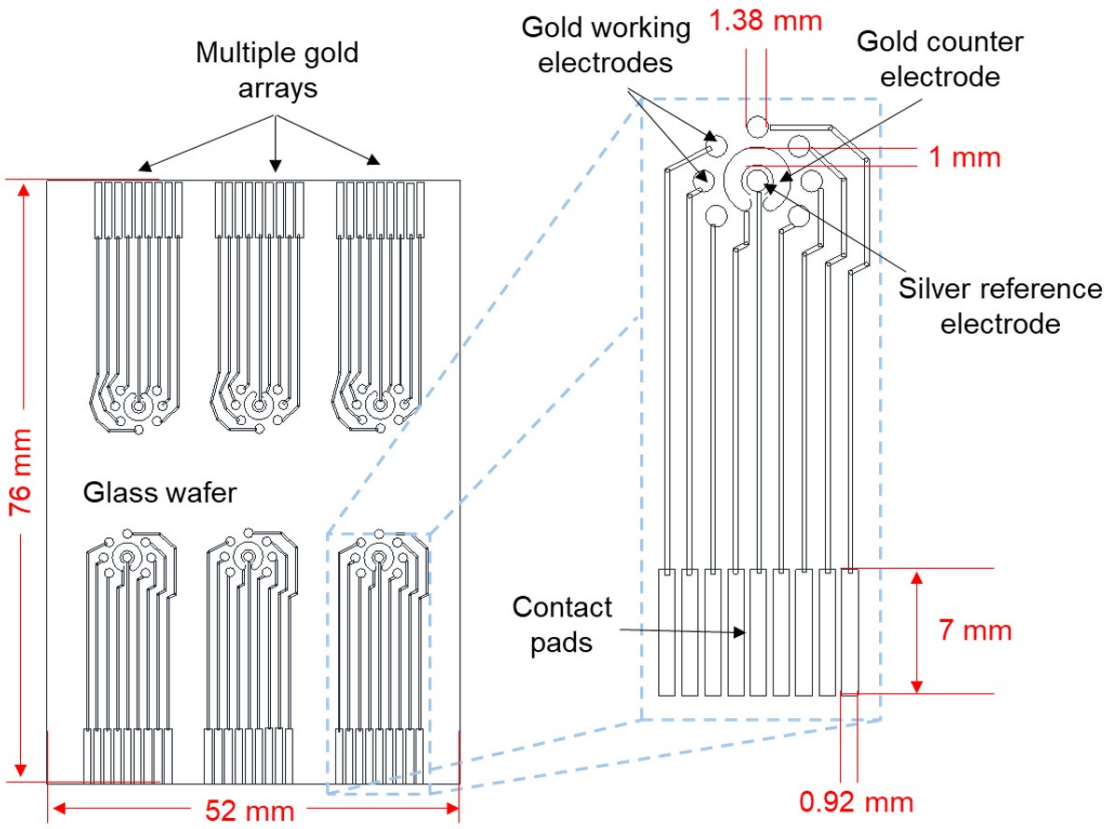

Figure 4.3.11: *Design and dimensions of the gold arrays. Created using AutoCAD.*

Initially, it was decided to exclude the silver RE in order to simplify the fabrication process. Ultimately, a surface RE may not be necessary as an external RE can be used during sensor fabrication. If non-Faradaic EIS is employed as the sensing technique, then a RE is also not required due to the small magnitude potentials applied across the system. In order to maximise array production while also keeping costs low, six individually arrays would be fabricated on preexisting glass wafers. This allowed a maximum of 12 arrays to be fabricated per batch, as a maximum of two glass slides can fit in the evaporation chamber at once. The working electrodes had a diameter of 1.38 mm and were number 1-7 moving clockwise around the face of the array (figure 4.3.12). Each electrode on the array had a corresponding contact pad, which were designed and spaced to fit into and

match up with commercially available PCB card edge connectors. The terminal end of the edge connector could then be connected to a switch box and finally to the potentiostat, as seen in figure 4.3.12.

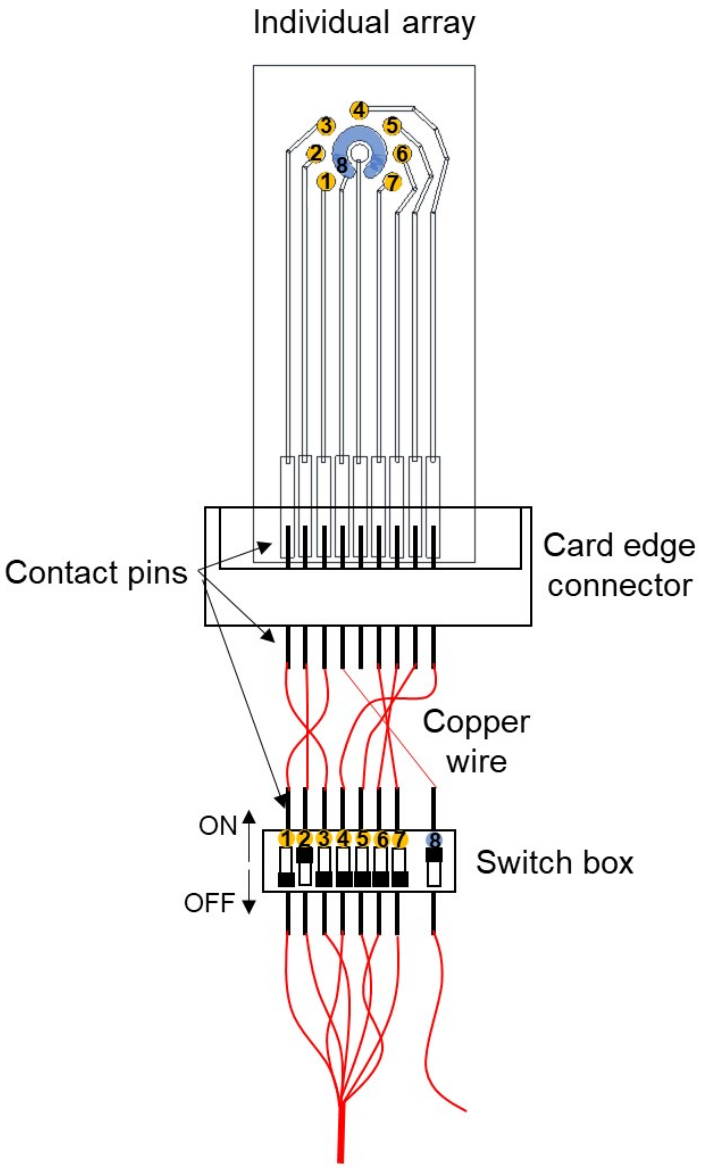

Figure 4.3.12: *Array and associated hardware: The contact pins on the card edge connector are connected to a switch box via copper wiring. Each of the wires associated with the WEs are soldered together after the switch box (1-7) and the counter electrode's wire is left separate (8). This allows connection to the potentiostat and by moving the switches to the 'ON' or 'OFF' positions, the individual WEs can be electrically addressed individually or simultaneously.*

The gold array was fabricated through processes of thermal evaporation, spin coating, photolithography, and chemical etching. First the glass substrate

was covered with a 15 nm chromium layer. This increases the surface area and improves the adhesion of the subsequent gold layer. A 100 nm gold layer was then deposited, with the thicknesses of both the chromium and gold layers being monitored using a quartz crystal microbalance. A photoresist was then spin coated to the surface and allowed to cure for approximately 20 minutes. A photomask containing the array design was placed on top of the cured photoresist and the surface was exposed to UV radiation. This chemically altered the parts of the photoresist which were not concealed by the photomask. This could then be washed away using a tetramethylammonium hydroxide (TMAH) solution. The exposed gold and chromium was subsequently removing by chemical etching and the remaining photoresist was removed by washing with acetone (figure 4.3.13). A detailed methodology for this fabrication process can be found in the materials and methods chapter.

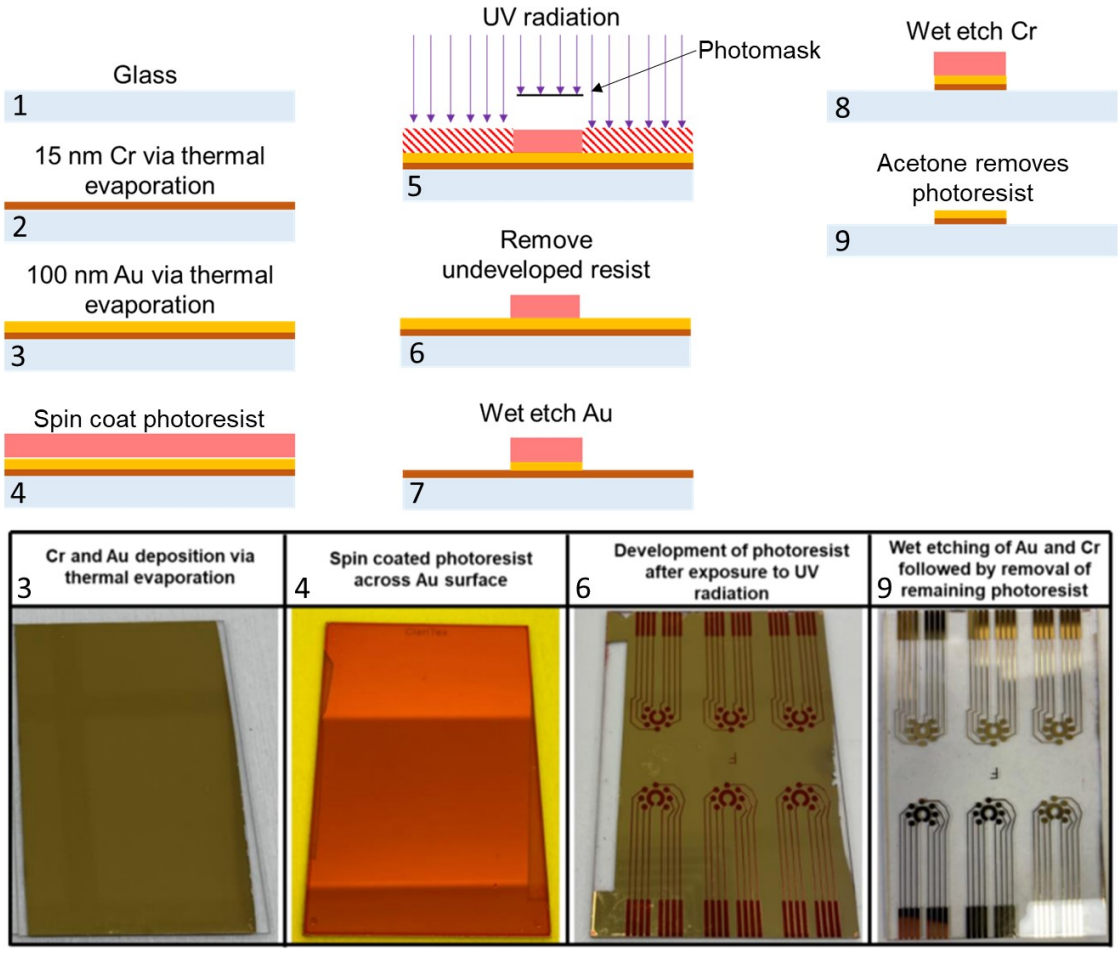

Figure 4.3.13: *Thermal evaporation, spin coating, and wet etching procedures (1-9) used for the fabrication of the gold arrays. The images correspond to the surfaces at stages 3, 4, 6, and 9 respectively.*

Once the fabrication was completed a diamond scribe was used to separate the individual arrays. The array could then be integrated with the card edge connector, as seen in figure 4.3.14. The exposed copper wires were insulated using heat shrink tubing and the switch box was mounted on a small printed circuit board for stability.

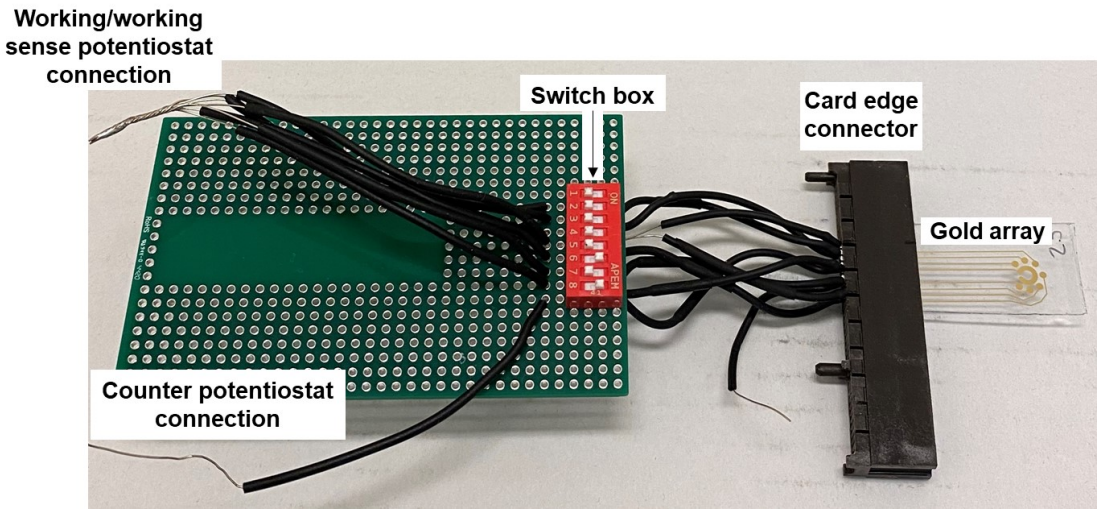

Figure 4.3.14: *Image of the hardware and integrated gold array.*

4.3.3 Characterisation of the Gold Array

Before any electropolymerised films were transferred to the array setup, its physical and electrochemical properties were probed. The surface topography was investigated using atomic force microscopy (AFM), which uses a cantilever with a very sharp tip (less than 10 nm) to scan over the area of interest. By measuring the forces between the AFM tip and the surface a 3D profile can be generated [244]. The AFM tips (model: NCHV-A) were obtained from Bruker Nano Analytics which were made of antimony (n) doped silicon (cantilever dimensions: tip = 4 μm, length = 125 μm, and width = 40 μm. cantilever properties: resonance frequency = 320 kHz, spring constant = 42 N/m). The measurements were carried out in tapping mode over a surface area of 1 μm^2 (Instrument parameters: Igain = 50 Hz, Pgain = 0.005, set point = 0.6 V, drive amplitude = 0.607 V, drive frequency = 320 kHz).

The gold WEs and CE were examined using an optical microscope and AFM, the results are presented in figure 4.3.15. The face of the array can be

seen in figure 4.3.15 (A) which has an approximate magnification of 10X. An AFM scan of a 0.25 x 0.25 μm region of one of the WEs and its corresponding 3D topography can be seen in figure 4.3.15 (B) and (C) respectively. The face of the array is well defined with no signs of damage or breaks in the gold. This suggests that the chemical etching step during the fabrication was successful. In the AFM scans individual gold crystals can be seen, which are characteristic of the growth process of the deposited gold [245]. They have an average diameter of 58 $\pm$ 14 nm (taken from 500 clusters across 3 different arrays). The surface texture is also reported in figure 4.3.15 (D) which corresponds to the diagonal profile indicated by the dotted red line in figure 4.3.15 (B) and (C). The surface had an average peak to valley roughness of 1.9 $\pm$ 0.6 nm measured across three WEs on three different arrays. This suggests that the surface of the electrodes have a similar roughness from array to array which should help reproducibility when modifying the surfaces.

The electrochemical performance of the arrays were also investigated using CV an EIS and the results presented in figure 4.3.16. In order for the face of the array to be in contact with the electrolyte solution it was clamped in a Teflon cell with an 'O' ring diameter of 14 mm (figure 4.3.16 (A)). An external Ag/AgCl RE was used for all electrochemical measurements. While the area of gold in contact with the electrolyte solution will vary from array to array and electrode to electrode, this should not limit the analytical performance of the biosensor as each electrode will be used as its own reference or baseline before analyte detection.

The platform demonstrated good reproducibility with the reduction and oxidation

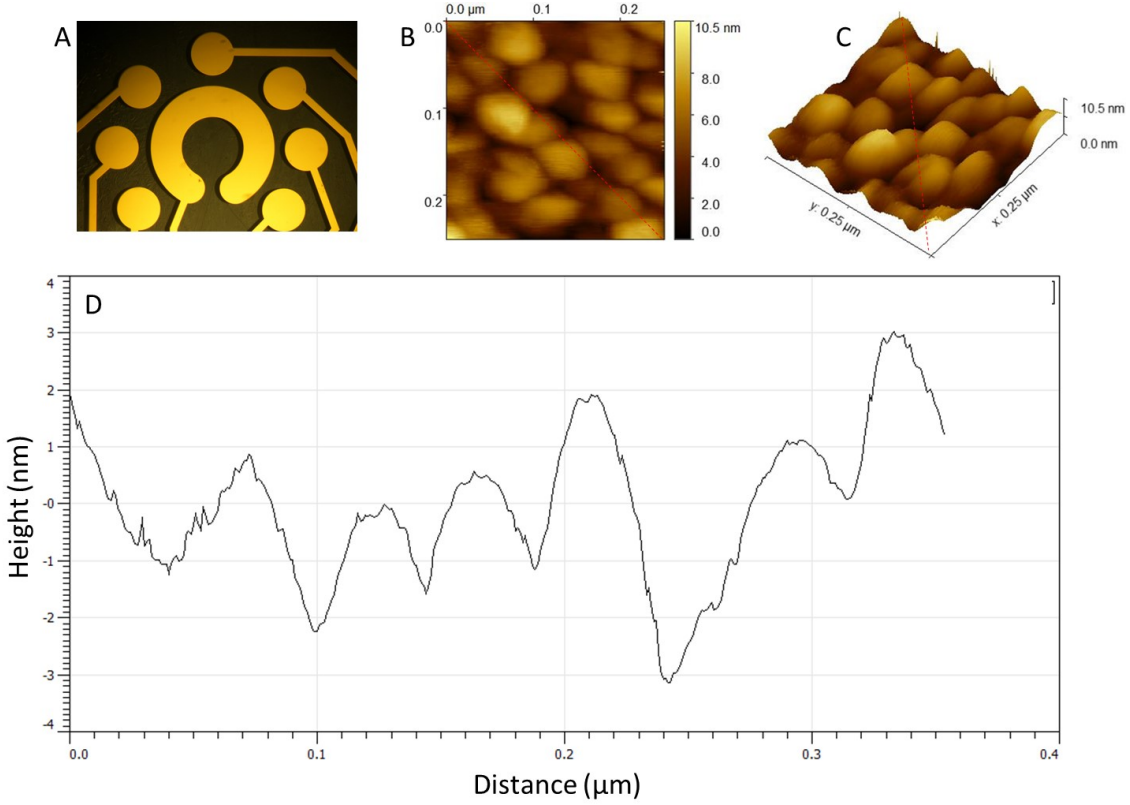

Figure 4.3.15: A) *Image taken using an optical microscope with a 10X magnification.* ***B)*** *AFM scan of a 0.25 x 0.25 µm region of WE 4 and* ***C)*** *the corresponding 3D topography.* ***D)*** *The surface texture corresponding to the diagonal profile indicated by the dotted red line in (B) and (C).*

of the redox probed occurring at 189 ± 5 and 317 ± 5 mV respectively, averaged across all 7 WEs. As seen in figure 4.3.16 (B), some of the WEs had more gold in contact with the electrolyte solution than others, this is clear by comparing WEs 1 and 7. This resulted in variations in the magnitude of the redox peaks, which can be explained by considering the Randles-Sevcik equation, which tells us that the peak current is directly proportional to the surface area of the electrode. The EIS response was also similar across all 7 WEs with a small amount of charged transfer resistance observed at high frequencies and the response then being dominated by diffusion controlled processes, which is characteristic of an unmodified electrode in a strong electrolyte solution. Furthermore, slight

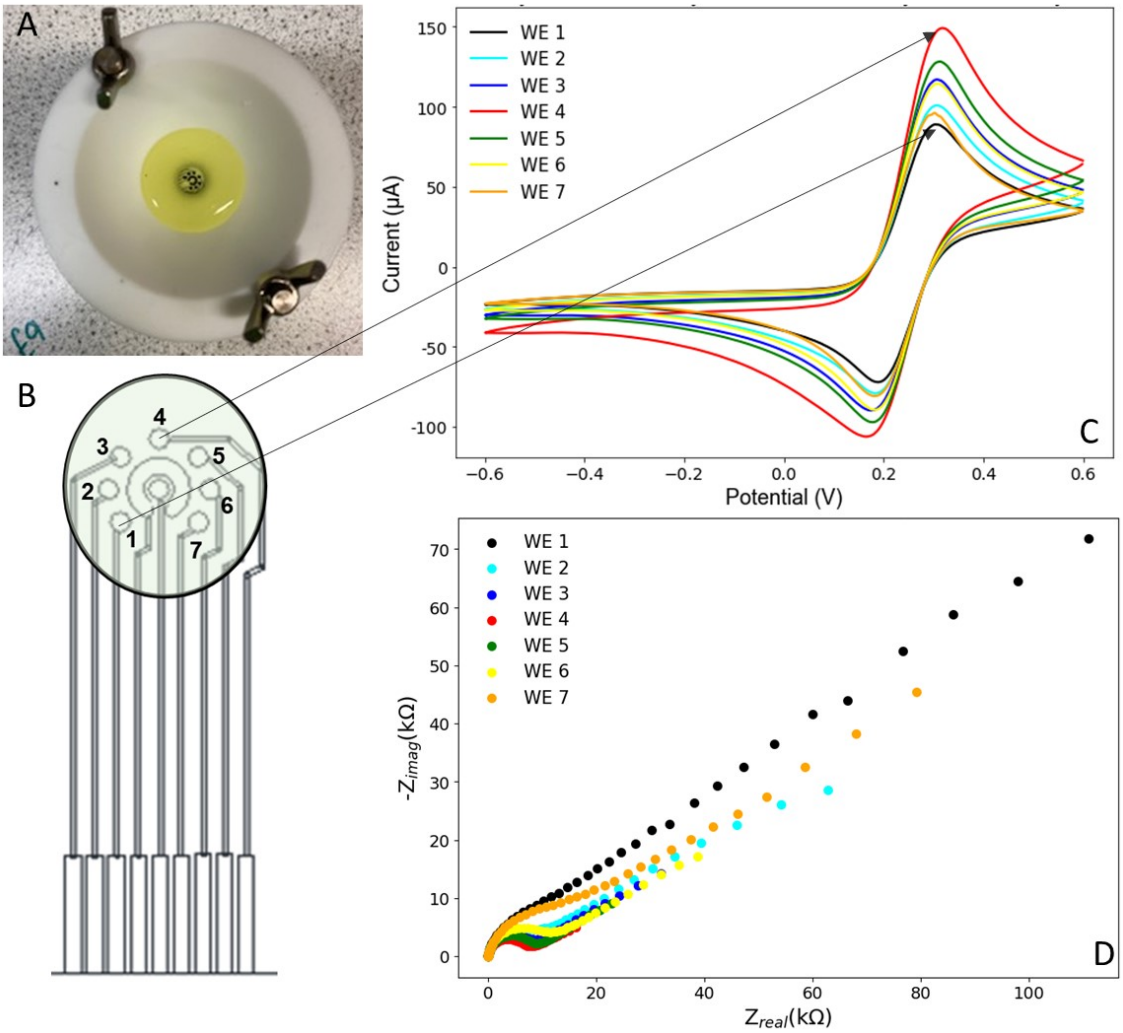

Figure 4.3.16: A) *Image from above of the face of the array clamped in the Teflon cell.* ***B)*** *Schematic of the 'O' ring with the individual WEs having different amounts of gold surface in contact with the electrolyte solution.* ***C)*** *Cyclic voltammogram and* ***D)*** *EIS of WEs 1-7 in 10 mM* $Fe(CN)_6^{-3/-4}$ *in 1 X PBS (1 M KCl). Electrode area = 0.03* cm^2.

differences between different WEs should not have a major impact on the reproducibility of the biosensing response as a baseline will be taken for each individual electrode before antigen binding is measured.

The system was further investigated using CV by varying the scan rate and also measuring the response across multiple WEs simultaneously (figure 4.3.17). As previously discussed the peak current is directly proportional to the surface area of the electrode. Therefore, it was expected that the magnitude of the redox

peaks would increase by a factor corresponding to the number of WEs switched 'ON'. This was observed when the potential was applied cross 3 and 6 WEs simultaneously, with the response increasing 3 and 6 fold as seen in figure 4.3.17 (B) and (C) respectively. The peak current was plotted against the square root of the scan rate, which showed a linear relationship (Figure 4.3.17 (D). This is the characteristic behaviour of a solution-based, pseudo first-order redox probe, which is expected for $Fe(CN)_6^{-3/-4}$.

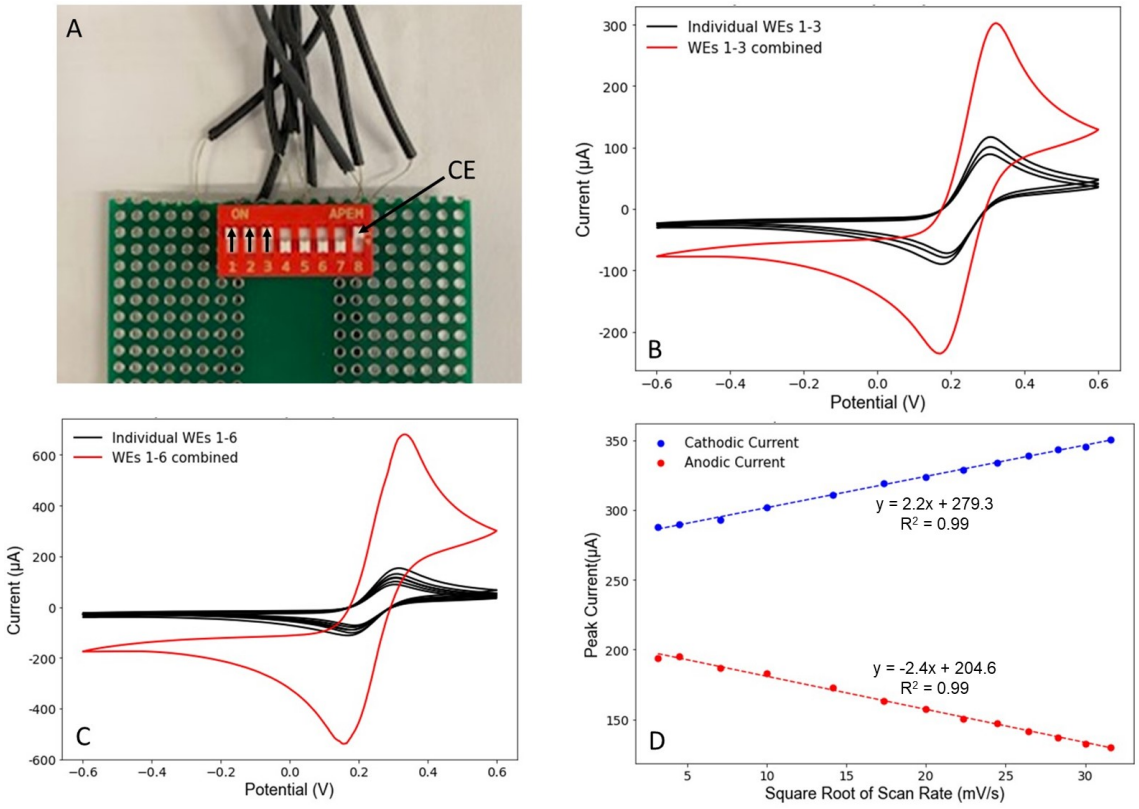

Figure 4.3.17: A) *Image of the switch box showing WEs 1-3 in the 'ON' position along with switch 8 which corresponds to the CE. Cyclic voltammograms of WEs 1-3* ***(B)*** *and WEs 1-6* ***(C)*** *compared to the individual WEs.* ***D)*** *Oxidation and reduction peak current as a function of the square root of the scan rate*

These results demonstrate that the fabricated gold arrays and associated hardware components are working as expected, showing suitable stability and reproducibility. This should allow the 4-NBDT derived film to be transferred from

the Au/Si substrates to the in house arrays.

4.3.4 Transferring the Optimised 4-NBDT Film to the Arrays

The parameters and conditions for 4-NBDT electropolymerisation which were optimised on the Au/Si substrates were conserved for the arrays. 10 mM 4-NBDT in 0.5 M H_2SO_4 was electropolymerised by holding the applied potential at -0.4 V for 25 seconds (figure 4.3.18). However, the small size of the WEs in the array meant that contact angle and ellipsometry could not be used to measure the properties of the film. Thus, only CV and EIS could be employed. Figure 4.3.18 (A) shows the current pasted during electropolymerisation. The current density on the array was over 17 times greater than that for the Au/Si substrates (44.67 $\pm$ 2.18 and 2.61 $\pm$ 0.04 mC/cm^2 respectively). Charged species in solution experience an increase in flux towards the electrode surface at higher current densities, this can result in higher electropolymerisation efficiency.

The impedance response of the film on the array followed the same trend observed on the Au/Si substrates. The response of the NO_2 surface before reduction was dominated by R_{ct} ($\approx$ 600 kΩ). After reduction the NH_2 surface had a smaller R_{ct} ($\approx$ 14.5 kΩ) and was diffusion controlled, which can be explained by considering the different charges at the interface, as discussed in section 4.3.1.4. The trend in the redox activity of the probe (figure 4.3.18) was also conserved before and after reduction. With the NO_2 surface completely suppressing the oxidation and reduction of $Fe(CN)_6{}^{-3/-4}$, after reduction the activity then increases. These results suggest that the 4-NBDT film has been successfully transferred to the array

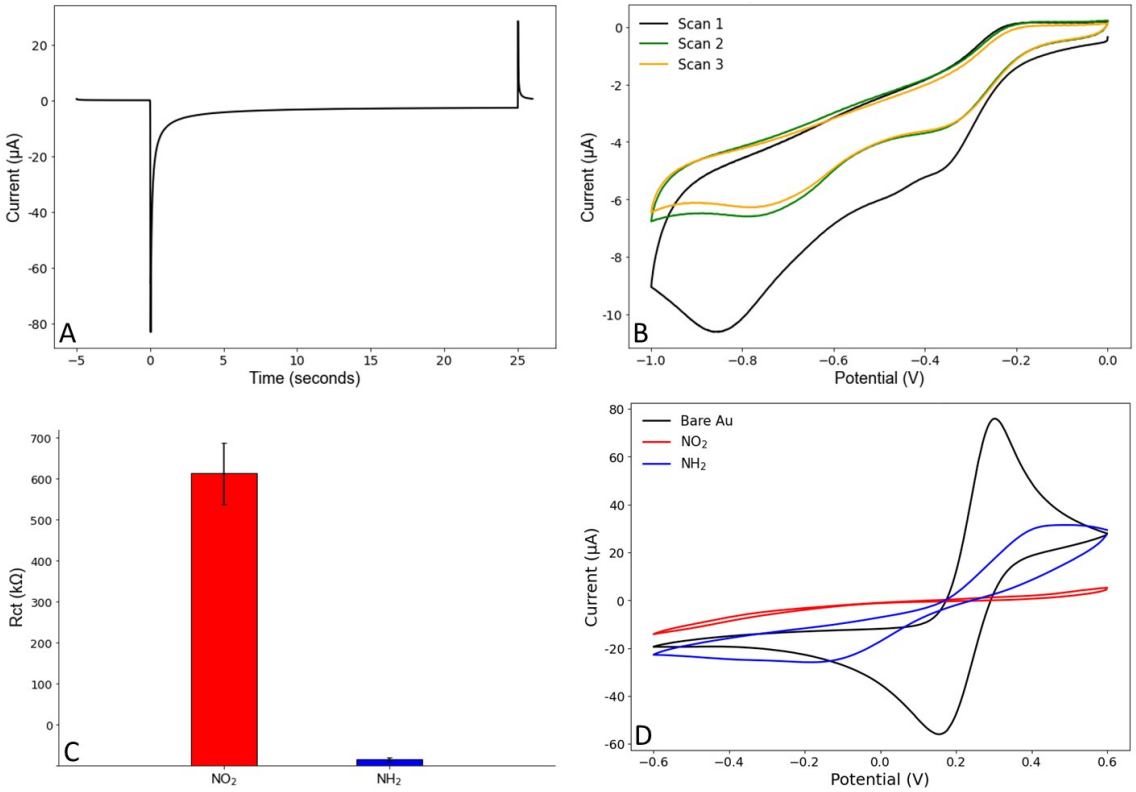

Figure 4.3.18: A) *Current past as a function of time under a potential of -0.4 V.* ***B)*** *Cyclic voltammogram of NO_2 surface in a 10% ethanol solution containing 1 M KCl.* ***C)*** *Charge transfer resistance of surface before (red) and after (blue) NO_2 reduction.* ***D)*** *Cyclic voltammetry of 10 mM $Fe(CN)_6^{-3/-4}$ in 1 X PBS (1 M KCl) on bare Au, the surface before (red) and after (blue) reduction of the NO_2 surface. Electrode area = 0.03 cm^2, n = 3.*

platform, and control over the physical and electrochemical properties has been retained. This should provide a stable and reproducible surface for investigating Nb coupling and eGFP detection.

4.4 Conclusion

The initial focus of this research chapter was to identify suitable monomer units that could be electropolymerised onto the WE surface. Monomers were selected based on the ease of film fabrication and the control over their physical and electrochemical properties. Despite being widely reported in the literature, neither pyrrole-3-carboxylic acid nor 4-carboxybenzene diazonium proved suitable for

electropolymerisation. It is possible that with more extensive optimisation procedures, such as varying the monomer concentrations, solvents, and electrode material suitable electropolymerised films could be formed. However, given that the monomer concentrations used were at the high end of those commonly reported in literature, and considering the wide range of potential cycles and times investigated, it was deemed more efficient to initially identify a monomer that showed promising potential for forming an electropolymerised film. Subsequently, the conditions could then be optimised to produce the most desirable films for the specific application.

This was the case for 4-nitrobenzenediazonium tetrafluoroborate (4-NBDT) which allowed for the fabrication of electropolymerised films in a straightforward manner. Applying a potential of -0.4 V for varying time periods allowed control over the films thickness to near nanometer precision which in turn allowed for fine tuning of the electrochemical properties of the interface. It is hoped that having control over such properties will allow the biosensing response in the final platform to also be controlled and optimised. It was decided that 25 seconds was sufficient to produce a film which offered good insulation of the electrode surface while remaining relatively thin ($\approx$ 4 nm). This should help reduce non-specific interactions with the gold surface while also keeping biorecognition elements in close spatial contact with the transducer. Through electrochemical reduction, the surface NO_2 groups could be converted to the corresponding primary amines which should allow for further bioconjugations in a controlled and stable manner.

In parallel with the electropolymerised film optimisation, gold electrode ar-

rays were also successfully fabricated. Through careful design and processing of the arrays along with the customised hardware components, the WEs could be individually or simultaneously electrically addressed. Furthermore, they could be easily integrated with preexisting potentiostats which opens the door to developing in house, custom array architectures for specific purposes moving forward. The gold surfaces were shown to be electrochemically stable and relatively flat (peak to valley roughness = 1.9 $\pm$ 0.6 nm). This allowed the optimised 4-NBDT derived film to be transferred from the Au/Si substrates to the array platform.

This new system should help overcome some of the challenges encountered in chapter 3. Namely, reducing non-specific eGFP interactions with the gold surface, allowing surface components such as NbGFP and oligopeptides to be coupled to the interface in a more controlled and robust manner, and also increasing the stability of the surface which should allow application of a wider range of electrical potentials for controlling the confirmation of oligopeptides. The next chapter focuses on NbGFP coupling to the electropolymerised films along with optimising eGFP detection.

Chapter 5. NbGFP Coupling and eGFP detection

Abstract: *This chapter involves optimisation of the functionalisation layer on gold electrodes towards covalent coupling of NbGFP and subsequent sensitive detection of eGFP. Herein, different surface activation and NbGFP coupling strategies are adapted from the literature. These different fabrication strategies are characterised using ellipsometry, cyclic voltammetry, electrochemical impedance spectroscopy, surface plasmon resonance and fluorescence microscopy. As the 4-NBDT derived film could not be successfully activated a different functionalisation layer derived from tyramine is fabricated and optimised for NbGFP coupling. Specific NbGFP-eGFP interactions are monitored using surface plasmon resonance and this system is used to optimise the eGFP detection response. Different detection methods are employed including Faradaic and non-Faradaic electrochemical impedance spectroscopy and surface plasmon resonance. The final biosensing platform is then characterised using X-ray photoelectron spectroscopy.*

5.1 Introduction

Fabricating a functionalisation layer on the WE not only serves to help reduce non-specific interactions on the gold surface, but also offers a more stable interface to covalently couple the NbGFP. This will undoubtedly increase the stability of the platform compared to directly immobilising the biomolecules to the gold surface, as investigated in chapter 3. This will also allow the orientation of the NbGFP on the surface to be controlled by carrying out site-specific coupling. This has been shown to improve the overall performance of biosensing platforms [128]. Furthermore, covalent attachment of NbGFP and oligopeptides will allow a wider range of electrical potentials to be applied across the interface which may improve the capacity of the system to switch from an 'OFF' to an 'ON' state.

When designing a covalent coupling strategy careful consideration needs to be given to the crosslinker's length, reactivity and stability. As discussed previously, the receptor component needs to be in close spatial contact with the trans-

ducer, or antigen binding will not be detectable. Therefore, excessively long surface linkages should be avoided. Non-specific and highly reactive crosslinkers can lead to poor control over receptor orientation and low reproducibility [246]. While linkages which are unstable or reversible will lead to degradation and limited shelf life. The strategy must also take into consideration which functional groups are present and available for chemical reactions on both the surface and the biomolecules of interest. However, it can still be difficult to precisely predict in advance which coupling strategy will produce the best overall response in the final biosensing platform. Therefore, different approaches and optimisation procedures should be carried out in order to gain a better understanding of the particular physical, chemical, and electrochemical properties of the system under investigation.

It is also important to not lose sight of the fact that the function of the biosensing platform is analyte detection. Therefore, during receptor coupling optimisation, the system should be continuously checked for its sensitivity to its particular target analyte, as getting the highest concentration of receptors on the surface may not result in the highest response after antigen binding [164]. Different detection methods can also be employed, as while a system may not be sensitive to measured changes in the resistive properties of the interface, the same system could be extremely sensitive to capacitive changes.

This chapter investigates different Nb coupling strategies in order to produce the highest eGFP binding response. Different strategies are adapted from the literature and Nbs with different surface modifications are employed.

5.2 Aims and Objectives

Aim 1: Investigating different bioconjugation strategies, focusing on the concentration and orientation of the Nbs on the surface will maximise the system's capacity for NbGFP-eGFP interactions.

Aim 2: Having the maximum amount of surface NbGFP-eGFP interactions will provide the best opportunity to further optimise the system to achieve the highest signal response.

Aim 3: The electropolymerised film optimised in chapter 4 may not be suitable for coupling the Nbs to produce the highest signal response following eGFP binding. Therefore, this film may need to be re-optimised or changed completely.

Aim 4: Having the optimal signal response will allow the switching capacity of the system to be investigated with the highest accuracy when oligopeptides are incorporated onto the surface in the future.

Objective 1: Covalently couple Nbs to electropolymerised films on the gold surface.

Objective 2: Compare the signal response for Nbs which have been coupled in a controlled orientation versus a random orientation.

Objective 3: Optimise the system in terms of detection method and detection conditions to produce the highest signal response.

5.3 Results and Discussion

Notes: *In order to save time, money, and materials the majority of NbGFP coupling in this chapter was carried out on commercial rod electrodes or Au/Si substrates.*

5.3.1 Comparing Different NbGFP Coupling Strategies.

With the aim to investigate NbGFP conjugation, the 4-NBDT derived film which was optimised in section 4.3.1.4 was transferred to the commercial rod electrodes. However, the electropolymerisation time needed to be increased from 25 to 50 seconds in order for the NO_2 terminated film to completely suppress the redox activity of $Fe(CN)_6^{-3/-4}$ (figure 5.3.1). This was likely due to the increased surface roughness of the rod electrodes compared to the gold arrays or Au/Si substrates. After reduction of the NO_2 surface, the electrochemical properties followed the same trend as observed on the Au/Si substrates and gold arrays. This suggests a successful transfer of the electropolymerised film.

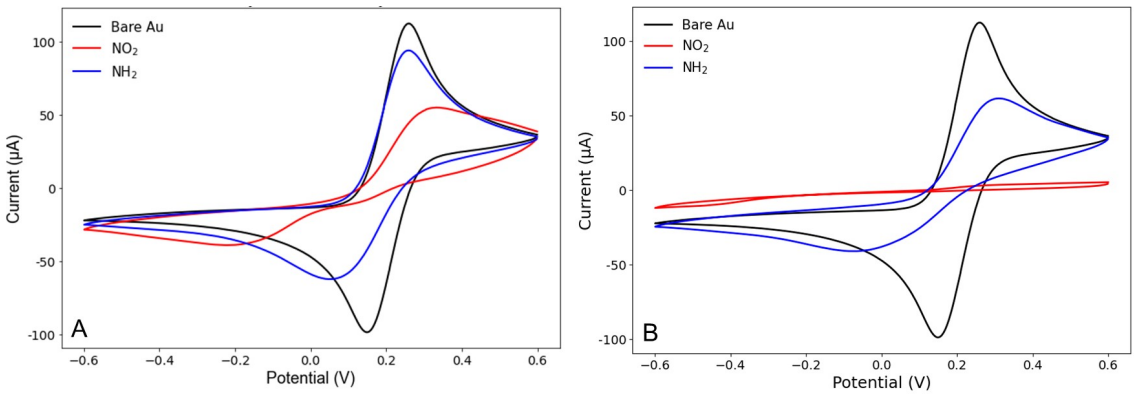

Figure 5.3.1: *Cyclic voltammogram of the redox activity of 10 mM $Fe(CN)_6^{-3/-4}$ in 1 X PBS (1 M KCl) on the bare Au surface (black) the NO_2 surface (red) and NH_2 surface (blue) after **(A)** 25 seconds electropolymerisation time and **(B)** 50 seconds electropolymerisation time. Working electrode area = 0.03 cm^2.*

Three distinct coupling strategies were taken from the literature (figure 5.3.2). Strategy 1, used N,N′-Disuccinimidyl carbonate (DSC) in Dimethylformamide (DMF), which allowed for a simple two step coupling strategy [122]. Nucleophilic attack of the lone pair of electrons on the surface NH_2 groups with the carbonyl carbon of DSC forms a succinimide ester (activated surface). This then allows any free lysine residues on the NbGFP to couple to the surface via carbamide formation. This method of coupling results in a extremely small linkage between the NbGFP and the underlying film, which is often called a 'zero length linkage'.

Strategy 2, is again non-site specific, meaning the NbGFP will have a random orientation on the surface. However, this method involves nucleophilic attack of the surface amine to one of the carbonyl carbons of succinic anhydride (SA) in DMF [247]. This results in a ring opening reaction exposing a terminal carboxylic acid functionality (figure 5.3.2, strategy 2). This can then be activated using NHS/EDC chemistry and coupled to any free lysine residue on the NbGFP. The 1,4-diamide linkage formed using this method may offer increased stability compared to the carbamide linkage formed using DSC.

Strategy 3, is site-specific and takes advantage of the His_6-tag (6 histidine residues) which comes coupled to the C-terminal of the Nb from the manufacturer (Chromotek). Divinyl sulfone (DVS) with triphenylphosphine (catalyst) in acetonitrile (ACN), was used to activate the surface via a hydroamination reaction [128]. The imidazole groups in the His_6-tag should preferentially react with the alkene residue over any free lysine groups, which should result in the NbGFP having a

controlled orientation on the surface.

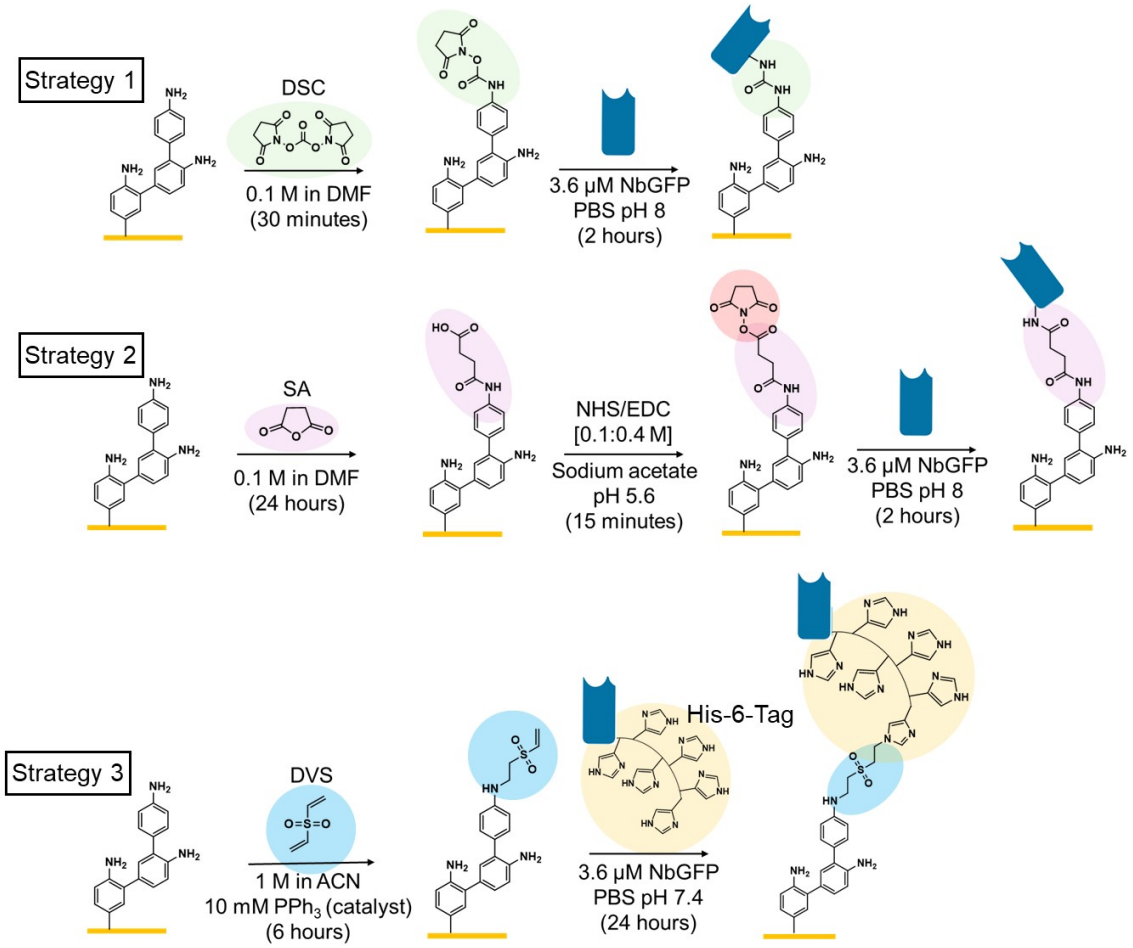

Figure 5.3.2: *Reaction schemes of the three different coupling strategies taken from the literature. The 6 histidines have been represented by their reactive imidazole residues in strategy 3 for simplicity. Not drawn to scale.*

DSC coupling (strategy 1) was investigated first, and initially monitored using CV and EIS. Three experiments were set up, which included a positive control where the DSC was present in the DMF, a control where just DMF (no DSC) was incubated on the surface, and another control where the surface was left unchanged after electrochemical reduction (figure 5.3.3).

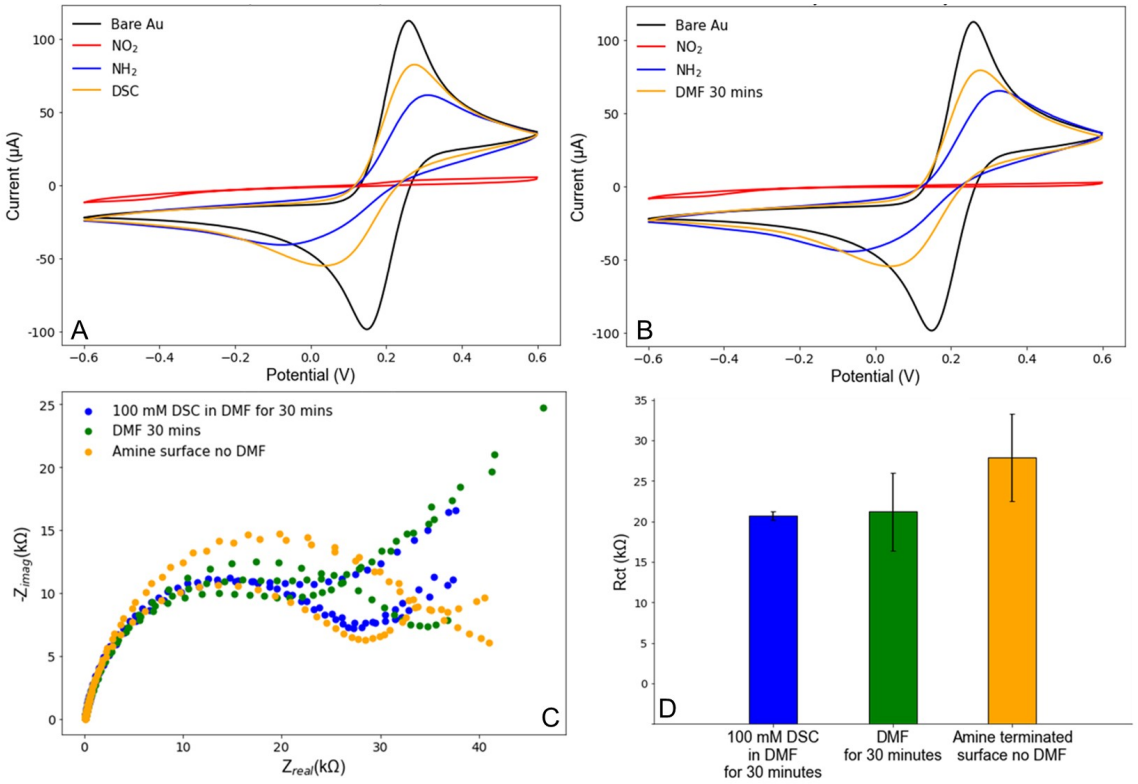

Figure 5.3.3: *Cyclic voltammetry of the redox activity of 10 mM* $Fe(CN)_6^{-3/-4}$ *in 1 X PBS (1 M KCl) after a 30 minute incubation of DSC in DMF* ***(A)*** *and only DMF* ***(B)****. The Nyquist plot of the corresponding surfaces after NbGFP incubation for 2 hours in PBS (pH 8)* ***(C)*** *and the corresponding* R_{ct} *values* ***(D)****. Electrode area = 0.03* cm^2*, n = 3.*

As seen in figure 5.3.3 (A) and (B), it seems the CV response after incubation is due to the presence of the DMF solvent and not due to DSC activation. This was confirmed using EIS (figure 5.3.3 (C) and (D)) which showed that after NbGFP incubation the R_{ct} response was the same regardless if DSC was used. Therefore, from these results it is unclear if DSC is activating the surface at all or if any Nbs are being covalently attached.

If the Nbs are non-covalently interacting with the surface they may be easily removed after overnight incubation in PBS. This was investigated using EIS, and the R_{ct} values are reported in figure 5.3.4 (A). NbGFP was incubated on the surface which had been exposed to DMF for 30 minutes (DSC was not used). The measure R_{ct} was $\approx$ 20 kΩ which remained unchanged after over incubation

in PBS followed by rinsing with copious amounts of PBS. This suggests that the NbGFP is relatively stable on the surface.

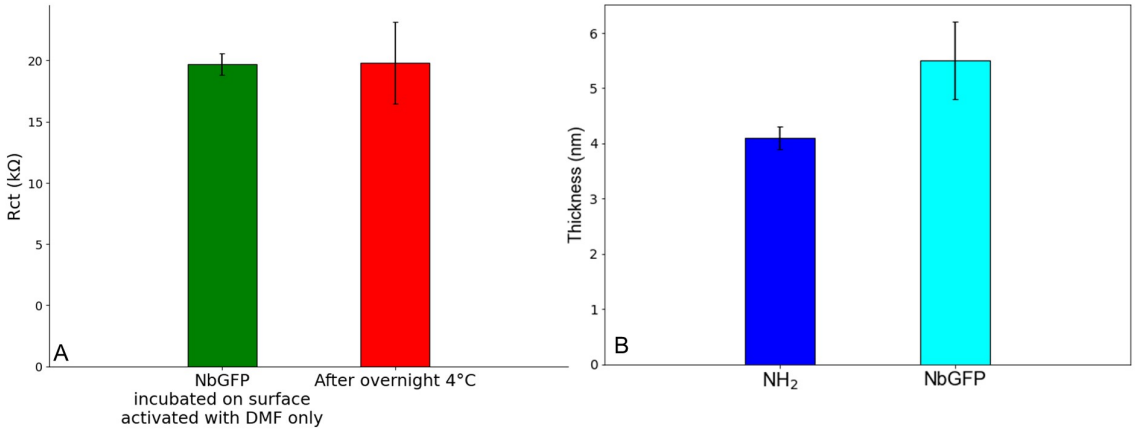

Figure 5.3.4: A) *The R_{ct} after NbGFP incubation the NH_2 terminated surface which was exposed to DMF without DSC (green) and after incubation in PBS overnight at 4°C (red).* ***B)****The ellipsometry thickness of the NH_2 surface and after NbGFP incubation. The electrode area for the ellipsometry experiments = 0.2 cm^2 and for the EIS experiments = 0.03 cm^2, n = 3.*

The thickness of the NbGFP on the surface was also measured using ellipsometry (figure 5.3.4 (B)), which gave a Nb thickness of $\approx$ 1.5 nm. This is significantly smaller than the measured thickness of the NbGFP on the bare Au surface $\approx$ 3.7 nm. A possible explanation for this is that the NbGFP is diffusing/embedding itself into the 4-NBDT derived film and/or the increased surface of the diazonium derived film on the surface. This would account for the reduction in the ellipsometry thickness and the stability of the NbGFP on the surface. However, it could also be the case that the DSC is still activating the surface but this change is not detectable. As the NbGFP seems to be relatively stable on the surface, the systems sensitivity towards eGFP and further control experiments were carried out.

First, to ensure NbGFP was definitely on the surface and the measured changes in the R_{ct} where not due to solvent effects, PBS control experiments were carried out. NbGFP was incubated in PBS (pH 8) for two hours on the DSC

activated surface. The control experiment consisted of incubating PBS (pH 8) on the surface for 2 hours without any Nbs present (figure 5.3.5).

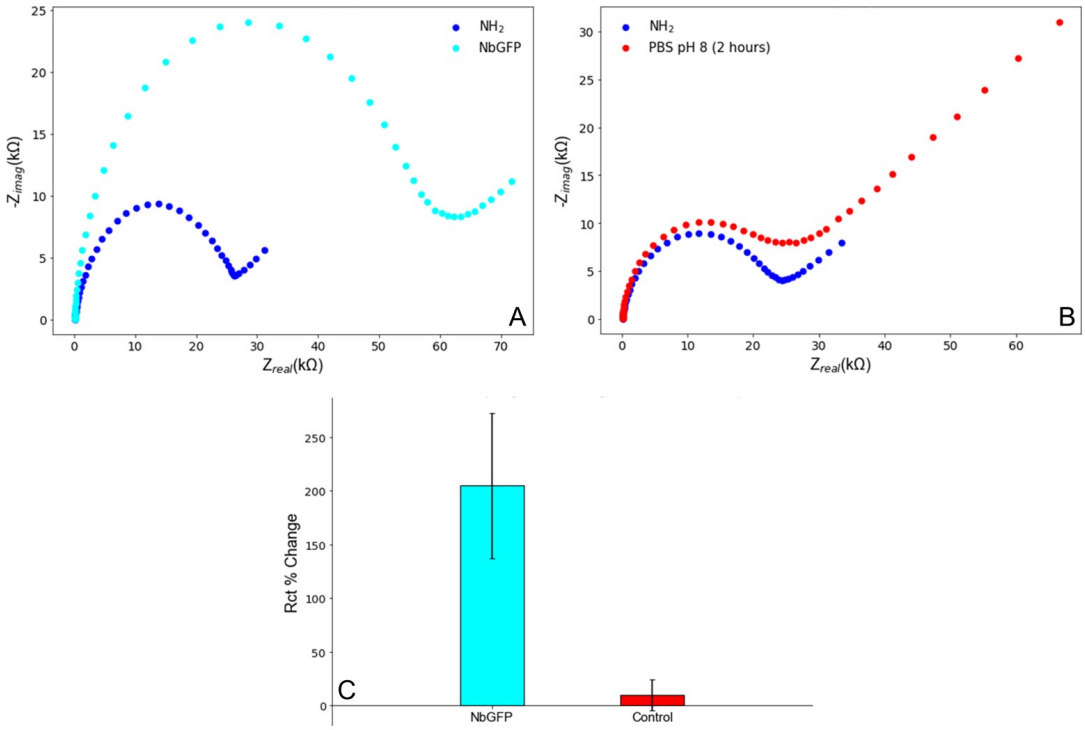

Figure 5.3.5: *Nyquist plots showing EIS response in 10 mM Fe(CN)$_6^{-3/-4}$ in 1 X PBS (1 M KCl) after NbGFP incubation* ***(A)*** *and incubation with only PBS* ***(B)****.* ***(C)*** *The corresponding R_{ct} values for both experiments. Working electrode area = 0.03 cm^2, n = 3.*

When NbGFP was present in the PBS solution the R_{ct} increased by $\approx$ 200%, when just PBS was incubated the response essentially remained the same. These results confirm that the change in R_{ct} is due to the presence of NbGFP on the surface.

Next, three different concentrations of NbGFP was used and the EIS response after eGFP incubation was investigated. Before eGFP was incubated the surfaces were stabilised in PBS over night and then continuously washed and measured until a stable EIS baseline was achieved. 14 μg/mL eGFP in PBS was then incubated on the surface for 30 minutes with gentle agitation every 5 minutes. The surface was then rinsed with PBS to remove any non-specifically bound

eGFP before being measured (figure 5.3.6).

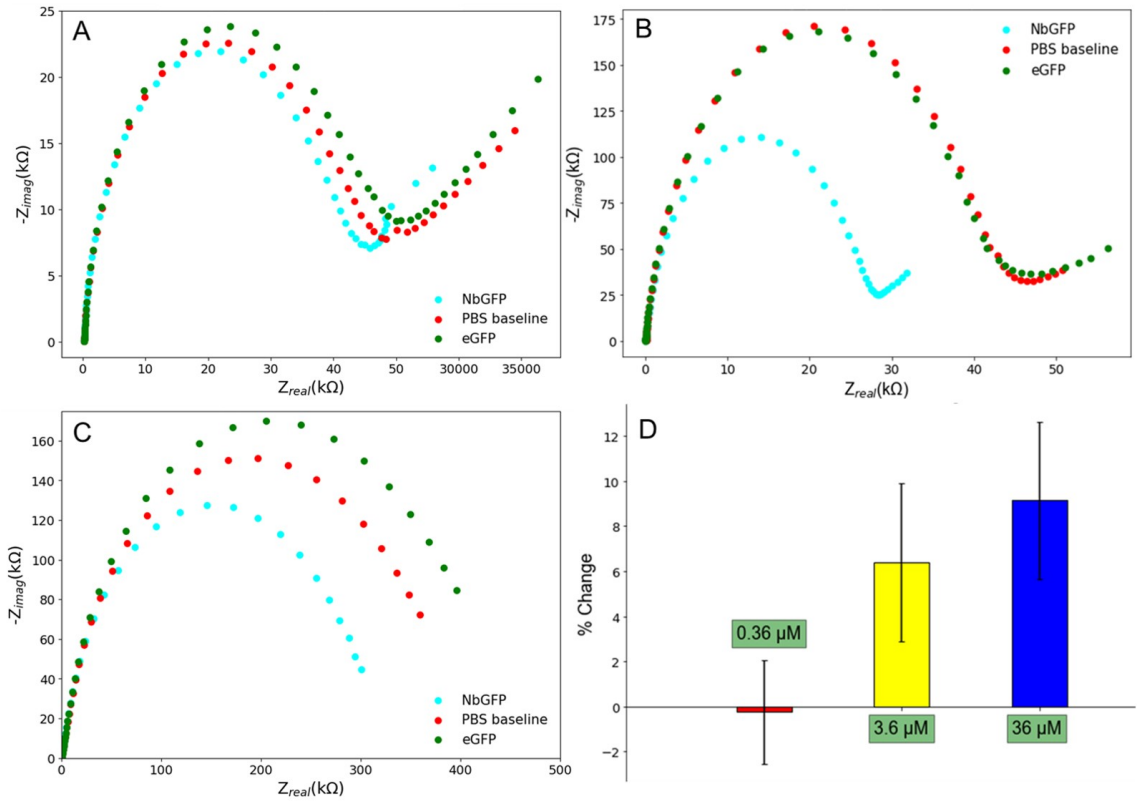

Figure 5.3.6: *Nyquist plot of EIS response in 10 mM $Fe(CN)_6^{-3/-4}$ in 1 X PBS (1 M KCl) of eGFP binding for different NbGFP concentrations,* ***(A)*** *= 0.36 μM,* ***(B)*** *= 3.6 μM,* ***(C)*** *= 36 μM.* ***(D)*** *The corresponding R_{ct} values for the three experiments. Working electrode area = 0.03 cm^2, n = 3.*

The Nyquist plots in figure 5.3.6 show that increasing the NbGFP concentration results in a increase in R_{ct}, further indicating that they are on the surface. Furthermore, there was a positive correlation between increasing the concentration of NbGFP on the surface and the EIS signal response after eGFP incubation (figure 5.3.6 (D)). However, the maximum R_{ct} percentage change after using 36 μM NbGFP was only around 9-10%. This is relatively small and would likely be unsuitable for monitoring the switching capacity of the NbGFP-C8K system in the future. There is also significant variation which could be due to heterogeneous nature of the underlying diazonium derived films.

One potential problem may be that during the electrochemical reduction of the NO_2 groups, only those in close proximity to the gold surface are actually being reduced. This would leave many of the NO_2 groups at the surface-solution interface unconverted and therefore, not capable of being activated using DSC (figure 5.3.7). This hypothesis is supported by some literature reports, in particular, Richard et al. (2018) suggested that the conversion of the NO_2 to NH_2 was limited by the charge transfer process into the organic film, rather than proton availability [237]. As a consequence, the first NO_2 groups to be converted are those located close to the electrode surface.

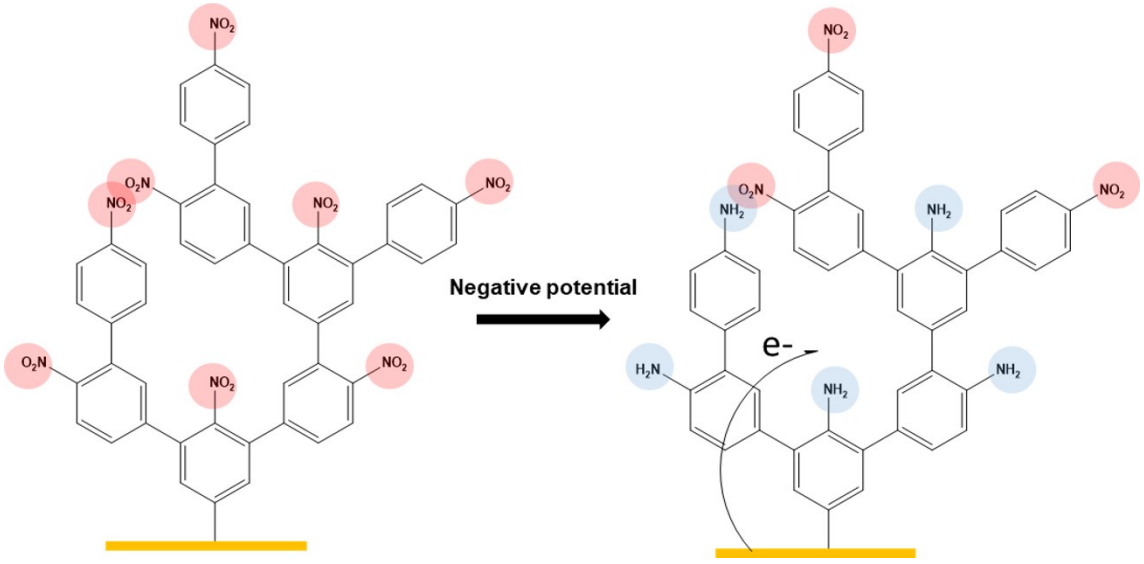

Figure 5.3.7: *Schematic showing only the NO_2 groups close to the electrode surface converted to the corresponding NH_2 groups.*

To overcome this, instead of scanning the potential back and forth to reduce the nitro groups, the potential was held at -0.85 V for different time periods. The change in R_{ct} was then measured after NbGFP coupling and eGFP detection respectively. For these experiments the in-house arrays were used, as the final system would need to be optimised on the arrays either way. furthermore, their planar geometry allowed fluorescent microscopy to be employed to detect the presence of eGFP

on the surface (figure 5.3.8).

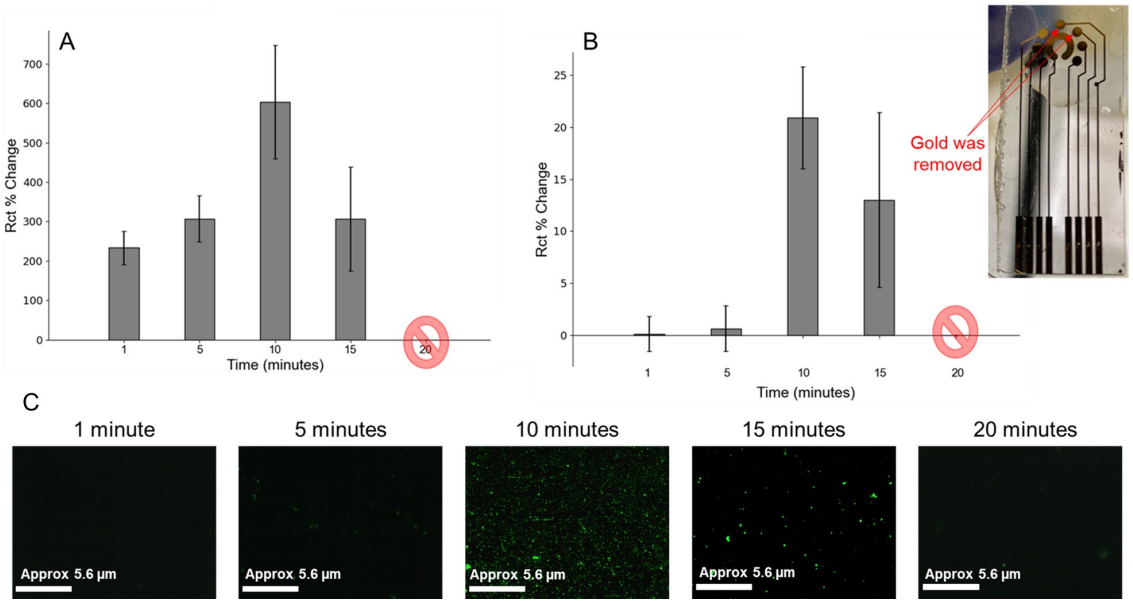

Figure 5.3.8: *Percentage change in the R_{ct} values of NbGFP coupling* ***(A)*** *and eGFP detection* ***(B)*** *as a function of NO_2 reduction time. Measured with EIS using 10 mM $Fe(CN)_6^{-3/-4}$ in 1 X PBS (1 M KCl).* ***(C)*** *Fluorescent microscopy images after eGFP incubation as a function of NO_2 reduction time. The Working electrode area = 0.03 cm^2, n = 3.*

These results seem to back up the claim that the limiting factor in NO_2 reduction is the charge transfer process through the organic film. Applying the potential for longer time periods gives NO_2 groups further away from the electrode a chance to be reduced. 10 minutes of NO_2 reduction produced the highest NbGFP coupling response along with the highest eGFP detection response $\approx$ 20%. This is backed up by the fluorescent microscopy images in figure 5.3.8 (C). This is compared to around 9% when they were reduced by scanning the potential between 0 and -1 V for 3 cycles. However, holding the potential at -0.85 V for longer than 10 minutes had a negative impact on NbGFP binding and subsequent eGFP detection. Furthermore, at 20 minutes no EIS measurement could be made on the electrodes indicating the system had been damage. Upon close visual inspection it was clear that gold was being removed from the surface after holding the potential for this

long (figure 5.3.8). Therefore, 10 minutes was selected as the most appropriate NO_2 reduction time. It should be noted that these results don't necessarily mean that the NbGFP is being covalently coupled to the surface. The increased conversion of NO_2 groups to NH_2 could be allowing the Nbs to more easily diffuse and embed themselves into the film as previously discussed.

Fluorescent control studies were carried to understand if eGFP was interacting with the NbGFP (regardless of whether or not it was covalently attached to the surface) or non-specifically with the surface (figure 5.3.9).

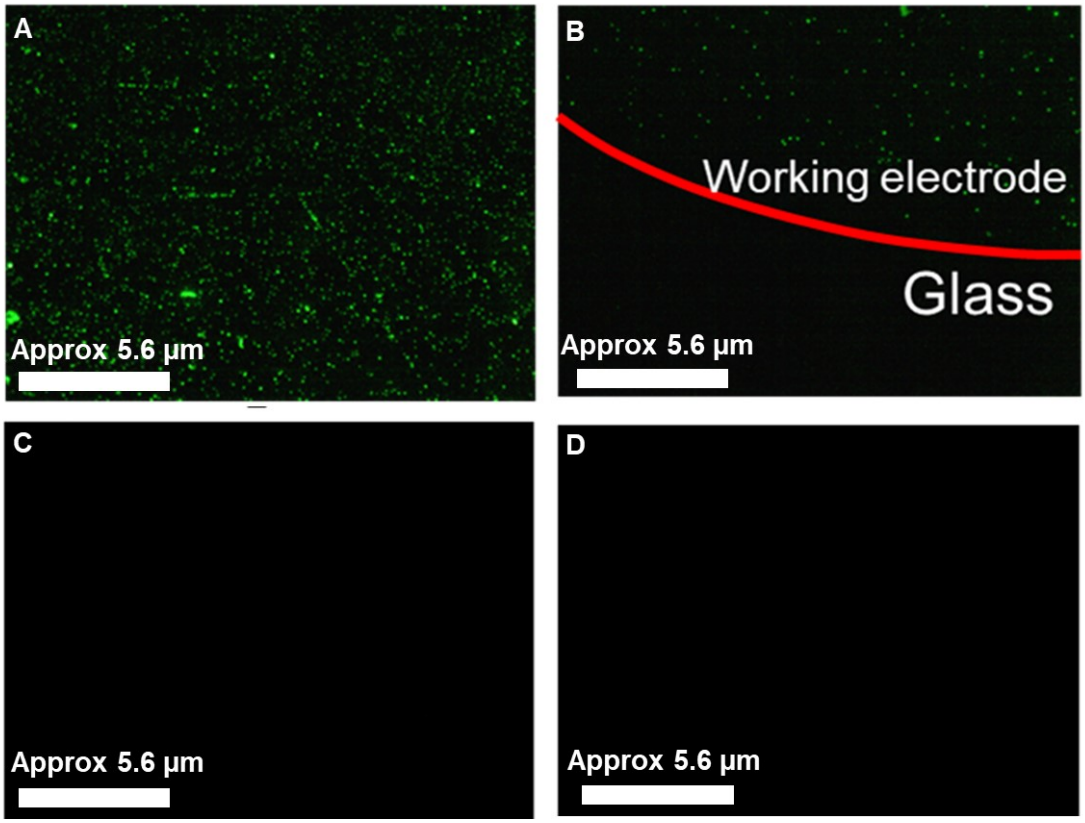

Figure 5.3.9: *Fluorescent microscopy images after eGFP incubation on* ***(A)*** *NbGFP coupled to the surface using DSC.* ***(B)*** *Showing the boundary of the WE and the underlying glass substrate.* ***(C)*** *eGFP incubation on the NO_2 terminated film and* ***(D)*** *eGFP incubation on the NH_2 terminated surface.*

From the fluorescent control studies it seems that the eGFP interacts predominately with the surface only when NbGFP is present. This suggests that regard-

less of whether the NbGFP is covalently attached to the surface as expected from coupling strategy 1, or non-specifically embedded in the film itself, the binding sites are still available to interact with the eGFP in the surrounding environment.

Since the maximum eGFP detection response using EIS was only ≈ 20%, it was decided to investigate incubating the NbGFP and eGFP on the surface for longer time periods in order to improve the response. First the eGFP was incubated on the surface for 1 hour rather than 30 minutes (5.3.10). However, this did not increase the change in R_{ct}.

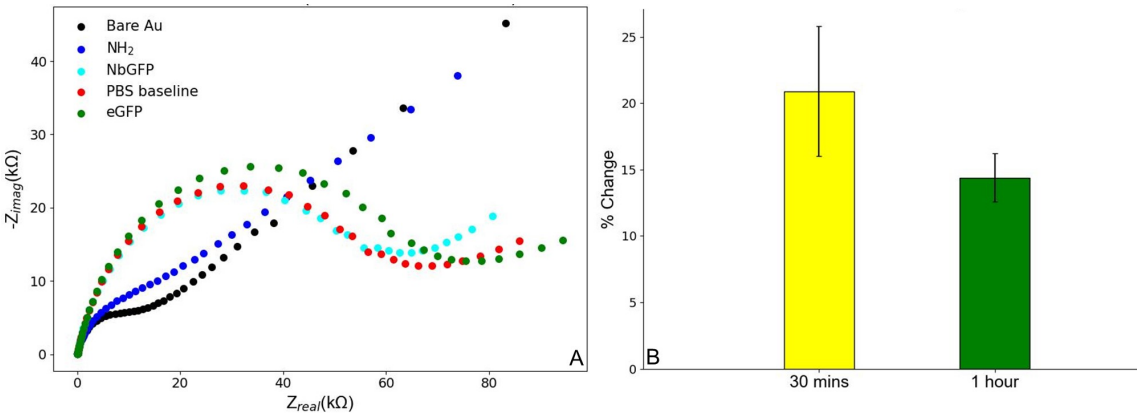

Figure 5.3.10: ***(A)*** *Nyquist plots of each stage of sensor fabrication including 1 hour eGFP incubation, measured using EIS in 10 mM* $Fe(CN)_6^{-3/-4}$ *in 1 X PBS (1 M KCl).* ***(B)*** *The* R_{ct} *percentage change for eGFP detection after a 30 minute and 1 hour incubation. Working electrode area = 0.03* cm^2*, n = 3.*

The NbGFP was also incubated on the surface for 24 hours at pH 7.3, as this should allow the Nbs to bind to the surface under physiological pH conditions for the maximum amount of time that is reasonable for biosensor fabrication. However, again this did not improve the eGFP detection response (figure 5.3.11).

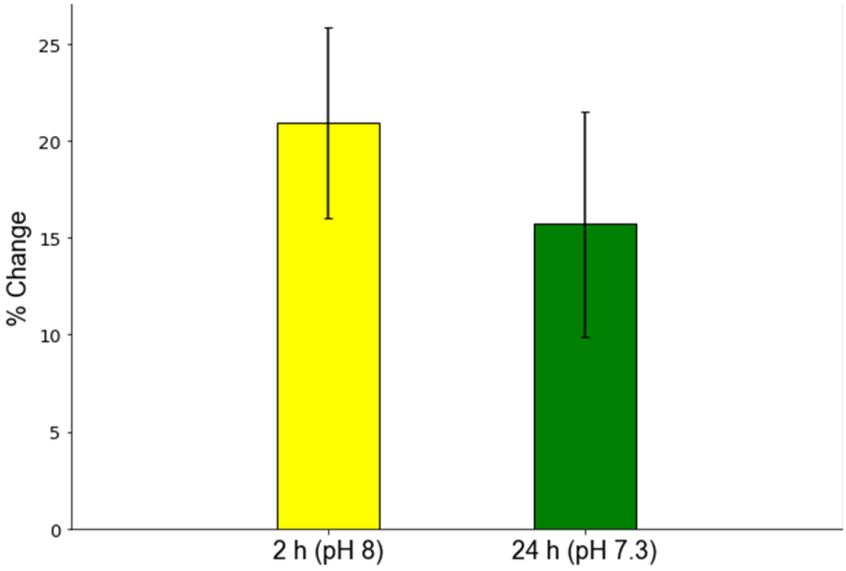

Figure 5.3.11: *eGFP detection after NbGFP incubation for 2 hours at pH 8 (yellow) and 24 hour at pH 7.3 (green). Working electrode area = 0.03 cm^2, n = 3.*

At this point it was decided to investigate NbGFP coupling strategies 2 and 3, to see if an improvement in the eGFP detection response could be obtained. The optimised 10 minute NO_2 reduction time was retained and the surfaces were functionalised according to the schemes outline in figure 5.3.2. Again 14 μg/mL eGFP in 1 X PBS was incubated on the surface for 30 minutes with gentle aspiration every 5 minutes. Each step of surface modification for the SA and DVS coupling strategies were monitored using EIS, and the corresponding eGFP detection responses were compared with the DSC coupling strategy (figure 5.3.12).

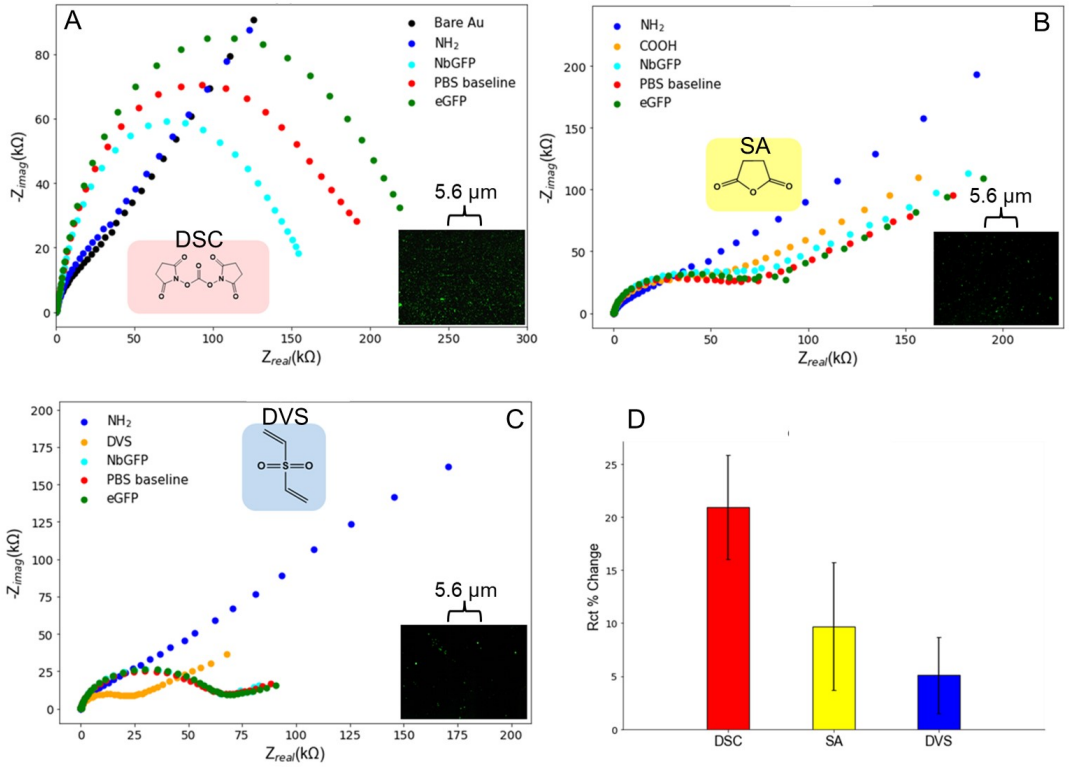

Figure 5.3.12: *Nyquist plots of NbGFP coupling monitored using EIS in 10 mM* $Fe(CN)_6^{-3/-4}$ *in 1 X PBS (1 M KCl).* ***(A)*** *Coupling strategy 1, using DSC.* ***(B)*** *Coupling strategy 2 using SA.* ***(C)*** *Coupling strategy 3, using DVS.* ***(C)*** *The corresponding eGFP detection responses for each coupling strategy. Working electrode area = 0.03* cm^2*, n = 3.*

Unfortunately, eGFP detection using coupling strategies 2 and 3 dropped to ≈ 10 and ≈ 5% respectively (figure 5.3.12 (D)). These percentage changes in the R_{ct} would again be too low and too similar to the natural baseline variation (≈ 5-10%) to accurately measure the switching capacity of the platform when oligopeptides are incorporated into the system. Before any further optimisation was carried out to improve the eGFP signal response, it was decided to investigate eGFP binding for each NbGFP coupling strategy using SPR.

For each coupling strategy 4 experiments were carefully designed to concluded if the surface was being activated by any of the three methods. The 4-NBDT derived films were fabricated on gold SPR substrates and the nitro groups

were reduced to the corresponding primary amines by holding the reduction potential at -0.85 V for 10 minutes. Due to the use of organic solvents the biosensor fabrication steps had to be be done outside of the SPR equipment. Only eGFP binding could be carried out inside the SPR's flow cell. For each coupling strategy eGFP was injected onto 4 different surfaces: The positive control was the surface with all fabrication steps fully carried out, as described in figure 5.3.2. The second control was eGFP injection onto the surfaces which had no NbGFP in the PBS incubation solution (all other steps remained the same). The third control was eGFP injection onto the surface which had no coupling reagent (DSC, SA, DVS) in the organic solvent (DMF or ACN) during the activation step (all other steps remained the same). Finally, the forth control was eGFP injection onto the unmodified NH_2 terminated surfaces (figure 5.3.13).

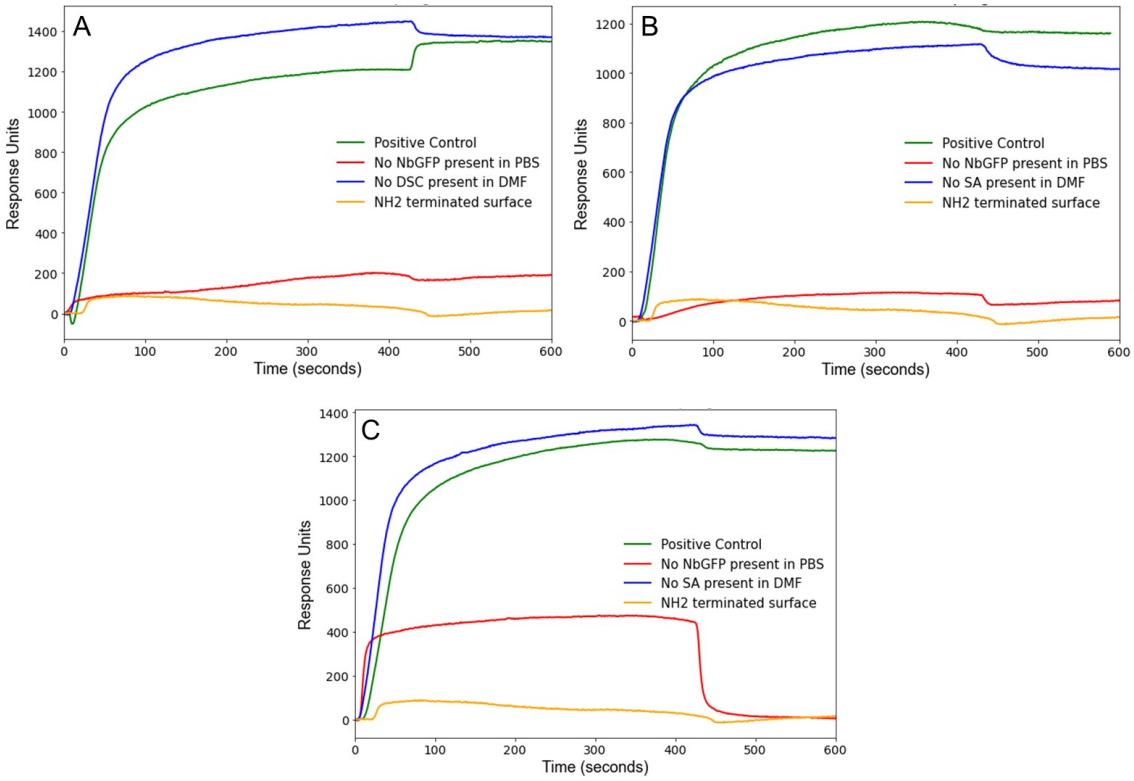

Figure 5.3.13: *SPR traces for eGFP binding on control surfaces for* ***(A)*** *DSC,* ***(B)*** *SA, and* ***(C)*** *DVS coupling strategies.*

The results shown in figure 5.3.13 show an interesting trend between the controls for all three NbGFP coupling strategies. eGFP does not significantly interact with any of the surfaces when NbGFP has been excluded or the NH_2 surfaces have be unmodified (RU < 200 RU). eGFP binding is essentially the same for the positive controls and when the coupling reagents have be excluded. This confirms that the presence of the coupling reagents (DSC, SA, and DVS) are not having a significant impact on the eGFP binding response. This further backs up the original hypothesis that the majority of NbGFP interactions at the surface are non-specific. A possible explanation for the lack or limited surface activation may lie with the properties of the surface amines themselves. Unlike some of the literature reports the coupling strategies were based off, these surfaces contain aromatic amines. The nucleophilicity of aromatic amines is weaker compared to equivalent aliphatic amines (figure 5.3.14). This is because the amine can donate its electron density to the aromatic ring. This allows the formation of stable resonance structures which results in the lone pair of electrons on the nitrogen being less likely to react [248]. Furthermore, due to the ortho substitutions resulting from the free radical polymerisation process, the steric hindrance around some of the surface amines may also be limiting their nucleophilicity (figure 5.3.14 (B)).

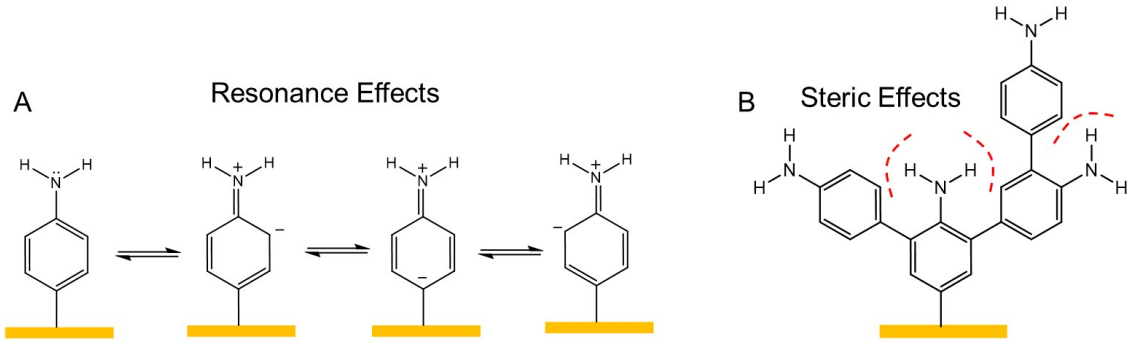

Figure 5.3.14: *Resonance stability **(A)** and steric effects **(B)** on the nucleophilicity of 4-NBDT derived films.*

Given this, is was decided to compare the primary aromatic amines of the 4-NBDT derived films with primary aliphatic amines of tyramine derived films.

5.3.2 Electropolymerisation of Tyramine

Tyramine (4-(2-aminoethyl)phenol) is a naturally occurring amine which is derived from the amino acid tyrosine. It has been used extensively for surface modifications and electrochemical biosensor development [249, 250]. A non-conductive, tyramine derived polymer (Ptyr) can be formed by anodic electropolymerisation [91, 251]. Tyramine's structure and an electropolymerisation mechanism can be seen in figure 5.3.15 [252].

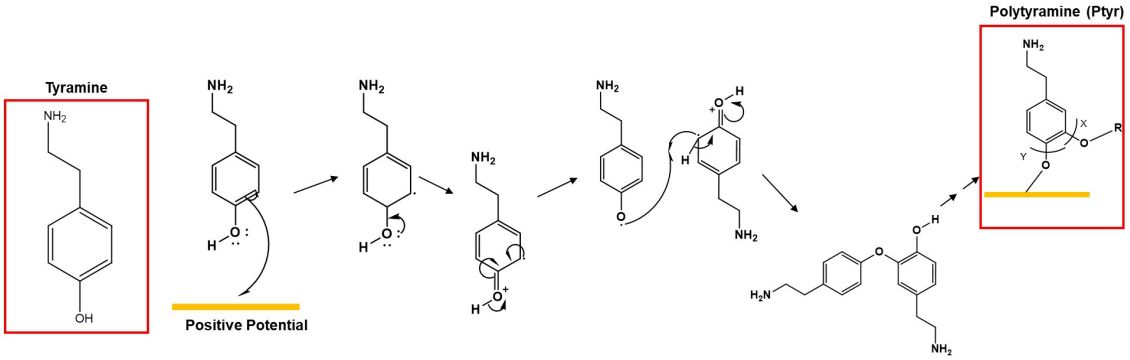

Figure 5.3.15: *Electropolymerisation mechanism of tyramine taken from Ref [252].*

The primary amine in tyramine is separated from the aromatic ring by a two carbon chain and electropolymerisation proceeds in the para position to the amine sub-

stituent. This should cause the lone pair of electrons on the nitrogen to be more nucleophilic compared to the 4-NBDT derived films (as discussed in section 5.3.1). Another benefit of using tyramine as a monomer is that once electropolymerised the amines are already present. There is no need for any further modifications, the amines can be activated straight away and subsequent coupling of biomolecules can be carried out. This removes a biosensor fabrication step, simplifying the overall process.

As with the monomers discussed in section 4.3.1, the Ptyr film on the surface needed to be optimised in terms of its physical and electrochemical properties. 25 mM tyramine was dissolved in a 300 mM NaOH methanol solution and poured into the electrochemical cell. The potential was scanned from 0 to 1.6 V at 100 mV/s to investigate the tyramine oxidation potential (figure 5.3.16).

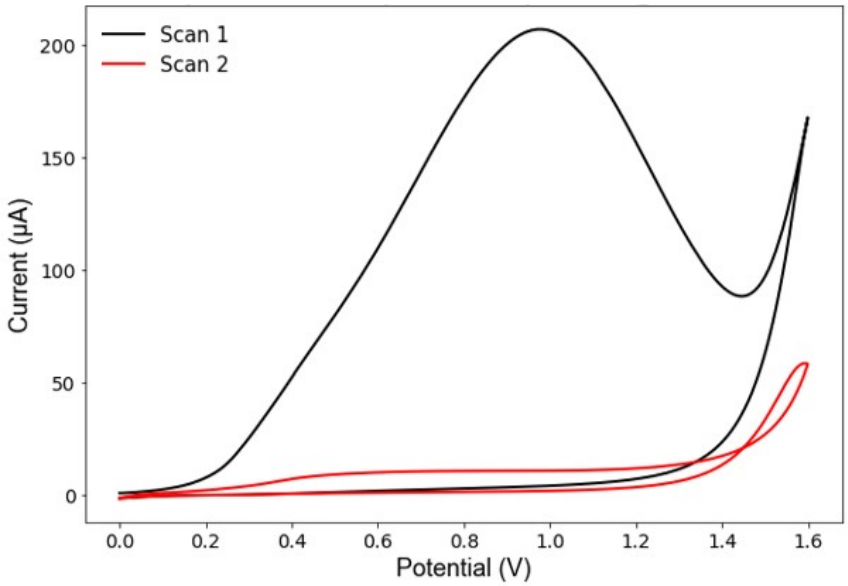

Figure 5.3.16: *Cyclic voltammogram of 25 mM tyramine in a 300 mM NaOH methanol solution, scan rate = 100 mV/s.*

A broad reduction peak was observed just below 1 V which disappeared on subsequent scans. The Ptyr film growth should be self limiting due to the limited

charge transfer through the non-conducting film [252]. Two scans was enough to completely suppress the redox activity of $Fe(CN)_6^{-3/-4}$ when the surface was investigated with CV (figure 5.3.17 (A)). The R_{ct} values showed significant variation (76.4 ± 16.7 kΩ) between different electrodes (figure 5.3.17 (B)). This is likely due to increased surface roughness of the commercial rod electrodes coupled with the heterogeneous nature of the Ptyr surface.

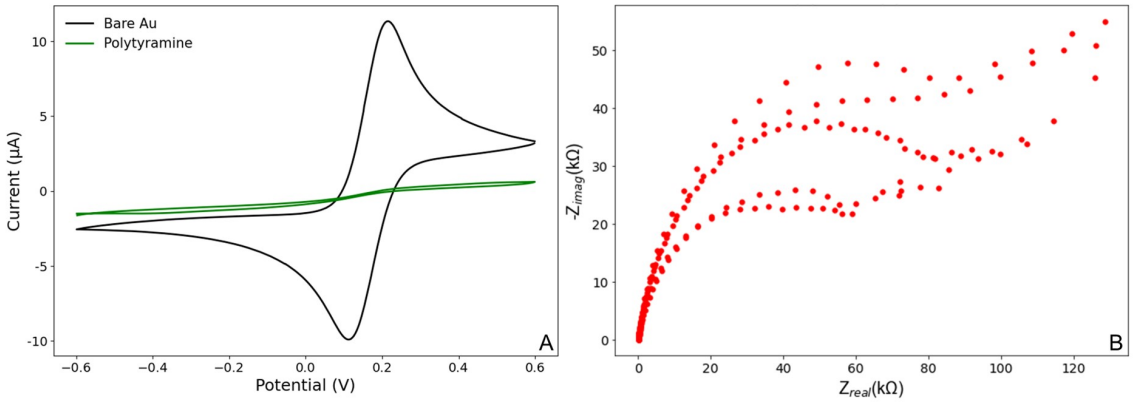

Figure 5.3.17: ***(A)*** *Cyclic voltammogram of 10 mM $Fe(CN)_6^{-3/-4}$ in 1 X PBS (1 M KCl) on the bare Au surface (black) and the Ptyr film (green).* ***(B)*** *Nyquist plot showing EIS response of 10 mM $Fe(CN)_6^{-3/-4}$ in 1 X PBS (1 M KCl) on Ptyr surfaces across 6 different electrodes. Working electrode area = 0.03 cm^2, n = 6.*

The thickness of the film measured using ellipsometry was 5.4 ± 0.3 nm which was similar to the optimised thickness of the 4-NBDT derived film (4.1 ± 0.3 nm). Therefore it was decided to compare the surface activation and NbGFP coupling with the 4-NBDT derived surface using coupling strategy 1 from section 5.3.1. This will allow comparison of two films one with a primary aromatic amine and the other with a primary aliphatic amine (figure 5.3.18).

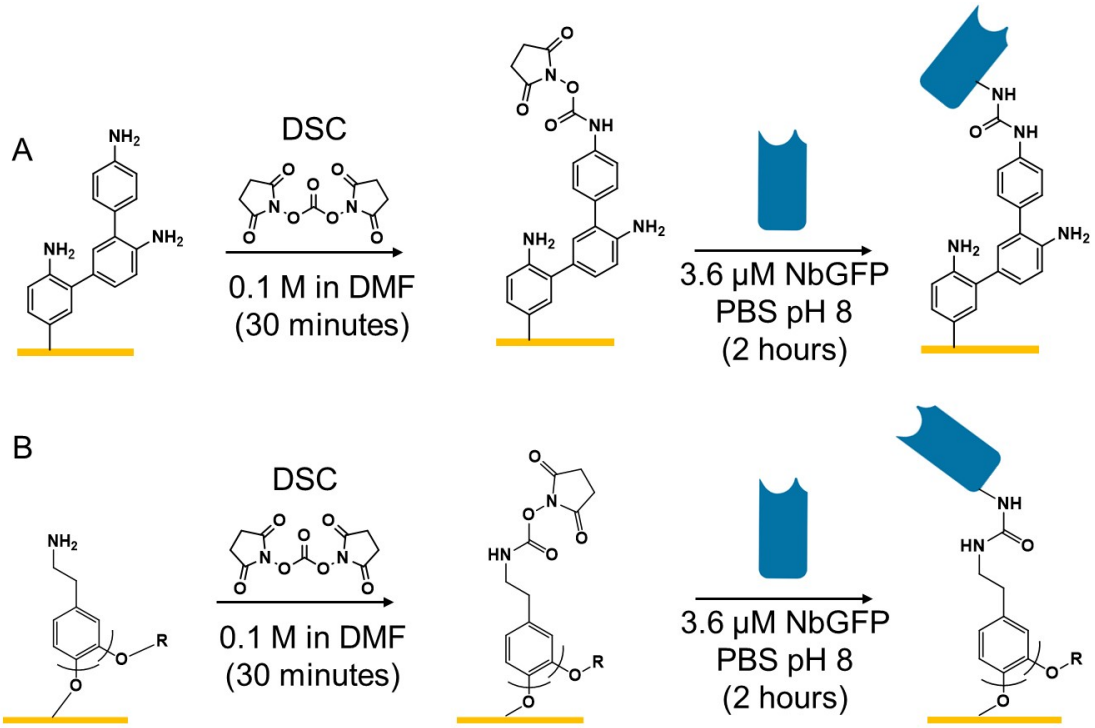

Figure 5.3.18: *Reaction scheme for DSC activation and NbGFP coupling on* ***(A)*** *the 4-NBDT derived film and* ***(B)*** *the Ptyr film.*

As with the 4-NBDT derived films, careful control experiments were designed in order to understand if DSC was activating the surface and NbGFP was being covalently coupled. For the positive control 100 mM DSC in DMF was incubated on the Ptyr surface for 30 minutes. The negative control consisted of incubating just DMF (no DSC present) on the Ptyr surface. NbGFP was then incubated on both surfaces and the subsequent EIS responses were recorded and compared (figure 5.3.19).

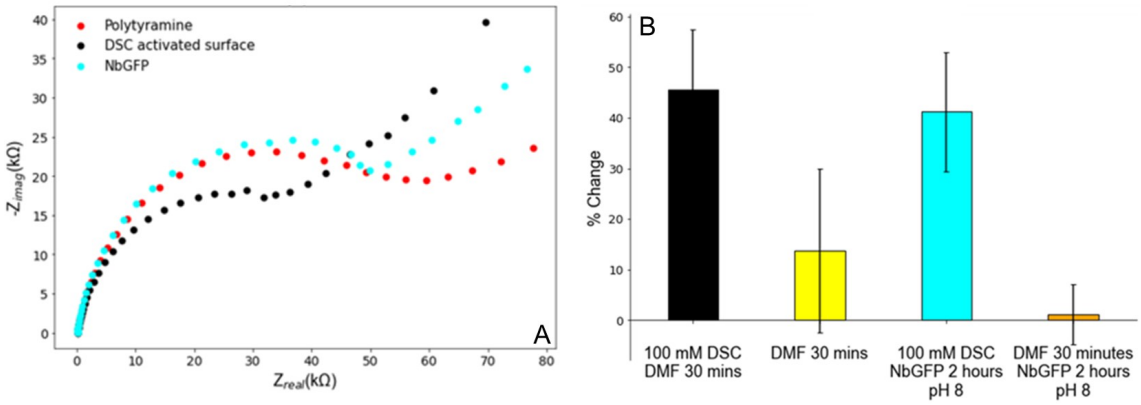

Figure 5.3.19: ***(A)*** *Nyquist plot of EIS response of 10 mM $Fe(CN)_6^{-3/-4}$ in 1 X PBS (1 M KCl) after different steps of biosensor fabrication.* ***(B)*** *The associated % change in R_{ct} values after NbGFP coupling on the positive and negative control surfaces. Working electrode area = 0.03 cm^2, n =3.*

From these results it is clear that the DSC is having an effect on surface activation and NbGFP coupling. When DSC in present in the DMF solution the percentage change in R_{ct} is $\approx$ 45 % compared to $\approx$ 12 % when just DMF was incubated on the surface. Furthermore, after NbGFP was incubated on the surface which had been activated by DSC the R_{ct} increased by $\approx$ 40 %. This is compared to a negligible change when NbGFP was incubated on the surface which had just being incubated with DMF. Each step was also monitored using CV however due to the insulating nature of the Ptyr film the change in the redox activity of $Fe(CN)_6^{-3/-4}$ was hard to track (figure 5.3.20). However, when the CV response on the bare Au surface was omitted it was clear that the response after each fabrication step followed the same trend observed with the EIS experiments. For the positive control surface the reduction current increased from 15 to 20 μA after DSC activation and subsequently decreased again to $\approx$ 17 μA after NbGFP coupling. This is mirrored in the EIS response with the R_{ct} values decreasing after DSC activation and increasing again after NbGFP coupling. For the negative control this trend was

not observed in the CV response (figure 5.3.20 (C)).

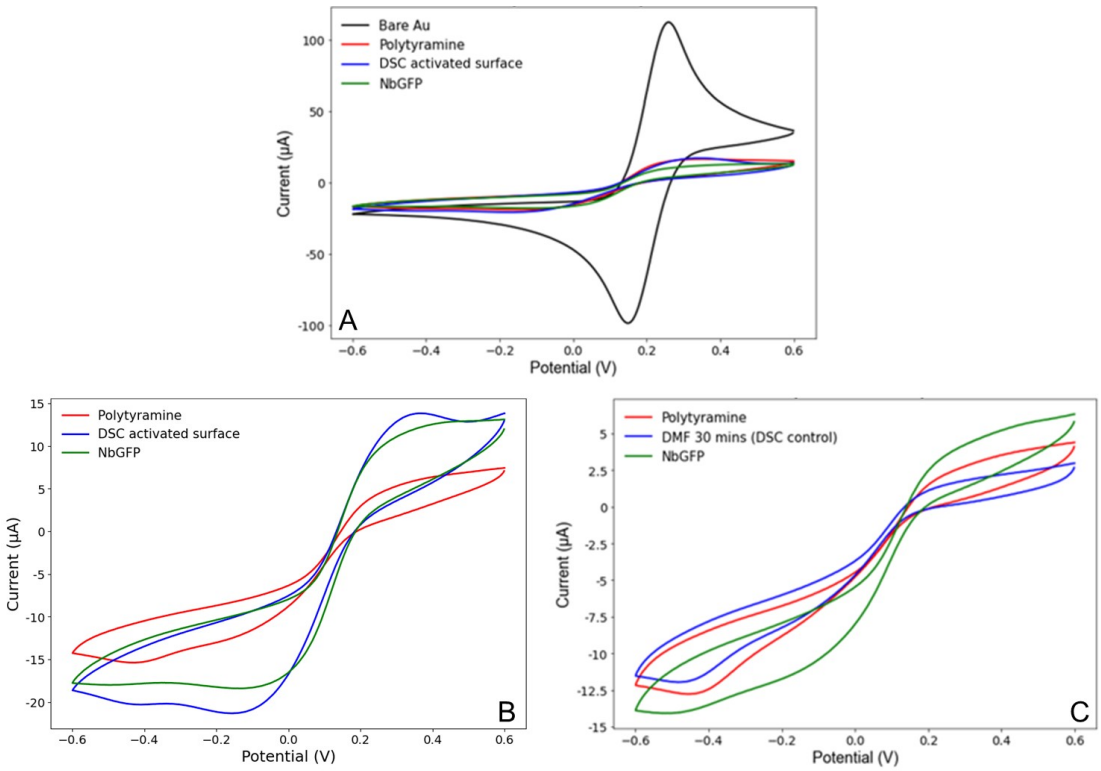

Figure 5.3.20: *Cyclic voltammogram of 10 mM* $Fe(CN)_6^{-3/-4}$ *in 1 X PBS (1 M KCl) on the positive control surface with* ***(A)*** *and without* ***(B)*** *the bare Au response and* ***(C)*** *on the negative control surface without the bare Au response.*

These results back up the hypothesis that the lack of surface activation and NbGFP coupling on the 4-NBDT derived films was due to the reduced nucleophilicity of the aromatic amines.

The new Ptyr based system was then optimised in order to obtain the highest eGFP binding response. Two different concentrations of tyramine was used and three different scan rates investigated (50, 100, and 200 mV/s). It was hoped that given that the NbGFP seemed to be covalently coupled to the surface, tuning the physical and electrochemical properties of the interface would allow the optimum eGFP binding response to be obtained.

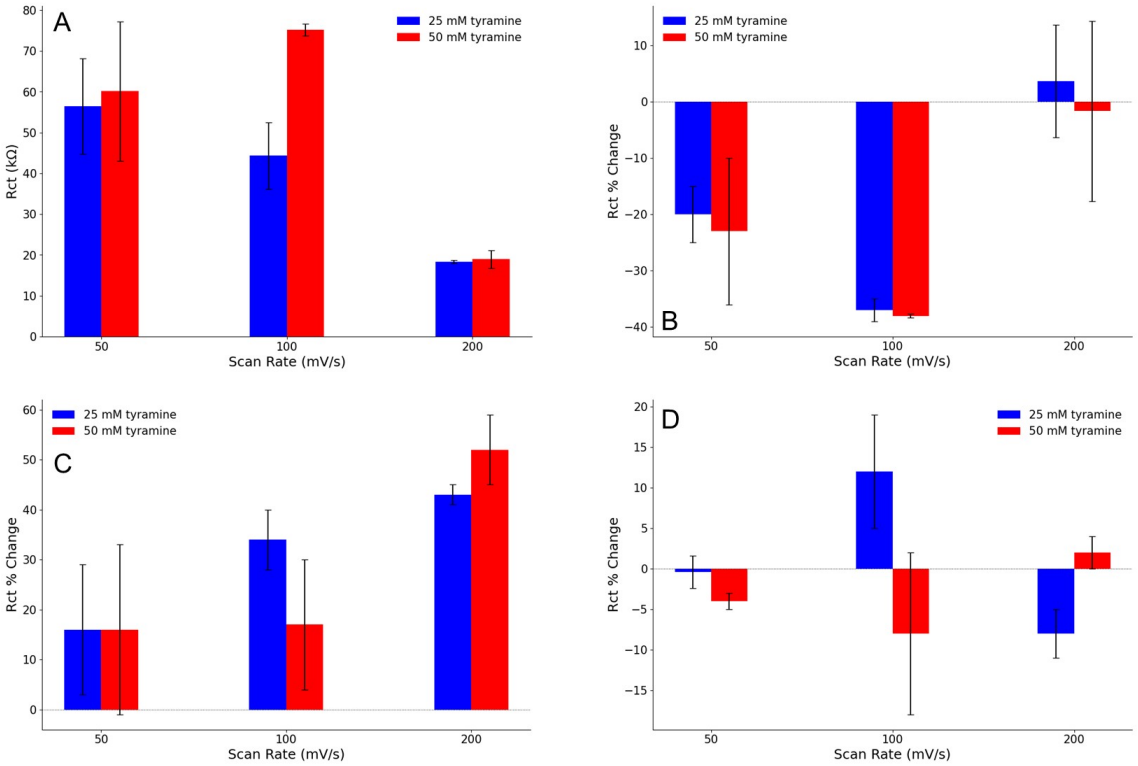

Figure 5.3.21: (A) *R_{ct} of 25 and 50 mM tyramine electropolymerised for 2 cycles between 0 and 1.6 V at 50, 100, and 200 mV/s. Percentage change in R_{ct} after DSC activation **(B)**, NbGFP coupling **(C)**, and eGFP detection **(D)**. Working electrode area = 0.03 cm^2, n =3.*

Increasing the scan rate should result in a less dense Ptyr film on the surface. This general trend is reflected in figure 5.3.21 (A), with the R_{ct} decreasing as the scan rate is increases from 50 to 200 mV/s. The only outlier from this trend is 50 mM tyramine electropolymerised at 100 mV/s. This could be due to the specific condition of the working electrodes used, as the roughness would likely vary greatly due to the manual polishing used to clean the electrodes. Changes in R_{ct} after DSC activation, NbGFP coupling, and eGFP detection could be tracked across both tyramine concentrations and the three scan rates used. For both tyramine concentrations DSC activation caused a drop in the measured R_{ct} of ≈ 25 and 35 % for scan rates of 50 and 100 mV/s respectively. Interestingly, on the Ptyr films formed using 200 mV/s the DSC activation had very little effect on

the R_{ct}. However, the same surface produced the largest response after NbGFP coupling, $\approx$ 45 and 55 % change for 25 and 50 mM tyramine respectively. This is likely due to the heterogeneous and low density Ptyr film formed using 200 mV/s resulting is little resistance to charge transfer across the interface. DSC is a small molecule which results in a small chemical change at the surface which causes little to no change in the electrochemical properties of the Ptyr film. NbGFP is a relatively large biomolecule compared to DSC and significantly increases the R_{ct} when on the surface. This also explains why the NbGFP coupling produced the smallest response on the Ptyr film which had the highest R_{ct} to begin with (50 mV/s). As the surface already had a relatively high R_{ct} the measured increase after NbGFP coupling is not as high as a film which started with a relatively low R_{ct}. In terms of the eGFP detection response, the highest change in R_{ct} was achieved using 25 mM tyramine for 2 cycles at 100 mV/s. However, this only resulted in a R_{ct} change of $\approx$ 12%, which again was too similar to the natural baseline variation (5-10 %) to accurately measure the switching efficiency when oligopeptides are incorporated onto the surface in the future.

At this point as the eGFP response could not be significantly increase by tuning the properties of the underlying Ptyr film, different NbGFP coupling strategies, concentrations, and times were investigated.

5.3.3 NbGFP coupling strategies on Ptyr films

Before moving away from DSC activation completely, it was decided to compare NbGFP incubation for 2 hours at pH 8 and 24 hours at pH 5.5 (figure 5.3.22). A pH range of 5.4 - 5.6 was previously shown to be the optimal pH for NbGFP immobilisation on mercaptoundecanoic acid terminated surfaces via NHS/EDC coupling [164]. This could be due to greater protonation of lysine residues resulting in slower NbGFP coupling over a longer time period, causing the receptors on the surface to have a more optimal spacing.

The change in R_{ct} after NbGFP coupling for 24 hours was over 4 times greater than 2 hours at pH 8 (figure 5.3.22 (C)). However, the variation between different the electrodes was significantly higher $\approx$ 200 % compared to $\approx$ 10 % for NbGFP coupling at pH 8 for 2 hours. Despite the seemingly higher amount of NbGFP on the surface after 24 hours at pH 5.5, there was no significant difference in eGFP detection compared to 2 hours at pH 8. Both methods showed an R_{ct} change of between 10-12 % (figure 5.3.22 (E)).

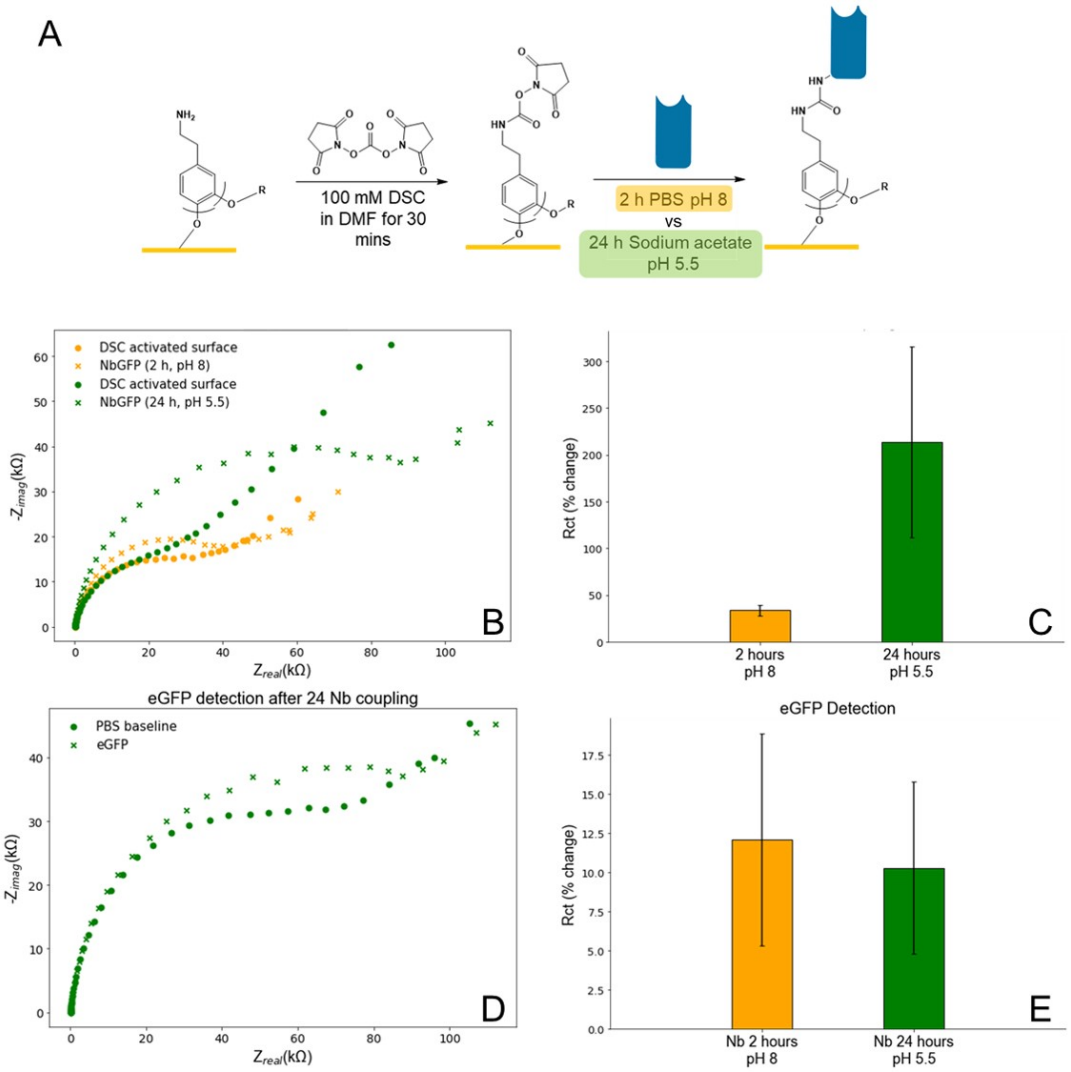

Figure 5.3.22: ***(A)*** *Reaction scheme of Ptyr activation using DSC and subsequent NbGFP coupling. EIS of 10 mM* $Fe(CN)_6^{-3/-4}$ *in 1 X PBS (1 M KCl) with* ***(B)*** *showing the Nyquist plots of NbGFP coupling after incubation for 2 and 24 hours at pH 8 and 5.5 respectively.* ***(C)*** *Sowing the subsequent percentage changes in* R_{ct} *after NbGFP coupling.* ***(D)*** *Showing the Nyquist plots before and after eGFP binding and* ***(E)*** *the corresponding percentage changes in* R_{ct}*. Working electrode area = 0.03* cm^2*, n =3.*

Despite optimisation of the Ptyr film and the NbGFP coupling conditions, a sufficient eGFP response could not be obtained. Therefore, as with the 4-NBDT derived films, it was decided to investigate different NbGFP coupling strategies on the Ptyr films (figure 5.3.23).

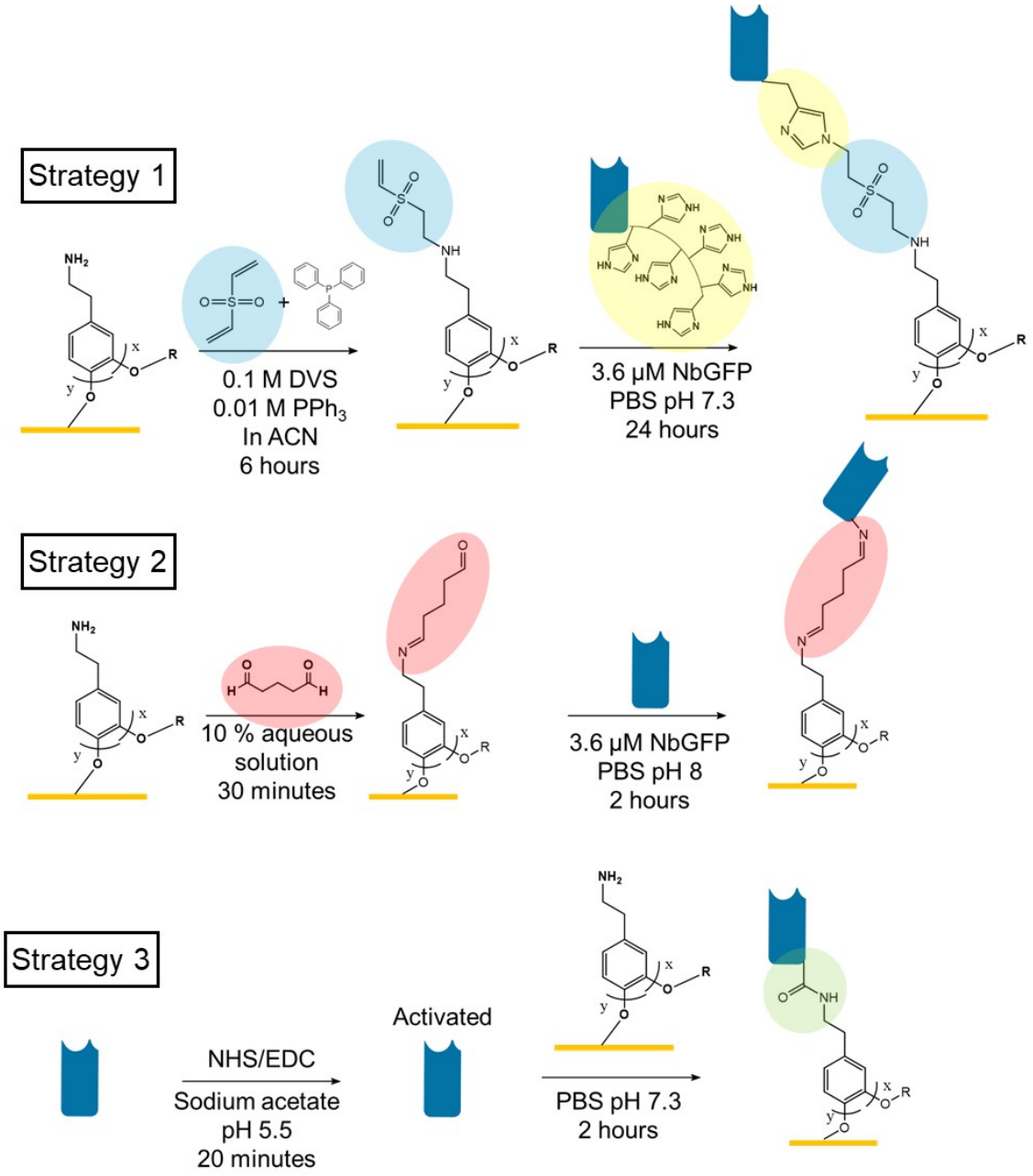

Figure 5.3.23: *Strategy 1: NbGFP coupling using DVS as previously discussed. Strategy 2: NbGFP coupling using a 10 % glutaraldehyde solution. Strategy 3: NbGFP coupling using NHS/EDC.*

As with the 4-NBDT derived films, DVS in the presence of a catalyst (PPh_3) was used for the site specific coupling of NbGFP (figure 5.3.23, strategy 1.). Glutaraldehyde was also investigated due to its highly reactive nature, it was hoped that getting as much NbGFP onto the surface may give a better eGFP detection

response. For this coupling strategy a 1 M ethanolamine incubation was carried out after NbGFP coupling to 'block' any remaining aldehyde groups on the surface (this step is omitted from figure 5.3.23, strategy 2). Finally, NHS/EDC coupling was used, in which the NbGFP was first incubated in a 0.1/0.4 M solution of NHS/EDC in order to activate any free carboxylic acid residues on the Nb's surface. This activated NbGFP was then incubated on the Ptyr film for 2 hours at pH 8 (figure 5.3.23, strategy 3). However, this method runs the risk of crosslinking the Nbs together in solution, as any activated carboxylic acids residues on one Nb could react with any free lysine residues on another Nb. The percentage changes for surface activation, NbGFP coupling, and eGFP detection are presented in figure 5.2.24.

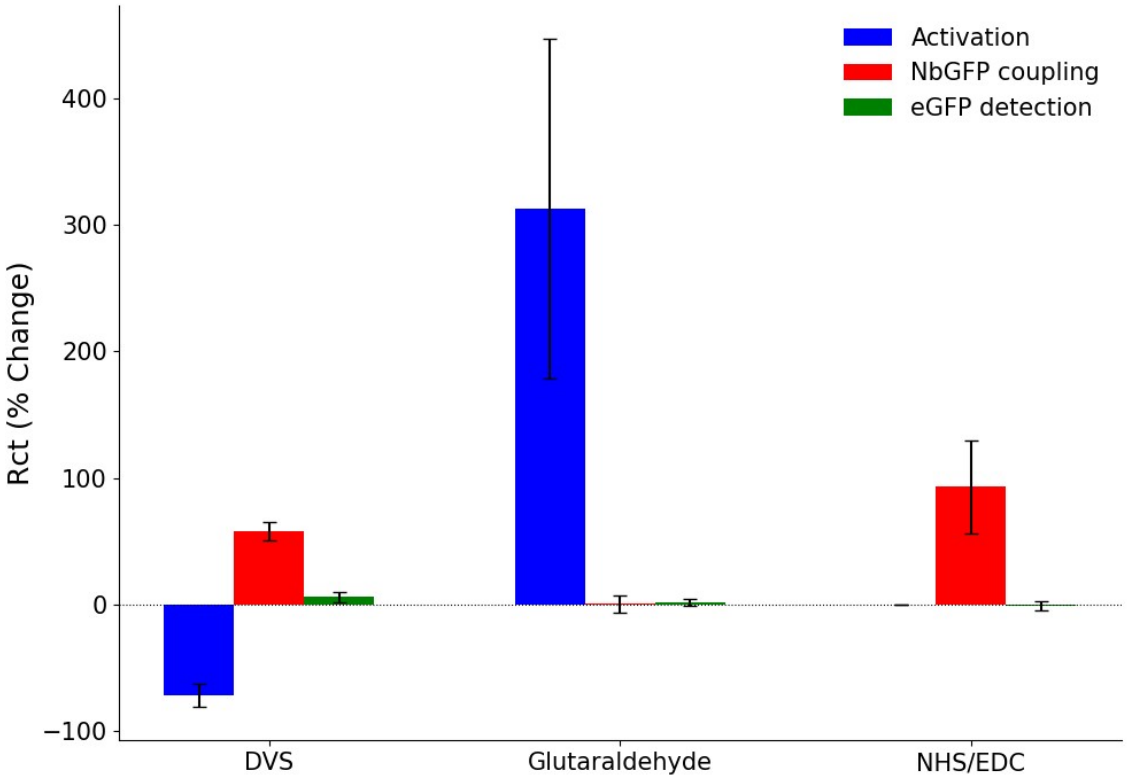

Figure 5.3.24: *Percentage changes in the R_{ct} values for the activation (blue), NbGFP coupling (red), and eGFP detection (green) for the coupling strategies outlined in figure 5.3.23. Working electrode area = 0.03 cm^2, n =3.*

For strategy 1, the DVS activation step resulted in a large decrease in the R_{ct} of $\approx$ -72%. Subsequent NbGFP coupling then increased the R_{ct} by $\approx$ 58%, while after eGFP incubation the R_{ct} only changed by $\approx$ 6%. When Glutaraldehyde was used to activate the surface, the R_{ct} change was large (313 $\pm$ 134%), this seemed to result in the loss of sensitivity with no significant change in R_{ct} detectable after NbGFP coupling and eGFP incubation. Finally, using strategy 3 the Nbs themselves were activated in solution and therefore, no surface activation step could be measured. While the NbGFP coupling step looked promising, showing an increase in the R_{ct} of $\approx$ 93%, again there was no significant change in the R_{ct} after eGFP incubation. None of the NbGFP coupling strategies investigated were able to improve the eGFP detection response, with the greatest change of $\approx$ 10-12% obtained using DSC.

From the experiments conducted so far the sensitivity of the platform to the presence of eGFP is extremely low. Therefore, it was decided to couple eGFP directly to the Ptyr surface without any NbGFP present to understand if the antigen can be detected at the surface using faradaic EIS (figure 5.3.25). Positive and negative control experiments were set up, where after DSC activation the eGFP was incubated on the surface in PBS pH 8 for 2 hours (positive control), and only PBS pH 8 for 2 hours (negative control).

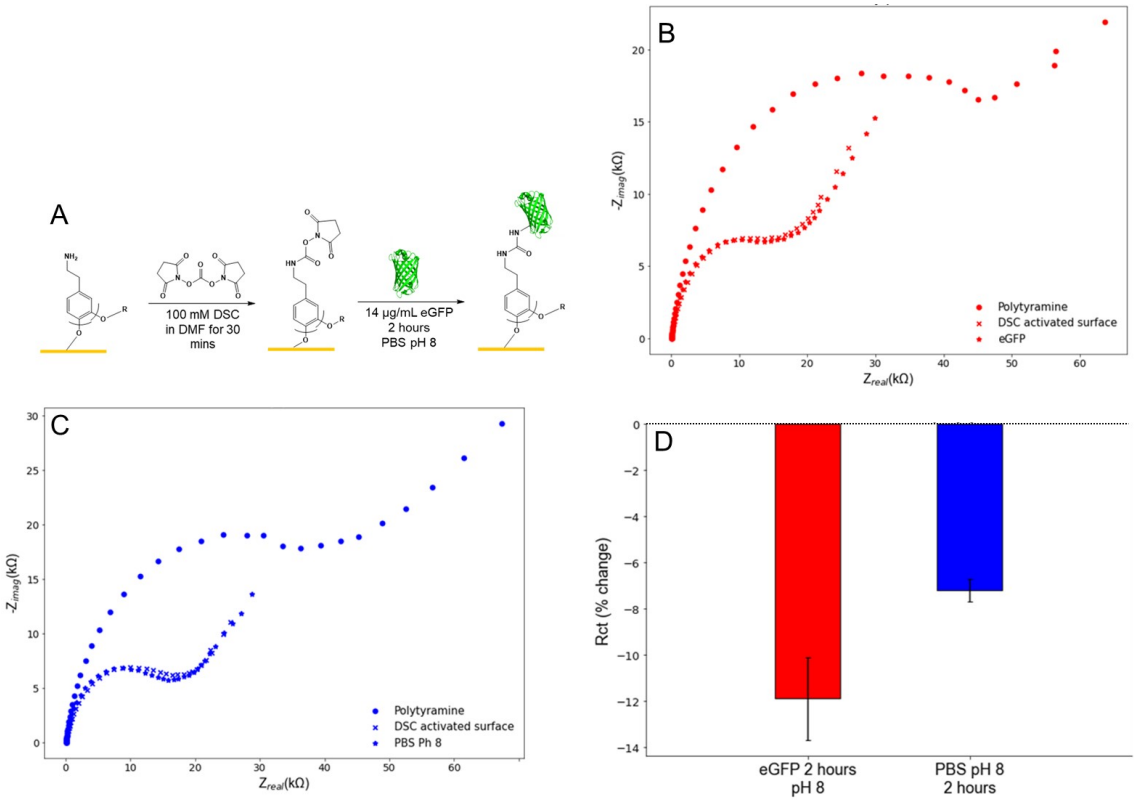

Figure 5.3.25: (A) *Reaction scheme of coupling eGFP directly to the Ptyr surface using DSC. The EIS response of 10 mM $Fe(CN)_6^{-3/-4}$ in 1 X PBS (1 M KCl) with* ***(B)*** *showing the Nyquist plot for the postive control experiment (eGFP present) and* ***(C)*** *showing the Nyquist plots for the negative control (only PBS).* ***(D)*** *The corresponding percentage changes in R_{ct} for the positive and negative control experiments. Working electrode area = 0.03 cm^2, n =3.*

Covalently coupling the eGFP to the surface using DSC did not achieve a higher eGFP detection response compared to when NbGFP was on the surface ($\approx$ 12% for both). Therefore, it may be the case that eGFP does not produce a large enough change in the resistive properties of the surface for faradaic EIS to be an effective detection method. Therefore, it was decided to investigate if the eGFP could be detected using non-faradaic EIS.

5.3.4 Capacitance detection of eGFP

In the case of electrochemical biosensors, capacitance can be though of as the ability of surface components to collect and store electrical charge. Components which exhibit capacitance properties have an internal impedance which restricts the flow of current through the capacitor. This internal impedance is know as 'capacitive reactance' which is dependent on the applied frequency in an EIS measurement [253]. The total capacitance is inversely proportional to the total impedance of the electrochemical system [254]. However, the total capacitance itself can be described by equation 14.

$$\frac{1}{C_{total}} = \frac{1}{C_{ins}} + \frac{1}{C_{rec}} + \frac{1}{C_{dl}} \tag{14}$$

Where C_{ins} = the capacitance of the insulating layer, C_{rec} = the capacitance of the biorecognition layer, and C_{dl} = the capacitance of the electrical double layer at the receptor-solution interface (figure 5.3.25). Due to this relationship, the lowest capacitance change will dominate the total capacitance response. Therefore, it is important that the biosensing interface is designed so the capacitance of the insulating and biorecognition layers are as high as possible. Otherwise, they may dominate the capacitance response and changes in the double layer capacitance following antigen binding may not be detectable (figure 5.3.26).

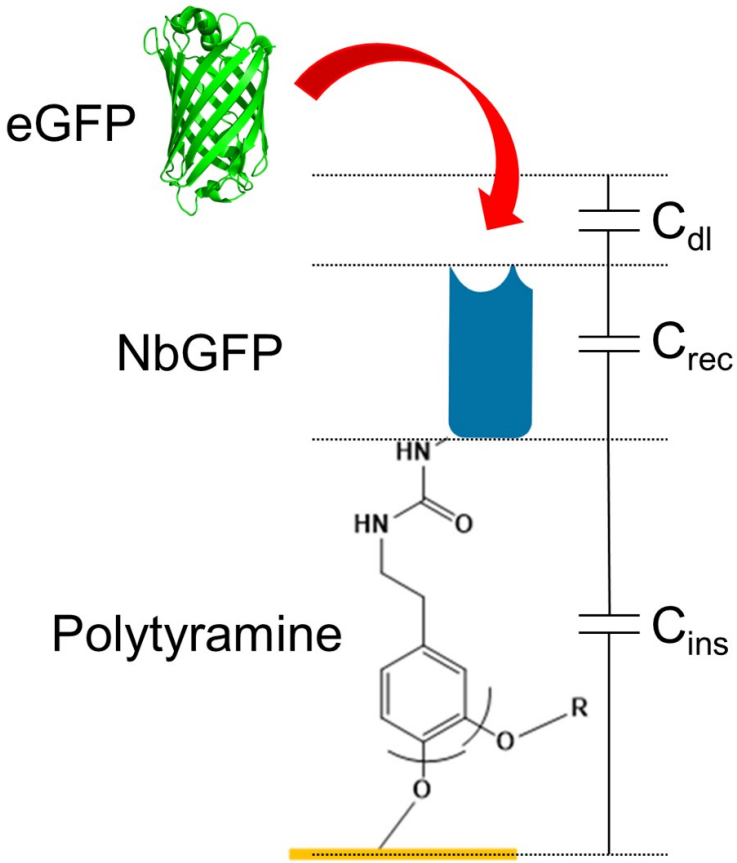

Figure 5.3.26: *Different Capacitance layers of the biosensing interface. Not drawn to scale.*

It is also important to note that this model of the interface assumes that the biorecognition layer completely covers the surface forming a perfectly insulating layer. In the system under investigation this will not be the case which may result in a decrease in the overall sensitivity of the platform.

It was hoped that due to the non conducting nature of the Ptyr film, that this system would be more sensitive to changes in capacitance at the electrical double layer compared to changes in resistance. This method also has the benefit of not needing a redox probe in the PBS solution as the R_{ct} is no longer being investigated. Non-faradaic EIS was employed to monitor the fabrication steps of the biosensing interface (figure 5.3.27). The only significant change in the EIS

spectrum was in the imaginary component (figure 5.3.27 (A) and (B)). However, this makes sense as in an impedance measurement the real component represents the resistive elements of the system while the imaginary component often represents reactive elements such as capacitors and inductors [195]. Instead of fitting an equivalent circuit model to the EIS response, it was easier to find the frequency which resulted in the largest changes after each surface modification step. This was around 100 Hz and the change in response at this frequency was monitored.

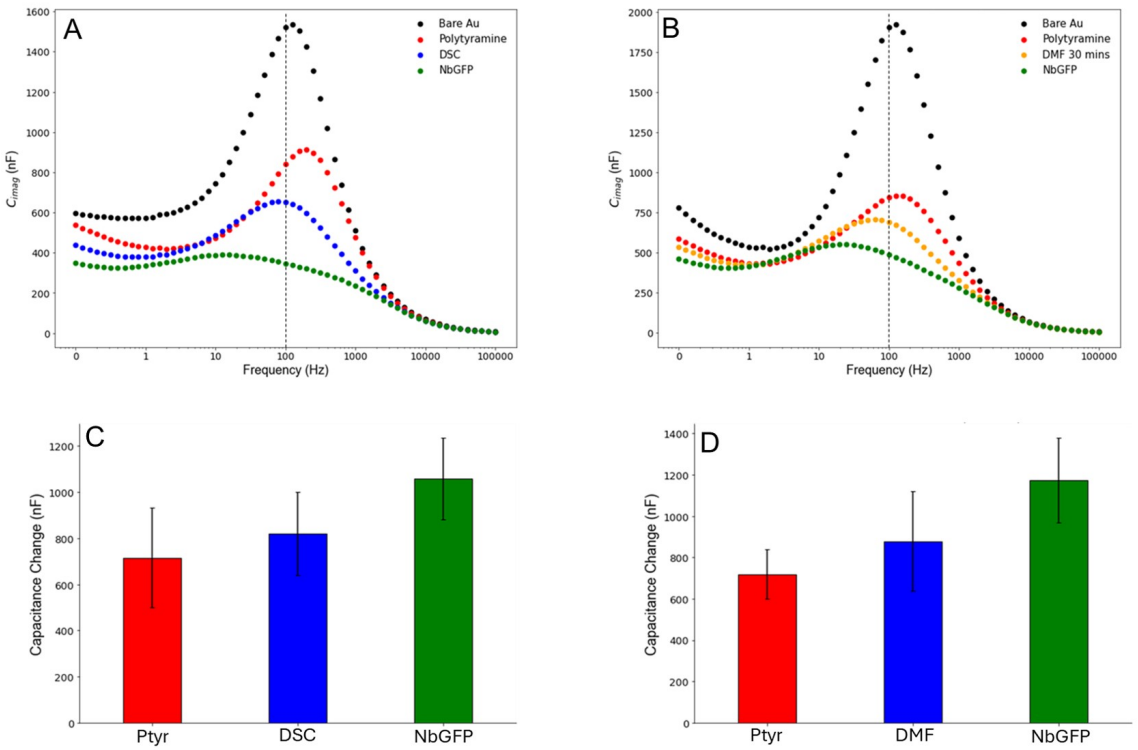

Figure 5.3.27: *Non faradaic EIS carried out in 1 X PBS with Bode plots* ***(A)*** *and* ***(B)*** *showing the change in capacitance vs applied frequency for the positive and negative control surfaces respectively.* ***(C)*** *and* ***(D)*** *show the average change in capacitance after each fabrication step. Working electrode area = 0.03 cm^2, n =3.*

A control experiment was also carried out in which DSC was omitted from the DMF solution (figure 5.3.27 (B) and (D)). Both experiments seem to produce a similar capacitance change after NbGFP incubation was carried out, regardless

if DSC was used to activate the Ptyr surface. Therefore, from this it is difficult to determine if the response corresponded to NbGFP covalently coupling to the interface or non-specifically adsorbing. Three different concentrations of eGFP were then incubated on the two surfaces. It was hoped that the system in which the surface was activated with DSC produced a higher response (figure 5.3.28).

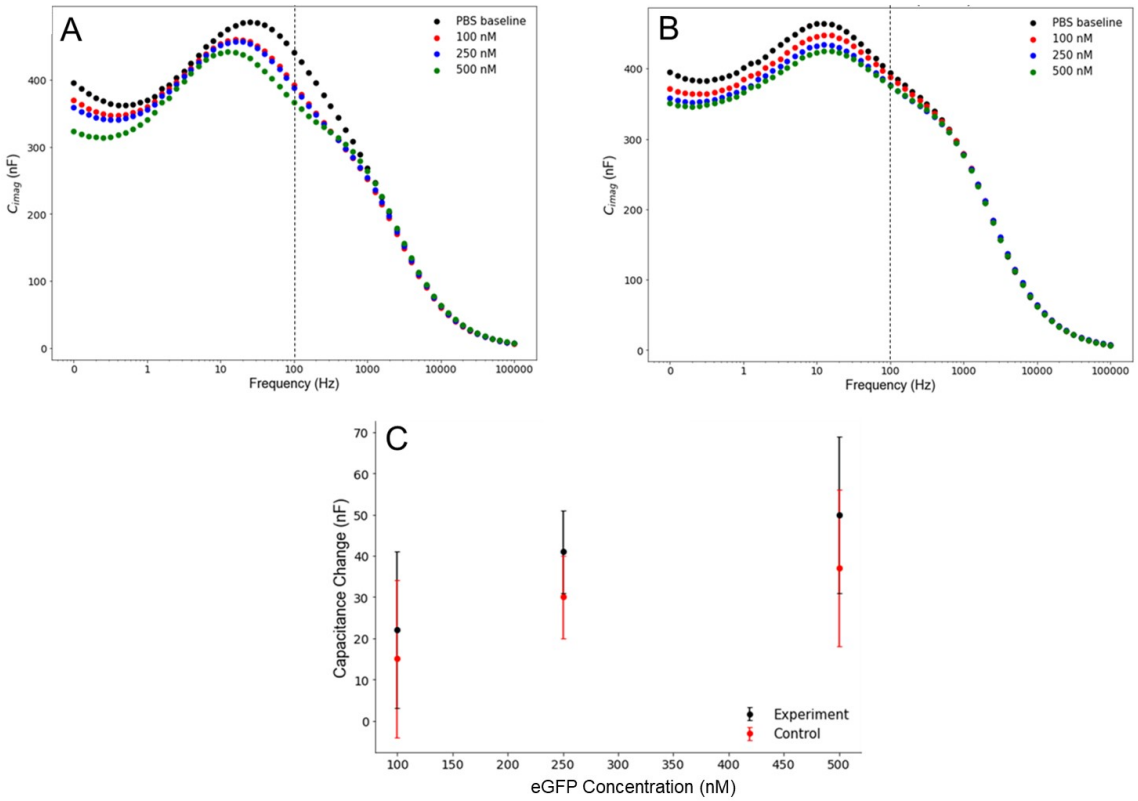

Figure 5.3.28: *Non faradaic EIS carried out in 1 X PBS with Bode plots **(A)** and **(B)** showing the change in capacitance vs applied frequency after different concentrations of eGFP was incubated on the two surface. **(C)** Shows the corresponding average change in capacitance measured at 100 Hz for eGFP incubations on both surfaces. Working electrode area = 0.03 cm^2, n =3.*

When DSC was used to activate the interface the change in capacitance went from ≈ 20 nF after 100 nM eGFP incubation to ≈ 50 nF after 500 nM eGFP incubation. This demonstrates that the response is concentration dependent however, there was significant overlap of the error bars when the experiment was repeated on the surface which was not activated with DSC (figure 5.3.28 (C)). When no DSC

was use the response changed from $\approx$ 15 nF after 100 nM eGFP incubation to $\approx$ 37 nF after 500 nM eGFP incubation. Again this makes it difficult to discern how much of the response corresponds to specific NbGFP-eGFP interactions where the NbGFP is actually covalently coupled to the interface.

As the eGFP detection responses have been low and there seems to a significant amount of non specific interactions with both NbGFP and eGFP with the surface, it was decided to completely change both the coupling strategy and the Nb itself. A more tailored approach was designed which would allow the NbGFP to be coupled to the interface without the need for organic solvents. Specific modifications were also carried out to the Nb which would allow the binding sites to be located at the opposite side of the Nb which was used to couple to the interface.

5.3.5 Maleimide Coupling using Cysteine Terminated Nanobodies

In order to activate the Ptyr surface under aqueous conditions, sulfosuccinimidyl-4-(N-maleimidomethyl)cyclohexane-1-carboxylate (sulfo-SMCC) was used. The sulfo group adds enough polarity to the molecule to make it water soluble at room temperature. Like DSC, one side of the sulfo-SMCC molecule contains a succinimidyl group however, the other side consists of a maleimide which at neutral pHs is 1000 times more reactive towards thiols compared to amines [121, 125]. Therefore, a new Nb specific for eGFP was purchased from NanoTag Biotechnologies Ltd. which included a C-terminal cysteine residue (cys-NbGFP). While the amino acid sequence for this cys-NbGFP is not currently in the public domain, NanoTag confirmed that this cysteine is located on the opposite side of the Nb with respect to the binding site. Therefore, if Nb coupling is carried out using this cysteine residue the binding site should be orientated out into the surrounding environment (figure 5.3.29).

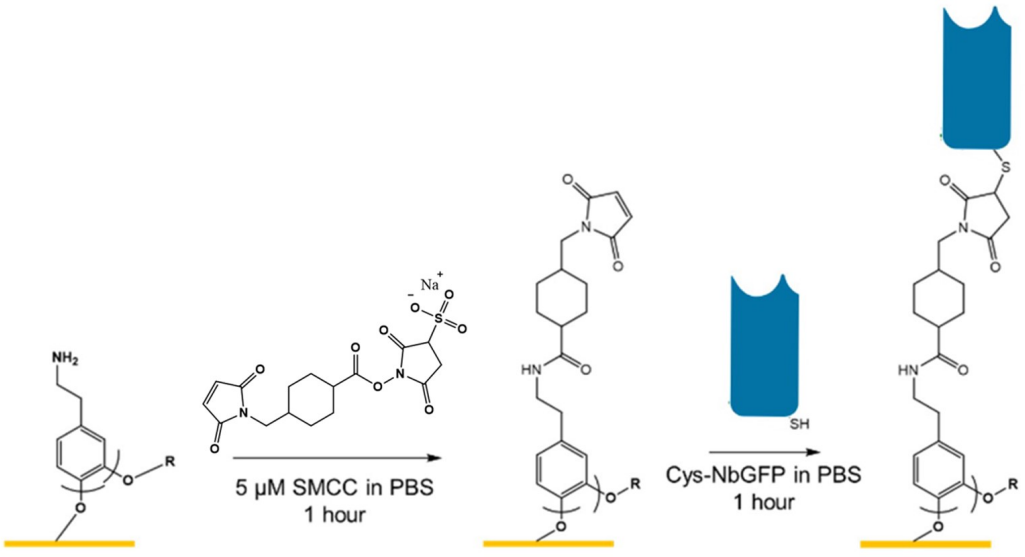

Figure 5.3.29: *Schematic of surface activation using SMCC followed by cys-NbGFP coupling.*

As this surface modification strategy (figure 5.3.29) can be carried out entirely in PBS, SPR can be used to monitor each fabrication step (figure 5.3.30). Ptyr was electropolymerised outside the SPR by scanning the potential between 0 and 1.6 V for 2 cycles at 100 mV/s, as previously discussed. The Au SPR substrate was then placed inside the SPR's flow cell and SMCC (5 μM) and cys-NbGFP (3.6 μM) were injected.

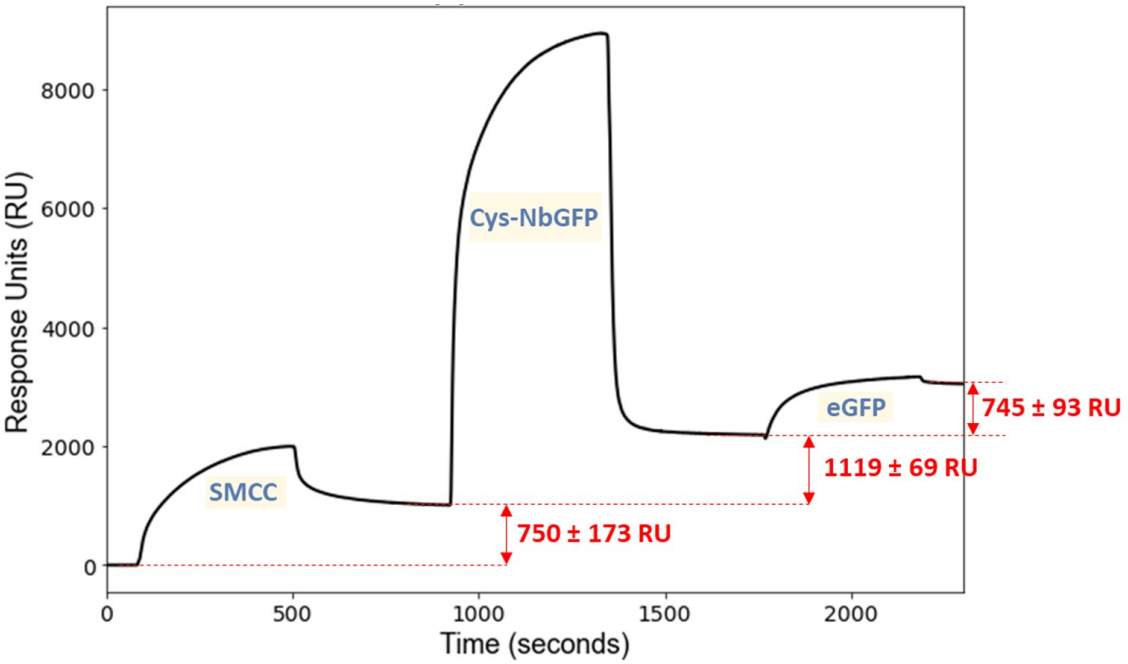

Figure 5.3.30: *SPR trace of SMCC, cys-NbGFP, and eGFP injected onto a Ptyr surface, n = 3.*

SMCC injection resulted in a baseline change of 750 $\pm$ 173 RU suggesting that surface activation was successful. The cys-NbGFP and eGFP injections resulted in a change of 1119 $\pm$ 69 RU and 745 $\pm$ 93 respectively. In order to ensure this response corresponded to NbGFP-eGFP interactions where the cys-NbGFP were covalently attached to the surface, a number of control experiments were designed. eGFP injection on the fully functionalised surface was compared to eGFP injection on: The surface which was activated with SMCC but no cys-NbGFP was

injected, the surface was not activated with SMCC but cys-NbGFP was injected, the unmodified Ptyr surface, and the bare Au surface (figure 5.3.31).

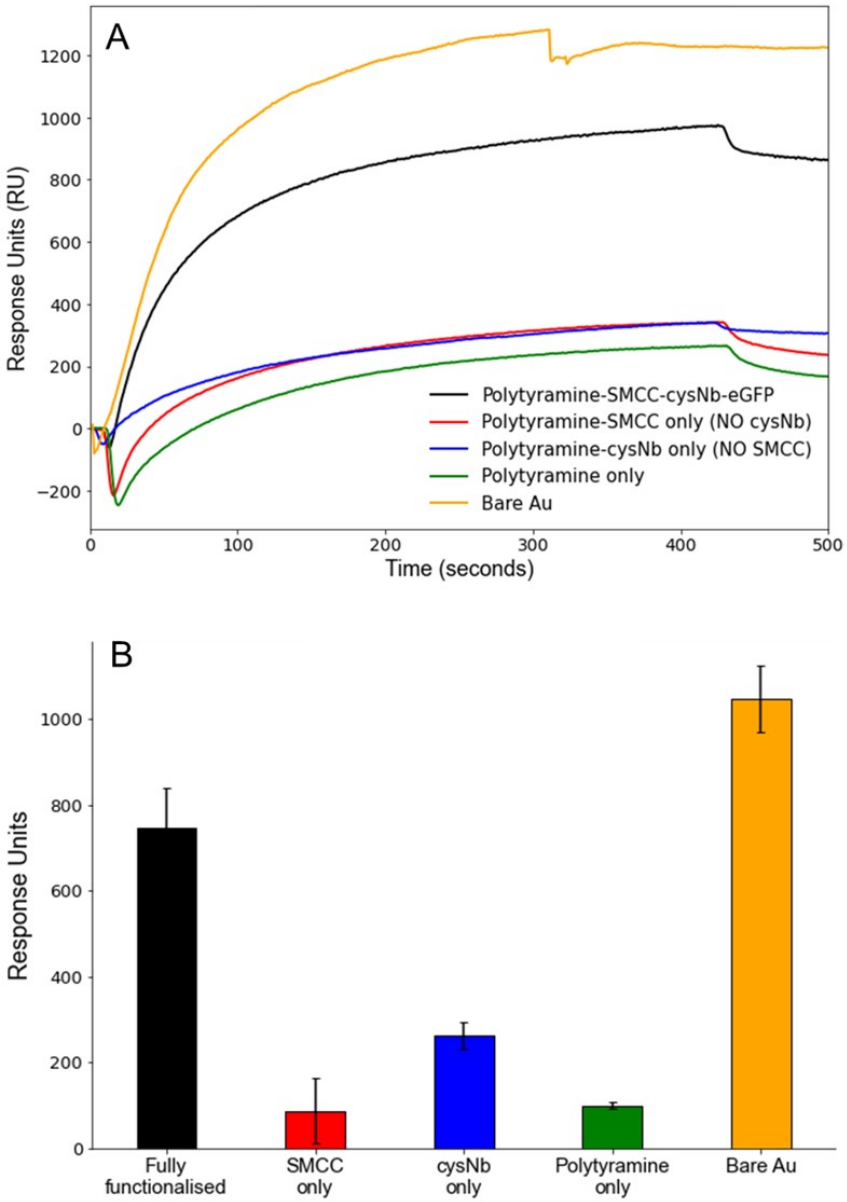

Figure 5.3.31: ***(A)*** *SPR traces of eGFP injection on the different control surfaces.* ***(B)*** *Average SPR response after eGFP injection on the different control surfaces, n = 3.*

As previously seen, when eGFP was injected onto the fully functionalised surface the binding response was ≈ 750 RU. Likewise, when eGFP was injected onto the bare Au surface the response change was ≈ 1000 RU (as investigated in section 3.3.2.4). However, when eGFP was injected onto the other control surfaces (figure

5.3.31) the binding response did not reach above 300 RU. From these results it seems that the Ptyr film forms an sufficient barrier to prevent eGFP from non-specifically interacting with the Au surface. Furthermore, it also seems that eGFP does not significantly interact with the surface unless it has been activated with SMCC and cys-NbGFP has been injected. This confirms that not only is eGFP binding to the Nbs on the surface, but the cys-NbGFP is covalently attached to the Ptyr film and not just non-specifically adsorbed. Therefore, this system seems the most suitable for investigating control over eGFP binding using oligopeptides.

This platform was then transferred to the rod electrodes and the fabrication steps were monitored using CV and EIS (figure 5.3.32).

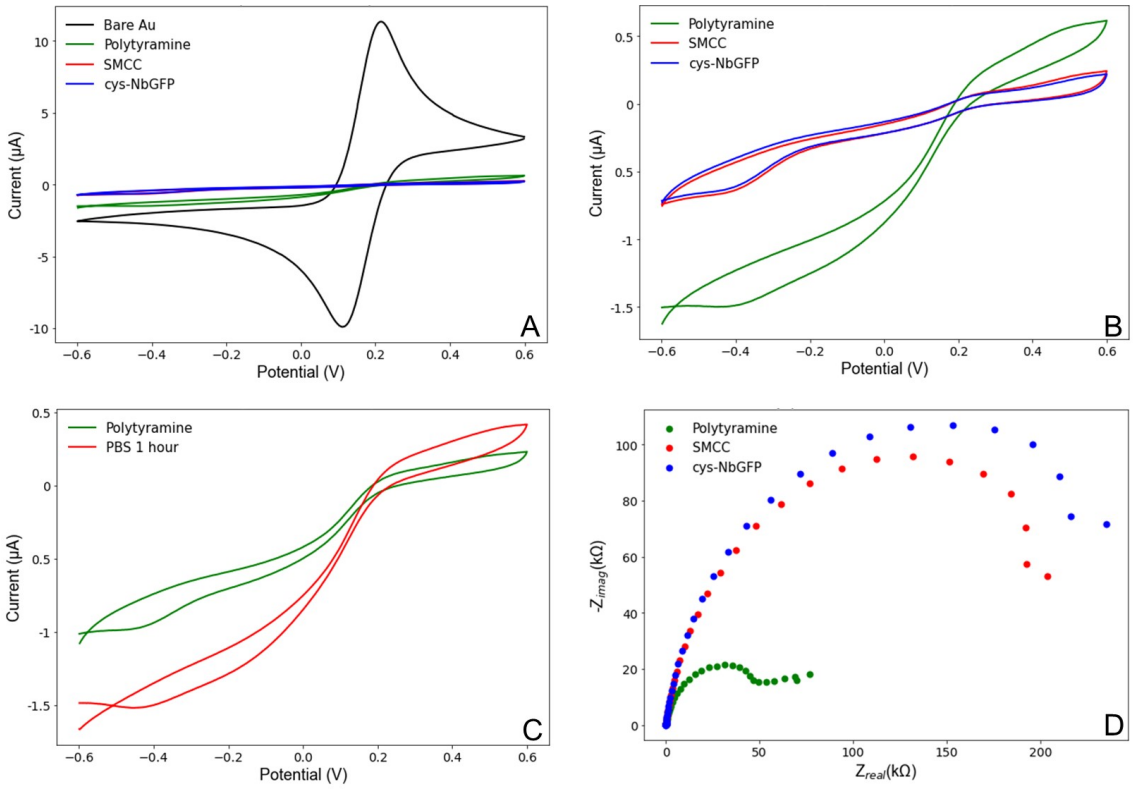

Figure 5.3.32: *Cyclic voltammetry of 10 mM $Fe(CN)_6^{-3/-4}$ in 1 X PBS (1 M KCl) with* ***(A)*** *and without* ***(B)*** *the response on the bare Au surface.* ***(C)*** *PBS control, no SMCC present.* ***(D)*** *Nyquist plot showing the EIS response after each surface modification step. Working electrode area = 0.03 cm^2.*

Due to the highly resistive nature of the Ptyr film, it was difficult to resolve the

subsequent fabrication steps (figure 5.3.32 (A)). However, when the bare Au response was omitted from the spectra it was clear that the SMCC activation step further decreased the redox activity of the $Fe(CN)_6^{-3/-4}$ probe at the surface (figure 5.3.32 (B)). After this step the cys-NbGFP coupling could not be detected as the redox activity of the probe was already at a minimum. The PBS control experiment (figure 5.3.32 (C)) confirmed that this decrease was due to the SMCC activation and not a solvent effect. Faradaic EIS was also used to monitor the different fabrication steps (figure 5.3.32 (D)). These results follow the same trend as the CV response with the R_{ct} increasing dramatically ($\approx$ 150 kΩ), while only a small change was observed after cys-NbGFP coupling ($\approx$ 25 kΩ).

Different cys-NbGFP concentrations were used in order to optimise the eGFP binding response (figure 5.3.33).

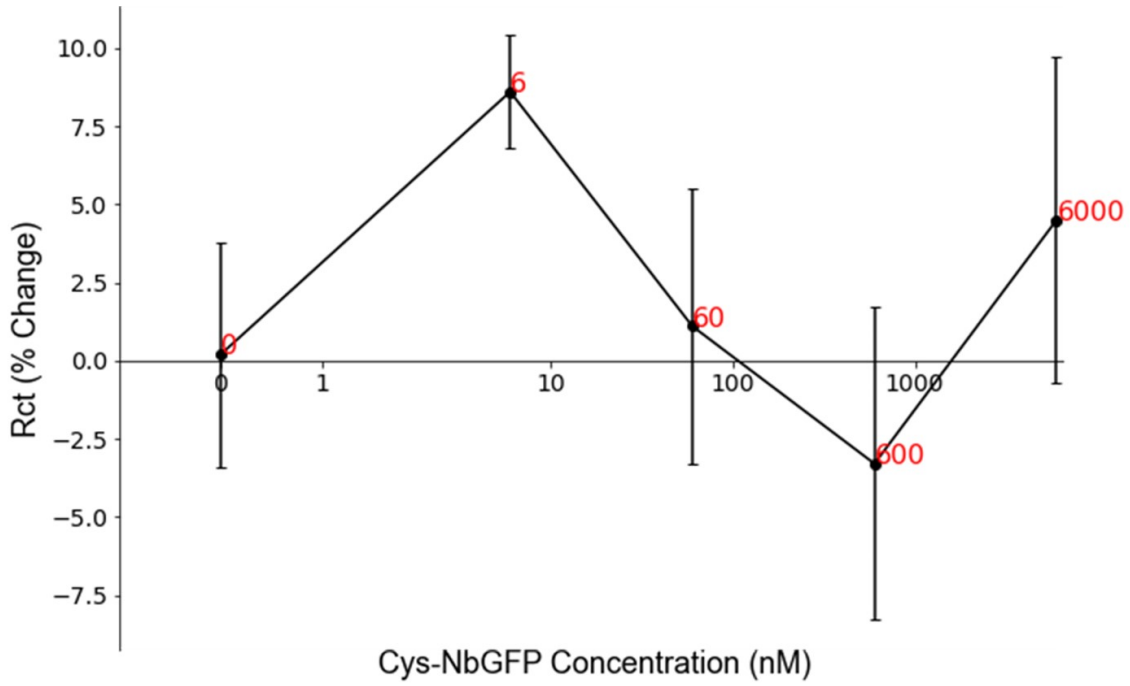

Figure 5.3.33: *Percentage change in R_{ct} after 14 μg/mL eGFP was incubated on the surface after different cys-NbGFP concentrations (shown in red) were used. Working electrode area = 0.03 cm^2, n =3.*

Regardless of the concentration of cys-NbGFP coupled to the surface, the eGFP incubation did not change the magnitude of the R_{ct} by more than 10%. This was also observed after cys-NbGFP coupling when measured with EIS and CV. It seems that due to the film already having a relatively high R_{ct} the coupling of cys-NbGFP or subsequently the eGFP has little measurable effect on the resistive properties of the interface. However, from the SPR results (figure 5.3.31) the eGFP has been confirmed to be present on the surface. Therefore, optimising the detection method and conditions may be the most appropriate method to achieve a high eGFP detection response.

Before this optimisation was carried out, it was decided to incorporate the oligopeptides onto the surface to ensure this fabrication method was suitable for C8K coupling. Due to the presence of a C-terminal cysteine residue on the C8K molecule (figure 3.3.7), it could be coupled to the SMCC activated surface simultaneously with the cys-NbGFP. The same procedure for cys-NbGFP coupling was followed for C8K and a molar ratio of 1:5 cys-NbGFP:C8K. These surface modifications were monitored using EIS (figure 5.3.34). When only C8K was incubated on the surface the R_{ct} increased by $\approx$ 400%, however the variation from electrode to electrode was extremely large $\approx$ 600%. When C8K was incubated with cys-NbGFP simultaneously, the R_{ct} increased $\approx$ 300% but the variation was significantly smaller $\approx$ 50%. This was similar to the results obtained when C8K oligopeptides were coupled to the bare Au surface (section 3.3.2). It seems the flexible nature of the C8K molecules on the surface result in a heterogeneous surface with high variability. The presence of the cys-NbGFP introduces some

order, perhaps helping to space out the C8K molecules on the surface, which in turn reduces the variability. This variability was also seen when eGFP was incubated on the two surfaces (figure 5.3.34 (D)). While the avergae percentage change in R_{ct} was extremely small the variability was much greater on the C8K surface compared to the cys-NbGFP:C8K [1:5] surface.

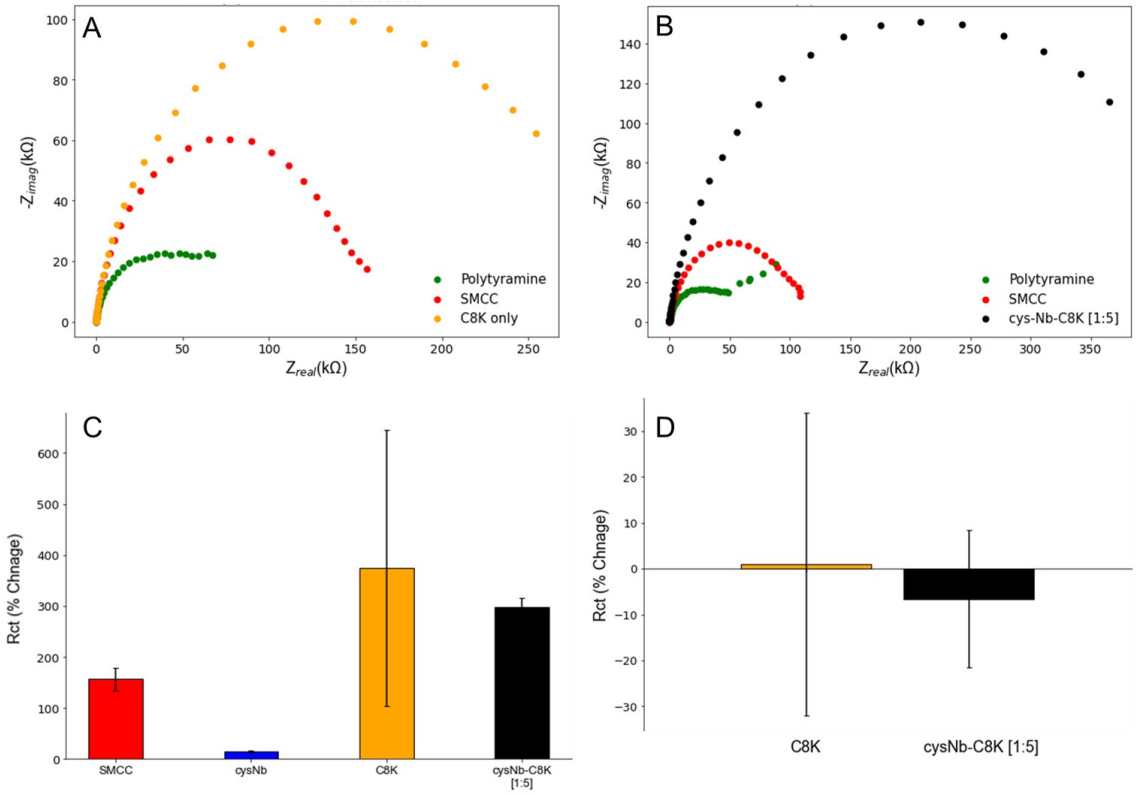

Figure 5.3.34: *EIS of 10 mM $Fe(CN)_6^{-3/-4}$ in 1 X PBS (1 M KCl) with Nyquist plot* ***(A)*** *showing C8K and* ***(B)*** *cys-NbGFP:C8K [1:5] coupling to the SMCC activated surface.* ***(C)*** *The average percentage change in R_{ct} after SMCC activation, cys-NbGFP, C8K, and Cys-NbGFP:C8K [1:5] couling.* ***(D)*** *The average percentage change in R_{ct} after eGFP incubation on the two surface. Working electrode area = 0.03 cm^2, n =3.*

The eGFP detection response did not increase when C8K was included on the surface. However, these results indicate that the oligopeptides are present and this coupling strategy is suitable for coupling C8K to the surface. It was decided to first optimise the eGFP binding response without the C8K on the surface.

5.3.6 eGFP Detection Optimisation

In order to investigate the factors which control the eGFP signal response, two cys-terminated Nbs with opposite surface charges were employed. The cys-NbGFP which has been used so far has a surface charge of +2.825 (this information was obtained from NanoTag directly). A cys-NbGFP clone was also obtained from NanoTag which was specifically engineered to have a surface charge of -2.830. Both these Nbs were coupled to the Ptyr film using SMCC as described in figure 5.3.29. eGFP was incubated on both Nb surfaces and the R_{ct} change measured using faradaic EIS (figure 5.3.35).

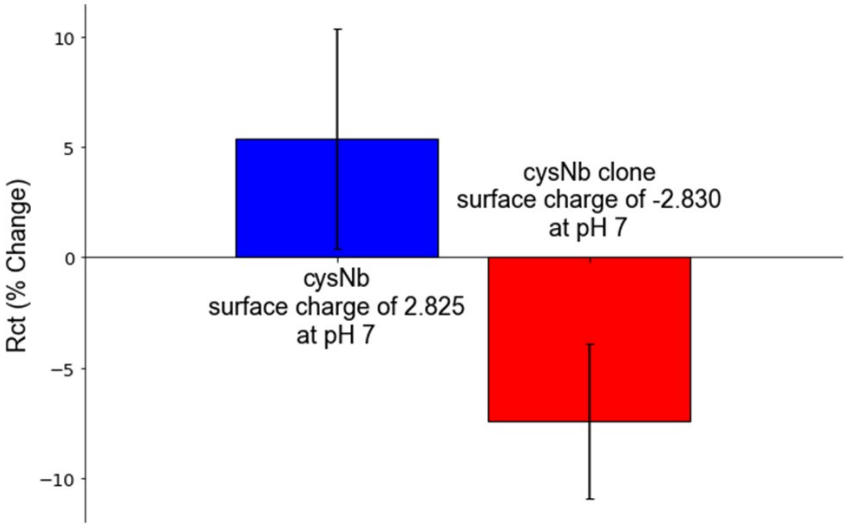

Figure 5.3.35: *Percentage change in R_{ct} after eGFP incubation on nanobody surfaces with opposite surface charges. Working electrode area = 0.03 cm^2, n = 3.*

Unfortunately, for both Nb surfaces the change in R_{ct} was small $\approx$ 5%. However, the positively charged Nb surface resulted in an increase in the R_{ct} while the negatively charged surface resulted in a decrease. This was unexpected as the $Fe(CN)_6^{-3/-4}$ redox probe is anionic and should be electrostatically repelled away from the negatively charged surface to a greater extend than to the posi-

tively charged surface. eGFP has an isoelectric point of 6.2 and would be slightly negatively charged under the EIS measurement conditions [255]. However, it is unclear what the overall charge for these specific NbGFP-eGFP complexes would be. It could also be the case that the electrostatic interactions may not be the dominant force between the surface and the probe. The probe may be more easily able to interact with hydrophilic regions on the negatively charged Nbs, which may have been introduced during the bioengineering process to change the magnitude of the surface charge. Also, eGFP binding may result in a conformational change in the Nb's structure causing different amino acid residues to become exposed. Therefore, the surface charge of the Nbs in solution may be dramatically different comapred to the NbGFP-eGFP complex on the surface.

In order to investigate the effect of surface charge further, eGFP incubation and the EIS measurements were carried out over wide pH range. The cys-NbGFP with a surface charge of +2.825 was used for these experiments. First, the stability of eGFP to different pHs was investigated using a fluorescence spectroscopy, with an excitation wavelength set to 488 nm which produced an emission signal around 508 nm (figure 5.3.36 (A)). The fluorescence intensity was extremely low below pH 3 and steadily increased to a maximum of $\approx$ 30,000 a.u. at pH 9. This is in line with literature results which indicate that eGFP experiences fluorescence quenching and structural modifications below pH 6 [256]. When EIS measurements were carried out there was a large change in the response for pH 4 and 5 of $\approx$ 75% and $\approx$ 55% respectively. However, this was likely due to the denatured eGFP interacting with the surface non-specifically, which was confimed by carrying out a

Nb control (figure 5.3.36 (D)). When no NbGFP was present on the surface the R_{ct} increase by ≈ 140%. This indicates that the change in R_{ct} observed when NbGFP is present does not correspond to specific NbGFP-eGFP interactions. Over the pH range which eGFP seems to be stable (pH 6-10) there is a negative correlation between the pH and the percentage change in the R_{ct} (figure 5.3.36 (C)). As the pH reaches and passed the isoelectric point of the cys-NbGFP (Ip = 9.3) the R_{ct} begins to decrease. These results indicate that while the pH has an effect on the EIS response it was not enough to change the magnitude by more that 10%. As previously discussed this change is not sufficient to accurately measure the switching capacity of the platform as the natural baseline variation can be between 5-10% for faradaic EIS measurements.

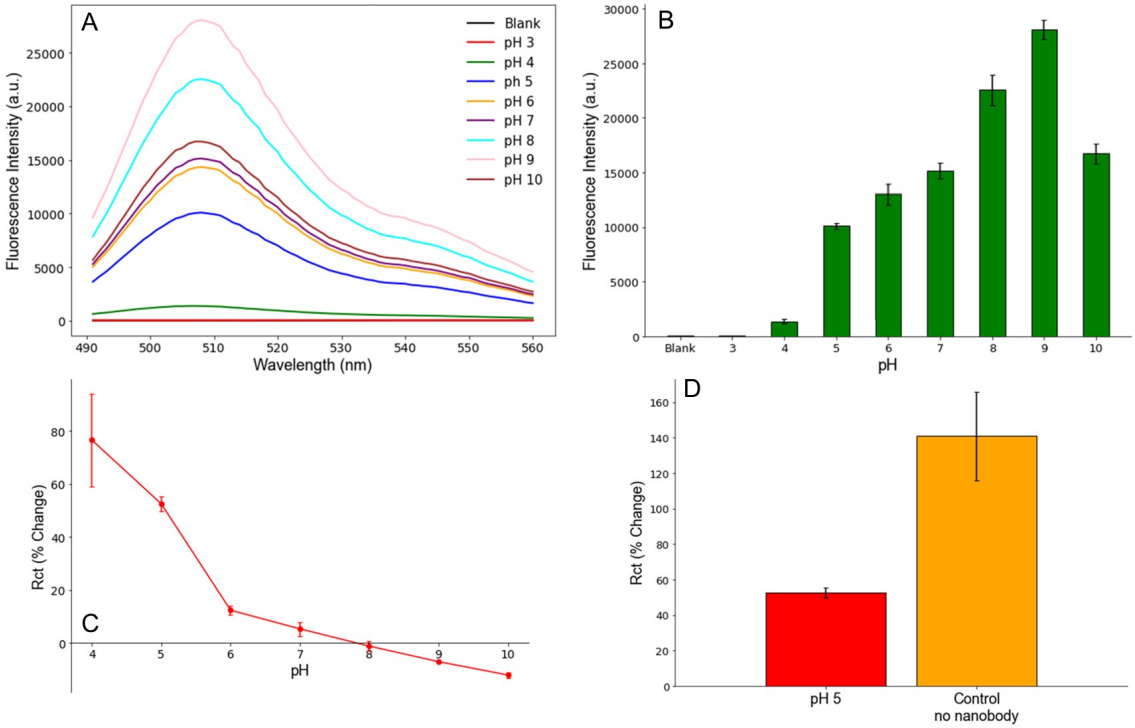

Figure 5.3.36: ***(A)*** *Fluorescence spectrum of the eGFP excited at 488 nm as a function of solution pH.* ***(B)*** *Average fluorescence intensity of eGFP as a function of pH.* ***(C)*** *Percentage change in R_{ct} as a function of pH.* ***(D)*** *Percentage change in R_{ct} at pH 5 with (red) and without (orange) cys-NbGFP on the surface. Working electrode area = 0.03 cm^2, n = 3.*

Therefore, instead of trying to alter the surface charges it was decided instead to try an increase the Debye length at the interface. The Debye length can be thought of as the distance over which an the electrical potential can extend [257]. Ions present is the solution can screen the electrostatic force, thereby decreasing the Debye length. If the Debye length is significantly shorter that the distance of the Nb's binding site to the electrodes surface, the electrical potential may be dampened resulting in a loss of sensitivity. Shoute et al. (2023) calculated that in a 1 X PBS solution the Debye length would extend only 0.7 nm from the electrode surface [108]. While in a 0.001 X PBS solution the Debye length would extend to approximately 23 nm. Using ellipsometry data basic ChemDraw calculations it was estimated that the NbGFP's binding site is at least 10 nm from the electrode surface. Thus, it was decided to employ non-Faradaic EIS once more however, this time the eGFP binding would be measured using a 0.001 X PBS solution.

The eGFP incubation was carried out in 1 X PBS, the surface was then washed with with copious amounts of 0.001 X PBS solution. The EIS measurement was kept the same except there was no redox probe present and 0.001 X PBS was used as the measurement solution. There was no R_{ct} region of the EIS spectrum as there was no $Fe(CN)_6^{-3/-4}$ present (figure 5.3.37 (A)). However, in the low frequency range ($\approx$ 200 mHz) there was a significant difference after eGFP incubation in the imaginary component of the capacitance when 0.001 X PBS was used compared to 1 X PBS (figure (C) and (D)).

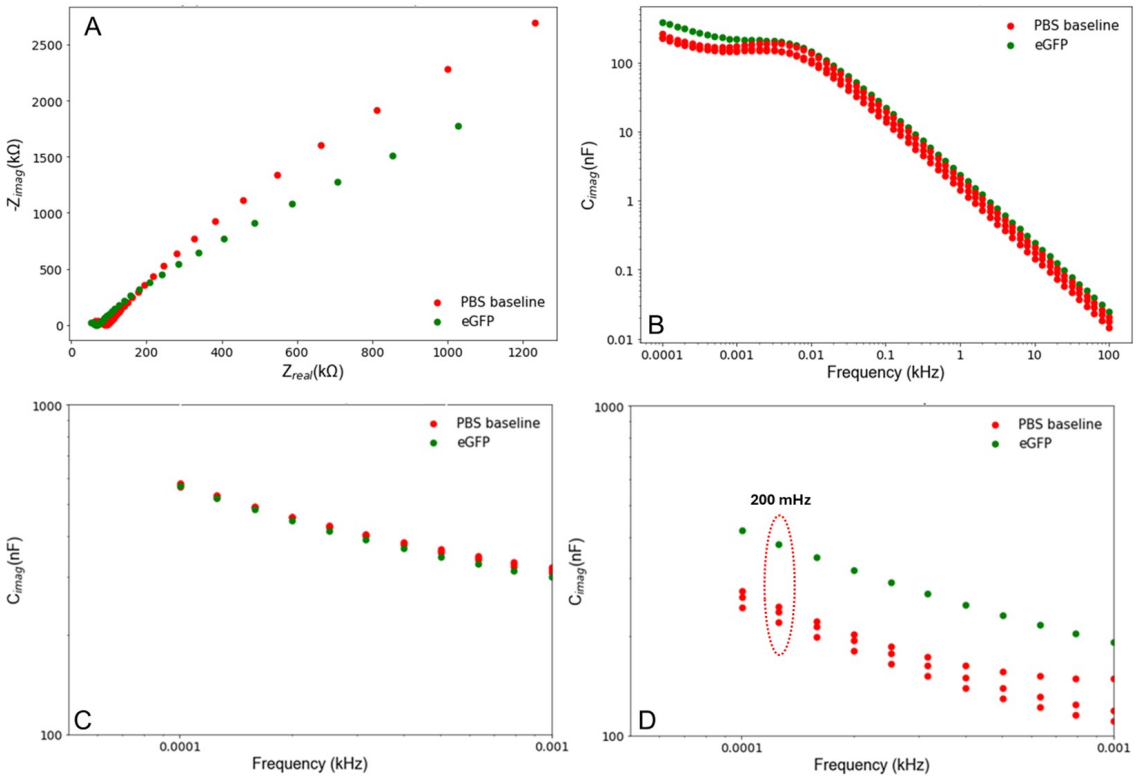

Figure 5.3.37: *Non-Faradaic EIS carried out in 0.001 X PBS.* ***(A)*** *Nyquist plot of the stable PBS baseline before eGFP incubation (red) and after eGFP incubation (green).* ***(B)*** *Bode plot showing three baseline measurements before (red) and after (green) eGFP incubation. Bode plots showing the low frequency range of the EIS spectrum when the measurement was carried out in 1 X PBS* ***(C)*** *and 0.001 X PBS* ***(D)****. Working electrode area = 0.03 cm^2.*

From these results, 200 mHz was chosen as the frequency to monitor the change in capacitance after eGFP incubation. Three control experiments were designed to determine if specific NbGFP-eGFP interactions could be detected. First the eGFP was incubated on the SMCC surface without any Nbs present, the second was eGFP incubated on the surface with NbGFP coupled to the interface, and finally, eGFP was incubated on the surface with Nbs specific for red fluorescent protein (NbRFP) coupled to the interface (figure 5.3.38).

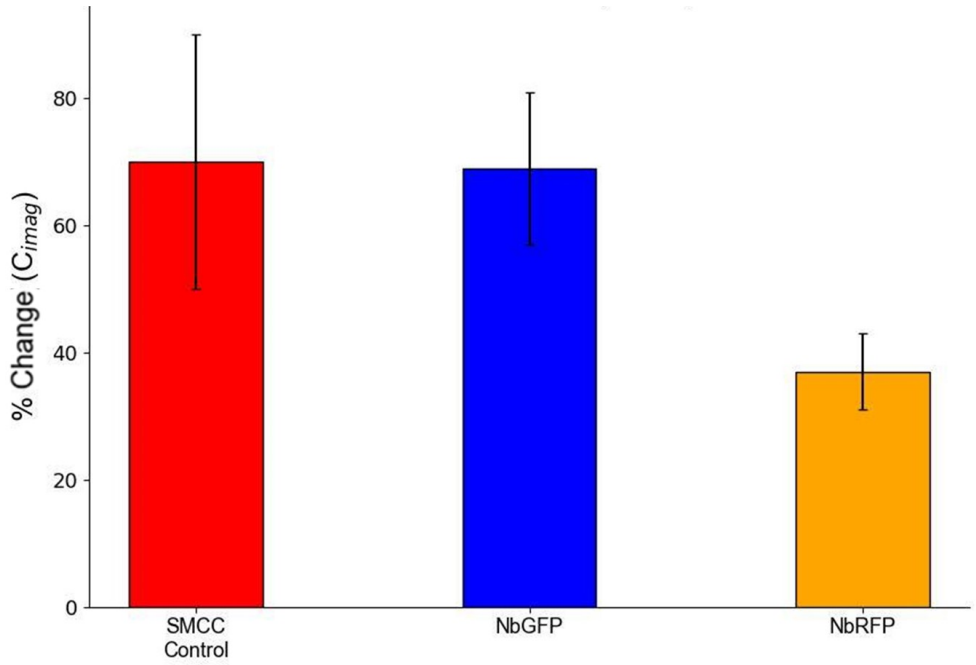

Figure 5.3.38: *The percentage change in capacitance after eGFP incubation on the three different surfaces. Working electrode area = 0.03 cm^2, n = 3.*

The percentage change in capacitance after eGFP incubation was the same on the SMCC and NbGFP surfaces ($\approx$ 70%). This suggested that the system could not detect specific NbGFP-eGFP interactions. However, when eGFP was incubated on the surface with NbRFP, the percentage change was only $\approx$ 40%. This indicated that the eGFP can interact with the SMCC surface through thiol-maleimide coupling or other non-specific interactions. The NbRFP essentially blocks the surface as it does not bind eGFP therefore, this allows the NbGFP binding response to be resolved into two separate surface interactions. 40% of the response corresponds to eGFP non-specifically interacting with the surface, and the remaining 30% corresponds to specific NbGFP-eGFP interactions. 30% is a significant signal response for non-faradaic EIS detection, which has the added benefit of not needing a redox probed added to the PBS solution. These results demonstrate that controlling the ionic strength of the analytical solution can sig-

nificantly improve the biosensing signal response.

As NbGFP has been successfully covalently attached to the Ptyr film using SMCC, and now specific NbGFP-eGFP interactions have been demonstrated, the biosensing interface was characterised using XPS. Figure 5.3.39 shows the high resolution spectra for the Au 4f, C 1s, O 1s, and N 1s XPS regions on bare Au, Ptyr, Ptyr-SMCC, and Ptyr-SMCC-NbGFP surfaces. Across all samples, sulphur could not be detected therefore, the spectra were omitted from figure 5.3.39. As the cys-NbGFP is known to contain a C-terminal cysteine residue, sulphur is definitely present on the Nb's surface. However, the concentration seems to be too low to be detected using XPS.

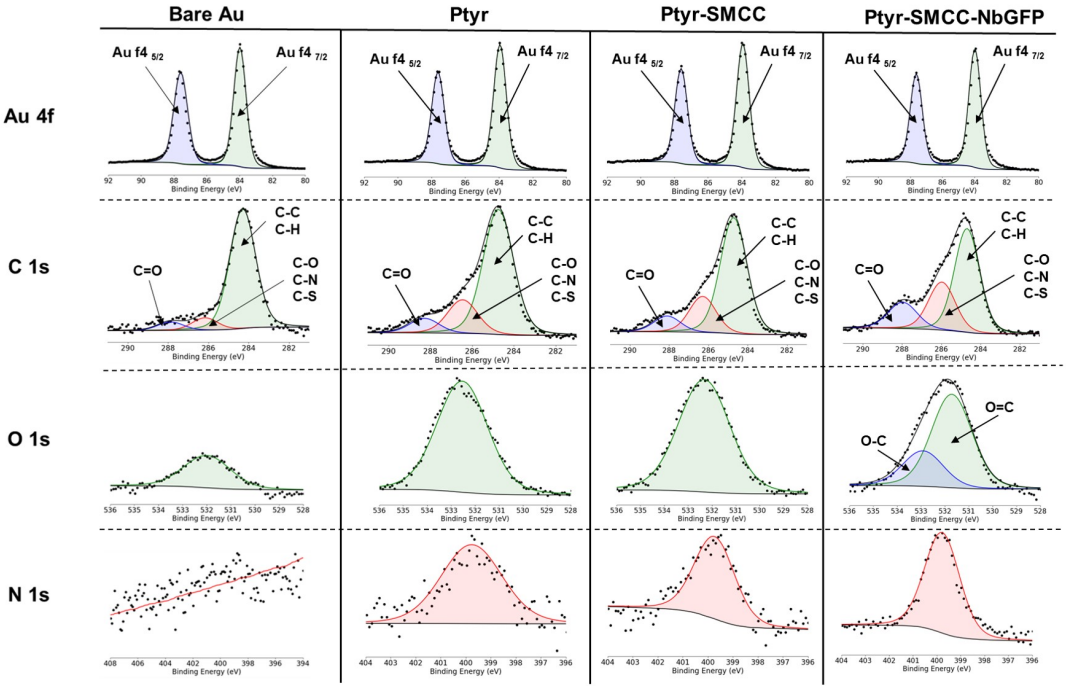

Figure 5.3.39: *High resolution spectra for the Au 4f, C 1s, O 1s, and N 1s XPS regions on bare Au, Ptyr, Ptyr-SMCC, and Ptyr-SMCC-NbGFP surfaces. Four measurements were carried out across two different samples.*

The presence of the Ptyr film on the surface was confirmed by XPS, with the ratio of C/Au increasing from 0.8 on the bare Au surface to 7.3 after Ptyr elec-

tropolymerisation. Nitrogen was also detected after functionalisation with a relative atomic percentage on 5.3 $\pm$ 1.7 %. This is expected as the Ptyr film contains primary amines. Furthermore, SMCC activation caused an increase in the ratio of C/Au and O/Au of 1.5 and 0.2 respectively. Finally, the presence of the cys-NbGFP on the surface was confirmed by the increase in the ratio of carbon, oxygen, and nitrogen to gold. The high resolution O 1s spectra could also be resolved into the corresponding sub peaks (C=O and C-O) after Nb coupling. The Ptyr and Ptyr-SMCC surface only showed one peak corresponding to the O=C chemical environment. Nitrogen is a common element to all amino acids therefore, an increase in the relative atomic percentage of nitrogen on the surface is expected after Nb coupling.

	Relative Atomic %				Relative Components %				
	Bare Au	Ptyr	SMCC	NbGFP	Components	Bare Au	Ptyr	SMCC	NbGFP
Au	52.5 ± 2.1	9.5 ± 1.3	8 ± 1.4	7.0 ± 0.1	4f 7/2 4f 5/2	28.5 ± 2.3 23.1 ± 0.1	5.0 ± 0.4 3.7 ± 0.3	4.3 ± 0.2 3.3 ± 0.2	3.3 ± 0.4 2.4 ± 0.2
C	40.5 ± 3.5	68 ± 1.4	70 ± 1.4	68 ± 2.8	C-C/C-H C-O C-N C-S C=O	32.3 ± 6.1 4.0 ± 2.0 3.4 ± 0.5	47.3 ± 4.0 12.2 ± 5.0 8.6 ± 4.0	56.9 ± 2.0 15.6 ± 0.8 7.2 ± 0.8	42.3 ± 7.4 15.5 ± 4.0 10.4 ± 0.7
O	7.5 ± 2.1	17 ± 1.4	16.5 ± 2.1	16 ± 0.2	O=C O-C	7.5 ± 2.1 --	17 ± 1.4 --	16.5 ± 2.1 --	4.3 ± 0.6 12.4 ± 0.1
N	--	5.3 ± 1.7	5.5 ± 0.7	10 ± 1.4	N 1S	--	5.3 ± 1.7	5.6 ± 1.1	9.5 ± 1.5
S	--	--	--	--	S 2p	--	--	--	--

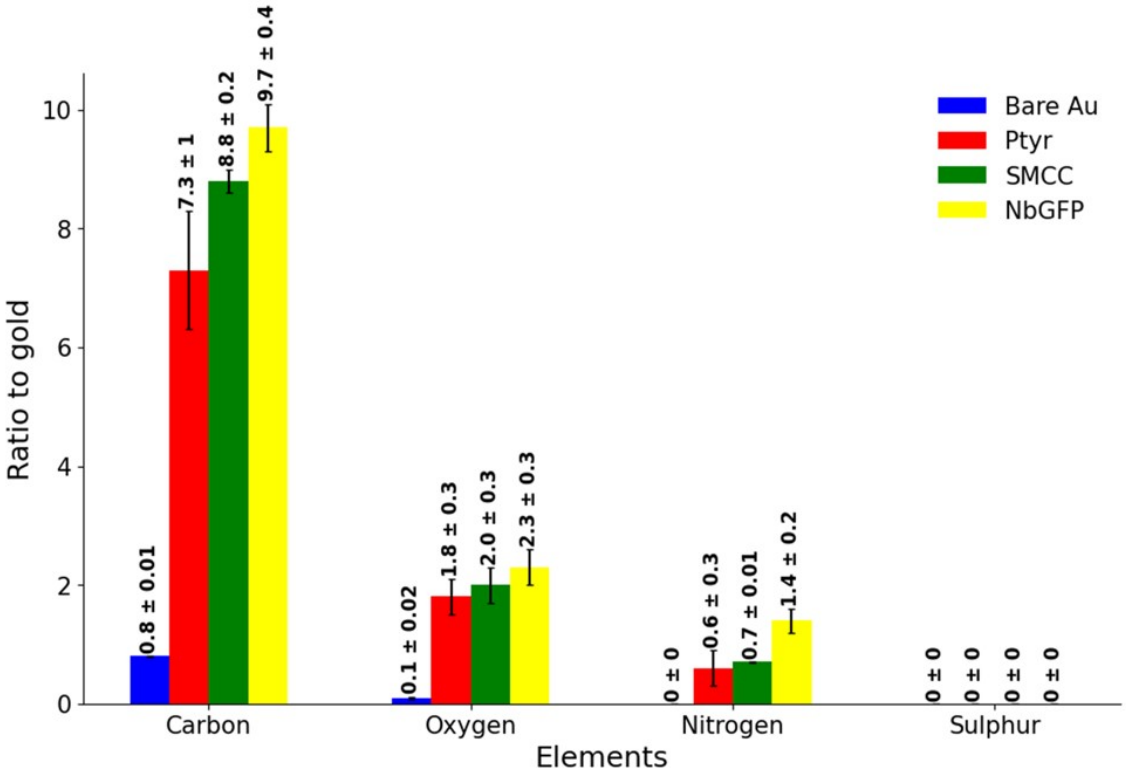

Figure 5.3.40: top: *Relative atomic and component percentages for the bare Au, Ptyr, Ptyr-SMCC, and pTYR-SMCC-NbGFP surfaces.* ***bottom:*** *Comparison of the ratios of carbon, oxygen, nitrogen, and sulphur to gold for the four samples. Four measurements were carried out across two different samples and all values are reported as the average ± the standard deviation of the sample.*

5.4 Conclusion

The 4-NBDT derived films which were optimised in chapter 4 were investigated for the coupling of NbGFP to the biosensing interface. It was discovered that holding the reduction potential at -0.85 V for 10 minutes was more efficient at converting the NO_2 groups into NH_2 groups. This suggests that the rate limiting step for this conversion was the charge transfer through the organic film and not proton availability. However, SPR control experiments showed that this surface could not be activated by various strategies reported in the literature. The Nbs seemed to be non-specifically absorbing into the film which was backed up by ellipsometry and fluorescent microscopy experiments. It was hypothesised this was due to the limited nucleophilicity of the aromatic amines due to their resonance stabilisation.

This seemed to be confirmed when the 4-NBDT derived films were replaced by the tyramine derived films. It was initially showed that Ptyr films were suitable for activation using DSC and Nbs were covalently coupled to the interface. This was likely due to the increased nucleophilicity of the aliphatic amines compared to the aromatic amine of the 4-NBDT derived films. However, when eGFP detection was carried out electrochemically, a maximum signal response of $\approx$ 10% was obtained. Optimisation of the Ptyr film was carried out along with investigating different Nb concentrations and coupling strategies however, these efforts did not imporve the detection response.

It was decided to adopt a more tailored approach to surface activation and Nb coupling. Sulfo-SMCC was used to introduce a maleimide group onto the Ptyr surface. This could be carried out in PBS removing the need for organic solvents

which can have a detrimental effect on the surface. Nbs were purchased from NanoTag Biotechnologies which had a C-terminal cysteine residue. Under neutral pHs the thiol group of the cysteine is around 1000 times more reactive towards the maleimide groups compared to the free lysine residues on the Nb's surface. SPR was used to monitor each fabrication step and subsequent eGFP binding. These experiments demonstrated specific NbGFP-eGFP interactions on the Ptyr-SMCC-cysNbGFP surface. Furthermore, control experiments also demonstrated the Ptyr film's capacity to protect the gold surface from non-specific interactions with NbGFP and eGFP. This surface activation strategy was also suitable for coupling the C8K oligopeptides simultaneously with the cys-NbGFP due to the presence of a C-terminal cysteine residue at the end of the oligopeptides.

When eGFP detection was carried out electrochemically the response was again extremely low $\approx$ 5-10%. It was shown that varying the surface charge of the Nbs effected the EIS detection response but still did not significantly increase the magnitude. However, when the Debye length was increased by lowering the ionic strength of the PBS solution to 0.001 X PBS, a significant change in the capacitance was observed after eGFP incubation. This was likely due to the prevention of the measured electrical potential from being dampened thus, improving the signal response. Through careful control experiments a signal response of $\approx$ 30% could be contributed to specific NbGFP-eGFP interactions. This is a significant response for non-Faradaic EIS and offers a promising method for the sensitive detection of eGFP moving forward. Finally, this surface was analysed using XPS to further characterise each fabrication step.

Chapter 6. Concluding Remarks and Future Work

This thesis involved a range of different studies and investigations which together guide the development of electrically switchable surfaces, towards on-demand biosensing in cell and gene therapy bioprocessing. In particular, this research has demonstrate the capacity of charged oligopeptides to change their surface confirmation in response to applied potentials, and has laid the ground work for developing more sensitive biosensing platforms in the future. Advanced surface characterisation techniques such as SPR, EIS, CV, and XPS formed the conclusions of this research, and provided valuable insights into surface architectures along with the physical, chemical, and electrochemical properties of the electrode-solution interface. These strategies and insights can be applied to a wide range of biotechnologies involving surface modifications.

The following section outlines the findings and conclusions from research chapters 3-5, and finally discusses the author's suggestions for future investigations.

Chapter 3 was primarily concerned with the modification of gold substrates with NbGFP and C8K oligopeptides for the modulation of NbGFP-eGFP interactions. It was initially demonstrated through XPS, ellipsometry, and EIS that NbGFP could be directly immobilised onto gold surfaces via incubation in PBS (pH 5.6) for 2 hours. Using the same protocol C8K oligopeptides were also functionalised to the surface however, due to their flexible nature seemed to adopt a 'flat' confirmation. This caused the C8K to take up a large surface footprint which prevented high packing densities. This was also evident when Nbs and C8K were incubated on gold electrodes and measured using EIS. When only NbGFP was

incubated on the rod electrodes a clear change in the R_{ct} was observe. This indicates that the Nbs form a relative packed layer on the surface which limits the reduction and oxidation of the probe at the interface. In contrast, when C8K was included on the surface there was no significant change in R_{ct} suggesting that the layer was loosely packed with large amount of gold surface exposed to the surrounding solution. This resulted in a large amount of non-specific interactions between the eGFP and the interface as SPR studies showed that eGFP has a high affinity towards the gold surface. This made it difficult to determine how much of the binding response corresponded to specific NbGFP-eGFP interactions and non-specific eGFP-surface interactions. Regardless, applying electrical potentials across the interface when C8K was present modulated the interactions of eGFP with the surface (when monitored using SPR). This suggested that C8K underwent a confirmational change which restricted eGFP from binding to the interface.

Another, important conclusion from this chapter was the need to better insulate the gold surface from the surrounding environment along with having a more controlled method for coupling the NbGFP and C8K to the surface. A convenient way to address both needs was to incorporate a functionalisation layer in the form of an electropolymerised film. This should also improve the stability of the surface components which in turn will lengthen the self-life of the final biosensing platform.

Chapter 4 involved investigating different monomer units for fabricating an electropolymerised film which could be controlled in terms of its physical and

electrochemical properties. Using 4-NBDT allowed greatest control over the film's thickness by varying the applied potential time. The growth of the film occurred in two distinct phases, the first of which was characterised by an increase in film density but not thickness. The second phase, which started after 25 seconds saw a rapid increase in film thickness to around 9 nm after 10 minutes. This suggested that the radicals preferentially react with the gold surface before polymerising with molecules which had already been attached to the surface. An electropolymerisation time of 25 seconds was chosen for film fabrication as this produced this thinnest film ($\approx$ 4 nm) while still completely suppressing the redox activity of the $Fe(CN)_6^{-3/-4}$ redox probe. It was hoped that this would help reduce non-specific interactions with the gold surface moving forward.

In parallel with these electropolymerisation studies, electrode arrays were also fabricated. It was an initial goal of this research project to develop in-house arrays with working electrodes that could be individually or simultaneously electrically addressed. This would allow multiple analytes from the same sample to be detected at once or across different time points. This would also be important for future work carried out in the group, which would likely include the development of a microfluidic platform which would allow convenient integration of the biosensing platform with existing bioreactors. Array fabrication was carried out using cleanroom processes including thermal evaporation, spin coating, photolithography, and chemical etching. Biosensing hardware was also fabricated which allowed the arrays to be electrically addressed using preexisting potentiostats. The electrode array worked as expected and allowed the seamless transfer of the opti-

mised 4-NBDT derived films from the Au/Si substrates to the arrays.

Chapter 5, which was the final research chapter of this thesis, focused primarily on NbGFP coupling to the electropolymerised films, and optimising the eGFP detection response. Initially, 4-NBDT derived films were used for NbGFP coupling however, through various control experiments involving EIS, SPR, and fluorescent microscopy it seemed that the aromatic amines could not be effectively activated for NbGFP coupling. This was due to the resonance stability provided by the aromatic ring, which reduced the nucleophilicity of the amines. This was overcome by utilising tyramine derived films, which contained an aliphatic amine. The polytyramine films were optimised to completely insulate the electrode from the surrounding environment. This was achieved using 25 mM tyramine, scanning the potential between 0 and 1.6 V for two cycles at 100 mV/s. This resulted in a film thickness of $\approx$ 5 nm which was comparable to the 4-NBDT derived films and would keep the Nbs in close spatial contact with the transducer. While many coupling strategies were adapted from the literature, the use of organic solvents for film activation still limited the number of control experiments which could be carried out, particularly using SPR. Therefore, the surface activation and NbGFP coupling steps were redesigned so they could be carried out in an aqueous environment. Furthermore, the Nb was engineered to contain a C-terminal cysteine residue which allowed for site-specific coupling. This resulted in control over the orientation of the Nb's binding site on the surface. SPR control experiments confirmed specific NbGFP-eGFP interactions and also demonstrated the capacity of the polytyramine film to prevent a large amount of non-specific interactions be-

tween eGFP and the gold surface.

Finally, it was shown that due to the non-conducting nature of the tyramine derived films that the system was more sensitive to capacitance changes rather than changes in resistance. Therefore, by utilising non-Faradaic EIS and optimising the ionic strength of the measurement solution, a significant signal response could be detected following eGFP incubation. This has the added benefit of not needing to include a redox probe to carried out the detection which will be beneficial for the end application of the biosensing platform. Further control experiments demonstrated that there was still non-specific interactions between the eGFP and the SMCC activated surface. However, for the first in this research, 30 % of the signal response could be attributed to specific NbGFP-eGFP interactions measured using an electrochemical detection method.

Given the above, future research should focus on limiting the amount of non-specific interactions between the eGFP and the SMCC activated surface. This could involved optimising the NbGFP concentration on the surface or incorporating a blocking agent such polyethylene glycol. Once these interactions have been limited oligopeptides can be included on the surface. The presence of the electropolymerised film and covalent coupling of the biomolecules should allow larger magnitude potentials to be applied. This may result in a more effective change in the confirmation of the oligopeptides offering significant control over NbGFP-eGFP interactions. Once a high switching capacity has been demonstrated the platforms stability and resistance to fouling should be investigated in more complex media (such as cell culture media and real cell samples). The de-

signs of the electrode arrays may also need to be optimised in order to be successfully incorporated into microfluidic devices. This will be important for integration with bioreactor platforms in the future.

The Ptyr-SMCC platform offers a robust surface to directly immobilise receptor components in a controlled orientation for the label free detection of analytes. This makes the platform promising for use in the bioprocessing of cell and gene therapies. Other receptor components should also be investigated such as different Nbs, aptamers, enzymes, and antibodies. This may allow the platform to be quickly modified for the detection of various analytes in different settings, by simply switching the recognition components. It would also be interesting to investigate if the platform could be directly transferred to electrodes fabricated through different techniques such as screen printing, and made from different materials such as carbon. This would improve the platform's versatility and adaptability, potentially making it a universal tool for a wide range of applications. The use of different materials could also influence the sensitivity and specificity of the platform, opening up new avenues for optimisation

Chapter 7. Materials and Methods

7.1 Chemicals and biomolecules Used

The following chemicals were purchased from Sigma Aldrich and used as received: Sulfuric acid (95-98%), hydrochloirc acid (37% aqueous solution) hydrogen peroxide (30% aqueous solution), acetic acid ($\geq$ 99.8%), sodium acetate ($\geq$ 99%), sodium hydroxide ($\geq$ 97), ethanol (HPLC grade, $\geq$ 99.9%), methanol (anhydrous, 99.5%), dimethylformamide (anhydrous, 99.8%), acetonitrile (anhydrous, 99.8%), potassium hexacyanoferrate (III) ($\geq$ 99%), potassium hexacyanoferrate (II) trihydrate ($\geq$ 98.5%), potassium chloride ($\geq$ 99%), pyrrole-3-carboxylic acid ($\geq$ 96%), sodium nitrite ($\geq$ 99.9%), 4-aminobenzoic acid ($\geq$ 99%), 4-nitrobenzenediazonium tetrafluoroborate (97%), N,N′-disuccinimidyl carbonate ($\geq$ 95%), succinic anhydride ($\geq$ 99%), N-hydroxysuccinimide (98%),N-(3-dimethylaminopropyl)-N′-ethyl-carbodiimide hydrochloride ($\geq$ 98%), divinyl sulfone ($\geq$ 98%), tyramine ($\geq$ 98%), triphenylphosphine ($\geq$ 99%), glutaraldehyde solution (50 wt.% in water), 4-(N-maleimidomethyl)cyclo-hexane-1-carboxylic acid 3-sulfo-N-hydroxysuccinimide ester sodium salt.

Nanobodies specific for green-fluorescent-protein (category number: gt), and enhanced-green-fluorescent protein (category number: EGFP) were purchased from Chromotek. Nanobodies with a C-termial cysteine residue were purchased from NanoTag Biotechnologies Ltd. (Germany).

When water is mentioned in this research, this always is referring to ultra high pure water obtained from a Milli-Q water system (resistance = approx. 17.6 MΩ.cm).

C8K (cys-lys(ε-lys)$_7$, purity above 90%) was purchased from Peptide Protein Research Ltd (UK).

Phosphate buffered saline tablets were purchased from Thermo Fischer Scientific Ltd. One table was dissolved in 100 mL of water to create a 1 X PBS solution (pH 7.3-7.4, consisting of KH_2PO_4 1.8 mM, NaCl 137 mM, $Na_2HPO_4 \cdot 7H_2O$ 10 mM, KCl 2.7 mM).

7.2 Materials Used

Gold-glass SPR substrates (product code: 13206060-30) were purchased from ATG Scientific Ltd. (UK), which consisted of polycrystalline gold surfaces (100 nm) on glass substrates, sized 1 cm x 1 cm. For ellipsometry, XPS, and contact angle studies, gold-silicon wafers were purchased from George Albert PVD (Germany) and cut into 1 cm x 1cm pieces using a diamond scribe. These consisted of 100 nm of gold on silicon wafers with a titanium adhesion layer. Gold working electrodes (2 mm diameter, part number: CHI101P), Ag/AgCl (3 M KCl) reference electrodes (part number: CHI111P), and platinum counter electrodes (25 μm diameter, part number: CHI108P) were purchased from IJ Camberia Scientific Ltd. (UK). The electrochemical cells used in this research were fabricated from Teflon^{TM} through the University of Birmingham's work shop, located in the physics west building. Heat shrink tubing (10 x 200 mm, diameter 1.5 mm) were purchased from HellermannTyton. Switch boxes (8 switches, 16 pins, part number: NDS-08-V), PCB edge connectors (40 way, 1.27 mm, stock number: 718-8255), and copper wire (0.2 kg, 24 swg) were purchsed from RS Components

Ltd. (UK). Lead free solder (diameter 0.5 mm, part number: 3004364926) was purchased from Henkel.

7.3 Experimental Procedures

7.3.1 Substrate Treatment

The gold/glass and and gold/silicon substrates were cleaned using piranha solution. Sulfuric acid and hydrogen peroxide were mixed together in a shallow glass Petri dish in a 7:3 v/v ratio (10 mL total volume), surrounded by ice in a larger glass water bath. This mixture was allowed to react together for 10 minutes before the gold substrates were submerged in the piranha solution for 10 minutes. The substrates were then carefully removed using a stainless steel tweezers and washed with copious amounts of water and ethanol before being dried and stored under an argon atmosphere.

The commercial gold rod electrodes were manually polished using alumina slurry (0.05 μm) on an electrode polishing pad for 1 minutes in a figure of 8 motion. they were then sonicated in ethanol for 10 minutes to remove any excess alumina particles. Finally, they were cleaned electrochemically in 0.5 M sulfuric acid by scanning the potential from -0.4 to 1.6 V until a stable cyclic voltammogram was obtained (usually around 12 cycles). The electrodes were then washed with copious amounts of water and ethanol and dried under a stream of argon.

The in-house arrays were cleaned using copious amount of acetone and isopropyl alcohol before being dried and stored under an argon environment.

7.3.2 Surface Modification Strategies

7.3.2.1 NbGFP immobilisation directly on gold substrates

250 μL of NbGFP was received from ChromoTek (1 mg/mL) and immediately stored at 4°C until needed. A 3.6 μM solution was obtained by solubilising 7.5 μL of the NbGFP stock solution in 142.5 μL of sodium acetate buffer (pH 5.6). This solution was pipetted directly onto the gold surfaces ensuring the surface area that was to be analysed was fully covered with the solution. The surface was then placed inside an incubation camber on an orbital table with gentle agitation for 2 hours. Finally, the surface was rinsed with sodium acetate buffer and water to remove any non-specifically bound nanobodies. If the sample needed to be dried for characterisation (ellipsometry) it was gently dried under a stream of argon gas.

7.3.2.2 C8K oligopeptide immobilisation directly on gold substrates

C8K oligopeptides (cys-lys(ε-lys)$_7$, 0.2 mg) was received from Peptide Protein Research Ltd. and immediately stored at -20°C until needed. The C8K was the dissolved in 1 mL of sodium acetate buffer (pH 5.6) to give a concentration of 0.2 mg/mL and divided into 40 μL aliquots. The 40 μL aliquots were dissolved in sodium acetate buffer (pH 5.6) to achieve the appropriate concentration for the particular experiment being carried out. The solution was pipetted directly onto the gold surfaces ensuring the surface area that was to be analysed was fully covered with the solution. The surface was then placed inside an incubation camber on

an orbital table with gentle agitation for 2 hours. Finally, the surface was rinsed with sodium acetate buffer and water to remove any non-specifically bound C8K. If the sample needed to be dried for characterisation (ellipsometry) it was gently dried under a stream of argon gas.

7.3.2.3 NbGFP-C8K [1:5] molar ratio immobilisation directly on gold substrates

20 μL of the NbGFP stock solution and 40 μL of the C8K stock solution (preparation described in sections 7.3.2.1 and 7.3.2.2) were pipetted into 340 μL of sodium acetate buffer (pH 5.6). The solution was pipetted directly onto the gold surfaces ensuring the surface area that was to be analysed was fully covered with the solution. The surface was then placed inside an incubation camber on an orbital table with gentle agitation for 2 hours. Finally, the surface was rinsed with sodium acetate buffer and water to remove any non-specifically bound entities. If the sample needed to be dried for characterisation (ellipsometry) it was gently dried under a stream of argon gas.

7.3.2.4 Pyrrole-3-carboxylic acid

Pyrrole-3-carboxylic acid (100 mM) was dissolved in a 1 X PBS solution (pH 7.3-7.4) and poured into the electrochemical cell. The potential was the scanned from 0 to 1.2 V for up to 15 scans at 100 mV/s. The cell was then rinsed out with copious amount of PBS solution before surface characterisation was carried out.

7.3.2.5 4-carboxybenzene diazonium (in situ)

4-aminobenzoic acid (10 mM) was mixed with sodium nitrite (8 mM) in 0.5 M hydrochloric acid (kept in an ice bath) and allowed to react for 5 minutes. The solution was then quickly poured into the electrochemical cell and the potential scanned from 0.6 to -0.6 V for 2 scans at 100 mV/s. Subsequently the potential was held at -0.6 V for different periods of time (0.1 - 600 seconds). The cell was then rinsed with copious amounts of water before characterisation was carried out. If the sample needed to be dried for characterisation (ellipsometry) it was gently dried under a stream of argon gas.

7.3.2.6 4-nitrobenzenediazonium tetrafluoroborate

4-nitrbenzenediazonium tetrafluoroborate (10 mM) was dissolved in 0.5 M sulfuirc acid (8 mL) and poured directly into the electrochemical cell. The potential was scanned from 0.6 to -0.6 V for 2 cycles at 100 mV/s. Alternatively, the potential was held at -0.6 V for varying time periods (0.1 - 600 seconds). The cell was then rinsed with copious amount of water. For NO_2 reduction a solution of 0.1 M KCl in 10% ethanol was filtered and degassed. The solution was then poured into the cell and the potential was swept from 0 to -1 V for 3 cycles at 100 mV/s alternatively, the potential was held at -0.85 V for varying time periods (up to a maximum of 20 minutes).

7.3.2.7 Tyramine

Tyramine (25 mM) was dissolved in a solution of methanol containing 300 mM NaOH. Sonication was used to fully dissolve the tyramine. The solution was poured directly into the electrochemical cell and the potential was scanned from 0 to 1.6 V. The tyramine concentration, number of scans, and scan rate were all varied during the optimisation phase of film fabrication. The cell was then rinsed with copious amounts of methanol and water or with the solvent used for the next surface modification step (PBS, DMF, or ACN). If the sample needed to be dried for characterisation (ellipsometry) it was gently dried under a stream of argon gas.

7.3.3 Surface activation and NbGFP/C8K coupling

Notes: *The next section describes in detail the procedures used for activating the surface and coupling NbGFP and/or C8K oligopeptides to the interface. While the overall procedures remain the same, NbGFP concentrations and the incubation conditions may vary depending on the specific experiment. This is clearly stated in the research chapters where the experiments are discussed. Also, the volume of the incubation solutions needed to be changed depending on the size of the electrode used for the incubation. Likewise, if surface activation or NbGFP coupling was being carried out inside the SPR equipment, the minimum injection volume required to fill the injection loop was 300 μL.*

7.3.3.1 Disuccinimidyl carbonate (DSC)

DSC (15 mM) was dissolved in 2 mL DMF and incubated on the 4-NBDT or tyramine derived films for 30 minutes under gentle agitation. The surface was then rinsed with DMF and PBS (pH 8). NbGFP (3.6 μM) in PBS pH 8 was prepared the same way as described in section 7.3.2.1, except PBS was used instead of

sodium acetate buffer. This NbGFP solution was incubated on the DSC activated surface for 2 hours under gentle agitation. The surface was then washed with PBS (pH 7.3-7.4) and allowed to stabilise in PBS (pH 7.3-7.4) over night at 4°C.

7.3.3.2 Succinic Anhydride (SA)

SA (0.1 M) was dissolved in 2 mL DMF and incubated on 4-NBDT derived film for 24 hours under gentle agitation. The surface was then rinsed with DMF and sodium acetate buffer (pH 5.6). 0.4 M 1-Ethyl-3-[3-dimethylaminopropyl]carbodiimide hydrochloride (EDC) and 0.1 M N-hydroxysuccinimide (NHS) were dissolved in 2 mL sodium acetate buffer (pH 5.6) and incubated on the surface for 15 minutes. NbGFP (3.6 μM) in PBS (pH 8) was then incubated on the surface under gentle agitation for 2 hours. The surface was then washed with PBS (pH 7.3-7.4) and allowed to stabilise in PBS (pH 7.3-7.4) over night at 4°C.

7.3.3.3 Divinyl Sulfone (DVS)

DVS (1 M) was dissolved in 2 mL acetonitrile (ACN) containing triphenylphosphine (10 mM) and incubated on the 4-NBDT or tyramine derived films for 6 hours under gentle agitation. The surface was then washed with ACN and PBS (pH 7.4). NbGFP (3.6 μM) in PBS (pH 7.3-7.4) was then incubated on the surface under gentle agitation for 2 hours. The surface was then washed with PBS (pH 7.3-7.4) and allowed to stabilise in PBS (pH 7.3-7.4) over night at 4°C.

7.3.3.4 Glutaraldehyde

A 10% aqueous solution of glutaraldehyde was incubated on the tyramine derived films for 30 minutes under gentle agitation. The surface was the rinsed with copious amounts of water. NbGFP (3.6 μM) in PBS (pH 8) was then incubated on the surface under gentle agitation for 2 hours. Again the surface was rinsed with copious amounts of water before an ethanolamine (1 M) solution was incubated on the surface to block any remaining aldehyde groups. The surface was then washed with PBS (pH 7.3-7.4) and allowed to stabilise in PBS (pH 7.3-7.4) over night at 4°C.

7.3.3.5 NHS/EDC

NHS/EDC was added to a NbGFP solution in sodium acetate (pH 5.6) to obtain a final molar ratio of NHS/EDC equal to 0.1/0.4 M. This solution was allowed to react for 20 minutes under gentle agitation. This was then diluted in PBS (pH 7.3-7.3) to obtain a final NbGFP concentration of 3.6 μM. This was then incubated on the tyramine derived film for two hours. The surface was then washed with PBS (pH 7.3-7.4) and allowed to stabilise in PBS (pH 7.3-7.4) over night at 4°C.

7.3.3.6 Sulfo-SMCC

Sulfo-SMCC (5 μM) in PBS (pH 7.3-7.4) was incubated on the tyramine derived film for 1 hour under gentle agitation. The surface was then washed with copious amounts of PBS (pH 7.3-7.4). cys-NbGFP (3.6 μM) in PBS (pH 7.3-7.4) was then incubated on the SMCC activated surface for 1 hour. The surface was then

washed with PBS (pH 7.3-7.4) and allowed to stabilise in PBS (pH 7.3-7.4) over night at 4°C. The same procedure was followed for C8K and cysNbGFP-C8K [1:5] coupling.

7.3.4 eGFP incubation

250 μL of eGFP stock solution (1 g/L) was received from ChromoTek and immediately separated into 20 μL aliquots and stored at -20°C. Each 20 μL aliquot of eGFP stock was then solubilised in 1408 μL PBS (pH 7.3-7.4) to obtain a final eGFP concentration of 14 μg/mL or 500 nM. This eGFP solution was then incubated on the particular surface under investigation for 30 minutes with gentle agitation using a pipette every 5 minutes. The surface was then rinsed with copious amount of PBS (pH 7.3-7.4) to remove any non-specifically bound eGFP.

7.4 Surface Characterisation Techniques

7.4.1 Electrochemical Set Up

For the gold substrates (Au/glass and Au/si) a standard three electrode configuration was implemented, with the gold chip acting as the working electrode, an Ag/AgCl (3 M NaCl) reference electrode and a platinum wire counter electrode. Measurements were carried out in a Teflon cell (with Au substartes clamped between the O-rings) using a Gamry potentiostat (Reference 600) connected to a personal computer with Gamry 7.8 installed. The potentiostat was calibrated once a week using a Gamry calibration circuit board. All measurements were carried out inside a Faraday cage to limit external signals affecting the measurements.

The area of the working electrode was defined by the 'O' ring in the Teflon cell, which was either 0.2, 0.79 or 1.54 cm^2 (figure 7.4.1).

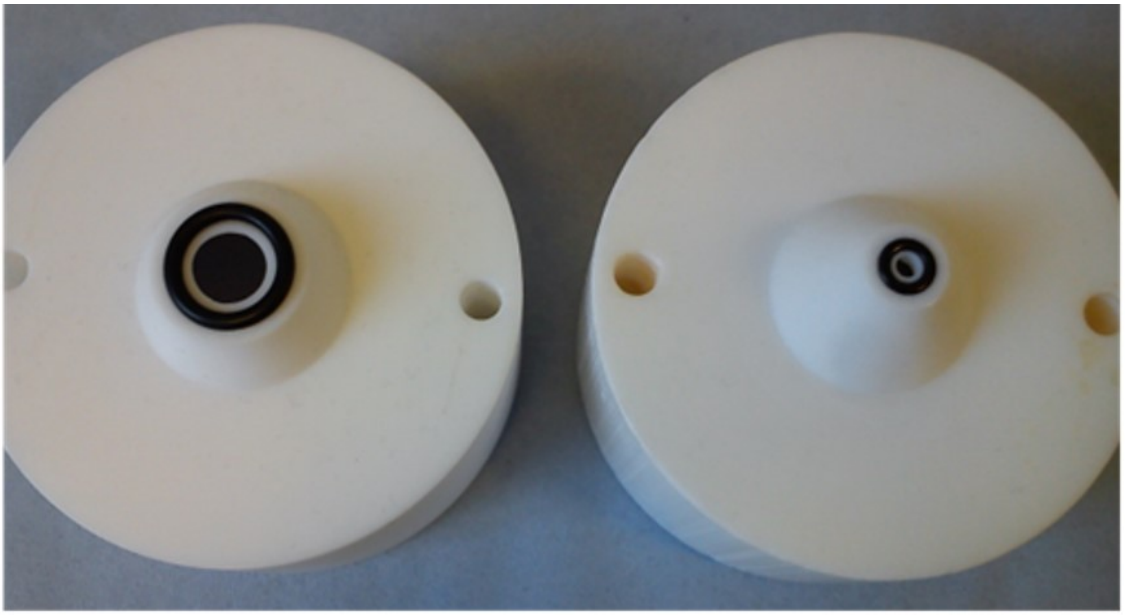

Figure 7.4.1: *Photograph of the underside of two Teflon^{TM} cells with O-ring areas 1.54 (left) and 0.2 cm^2 (right).*

It was decided that all potentials/currents would be applied and reported versus the Ag/AgCl (3 M NaCl) reference electrode and not the OCP. As potentials would likely be applied across the interface during experiments to control the oligopeptide's conformation, the Ag/AgCl electrode would likely provide a more stable reference.

The rod electrodes (working area = 0.03 cm^2) were used with the same set-up except instead of being clamped in the cell, they were inserted through the top of the cell and held in contact with the electrolyte solution with an external clamp. The counter and reference electrodes were also held in place in this manner.

The in-house arrays were clamped in the Teflon^{TM} cells as depicted in figure 4.3.16. The gold counter electrode was Incorporated into the array and an external Ag/AgCl (3 M NaCl) reference electrode was used.

7.4.2 Cyclic Voltammetry (CV)

CV measurements were carried out using the set-up described in section 7.4.1. The redox solution consisted of 10 mM $K_3Fe(CN)_6/K_4Fe(CN)_6$ in 1 X PBS with 1 M KCl. The potential was scanned from 0.6 to -0.6 V at a scan rate of 100 mV/s for two cycles. The step size was 1 mV and there was an initial voltage delay of 30 seconds. Data analysis was carried out using Gamry Echem Analyst software.

7.4.3 Electrochemical Impedance Spectroscopy (EIS)

Potentiostatic EIS was carried out using the redox probe $K_3Fe(CN)_6/K_4Fe(CN)_6$ in 1 X PBS with 1 M KCl. The input AC voltage was 10 mV, and the frequency was scanned from 100 KHz to 0.1 Hz at 10 points/decade. There was an initial voltage delay of 30 seconds. An expansion on the Randles equivalent circuit was used to model the experimental data data, which was discussed in detail in section 2.2.3. Data analysis was carried out using Gamry Echem Analyst software.

For non-Faradaic EIS the experimental parameter remained the same however, the redox probe was omitted from the electrolyte solution. Furthermore, no modelling of the non-Faradaic response was carried out, with single values reported at selected frequencies.

7.4.4 Ellipsometry

All ellipsometry measurements were carried out using an Alpha-SE ellipsometer from J.A. Woollam, which was turned on 30 minutes before use and calibrated before any measurements were taken. At least three separate measurements

were taken on each chip, with the light incident at an angle of 70°. All modelling and data fitting was carried out using CompletEASE software. After washing with piranha, a model was constructed of the bare gold chip to act as its own reference. This was achieved using a B-spline function (resolution 0.1 eV) with the 'fit optical constant' parameter set to 'ON'. The organic film on top of the gold surface was modelled using a Cauchy.mat model with the refractive index set to 1.5 (good for thin transparent films) and the 'fit optical constant' parameter set to 'OFF'.

7.4.5 Contact Angle (CA)

All CA measurements were carried out using an Attention optical tensiometer with Biolin OneAttension instrumentation and software. The machine was calibrated (ball calibration) before measurements were taken and the stage levelled. Dynamic contact angle measurements were taken in Sessile Drop mode with the drop in and out volumes set to 4 μL and the drop rate set to 0.5 μL/s.

7.4.6 Surface Plasmon Resonance (SPR)

All SPR measurements were carried out using a Reichert Technologies SPR. Before any experiments were carried out the SPR equipment was flushed out with 0.5% sodium dodecyl sulfate (SDS), 50 mM glycine pH 9.5 and water. The Running buffer which was usually 1 X PBS was prepared daily, which included filtering (.2 μm filter) and degassing of the solution. The temperature of the SPR was preset to 25°C for all measurements. The stage was cleaned with ethanol before each experiment and fresh immersion oil was then placed on the stage before the

Au substrate to minimise the refractive index change. The SPR response was stabilised before each experiment using the running buffer with the initial flow rate set to 100 μL/min then decreasing to 30 μL/min after 10-15 minutes. Blank injections of the running buffer were then carried out before each experiment to remove any impurities and/or pockets of air in the injection loop. All SPR injections were pre-programmed and consisted of an initial 7 minute loading phase which allowed the sample to be loaded into the injection loop. The injection phase also last 7 minutes with a flow rate of 30 μL/min using a 250 μL injection loop and finally, there was a dissociation or washing phase of the running buffer which lasted 7 minute with a flow rate of 30 μL/min.

The electrochemical SPR (eSPR) experiments followed the same cleaning and preparation steps however, the flow cell had a built in platinum counter electrode and Ag/AgCl (3 M NaCl) reference electrode. This changed the geometry and volume of the SPR's flow cell with resulted in slight modifications to the injection program. The initial 7 minute loading phase remained unchanged however, the injection phase required an initial 1500 μL/min injection burst for 3 seconds to quickly fill the larger cell volume which prevented lost of the SPR signal during the experiment. The dissociation phase also employed this 1500 μL/min injection burst for 3 seconds. Potentials were applied and currents monitored using a Gamry potentiostat (Reference 600) connected to a personal computer with Gamry 7.8 installed.

7.4.7 X-ray Photoelectron Spectroscopy (XPS)

XPS Analysis was performed using a Thermo NEXSA XPS fitted with a monochromated Al kα X-ray source (1486.7 eV), a spherical sector analyser and 3 multi-channel resistive plate, 128 channel delay line detectors. All data was recorded at 19.2W and an X-ray beam size of 200 x 100 μm. Survey scans were recorded at a pass energy of 160 eV, and high-resolution scans recorded at a pass energy of 20 eV. Electronic charge neutralization was achieved using a Dual-beam low-energy electron/ion source (Thermo Scientific FG-03). Ion gun current = 150 μA, ion gun voltage = 45 V. All sample data was recorded at a pressure below 10^{-8} Torr and a room temperature of 294 K. XPS peak fitting was performed using the CasaXP v2.3.19PR1.0 processing software. Either a Shirley or linear background was used and the relative sensitivity factors for quantification were built in to the CasaXPS library (figure 7.4.2). All XPS subpeaks were set to have the same full width half maximum (FWHM) and at least two measurements per sample were perfored at different surface locations.

Element	Relative Sensitivity Factor
Au 4f	6.25
C 1s	1
O 1s	2.93
N 1s	1.8

Figure 7.4.2: *Relative sensitivity factors for CasaXPS*

7.5 Gold Array Fabrication

A glass wafer (76 x 52 mm) was washed with acetone and isopropyl alcohol (IPA) before being dried with a N_2 gun. Chromium (Cr) and Au samples were placed in their respected crucibles inside a vacuum chamber. The wafer was then secured upside down to the roof of the chamber with non-conductive tape and the system was evacuated until the pressure reached below 10^{-6} Torr. A Cr adhesion layer was deposited onto the glass by applying a potential of 2.4 Vresulting is a current of 25 A through the Cr crucible (ramp speed = 5 A). The thickness of the deposited layer was monitored with a quartz crystal micro-balance (tooling = 1.2, density = 7.2). Next the Au layer was deposited by applying a potential of 4.8 V resulting in a current of 75 A through the Au crucible (ramp speed = 10% increase per minute). The thickness of the deposited layer was monitored with a quartz crystal micro-balance (tooling = 1.2, density = 19.32). The camber was then flushed with air and allowed to cool to room temperature over night before the sample was removed.

The gold surface was washed with IPA and dried with a N_2 gun. The sample was then secured to the stage of a spin coater by applying a vacuum. Between 3-5 mL of SPR 220-7.0 (Novalak based resist) was spin coated onto the Au surface at 2800 rpm, using a pre-set program. The resist was then baked at 90°C for 6 minutes followed by 160°C for 4 minutes. The sample was allowed to cool for 20 minutes before being transferred to the mask aligner. The appropriate photomask was placed on top of the sample and the surface was exposed to UV radiation for 35 seconds followed by 25 seconds of rest, this cycle was repeated

4 times.

The sample was developed in 100 mL of tetramethylammonium hydroxide (TMAH) on an automatic agitator for 6-7 minutes. The sample was toughly washed with D.I water and dried with a N_2 gun. The Au was etched for 40 seconds in 50 mL of potassium iodide and the rinsed with water. The Cr layer was etched with a chromium mask etchant CE-5M (dilute perchloric acid) for 10 seconds and then rinsed with D.I water. The remaining SPR 220 photoresist was removed by washing the surface with acetone.

7.6 Statistical Analysis

All measurements were repeated in triplicated unless otherwise stated and results are reported as the mean $\pm$ standard-deviation

References

[1] Abed El-Hakim El-Kadiry, Moutih Rafei, and Riam Shammaa. Cell therapy: types, regulation, and clinical benefits. *Frontiers in Medicine*, 8, **2021**.

[2] Oh Young Bang, Jin Soo Lee, Phil Hyu Lee, and Gwang Lee. Autologous mesenchymal stem cell transplantation in stroke patients. *Annals of Neurology*, 57, **2005**.

[3] Alireza Rezania, Jennifer E Bruin, Payal Arora, Allison Rubin, Irina Batushansky, Ali Asadi, Shannon O'dwyer, Nina Quiskamp, Majid Mojibian, Tobias Albrecht, et al. Reversal of diabetes with insulin-producing cells derived in vitro from human pluripotent stem cells. *Nature biotechnology*, 32(11):1121–1133, **2014**.

[4] Emelia J Benjamin, Michael J Blaha, Stephanie E Chiuve, Mary Cushman, Sandeep R Das, Rajat Deo, Sarah D De Ferranti, James Floyd, Myriam Fornage, Cathleen Gillespie, et al. Heart disease and stroke statistics—2017 update: a report from the american heart association. *circulation*, 135(10):e146–e603, **2017**.

[5] Reza Rikhtegar, Mehdi Yousefi, Sanam Dolati, Hosein Delavar Kasmaei, Saeid Charsouei, Mohammad Nouri, and Seyed Kazem Shakouri. Stem cell-based cell therapy for neuroprotection in stroke: A review. *Journal of cellular biochemistry*, 120(6):8849–8862, **2019**.

[6] Qasim A Rafiq, Karen Twomey, Michael Kulik, Christian Leschke, John O'Dea, Sarah Callens, Chiara Gentili, Frank P Barry, and Mary Murphy. Developing an automated robotic factory for novel stem cell therapy production. *Regenerative Medicine*, 11(4):351–354, **2016**.

[7] Bryan Wang, Annie C. Bowles-Welch, Carolyn Yeago, and Krishnendu Roy. Process analytical technologies in cell therapy manufacturing: State-of-the-art and future directions. *Journal of Advanced Manufacturing and Processing*, 4(1), **2022**.

[8] Linda Dekker and Karen M Polizzi. Sense and sensitivity in bioprocessing—detecting cellular metabolites with biosensors. *Current Opinion in Chemical Biology*, 40:31–36, **2017**. Synthetic Biology * Synthetic Biomolecules.

[9] Daniel A.M. Pais, Manuel JT Carrondo, Paula M Alves, and Ana P Teixeira. Towards real-time monitoring of therapeutic protein quality in mammalian cell processes. *Current Opinion in Biotechnology*, 30:161–167, **2014**. Chemical biotechnology • Pharmaceutical biotechnol-

ogy.

[10] Marc-Olivier Baradez, Daniela Biziato, Enas Hassan, and Damian Marshall. Application of raman spectroscopy and univariate modelling as a process analytical technology for cell therapy bioprocessing. *Frontiers in Medicine*, 5:47, **2018**.

[11] Mason Chilmonczyk and Andrei Fedorov. Improving cell manufacturing outcomes using in-line biomarker monitoring. *BioProcess international*, **2021**.

[12] Il-Hoon Cho, Dong Hyung Kim, and Sangsoo Park. Electrochemical biosensors: Perspective on functional nanomaterials for on-site analysis. *Biomaterials research*, 24(1):1–12, **2020**.

[13] Leland C Clark Jr and Champ Lyons. Electrode systems for continuous monitoring in cardiovascular surgery. *Annals of the New York Academy of sciences*, 102(1):29–45, **1962**.

[14] Daniel P Carroll and Paula M Mendes. Recent advances in surface modification and antifouling strategies for electrochemical sensing in complex biofluids. *Current Opinion in Electrochemistry*, page 101319, **2023**.

[15] Bárbara Santos Gomes, Eleonora Cantini, Stefano Tommasone, Joshua S Gibson, Xingyong Wang, Qiang Zhu, Jing Ma, James D McGettrick, Trystan M Watson, Jon A Preece, et al. On-demand electrical switching of antibody–antigen binding on surfaces. *ACS Applied Bio Materials*, 1(3):738–747, **2018**.

[16] Jiarong Zhang, Hui Sun, Wei Pei, Huijun Jiang, and Jin Chen. Nanobody-based immunosensing methods for safeguarding public health. *Journal of Biomedical Research*, 35(4):318, **2021**.

[17] George P Anderson, Jinny L Liu, Martha L Hale, Rachael D Bernstein, Martin Moore, Marla D Swain, and Ellen R Goldman. Development of antiricin single domain antibodies toward detection and therapeutic reagents. *Analytical Chemistry*, 80(24):9604–9611, **2008**.

[18] Reda Elshafey, Mohamed Siaj, and Mohammed Zourob. Dna aptamers selection and characterization for development of label-free impedimetric aptasensor for neurotoxin anatoxin-a. *Biosensors and Bioelectronics*, 68:295–302, **2015**.

[19] Rastislav Levicky, Tonya M Herne, Michael J Tarlov, and Sushil K Satija. Using self-assembly to control the structure of dna monolayers on gold: a neutron reflectivity study. *Journal of the American Chemical Society*, 120(38):9787–9792, **1998**.

[20] Lanying Li, Lele Wang, Qin Xu, Li Xu, Wen Liang, Yan Li, Min Ding, Ali Aldalbahi, Zhilei Ge, Lihua Wang, et al. Bacterial analysis using an electrochemical dna biosensor with poly-adenine-mediated dna self-assembly. *ACS applied materials & interfaces*, 10(8):6895–6903, **2018**.

[21] Joelle MJ LaFreniere, Emma J Roberge, and Jeffrey M Halpern. Reorientation of polymers in an applied electric field for electrochemical sensors. *Journal of The Electrochemical Society*, 167(3):037556, **2020**.

[22] J Justin Gooding. Advances in interfacial design for electrochemical biosensors and sensors: aryl diazonium salts for modifying carbon and metal electrodes. *Electroanalysis: An International Journal Devoted to Fundamental and Practical Aspects of Electroanalysis*, 20(6):573–582, **2008**.

[23] Marcel WJ Beulen, Miryam I Kastenberg, Frank CJM van Veggel, and David N Reinhoudt. Electrochemical stability of self-assembled monolayers on gold. *Langmuir*, 14(26):7463–7467, **1998**.

[24] Mathieu D'Amours and Daniel Bélanger. Stability of substituted phenyl groups electrochemically grafted at carbon electrode surface. *The Journal of Physical Chemistry B*, 107(20):4811–4817, **2003**.

[25] Dardan Hetemi, Vincent Noël, and Jean Pinson. Grafting of diazonium salts on surfaces: Application to biosensors. *Biosensors*, 10(1):4, **2020**.

[26] Guozhen Liu, Till Böcking, and J Justin Gooding. Diazonium salts: Stable monolayers on gold electrodes for sensing applications. *Journal of Electroanalytical Chemistry*, 600(2):335–344, **2007**.

[27] Paula M Mendes. Stimuli-responsive surfaces for bio-applications. *Chemical Society Reviews*, 37(11):2512–2529, **2008**.

[28] Elizabeth Ratcliffe, Robert J Thomas, and David J Williams. Current understanding and

challenges in bioprocessing of stem cell-based therapies for regenerative medicine. *British medical bulletin*, 100(1):137, **2011**.

[29] Karen Coopman and Nick Medcalf. From production to patient: challenges and approaches for delivering cell therapies. *Stem Book - Harvard Stem Cell Institute*, **2014**.

[30] Abed El-Hakim El-Kadiry, Moutih Rafei, and Riam Shammaa. Cell therapy: types, regulation, and clinical benefits. *Frontiers in Medicine*, page 2340, **2021**.

[31] Natalie M Mount, Stephen J Ward, Panos Kefalas, and Johan Hyllner. Cell-based therapy technology classifications and translational challenges. *Philosophical Transactions of the Royal Society B: Biological Sciences*, 370(1680):20150017, **2015**.

[32] Ali Golchin and Tahereh Zarnoosheh Farahany. Biological products: cellular therapy and fda approved products. *Stem cell reviews and reports*, 15(2):166–175, **2019**.

[33] Morgan L Maeder and Charles A Gersbach. Genome-editing technologies for gene and cell therapy. *Molecular Therapy*, 24(3):430–446, **2016**.

[34] Ali Golchin, Simzar Hosseinzadeh, and Leila Roshangar. The role of nanomaterials in cell delivery systems. *Medical Molecular Morphology*, 51(1):1–12, **2018**.

[35] A De Pieri, Y Rochev, and DI Zeugolis. Scaffold-free cell-based tissue engineering therapies: advances, shortfalls and forecast. npj regenerative medicine, 6, **2021**.

[36] Patty Weasler. Stem cell therapy: Uses, risks, how it works, Aug **2023**.

[37] Sep **2023**.

[38] Bryan Wang, Annie C Bowles-Welch, Carolyn Yeago, and Krishnendu Roy. Process analytical technologies in cell therapy manufacturing: state-of-the-art and future directions. *Journal of Advanced Manufacturing and Processing*, 4(1):e10106, **2022**.

[39] Rajesh Sharma, Susan TL Harrison, and Siew Leng Tai. Advances in bioreactor systems for the production of biologicals in mammalian cells. *ChemBioEng Reviews*, 9(1):42–62, **2022**.

[40] Helena Kilpinen, Angela Goncalves, Andreas Leha, Vackar Afzal, Kaur Alasoo, Sofie Ashford, Sendu Bala, Dalila Bensaddek, Francesco Paolo Casale, Oliver J Culley, et al. Common genetic variation drives molecular heterogeneity in human ipscs. *Nature*,

546(7658):370–375, **2017**.

[41] Teng Ma, Ang-Chen Tsai, and Yijun Liu. Biomanufacturing of human mesenchymal stem cells in cell therapy: influence of microenvironment on scalable expansion in bioreactors. *Biochemical Engineering Journal*, 108:44–50, **2016**.

[42] Peng-Xia Wan, Bo-Wen Wang, and Zhi-Chong Wang. Importance of the stem cell microenvironment for ophthalmological cell-based therapy. *World journal of stem cells*, 7(2):448, **2015**.

[43] Yonatan Y Lipsitz, Nicholas E Timmins, and Peter W Zandstra. Quality cell therapy manufacturing by design. *Nature biotechnology*, 34(4):393–400, **2016**.

[44] Andrew Campbell, Thomas Brieva, Lior Raviv, Jon Rowley, Knut Niss, Harvey Brandwein, Steve Oh, and Ohad Karnieli. Concise review: process development considerations for cell therapy. *Stem cells translational medicine*, 4(10):1155–1163, **2015**.

[45] C Watts. Pat–a framework for innovative pharmaceutical development manufacturing and quality assurance. In *FDA/RPSGB Guidance Workshop*, **2004**.

[46] Nicholas R Abu-Absi, Richard P Martel, Amanda M Lanza, Stacey J Clements, Michael C Borys, and Zheng Jian Li. Application of spectroscopic methods for monitoring of bioprocesses and the implications for the manufacture of biologics. *Pharmaceutical Bioprocessing*, 2(3):267–284, **2014**.

[47] Darrin Pochan and Oren Scherman. Introduction: Molecular self-assembly, **2021**.

[48] Quanmin Guo and Fangsen Li. Self-assembled alkanethiol monolayers on gold surfaces: resolving the complex structure at the interface by stm. *Physical Chemistry Chemical Physics*, 16(36):19074–19090, **2014**.

[49] Ian Ivar Suni. Substrate materials for biomolecular immobilization within electrochemical biosensors. *Biosensors*, 11(7):239, **2021**.

[50] Stefano Casalini, Carlo Augusto Bortolotti, Francesca Leonardi, and Fabio Biscarini. Self-assembled monolayers in organic electronics. *Chemical Society Reviews*, 46(1):40–71, **2017**.

[51] J Christopher Love, Lara A Estroff, Jennah K Kriebel, Ralph G Nuzzo, and George M White-

sides. Self-assembled monolayers of thiolates on metals as a form of nanotechnology. *Chemical reviews*, 105(4):1103–1170, **2005**.

[52] Judit Telegdi. Formation of self-assembled anticorrosion films on different metals. *Materials*, 13(22):5089, **2020**.

[53] Mark H Schoenfisch and Jeanne E Pemberton. Air stability of alkanethiol self-assembled monolayers on silver and gold surfaces. *Journal of the American Chemical Society*, 120(18):4502–4513, **1998**.

[54] Zafer Üstündağ, Mustafa Oğuzhan Çağlayan, Remziye Güzel, Erhan Pişkin, and Ali Osman Solak. A novel surface plasmon resonance enhanced total internal reflection ellipsometric application: electrochemically grafted isophthalic acid nanofilm on gold surface. *Analyst*, 136(7):1464–1471, **2011**.

[55] Raquel García-González, M Teresa Fernández-Abedul, Alberto Pernía, and Agustín Costa-García. Electrochemical characterization of different screen-printed gold electrodes. *Electrochimica Acta*, 53(8):3242–3249, **2008**.

[56] Yurui Xue, Xun Li, Hongbin Li, and Wenke Zhang. Quantifying thiol–gold interactions towards the efficient strength control. *Nature communications*, 5(1):4348, **2014**.

[57] Michael S Inkpen, Zhen-Fei Liu, Haixing Li, Luis M Campos, Jeffrey B Neaton, and Latha Venkataraman. Non-chemisorbed gold–sulfur binding prevails in self-assembled monolayers. *Nature chemistry*, 11(4):351–358, **2019**.

[58] Thomas Bürgi. Properties of the gold–sulphur interface: from self-assembled monolayers to clusters. *Nanoscale*, 7(38):15553–15567, **2015**.

[59] C Vericat, ME Vela, G Benitez, P Carro, and RC Salvarezza. Self-assembled monolayers of thiols and dithiols on gold: new challenges for a well-known system. *Chemical Society Reviews*, 39(5):1805–1834, **2010**.

[60] Yunsoo Choi, Hung-Vu Tran, and T Randall Lee. Self-assembled monolayer coatings on gold and silica surfaces for antifouling applications: A review. *Coatings*, 12(10):1462, **2022**.

[61] Warakorn Limbut, Proespichaya Kanatharana, Bo Mattiasson, Punnee Asawatreratanakul, and Panote Thavarungkul. A comparative study of capacitive immunosensors based on

self-assembled monolayers formed from thiourea, thioctic acid, and 3-mercaptopropionic acid. *Biosensors and Bioelectronics*, 22(2):233–240, **2006**.

[62] Keying Guo, Shofarul Wustoni, Anil Koklu, Escarlet Díaz-Galicia, Maximilian Moser, Adel Hama, Ahmed A Alqahtani, Adeel Nazir Ahmad, Fatimah Saeed Alhamlan, Muhammad Shuaib, et al. Rapid single-molecule detection of covid-19 and mers antigens via nanobody-functionalized organic electrochemical transistors. *Nature biomedical engineering*, 5(7):666–677, **2021**.

[63] Madhavi Pali and Ian I. Suni. Impedance detection of 3-phenoxybenzoic acid comparing wholes antibodies and antibody fragments for biomolecular recognition. *Electroanalysis*, 30(12):2899–2907, **2018**.

[64] Sarunas Zukauskas, Alma Rucinskiene, Vilma Ratautaite, Almira Ramanaviciene, Greta Pilvenyte, Mikhael Bechelany, and Arunas Ramanavicius. Electrochemical biosensor for the determination of specific antibodies against sars-cov-2 spike protein. *International Journal of Molecular Sciences*, 24(1), **2023**.

[65] Md. Ashaduzzaman, Aswathi Anto Antony, N. Arul Murugan, Swapneel R. Deshpande, Anthony P.F. Turner, and Ashutosh Tiwari. Studies on an on/off-switchable immunosensor for troponin t. *Biosensors and Bioelectronics*, 73:100–107, **2015**.

[66] Reda Elshafey, Mohamed Siaj, and Mohammed Zourob. Dna aptamers selection and characterization for development of label-free impedimetric aptasensor for neurotoxin anatoxin-a. *Biosensors and Bioelectronics*, 68:295–302, **2015**.

[67] Haiying Yang, Huafeng Zhou, Haoyong Hao, Qiaojuan Gong, and Kai Nie. Detection of escherichia coli with a label-free impedimetric biosensor based on lectin functionalized mixed self-assembled monolayer. *Sensors and Actuators B: Chemical*, 229:297–304, **2016**.

[68] Mong-Tung Lee, Chen-Chan Hsueh, Michael S Freund, and Gregory S Ferguson. Air oxidation of self-assembled monolayers on polycrystalline gold: the role of the gold substrate. *Langmuir*, 14(22):6419–6423, **1998**.

[69] Serge Cosnier. Biosensors based on electropolymerized films: new trends. *Analytical and Bioanalytical Chemistry*, 377:507–520, **2003**.

[70] Alex Palma-Cando, Ibeth Rendón-Enríquez, Michael Tausch, and Ullrich Scherf. Thin functional polymer films by electropolymerization. *Nanomaterials*, 9(8):1125, **2019**.

[71] Guocheng Yang, Yan Shen, Mingkui Wang, Hongjun Chen, Baifeng Liu, and Shaojun Dong. Copper hexacyanoferrate multilayer films on glassy carbon electrode modified with 4-aminobenzoic acid in aqueous solution. *Talanta*, 68(3):741–747, **2006**.

[72] MV Deshpande and DP Amalnerkar. Biosensors prepared from electrochemically-synthesized conducting polymers. *Progress in polymer science*, 18(4):623–649, **1993**.

[73] Laia Civit, Alex Fragoso, and Ciara K O'Sullivan. Thermal stability of diazonium derived and thiol-derived layers on gold for application in genosensors. *Electrochemistry Communications*, 12(8):1045–1048, **2010**.

[74] Emad A Khudaish, Khawla Y Al-Ajmi, and Salim H Al-Harthi. A solid-state sensor based on ruthenium (ii) complex immobilized on polytyramine film for the simultaneous determination of dopamine, ascorbic acid and uric acid. *Thin Solid Films*, 564:390–396, **2014**.

[75] T Menanteau, Eric Levillain, AJ Downard, and T Breton. Evidence of monolayer formation via diazonium grafting with a radical scavenger: electrochemical, afm and xps monitoring. *Physical Chemistry Chemical Physics*, 17(19):13137–13142, **2015]**, publisher=Royal Society of Chemistry.

[76] Nicholas Marshall and Jason Locklin. Reductive electrografting of benzene (p-bisdiazonium hexafluorophosphate): a simple and effective protocol for creating diazonium-functionalized thin films. *Langmuir*, 27(21):13367–13373, **2011**.

[77] Joël Lyskawa and Daniel Bélanger. Direct modification of a gold electrode with aminophenyl groups by electrochemical reduction of in situ generated aminophenyl monodiazonium cations. *Chemistry of Materials*, 18(20):4755–4763, **2006**.

[78] Gorachand Dutta, Flavio CB Fernandes, Pedro Estrela, Despina Moschou, and Paulo R Bueno. Impact of surface roughness on the self-assembling of molecular films onto gold electrodes for label-free biosensing applications. *Electrochimica Acta*, 378:138137, **2021**.

[79] Lung-Chieh Chen, Erick Wang, Chun-San Tai, Yuan-Chen Chiu, Chang-Wei Li, Yan-Ren Lin, Tsung-Han Lee, Ching-Wen Huang, Jung-Chih Chen, and Wen Liang Chen. Improving

the reproducibility, accuracy, and stability of an electrochemical biosensor platform for point-of-care use. *Biosensors and Bioelectronics*, 155:112111, **2020**.

[80] Samuel C Perry, Samantha M Gateman, Joseph Sifakis, Loredano Pollegioni, and Janine Mauzeroll. Enhancement of the enzymatic biosensor response through targeted electrode surface roughness. *Journal of The Electrochemical Society*, 165(12):G3074, **2018**.

[81] R Paul Brint, Donal J Coveney, Fergus L Lalor, George Ferguson, Masood Parvez, and Pik Yuen Siew. The origin of the remarkable stability of the 1 h-3, 5-dimethylpyrazole-4-diazonium cation: an x-ray crystallographic and mndo theoretical investigation. *Journal of the Chemical Society, Perkin Transactions 2*, 1(2):139–145, **1985**.

[82] Patty Weasler. Stem cell therapy: Uses, risks, how it works, Aug **2023**.

[83] Quentin Lenne, Vivien Andrieux, Gaël Levanen, Jean-Francois Bergamini, Pauline Nicolas, Ludovic Paquin, Corinne Lagrost, and Yann R Leroux. Electrochemical grafting of aryl diazonium salts in deep eutectic solvents. *Electrochimica Acta*, 369:137672, **2021**.

[84] Thibaud Menanteau, Marylène Dias, Eric Levillain, Alison J Downard, and Tony Breton. Electrografting via diazonium chemistry: The key role of the aryl substituent in the layer growth mechanism. *The Journal of Physical Chemistry C*, 120(8):4423–4429, **2016**.

[85] James D Firth and Ian JS Fairlamb. A need for caution in the preparation and application of synthetically versatile aryl diazonium tetrafluoroborate salts, **2020**.

[86] Zahra Tavakkoli, Hamed Goljani, Hassan Sepehrmansourie, Davood Nematollahi, and Mohammad Ali Zolfigol. New insight into the electrochemical reduction of different aryldiazonium salts in aqueous solutions. *RSC advances*, 11(42):25811–25815, **2021**.

[87] Akhtar Hayat, Lise Barthelmebs, and Jean-Louis Marty. Electrochemical impedimetric immunosensor for the detection of okadaic acid in mussel sample. *Sensors and Actuators B: Chemical*, 171:810–815, **2012**.

[88] Liam Gillan, Tuija Teerinen, Leena-Sisko Johansson, and Maria Smolander. Controlled diazonium electrodeposition towards a biosensor for c-reactive protein. *Sensors International*, 2:100060, **2021**.

[89] Lita Lee, Paula A Brooksby, and Alison J Downard. The stability of diazonium ion terminated

films on glassy carbon and gold electrodes. *Electrochemistry communications*, 19:67–69, **2012**.

[90] Fatma Ismail and Samuel B Adeloju. Galvanostatic entrapment of penicillinase into polytyramine films and its utilization for the potentiometric determination of penicillin. *Sensors*, 10(4):2851–2868, **2010**.

[91] Antonios V Pournaras, Theodora Koraki, and Mamas I Prodromidis. Development of an impedimetric immunosensor based on electropolymerized polytyramine films for the direct detection of salmonella typhimurium in pure cultures of type strains and inoculated real samples. *Analytica chimica acta*, 624(2):301–307, **2008**.

[92] Manihar Situmorang, J Justin Gooding, D Brynn Hibbert, and Donald Barnett. Electrodeposited polytyramine as an immobilisation matrix for enzyme biosensors. *Biosensors and bioelectronics*, 13(9):953–962, **1998**.

[93] Ally Mahadhy, Bo Mattiasson, Eva StåhlWernersson, and Martin Hedström. Evaluation of polytyramine film and 6-mercaptohexanol self-assembled monolayers as the immobilization layers for a capacitive dna sensor chip: A comparison. *Sensors*, 21(23):8149, **2021**.

[94] Asif Ahmed, Jo V Rushworth, John D Wright, and Paul A Millner. Novel impedimetric immunosensor for detection of pathogenic bacteria streptococcus pyogenes in human saliva. *Analytical chemistry*, 85(24):12118–12125, **2013**.

[95] Shazana Hilda Shamsuddin, Timothy D Gibson, Darren C Tomlinson, Michael J McPherson, David G Jayne, and Paul A Millner. Reagentless affimer-and antibody-based impedimetric biosensors for cea-detection using a novel non-conducting polymer. *Biosensors and Bioelectronics*, 178:113013, **2021**.

[96] Silvia Ferretti, Sally Paynter, David A Russell, Kim E Sapsford, and David J Richardson. Self-assembled monolayers: a versatile tool for the formulation of bio-surfaces. *TrAC Trends in Analytical Chemistry*, 19(9):530–540, **2000**.

[97] JE Butler, L Ni, R Nessler, KS Joshi, M Suter, B Rosenberg, J Chang, WR Brown, and LA Cantarero. The physical and functional behavior of capture antibodies adsorbed on polystyrene. *Journal of immunological methods*, 150(1-2):77–90, **1992**.

[98] Sónia AC Carabineiro and Bernard E Nieuwenhuys. Adsorption of small molecules on gold single crystal surfaces. *Gold Bulletin*, 42:288–301, **2009**.

[99] Magali Benoit, Nathalie Tarrat, and Joseph Morillo. Adsorption energy of small molecules on core–shell fe@ au nanoparticles: tuning by shell thickness. *Physical Chemistry Chemical Physics*, 18(13):9112–9123, **2016**.

[100] Elisabet Prats-Alfonso and Fernando Albericio. Functionalization of gold surfaces: recent developments and applications. *Journal of materials science*, 46:7643–7648, **2011**.

[101] Rudolf Holze. The adsorption of thiophenol on gold–a spectroelectrochemical study. *Physical Chemistry Chemical Physics*, 17(33):21364–21372, **2015**.

[102] Rainer C Hoft, Michael J Ford, Andrew M McDonagh, and Michael B Cortie. Adsorption of amine compounds on the au (111) surface: a density functional study. *The Journal of Physical Chemistry C*, 111(37):13886–13891, **2007**.

[103] Bárbara Simões, Wanda J Guedens, Charlie Keene, Karina Kubiak-Ossowska, Paul Mulheran, Anna M Kotowska, David J Scurr, Morgan R Alexander, Alexis Broisat, Steven Johnson, et al. Direct immobilization of engineered nanobodies on gold sensors. *ACS applied materials & interfaces*, 13(15):17353–17360, **2021**.

[104] Jeong Min Lee, Hyun Kyu Park, Yongwon Jung, Jin Kyeong Kim, Sun Ok Jung, and Bong Hyun Chung. Direct immobilization of protein g variants with various numbers of cysteine residues on a gold surface. *Analytical chemistry*, 79(7):2680–2687, **2007**.

[105] Kyoungsook Park, Jeong Min Lee, Yongwon Jung, Tsegaye Habtemariam, Abdela Woubit Salah, Cesar D Fermin, and Moonil Kim. Combination of cysteine-and oligomerization domain-mediated protein immobilization on a surface plasmon resonance (spr) gold chip surface. *Analyst*, 136(12):2506–2511, **2011**.

[106] Daniel R Thévenot, Klara Toth, Richard A Durst, and George S Wilson. Electrochemical biosensors: recommended definitions and classification. *Analytical Letters*, 34(5):635–659, **2001**.

[107] Dorothee Grieshaber, Robert MacKenzie, Janos Vörös, and Erik Reimhult. Electrochemical biosensors-sensor principles and architectures. *Sensors*, 8(3):1400–1458, **2008**.

[108] Lian CT Shoute, Gaser N Abdelrasoul, Yuhao Ma, Pedro A Duarte, Cole Edwards, Ran Zhuo, Jie Zeng, Yiwei Feng, Carmen L Charlton, Jamil N Kanji, et al. Label-free impedimetric immunosensor for point-of-care detection of covid-19 antibodies. *Microsystems & nanoengineering*, 9(1):3, **2023**.

[109] Hua Wang, Shengfu Chen, Lingyan Li, and Shaoyi Jiang. Improved method for the preparation of carboxylic acid and amine terminated self-assembled monolayers of alkanethiolates. *Langmuir*, 21(7):2633–2636, **2005**.

[110] Andrew D Vogt and Thomas P Beebe. Interactions of alcohols with hydroxyl-and methyl-terminated self-assembled monolayer surfaces studied by temperature-programmed desorption. *The Journal of Physical Chemistry B*, 103(40):8482–8489, **1999**.

[111] Marcel JE Fischer. Amine coupling through edc/nhs: a practical approach. *Surface plasmon resonance: methods and protocols*, pages 55–73, **2010**.

[112] Zeyang Li and Guan-Yu Chen. Current conjugation methods for immunosensors. *Nanomaterials*, 8(5):278, **2018**.

[113] Bo Johnsson, Stefan Löfås, and Gabrielle Lindquist. Immobilization of proteins to a carboxymethyldextran-modified gold surface for biospecific interaction analysis in surface plasmon resonance sensors. *Analytical biochemistry*, 198(2):268–277, **1991**.

[114] Kunal Pal, Allan T Paulson, and Dérick Rousseau. Biopolymers in controlled-release delivery systems. In *Modern biopolymer science*, pages 519–557. Elsevier, **2009**.

[115] Eleftherios P Diamandis and Theodore K Christopoulos. *Immunoassay*. Academic Press, **1996**.

[116] Rodica Elena Ionescu. Use of cysteamine and glutaraldehyde chemicals for robust functionalization of substrates with protein biomarkers—an overview on the construction of biosensors with different transductions. *Biosensors*, 12(8):581, **2022**.

[117] Stefano Farris, Jianhui Song, and Qingrong Huang. Alternative reaction mechanism for the cross-linking of gelatin with glutaraldehyde. *Journal of agricultural and food chemistry*, 58(2):998–1003, **2010**.

[118] Isabelle Migneault, Catherine Dartiguenave, Michel J Bertrand, and Karen C Waldron. Glu-

taraldehyde: behavior in aqueous solution, reaction with proteins, and application to enzyme crosslinking. *Biotechniques*, 37(5):790–802, **2004**.

[119] Oveimar Barbosa, Claudia Ortiz, Ángel Berenguer-Murcia, Rodrigo Torres, Rafael C Rodrigues, and Roberto Fernandez-Lafuente. Glutaraldehyde in bio-catalysts design: A useful crosslinker and a versatile tool in enzyme immobilization. *Rsc Advances*, 4(4):1583–1600, **2014**.

[120] David R Walt and Venetka I Agayn. The chemistry of enzyme and protein immobilization with glutaraldehyde, **1994**.

[121] Greg T Hermanson. *Bioconjugate techniques*. Academic press, **2013**.

[122] Sumita Swar, Veronika Máková, and Ivan Stibor. The covalent tethering of poly (ethylene glycol) to nylon 6 surface via n, n′-disuccinimidyl carbonate conjugation: A new approach in the fight against pathogenic bacteria. *Polymers*, 12(10):2181, **2020**.

[123] Aleksandra Karczmarczyk, Monika Dubiak-Szepietowska, Mariia Vorobii, Cesar Rodriguez-Emmenegger, Jakub Dostálek, and Karl-Heinz Feller. Sensitive and rapid detection of aflatoxin m1 in milk utilizing enhanced spr and p (hema) brushes. *Biosensors and Bioelectronics*, 81:159–165, **2016**.

[124] Katherine Leslee A Cimatu, Tharushi D Ambagaspitiya, Uvinduni I Premadasa, Narendra M Adhikari, Adelaide Kruse, Emily Robertson, Shanshan Guan, Lihan Rong, Rigoberto Advincula, and Benjamin J Bythell. Polymer-solvent interaction and conformational changes at a molecular level: Implication to solvent-assisted deformation and aggregation at the polymer surface. *Journal of Colloid and Interface Science*, 616:221–233, **2022**.

[125] Derek G Smyth, OO Blumenfeld, and W Konigsberg. Reactions of n-ethylmaleimide with peptides and amino acids. *Biochemical Journal*, 91(3):589, **1964**.

[126] Md Morsaline Billah, Christopher S Hodges, Henry CW Hays, and PA Millner. Directed immobilization of reduced antibody fragments onto a novel sam on gold for myoglobin impedance immunosensing. *Bioelectrochemistry*, 80:49–54, **2010**.

[127] Zhihua Li, Xue Zhang, Haishan Qi, Xiaowei Huang, Jiyong Shi, and Xiaobo Zou. A novel renewable electrochemical biosensor based on mussel-inspired adhesive protein for the

detection of escherichia coli o157: H7 in food. *Sensors and Actuators B: Chemical*, 372:132601, **2022**.

[128] Yingshuai Liu and Jie Yu. Oriented immobilization of proteins on solid supports for use in biosensors and biochips: a review. *Microchimica Acta*, 183:1–19, **2016**.

[129] Lei Shen, McKenna Schroeder, Tadeusz L Ogorzalek, Pei Yang, Fu-Gen Wu, E Neil G Marsh, and Zhan Chen. Surface orientation control of site-specifically immobilized nitroreductase (nfsb). *Langmuir*, 30(20):5930–5938, **2014**.

[130] Yiqing Zhou, Tianlin Guo, Guanghui Tang, Hui Wu, Nai-Kei Wong, and Zhengying Pan. Site-selective protein immobilization by covalent modification of gst fusion proteins. *Bioconjugate Chemistry*, 25(11):1911–1915, **2014**.

[131] K Terpe. Overview of tag protein fusions: from molecular and biochemical fundamentals to commercial systems. *Applied microbiology and biotechnology*, 60:523–533, **2003**.

[132] Mingyang Li, Fang Cheng, Haoqiang Li, Weiwei Jin, Chen Chen, Wei He, Gang Cheng, and Qing Wang. Site-specific and covalent immobilization of his-tagged proteins via surface vinyl sulfone–imidazole coupling. *Langmuir*, 35(50):16466–16475, **2019**.

[133] Xueming Li, Siyu Song, Yuxin Pei, Hai Dong, Teodor Aastrup, and Zhichao Pei. Oriented and reversible immobilization of his-tagged proteins on two-and three-dimensional surfaces for study of protein–protein interactions by a qcm biosensor. *Sensors and Actuators B: Chemical*, 224:814–822, **2016**.

[134] Sachin Ganpat Chavan, Ajay Kumar Yagati, Aneesh Koyappayil, Anna Go, Sangho Yeon, and Min-Ho Lee. Recombinant histidine-tagged nano-protein-based highly sensitive electrosensing device for salivary cortisol. *Bioelectrochemistry*, 144:108046, **2022**.

[135] Rhiannon K Iha, Karen L Wooley, Andreas M Nystrom, Daniel J Burke, Matthew J Kade, and Craig J Hawker. Applications of orthogonal “click” chemistries in the synthesis of functional soft materials. *Chemical reviews*, 109(11):5620–5686, **2009**.

[136] Rolf Chelmowski, Daniel Käfer, Stephan David Köster, Tim Klasen, Tobias Winkler, Andreas Terfort, Nils Metzler-Nolte, and Christof Wöll. Postformation modification of sams: Using click chemistry to functionalize organic surfaces. *Langmuir*, 25(19):11480–11485, **2009**.

[137] Fengchun Huang, Yingchao Zhang, Jianhan Lin, and Yuanjie Liu. Biosensors coupled with signal amplification technology for the detection of pathogenic bacteria: A review. *Biosensors*, 11(6):190, **2021**.

[138] Krishna Thapa, Wenyan Liu, and Risheng Wang. Nucleic acid-based electrochemical biosensor: Recent advances in probe immobilization and signal amplification strategies. *Wiley Interdisciplinary Reviews: Nanomedicine and Nanobiotechnology*, 14(1):e1765, **2022**.

[139] Ning Xia, Zhifang Sun, Fangyuan Ding, Yanan Wang, Wenna Sun, and Lin Liu. Protease biosensor by conversion of a homogeneous assay into a surface-tethered electrochemical analysis based on streptavidin–biotin interactions. *Acs Sensors*, 6(3):1166–1173, **2021**.

[140] Marissa A Morales and Jeffrey Mark Halpern. Guide to selecting a biorecognition element for biosensors. *Bioconjugate chemistry*, 29(10):3231–3239, **2018**.

[141] Shinya Oue, Akihiro Okamoto, Takato Yano, and Hiroyuki Kagamiyama. Redesigning the substrate specificity of an enzyme by cumulative effects of the mutations of non-active site residues. *Journal of Biological Chemistry*, 274(4):2344–2349, **1999**.

[142] Victor Crivianu-Gaita and Michael Thompson. Aptamers, antibody scfv, and antibody fab'fragments: An overview and comparison of three of the most versatile biosensor biorecognition elements. *Biosensors and Bioelectronics*, 85:32–45, **2016**.

[143] Wenhu Zhou, Po-Jung Jimmy Huang, Jinsong Ding, and Juewen Liu. Aptamer-based biosensors for biomedical diagnostics. *Analyst*, 139(11):2627–2640, **2014**.

[144] Chen-zhong Li, Hakan Karadeniz, Ece Canavar, and Arzum Erdem. Electrochemical sensing of label free dna hybridization related to breast cancer 1 gene at disposable sensor platforms modified with single walled carbon nanotubes. *Electrochimica Acta*, 82:137–142, **2012**.

[145] Suprava Patel, Rachita Nanda, Sibasish Sahoo, Eli Mohapatra, et al. Biosensors in health care: the milestones achieved in their development towards lab-on-chip-analysis. *Biochemistry research international*, 2016, **2016**.

[146] Sreenath Subrahmanyam, Sergey A Piletsky, and Anthony PF Turner. Application of natural receptors in sensors and assays. *Analytical chemistry*, 74(16):3942–3951, **2002**.

[147] Serge Muyldermans. Nanobodies: natural single-domain antibodies. *Annual review of biochemistry*, 82:775–797, **2013**.

[148] Gualberto Gonzalez-Sapienza, Martín A Rossotti, and Sofía Tabares-da Rosa. Single-domain antibodies as versatile affinity reagents for analytical and diagnostic applications. *Frontiers in immunology*, 8:977, **2017**.

[149] Edwin P Rock, Peter R Sibbald, Mark M Davis, and YUEH-HSIU Chien. Cdr3 length in antigen-specific immune receptors. *The Journal of experimental medicine*, 179(1):323–328, **1994**.

[150] Cyrus Chothia, Israel Gelfand, and Alexander Kister. Structural determinants in the sequences of immunoglobulin variable domain. *Journal of molecular biology*, 278(2):457–479, **1998**.

[151] Michiel M Harmsen, Robin C Ruuls, Isaäc J Nijman, Theodoor A Niewold, Leon GJ Frenken, and Bernard de Geus. Llama heavy-chain v regions consist of at least four distinct subfamilies revealing novel sequence features. *Molecular immunology*, 37(10):579–590, **2000**.

[152] Ruth C Ladenson, Dan L Crimmins, Yvonne Landt, and Jack H Ladenson. Isolation and characterization of a thermally stable recombinant anti-caffeine heavy-chain antibody fragment. *Analytical chemistry*, 78(13):4501–4508, **2006**.

[153] Jing Chen, Qing-hua He, Yang Xu, Jin-heng Fu, Yan-ping Li, Zhui Tu, Dan Wang, Mei Shu, Yu-lou Qiu, Hong-wei Yang, et al. Nanobody medicated immunoassay for ultrasensitive detection of cancer biomarker alpha-fetoprotein. *Talanta*, 147:523–530, **2016**.

[154] Aparajita Singh, Syed Khalid Pasha, Pandiaraj Manickam, and Shekhar Bhansali. Single-domain antibody based thermally stable electrochemical immunosensor. *Biosensors and Bioelectronics*, 83:162–168, **2016**.

[155] Ting He, Yanru Wang, Peiwu Li, Qi Zhang, Jiawen Lei, Zhaowei Zhang, Xiaoxia Ding, Haiyan Zhou, and Wen Zhang. Nanobody-based enzyme immunoassay for aflatoxin in agro-products with high tolerance to cosolvent methanol. *Analytical chemistry*, 86(17):8873–8880, **2014**.

[156] Hee-Joo Kim, Mark R McCoy, Zuzana Majkova, Julie E Dechant, Shirley J Gee, Sofia

Tabares-da Rosa, Gualberto G González-Sapienza, and Bruce D Hammock. Isolation of alpaca anti-hapten heavy chain single domain antibodies for development of sensitive immunoassay. *Analytical chemistry*, 84(2):1165–1171, **2012**.

[157] Anil Koklu, Shofarul Wustoni, Keying Guo, Raphaela Silva, Luca Salvigni, Adel Hama, Escarlet Diaz-Galicia, Maximilian Moser, Adam Marks, Iain McCulloch, et al. Convection driven ultrarapid protein detection via nanobody-functionalized organic electrochemical transistors. *Advanced Materials*, 34(35):2202972, **2022**.

[158] Bárbara Santos Gomes, Bárbara Simões, and Paula M Mendes. The increasing dynamic, functional complexity of bio-interface materials. *Nature Reviews Chemistry*, 2(3):0120, **2018**.

[159] Cheuk Chi Albert Ng, Astrid Magenau, Siti Hawa Ngalim, Simone Ciampi, Muthukumar Chockalingham, Jason Brian Harper, Katharina Gaus, and John Justin Gooding. Using an electrical potential to reversibly switch surfaces between two states for dynamically controlling cell adhesion. *Angewandte Chemie International Edition*, 51(31):7706–7710, **2012**.

[160] Yubo Wei, Qiang Zeng, Jianzhi Huang, Qiong Hu, Xinrong Guo, and Lishi Wang. An electroresponsive imprinted biosensor with switchable affinity toward proteins. *Chemical Communications*, 54(66):9163–9166, **2018**.

[161] Tom N Krupenkin, J Ashley Taylor, Evelyn N Wang, Paul Kolodner, Marc Hodes, and Todd R Salamon. Reversible wetting- dewetting transitions on electrically tunable superhydrophobic nanostructured surfaces. *Langmuir*, 23(18):9128–9133, **2007**.

[162] Igor Dzięcielewski, Jan Krajczewski, and Wojciech Dzwolak. ph-responsive mixed-thiol-modified surface of roughened gan: A wettability and sers study. *Applied Surface Science*, 502:144108, **2020**.

[163] Mitsuhiro Ebara, Masayuki Yamato, Takao Aoyagi, Akihiko Kikuchi, Kiyotaka Sakai, and Teruo Okano. Temperature-responsive cell culture surfaces enable “on- off” affinity control between cell integrins and rgds ligands. *Biomacromolecules*, 5(2):505–510, 2004.

[164] Barbara Sofia Fialho Simoes. Development of nanobody-based surfaces for on-demand smart switchable biosensing. July **2022**.

[165] Christopher Barner-Kowollik, Anja S Goldmann, and Felix H Schacher. Polymer interfaces: synthetic strategies enabling functionality, adaptivity, and spatial control. *Macromolecules*, 49(14):5001–5016, **2016**.

[166] Eleonora Cantini, Xingyong Wang, Patrick Koelsch, Jon A Preece, Jing Ma, and Paula M Mendes. Electrically responsive surfaces: experimental and theoretical investigations. *Accounts of Chemical Research*, 49(6):1223–1231, **2016**.

[167] Joerg Lahann, Samir Mitragotri, Thanh-Nga Tran, Hiroki Kaido, Jagannathan Sundaram, Insung S Choi, Saskia Hoffer, Gabor A Somorjai, and Robert Langer. A reversibly switching surface. *Science*, 299(5605):371–374, **2003**.

[168] Li Mu, Ying Liu, Shaoyu Cai, and Jilie Kong. A smart surface in a microfluidic chip for controlled protein separation. *Chemistry–a European Journal*, 13(18):5113–5120, **2007**.

[169] Alice Pranzetti, Sophie Mieszkin, Parvez Iqbal, Frankie J Rawson, Maureen E Callow, James A Callow, Patrick Koelsch, Jon A Preece, and Paula M Mendes. An electrically reversible switchable surface to control and study early bacterial adhesion dynamics in real-time. *Advanced materials (Deerfield Beach, Fla.)*, 25(15):2181, **2013**.

[170] Kaoru Tamada, Masahiko Hara, Hiroyuki Sasabe, and Wolfgang Knoll. Surface phase behavior of n-alkanethiol self-assembled monolayers adsorbed on au (111): An atomic force microscope study. *Langmuir*, 13(6):1558–1566, **1997**.

[171] UK ATMP Clinical Trials Database 2022: Number of Advanced Therapy Medicinal Product clinical trials in the UK continues to increase year-on-year - Cell and Gene Therapy — ct.catapult.org.uk. `https://ct.catapult.org.uk/news/press-release-uk-atmp-clinical-trials-database-2022-number-of-advanced\therapy-medicinal-product-clinical-trials-in-the-uk-continues-to-increase\-year-on-year`. [Accessed **18-12-2023**].

[172] Jon Rowley, Eytan Abraham, Andrew Campbell, Harvey Brandwein, and Steve Oh. Meeting lot-size challenges of manufacturing adherent cells for therapy. *BioProcess Int*, 10(3):7, **2012**.

[173] Ana S Simaria, Sally Hassan, Hemanthram Varadaraju, Jon Rowley, Kim Warren, Philip

Vanek, and Suzanne S Farid. Allogeneic cell therapy bioprocess economics and optimization: Single-use cell expansion technologies. *Biotechnology and bioengineering*, 111(1):69–83, **2014**.

[174] Chen-Yuan Kao, Jason A Mills, Carl J Burke, Barry Morse, and Bruno F Marques. Role of cytokines and growth factors in the manufacturing of ipsc-derived allogeneic cell therapy products. *Biology*, 12(5):677, **2023**.

[175] Xiaowei Guo. Surface plasmon resonance based biosensor technique: a review. *Journal of biophotonics*, 5(7):483–501, **2012**.

[176] Richard BM Schasfoort. *Handbook of surface plasmon resonance*. Royal Society of Chemistry, **2017**.

[177] P Anton Van Der Merwe. Surface plasmon resonance. *Protein-ligand interactions: hydrodynamics and calorimetry*, 1:137–170, **2001**.

[178] Daniel J Oshannessy, Michael Brighamburke, K Karl Soneson, Preston Hensley, and Ian Brooks. Determination of rate and equilibrium binding constants for macromolecular interactions using surface plasmon resonance: use of nonlinear least squares analysis methods. *Analytical biochemistry*, 212(2):457–468, **1993**.

[179] Craig S Schneider, Adip G Bhargav, Jimena G Perez, Aniket S Wadajkar, Jeffrey A Winkles, Graeme F Woodworth, and Anthony J Kim. Surface plasmon resonance as a high throughput method to evaluate specific and non-specific binding of nanotherapeutics. *Journal of Controlled Release*, 219:331–344, **2015**.

[180] Potentiostat-fundamentals.pdf. `https://www.gamry.com/assets/Application-Notes/Potentiostat-Fundamentals.pdf`. (Accessed on **12/18/2023**).

[181] Potentiostat fundamentals – electrochemistry resources. `https://electrochemistryresources.com/potentiostat-fundamentals/`. (Accessed on **12/18/2023**).

[182] RG Bates and JB Macaskill. Standard potential of the silver-silver chloride electrode. *Pure Appl. Chem*, 50(11-12):1701–1706, **1978**.

[183] potentiostat.pdf. `chrome-extension://efaidnbmnnnibpcajpcglclefindmkaj/https://`

www3.nd.edu/~kamatlab/documents/facilities/potentiostat.pdf. (Accessed on **01/15/2024**).

[184] Two,three,four electrode system gamry 4-probe potentiostats gamry instruments. https://www.gamry.com/application-notes/instrumentation/two-three-four-electrode-experiments/#:~:text=Three%2Delectrode%20setups%20have%20a,occur%20at%20the%20counter%20electrode. (Accessed on **01/15/2024**).

[185] Leonardo Pires Carneiro. *Development of an Electrochemical Biosensor Platform and a Suitable Low-Impedance Surface Modification Strategy*, volume 27. KIT Scientific Publishing, **2014**.

[186] Ir drop. https://www.corrosionpedia.com/definition/2203/ir-drop. (Accessed on **01/15/2024**).

[187] Potentiostat/galvanostat electrochemical instrument basics gamry instruments. https://www.gamry.com/application-notes/instrumentation/potentiostat-fundamentals/. (Accessed on **01/02/2024**).

[188] Noémie Elgrishi, Kelley J Rountree, Brian D McCarthy, Eric S Rountree, Thomas T Eisenhart, and Jillian L Dempsey. A practical beginner's guide to cyclic voltammetry. *Journal of chemical education*, 95(2):197–206, **2018**.

[189] José A Ribeiro, Elisa Silva, Patrícia S Moreira, and Carlos M Pereira. Electrochemical characterization of redox probes at gold screen-printed electrodes: efforts towards signal stability. *ChemistrySelect*, 5(17):5041–5048, **2020**.

[190] Giacomo Prampolini, Pengyun Yu, Silvia Pizzanelli, Ivo Cacelli, Fan Yang, Juan Zhao, and Jianping Wang. Structure and dynamics of ferrocyanide and ferricyanide anions in water and heavy water: An insight by md simulations and 2d ir spectroscopy. *The Journal of Physical Chemistry B*, 118(51):14899–14912, **2014**.

[191] Cyclic voltammetry basic principles, theory & setup | ossila. https://www.ossila.com/pages/cyclic-voltammetry. (Accessed on **01/17/2024**).

[192] A-S Feiner and AJ McEvoy. The nernst equation. *Journal of chemical education*, 71(6):493, **1994**.

[193] Edmund JF Dickinson and Andrew J Wain. The butler-volmer equation in electrochemical theory: Origins, value, and practical application. *Journal of Electroanalytical Chemistry*, 872:114145, **2020**.

[194] John Edward Brough Randles. Kinetics of rapid electrode reactions. *Discussions of the faraday society*, 1:11–19, **1947**.

[195] Alexandros Ch Lazanas and Mamas I Prodromidis. Electrochemical impedance spectroscopy– a tutorial. *ACS Measurement Science Au*, **2023**.

[196] Hend S Magar, Rabeay YA Hassan, and Ashok Mulchandani. Electrochemical impedance spectroscopy (eis): Principles, construction, and biosensing applications. *Sensors*, 21(19):6578, **2021**.

[197] Kevin M Tenny and Michael Keenaghan. Ohms law. **2017**.

[198] Sayed Habib Kazemi, Maryam Shanehsaz, and Mostafa Ghaemmaghami. Non-faradaic electrochemical impedance spectroscopy as a reliable and facile method: Determination of the potassium ion concentration using a guanine rich aptasensor. *Materials Science and Engineering: C*, 52:151–154, **2015**.

[199] Jun Huang, Zhe Li, Bor Yann Liaw, and Jianbo Zhang. Graphical analysis of electrochemical impedance spectroscopy data in bode and nyquist representations. *Journal of Power Sources*, 309:82–98, **2016**.

[200] Peter Nestler and Christiane A Helm. Determination of refractive index and layer thickness of nm-thin films via ellipsometry. *Optics Express*, 25(22):27077–27085, **2017**.

[201] JB Theeten and DE Aspnes. Ellipsometry in thin film analysis. *Annual Review of Materials Science*, 11(1):97–122, **1981**.

[202] Débora Gonçalves and Eugene A Irene. Fundamentals and applications of spectroscopic ellipsometry. *Química Nova*, 25:794–800, **2002**.

[203] Kent B Rochford. Polarization and polarimetry. **2001**.

[204] Huaiyu Wang and Paul K Chu. Surface characterization of biomaterials. In *Characterization of biomaterials*, pages 105–174. Elsevier, **2013**.

[205] Harland G Tompkins. *A user's guide to ellipsometry*. Courier Corporation, **2006**.

[206] Karsten Hinrichs and Klaus-Jochen Eichhorn. *Ellipsometry of functional organic surfaces and films*, volume 52. Springer, **2018**.

[207] Fred A. Stevie and Carrie L. Donley. Introduction to x-ray photoelectron spectroscopy. *Journal of Vacuum Science and Technology A*, 38(6):063204, 09 **2020**.

[208] X-ray photoelectron spectroscopy | thermo fisher scientific - uk. https://www.thermofisher.com/uk/en/home/materials-science/xps-technology.html#:~:text=XPS%20can%20measure%20elemental%20composition,10%20nm%20of%20the%20material. (Accessed on **01/23/2024**).

[209] Fred A Stevie and Carrie L Donley. Introduction to x-ray photoelectron spectroscopy. *Journal of Vacuum Science & Technology A*, 38(6), **2020**.

[210] H Seyama, M Soma, and BKG Theng. X-ray photoelectron spectroscopy. In *Developments in Clay Science*, volume 5, pages 161–176. Elsevier, **2013**.

[211] Cody V Cushman, Shiladitya Chatterjee, George H Major, Nicholas J Smith, Adam Roberts, and Matthew R Linford. Trends in advanced xps instrumentation. *Vac. Technol. Coat*, 9:25–31, **2017**.

[212] Minhaj Lashkor, Frankie J Rawson, Jon A Preece, and Paula M Mendes. Switching specific biomolecular interactions on surfaces under complex biological conditions. *Analyst*, 139(21):5400–5408, **2014**.

[213] Chun L Yeung, Xingyong Wang, Minhaj Lashkor, Eleonora Cantini, Frankie J Rawson, Parvez Iqbal, Jon A Preece, Jing Ma, and Paula M Mendes. Modulation of biointeractions by electrically switchable oligopeptide surfaces: structural requirements and mechanism. *Advanced materials interfaces*, 1(2):1300085, **2014**.

[214] Minhaj Lashkor, Frankie J Rawson, Alex Stephenson-Brown, Jon A Preece, and Paula M Mendes. Electrically-driven modulation of surface-grafted rgd peptides for manipulation of cell adhesion. *Chemical Communications*, 50(98):15589–15592, **2014**.

[215] Alice Pranzetti, Matthew Davis, Chun L Yeung, Jon A Preece, Patrick Koelsch, and Paula M Mendes. Direct observation of reversible biomolecule switching controlled by electrical stimulus. *Advanced Materials Interfaces*, 1(5):1, **2014**.

[216] Joshua S Gibson and Paula M Mendes. Elucidating the influence of electrical potentials on the formation of charged oligopeptide self-assembled monolayers on gold. *ChemPhysChem*, 22(7):684–692, **2021**.

[217] Marta H Kubala, Oleksiy Kovtun, Kirill Alexandrov, and Brett M Collins. Structural and thermodynamic analysis of the gfp: Gfp-nanobody complex. *Protein Science*, 19(12):2389–2401, **2010**.

[218] Capsid constructors. `https://capsidconstructors.github.io/lab-book/kinetics/spr.html`. (Accessed on **02/19/2024**).

[219] Katjuša Brejc, Titia K Sixma, Paul A Kitts, Steven R Kain, Roger Y Tsien, Mats Ormö, and S James Remington. Structural basis for dual excitation and photoisomerization of the aequorea victoria green fluorescent protein. *Proceedings of the National Academy of Sciences*, 94(6):2306–2311, **1997**.

[220] Amino acids. `https://www.vanderbilt.edu/AnS/Chemistry/Rizzo/stuff/AA/AminoAcids.html`. (Accessed on **02/08/2024**).

[221] Working electrode selection. `https://www.ijcambria.com/we_selection.htm`. (Accessed on **(/08/2024)**.

[222] Supakiet Chanarsa, Chammari Pothipor, Nawee Kungwan, and Kontad Ounnunkad. A poly (pyrrole-3-carboxylic acid) thin film modified screen printed carbon electrode as highly sensitive and selective label-free electrochemical immunosensing platform. **2020**.

[223] Luciano Pereira Rodrigues, Deusmaque Carneiro Ferreira, Lucas Franco Ferreira, Sara Cuadros-Orellana, Guilherme Corrêa de Oliveira, Ana G Brito-Madurro, Ronaldo Junio de Oliveira, Odonírio Abrahão, and Joao M Madurro. Electropolymerization of hydroxyphenylacetic acid isomers and the development of a bioelectrode for the diagnosis of bacterial meningitis. *Journal of applied electrochemistry*, 45:1277–1287, **2015**.

[224] Sereilakhena Phal, Besart Shatri, Avni Berisha, Paul Geladi, Britta Lindholm-Sethson, and Solomon Tesfalidet. Covalently electrografted carboxyphenyl layers onto gold surface serving as a platform for the construction of an immunosensor for detection of methotrexate. *Journal of Electroanalytical Chemistry*, 812:235–243, **2018**.

[225] Said Sadki, Philippe Schottland, Nancy Brodie, and Guillaume Sabouraud. The mechanisms of pyrrole electropolymerization. *Chemical Society Reviews*, 29(5):283–293, **2000**.

[226] Laura Valero Conzuelo, Joaquín Arias-Pardilla, Juan V Cauich-Rodríguez, Mascha Afra Smit, and Toribio Fernández Otero. Sensing and tactile artificial muscles from reactive materials. *Sensors*, 10(4):2638–2674, **2010**.

[227] Bruno Scrosati. *Applications of electroactive polymers*, volume 75. Springer, **1993**.

[228] Megan K Puglia and Patrick K Bowen. Cyclic voltammetry study of noble metals and their alloys for use in implantable electrodes. *ACS omega*, 7(38):34200–34212, **2022**.

[229] Xidan Zong, Na Kong, Jingquan Liu, Wenrong Yang, Mengmei Cao, and J Justin Gooding. The influence of graphene on the electrical communication through organic layers on graphite and gold electrodes. *Electroanalysis*, 26(1):84–92, **2014**.

[230] Guozhen Liu, Sridhar G Iyengar, and J Justin Gooding. An amperometric immunosensor based on a gold nanoparticle-diazonium salt modified sensing interface for the detection of hba1c in human blood. *Electroanalysis*, 25(4):881–887, **2013**.

[231] Alessandro Benedetto, Mirela Balog, Pascal Viel, Franck Le Derf, Marc Sallé, and Serge Palacin. Electro-reduction of diazonium salts on gold: Why do we observe multi-peaks? *Electrochimica Acta*, 53(24):7117–7122, **2008**.

[232] Alicia L Gui, Guozhen Liu, Muthukumar Chockalingam, Guillaume Le Saux, Jason B Harper, and J Justin Gooding. A comparative study of modifying gold and carbon electrode with 4-sulfophenyl diazonium salt. *Electroanalysis*, 22(12):1283–1289, **2010**.

[233] Camila F Olguín, Nicolás Agurto, Carlos P Silva, Carolina P Candia, Mireya Santander-Nelli, Juan Oyarzo, Alejandra Gómez, Juan F Silva, and Jorge Pavez. Tuning the covering on gold surfaces by grafting amino-aryl films functionalized with fe (ii) phthalocyanine: Performance on the electrocatalysis of oxygen reduction. *Molecules*, 26(6):1631, **2021**.

[234] Shaurya Prakash and Junghoon Yeom. *Nanofluidics and microfluidics: systems and applications*. William Andrew, **2014**.

[235] Kailash Chandra Khulbe, Takeshi Matsuura, Kailash Chandra Khulbe, and Takeshi Matsuura. Membrane characterization. *Nanotechnology in Membrane Processes*, pages 89–

133, **2021**.

[236] Paula M Mendes, Karen L Christman, Puru Parthasarathy, Eric Schopf, Jianyong Ouyang, Yang Yang, Jon A Preece, Heather D Maynard, Yong Chen, and J Fraser Stoddart. Electrochemically controllable conjugation of proteins on surfaces. *Bioconjugate chemistry*, 18(6):1919–1923, **2007**.

[237] William Richard, David Evrard, Bertrand Busson, Christophe Humbert, Laetitia Dalstein, Abderrahmane Tadjeddine, and Pierre Gros. The reduction of 4-nitrobenzene diazonium electrografted layer: An electrochemical study coupled to in situ sum-frequency generation spectroscopy. *Electrochimica Acta*, 283:1640–1648, **2018**.

[238] Paula A Brooksby and Alison J Downard. Electrochemical and atomic force microscopy study of carbon surface modification via diazonium reduction in aqueous and acetonitrile solutions. *Langmuir*, 20(12):5038–5045, **2004**.

[239] Birhanu Desalegn Assresahegn, Thierry Brousse, and Daniel Bélanger. Advances on the use of diazonium chemistry for functionalization of materials used in energy storage systems. *Carbon*, 92:362–381, **2015**.

[240] Chaomin Cao, Yin Zhang, Cheng Jiang, Meng Qi, and Guozhen Liu. Advances on aryldiazonium salt chemistry based interfacial fabrication for sensing applications. *ACS applied materials & interfaces*, 9(6):5031–5049, **2017**.

[241] Michel Delamar, Rachid Hitmi, Jean Pinson, and Jean Michel Saveant. Covalent modification of carbon surfaces by grafting of functionalized aryl radicals produced from electrochemical reduction of diazonium salts. *Journal of the American Chemical Society*, 114(14):5883–5884, **1992**.

[242] Alia Colni□ă, Daniel Marconi, and Ioan Turcu. Fabrication of interdigitated electrodes using molecular beam epitaxy and optical lithography. *Analytical Letters*, 49(3):378–386, **2016**.

[243] Ken-ichiro Ota, Gerhard Kreysa, and Robert F Savinell. *Encyclopedia of applied electrochemistry*. Springer New York, **2014**.

[244] Atomic force microscope principle | afm scanning | how afm works. `https://www.parksystems.com/learning-center/nano-academy/how-afm-works`. (Accessed on

03/05/2024).

[245] Suzhe Liang, Matthias Schwartzkopf, Stephan V Roth, and Peter Müller-Buschbaum. State of the art of ultra-thin gold layers: formation fundamentals and applications. *Nanoscale Advances*, 4(12):2533–2560, **2022**.

[246] Rafael C Rodrigues, Ángel Berenguer-Murcia, and Roberto Fernandez-Lafuente. Coupling chemical modification and immobilization to improve the catalytic performance of enzymes. *Advanced Synthesis & Catalysis*, 353(13):2216–2238, **2011**.

[247] Susan E Henkelis, Stephen J Percival, Leo J Small, David X Rademacher, and Tina M Nenoff. Continuous mof membrane-based sensors via functionalization of interdigitated electrodes. *Membranes*, 11(3):176, **2021**.

[248] Nucleophilicity trends of amines – master organic chemistry. `https://www.masterorganicchemistry.com/2018/05/07/nucleophilicity-of-amines/`. (Accessed on **03/20/2024**).

[249] S Loyprasert, Martin Hedström, P Thavarungkul, P Kanatharana, and Bo Mattiasson. Sub-attomolar detection of cholera toxin using a label-free capacitive immunosensor. *Biosensors and Bioelectronics*, 25(8):1977–1983, **2010**.

[250] Lam Dai Tran, Benoît Piro, Minh Chau Pham, Trung Ledoan, Chiara Angiari, Le H Dao, and Franck Teston. A polytyramine film for covalent immobilization of oligonucleotides and hybridization. *Synthetic Metals*, 139(2):251–262, **2003**.

[251] EV Suprun, HC Budnikov, GA Evtugyn, and Kh Z Brainina. Bi-enzyme sensor based on thick-film carbon electrode modified with electropolymerized tyramine. *Bioelectrochemistry*, 63(1-2):281–284, **2004**.

[252] Odonírio Abrahão Jr, Antonio Eduardo da Hora Machado, Fernando Freitas Siqueira Silva, João Marcos Madurro, Cláudio Márcio de Castro, and Milton Taidi Sonoda. Tyramine electropolymerization revisited by dft and experimental study. *Journal of molecular structure*, 1037:200–208, **2013**.

[253] Capacitive reactance - the reactance of capacitors. `https://www.electronics-tutorials.ws/filter/filter_1.html`. (Accessed on **03/27/2024**).

[254] Christine Berggren, Bjarni Bjarnason, and Gillis Johansson. Capacitive biosensors. *Electroanalysis*, 13(3):173–180, **2001**.

[255] Sangiliyandi Gurunathan, Jae Woong Han, Eunsu Kim, Deug-Nam Kwon, Jin-Ki Park, and Jin-Hoi Kim. Enhanced green fluorescent protein-mediated synthesis of biocompatible graphene. *Journal of nanobiotechnology*, 12:1–16, **2014**.

[256] Nathalia Vieira Dos Santos, Carolina Falaschi Saponi, Timothy M Ryan, Fernando L Primo, Tamar L Greaves, and Jorge FB Pereira. Reversible and irreversible fluorescence activity of the enhanced green fluorescent protein in ph: Insights for the development of ph-biosensors. *International Journal of Biological Macromolecules*, 164:3474–3484, **2020**.

[257] Thomas Chandy. Biocompatibility of materials and its relevance to drug delivery and tissue engineering. In *Biointegration of medical implant materials*, pages 297–331. Elsevier, **2020**.

Appendix

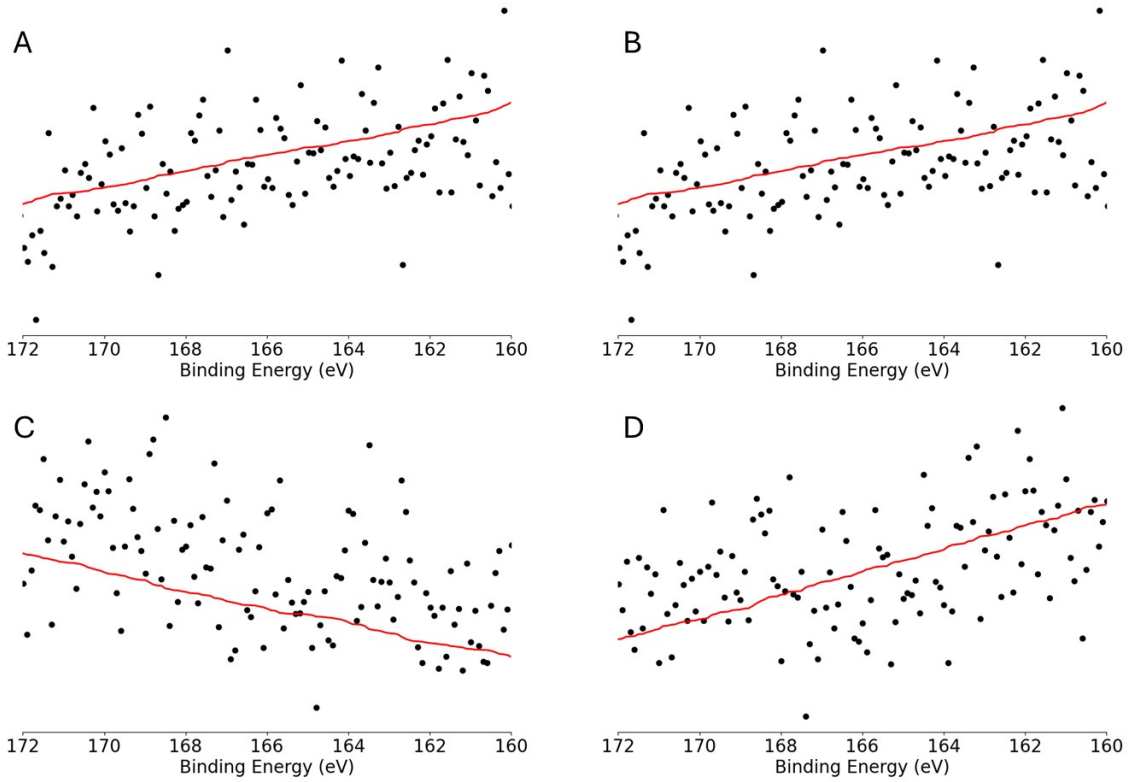

Figure 1: *XPS of S 2p high resolution scan on bare Au (A), NbGFP surface (B), C8K surface (C), and NbGFP-C8K [1:5] surface (D).*

For P3C in 0.5 M H_2SO_4 the oxidation peak gradually decreased to a minimum after 10 cycles. However, as with PBS there was no change in the CV or faradaic EIS when 10 mM $Fe(CN)_6^{-3/-4}$ was used as a redox probe. Regardless, to see if any polymerised P3C was present on the surface, NHS/EDC was used to activate the carboxylic acid groups and NbGFP was incubated on the surface (exact protocol can be found in the materials and methods section of this thesis). No significant change in the redox active of $Fe(CN)_6^{-3/-4}$ was observed in the CV. There was also no change in the charge transfer resistance in the Nyquist plot (figure 2).

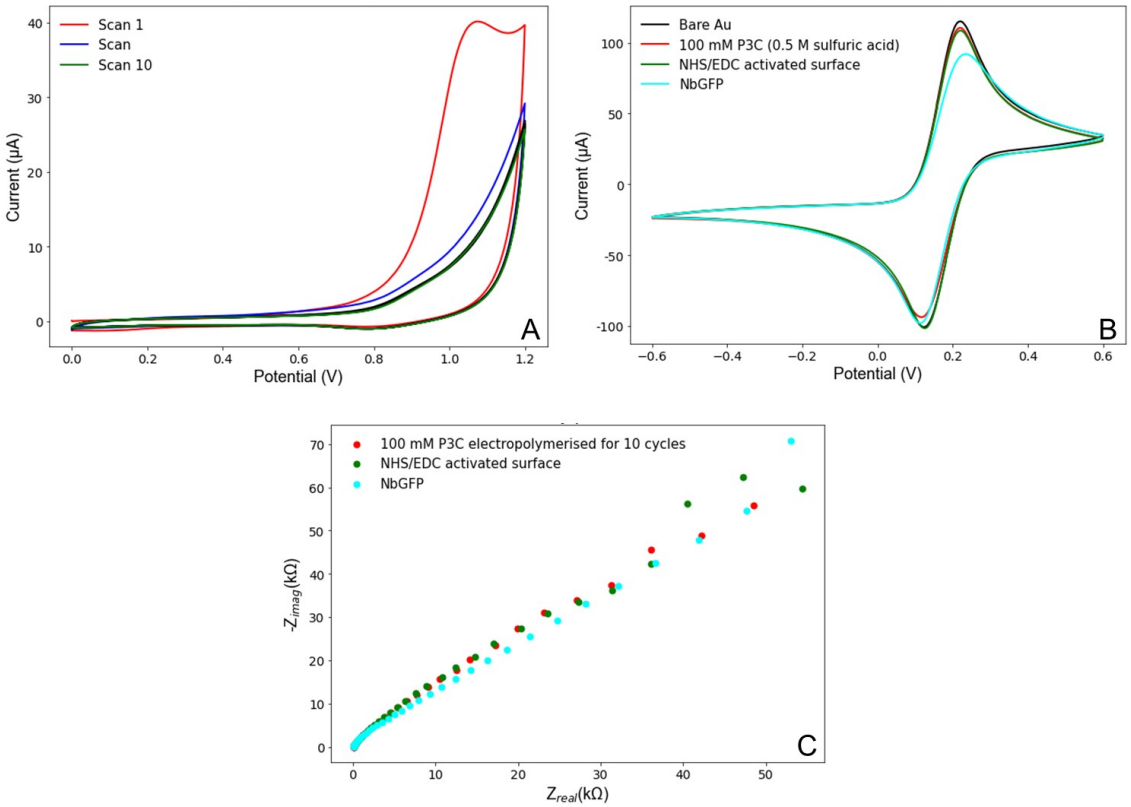

Figure 2: A) *CV of the electropolymerisation of 100 mM P3C in 0.5 M H_2SO_4.* ***B)*** *CV and* ***C)*** *Nyquist plot of the bare Au surface, 100 mM P3C in 0.5 M H_2SO_4 after 10 cycles, 15 minute NHS/EDC activation, and 2 h NbGFP incubation.*